UNIVERSITY OF SOUTHAMPTON

FACULTY OF SCIENCE

School of Physics and Astronomy

COUPLING OF UPSTREAM SOLAR WIND FEATURES TO DAYSIDE AURORAL IONOSPHERIC EVENTS

By

Katie Throp

Thesis submitted for the degree of DOCTOR OF PHILOSOPHY

July 2005

UNIVERSITY OF SOUTHAMPTON

ABSTRACT

SCHOOL OF PHYSICS AND ASTRONOMY

Doctor of Philosophy

COUPLING OF UPSTREAM SOLAR WIND FEATURES TO DAYSIDE AURORAL IONOSPHERIC EVENTS

by Katie Throp

An multi-instrument investigation into the characteristic response of the global Magnetospheric-Ionospheric system to variations in upstream solar wind parameters. A method of determining the propagation time is developed to couple transient variations in solar wind pressure and IMF orientation to auroral ionospheric signatures observed by a range of ground-based and satellite-borne instruments.

Three events are studied, chosen in order to examine the individual and combined impact of the two upstream features on the ionosphere. The first event is characterized by two brief swings of the interplanetary magnetic field (IMF) towards a southward orientation. Modeling is used to fit observed variations in the peak proton emission intensity and reproduce the spatial distribution of the proton emission observed by a range of instruments. The second event sees a brief southward IMF turning accompanied by an increase in the solar wind dynamic pressure. Filtering is used as an effective method of separating the slow convection variations from the higher frequency pressure front effects, providing a way of interpreting both the ground-based data and model results. The third event is characterized by a rapid increase in the upstream solar wind pressure during a period of northward IMF. Filtering reveals pressure front signatures comparable to the second event and evidence of enhanced high-latitude convection effects.

Contents

List of Figures

List of Appendices

In memory of my grandfather Richard Throp from who I inherited my thirst for knowledge…

Acknowledgements

I would firstly like to thank my two supervisors; Betty Lanchester and Mike Lockwood, for there unwavering support and guidance throughout the four years. No matter how busy you were you always found time for me, I am eternally grateful. I would also like to thank the other members of the Solar Terrestrial Group at Southampton, you know who you are, for not only providing a relaxed and motivating place to work, but also great companionship whilst at conferences and on campaign. Molly and Elaina I will always have the photos. I would like to send a special thanks to Alan Rodgers at the British Antarctic Survey for his continuing help and support. I will never be able to look at a rotating vortex without thinking of you. I would like to thank the Rutherford Appleton Laboratory and Southampton University for providing my funding, with out which this thesis would never have written. I also want to express my gratitude to everyone who provided me with the data, in particular to the people at Leicester University.

Thanks to both Professor Mark Lester and Professor Malcolm Coe for giving me a fair and surprisingly enjoyable viva. I hope you enjoyed it to.

Now for the none scientist....firstly my parents Steven and Margaret Throp. Words cannot begin to describe the gratitude I feel for your encouragement and support over the last 28 years. You have always been there for me, even during my wilderness years...

To Emma, my sister and best friend, you are an angel, never change. I have to say thanks to all my friends: my best mates Liz Galley, Claire Rose, Shaggy Taylor, Jim Dibley, Hannah Lucas, Georgia Warren, Alison Ford for their support especially whilst writing my thesis, I can't have been much fun to be around. To all my other friends, I am lucky to have you.

Lastly I would like to thank my boyfriend Simon Shaw. Thank you for putting up with me, I am amazed you can. You have always been there for me and for that I will be eternally grateful. XXX

Chapter 1.

Introduction

This study investigates the characteristic response of the global Magnetospheric-Ionospheric system to variations in upstream solar wind parameters. The dynamics of Earth's magnetospheric plasma are largely driven by the solar wind, though the magnetosphere is not a passive respondent as it plays an important role in determining the location and amount of energy transferred from the solar wind into the terrestrial environment. The primary coupling mechanism is magnetic reconnection, which leads to a connection between the magnetic fields of the solar wind and of the magnetosphere enabling the solar and terrestrial plasmas to mix and energy to be transferred into the Earth's near-space environment and the upper atmosphere. Although magnetic reconnection is responsible for the majority of energy and momentum transfer, other solar wind processes also contribute; upstream solar wind pressure changes can dramatically affect the precipitation of charged particles into the upper atmosphere.

Electrodynamic changes at the outer magnetospheric boundary, the magnetopause, are communicated to the polar ionosphere via field-aligned currents. The ionospheric signatures that result are generated by the temporal and spatial evolution of these field-aligned currents. What upstream variations cause which ionospheric currents is complex and is a key part of the study presented in this thesis, which combines satellite-borne and ground-based data with numerical model predictions in order to relate observed upstream signatures with ionospheric measurements. In addition, the model results are used to separate the ionospheric response to reconnection from the effects of ionospheric coupling with other upstream features.

1.1 The Solar Wind – Magnetosphere System

1.1.1 The Solar Wind

The Sun emits a continuous stream of electrons and ions (predominantly hydrogen with some helium and heavier ions) from the solar corona. This charged particle stream, known as the solar wind, is a highly conducting plasma which carries with it a remnant of the solar magnetic field, called the interplanetary magnetic field (IMF). The huge difference in gas pressure between the solar corona and interplanetary space causes the solar wind to expand outwards at supersonic speeds of order 500 kms^{-1}.

Measurements taken from space-borne instruments continuously monitor the highly variable speed, composition and magnetic field of the solar wind as it propagates Earthwards. The ACE satellite in a "halo" orbit around the L1 libration point, where the gravitational pull of the Sun and the Earth are in equilibrium, allows for up to a 1-hour forecast on the solar wind conditions that will potentially impinge on the Earth's magnetosphere. The Wind satellite has been moved between an L1 halo orbit to large "petal" orbits around the Earth and so has monitored interplanetary space at large distances away from the ACE satellite.

1.1.2 Solar Wind – Magnetosphere Coupling

The Earth is, to a large extent, protected from the solar wind plasma flow by its magnetic field. This magnetic shield slows the solar wind and deflects it around the Earth forming a low-density cavity in the interplanetary medium called the magnetosphere. Without the external forces this would maintain a spherical shape, however the dynamic pressure of the solar wind compresses the dayside and, because of momentum transfer across the magnetopause drags the nightside into an extended tail.

Since the solar wind hits the magnetospheric obstacle with supersonic speeds, a bow shock is generated. Generally it is located upstream of the magnetopause at a distance exceeding 10 R_E, however its position can vary depending on the changeable solar wind parameters. The shock is important because it modifies the properties of the solar wind flow before the flow interacts with the magnetosphere; the plasma is slowed to subsonic speeds and a substantial fraction of the particles' kinetic energy is converted into thermal energy. In addition, the plasma number density and magnetic field are increased behind the shock. This region of de-accelerated plasma is known as the magnetosheath and lies next to the outer boundary of the magnetosphere, the magnetopause. The position of the magnetopause and the size of the magnetospheric cavity is determined by the balance between the pressure of the solar wind confining it and the pressure exerted by the magnetosphere outward. For a typical solar wind momentum flux, the mean dayside magnetopause is found at about 10-15 R_E. It is the processes acting at this boundary that are responsible for determining the amount of energy the magnetosphere receives from the solar wind flow.

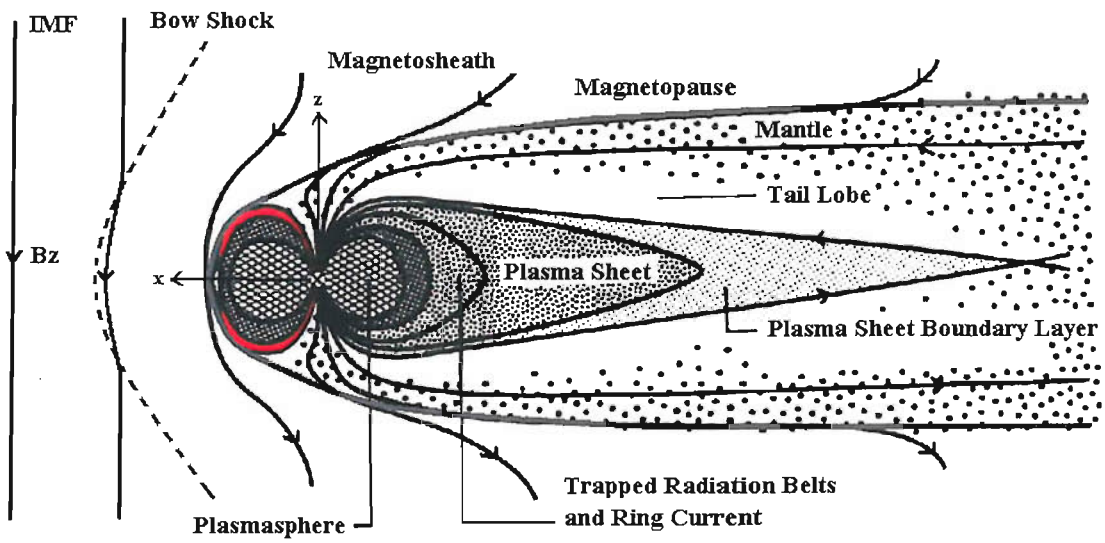

Figure 1.1 A schematic noon-midnight cross-section of the open magnetosphere and the geomagnetic tail [from Wolf, 1995]. The solid black lines represent the IMF and geomagnetic field lines, the arrowheads show the direction of the field. Magnetospheric convection of the field lines is observed in

response to dayside reconnection. The shaded regions differentiate between the different plasma regions. The red shaded area corresponds to the magnetic cusp.

Understanding the coupling of the variable solar wind to the magnetosphere requires fundamental knowledge of the properties of magnetised plasmas. Even with modern supercomputers and data storage keeping track of the separate orbits of particles in a plasma in the presence of electric and magnetic fields is not possible. The collective behaviour of charged particles is instead analysed using the concepts of fluid dynamics. Here, the motion of single particles is replaced by the average motion of many particles in a finite volume element of plasma. The theory that describes the macroscopic fluid motion of the electrically conducting plasma in the presence of electromagnetic fields is referred to as Magnetohydrodynamics (MHD). One implication of this theory is that, for large spatial scales, a packet of plasma remains bound to a specific field line (the so-called "frozen-in-flux theorem"), whether the field lines originate from the IMF or the Earth's geomagnetic field. Whenever the field line moves due to the action of external forces, the plasma tied to that field line is also set into motion. If the magnetopause is considered to be a closed boundary (with no magnetic field component normal to the surface), there is no transfer of mass (nor energy) across it. The terrestrial field lines forming this closed boundary have both ends attached to the Earth; therefore a method of changing the topology of these field lines is the most efficient way to allow for direct entry of mass into the magnetosphere. This method is "magnetic reconnection". Other mechanisms of mass and energy transfer across the magnetopause (for example wave-driven diffusion) are negligible in comparison.

Magnetic reconnection depends on the strength and relative orientation of the IMF with respect to the terrestrial magnetic field. The IMF in general is written as $\mathbf{B} = (B_X\mathbf{i}, B_Y\mathbf{j}, B_Z\mathbf{k})$, where the components B_X and B_Y are in the ecliptic plane and B_Z is perpendicular to it and the corresponding unit vectors are **i, j** and **k,** respectively. The

x axis points toward the Sun and y points toward dusk (antiparallel to the planetary motion) and **z** lies in the north-south plane of the Earth's magnetic field and is therefore referred to as pointing northward ($B_z > 0$) or southward ($B_z < 0$). This is the geocentric solar ecliptic (GSE) coordinate system (see Appendix A).

Near the nose of the dayside magnetopause, reconnection takes place when the IMF points southward because the geomagnetic field there points northward. The oppositely-directed fields reconnect, linking the IMF and terrestrial field lines so that the plasma from the two regimes mix by flowing along the reconnected field lines. These "merged" field lines split into two open field lines, so called because each have one end attached to the Earth and the other stretching out into the solar wind. The point at which this split first occurs marks the low-latitude boundary of the "cusp" where solar wind plasma is free to flow into the magnetosphere along newly-opened field lines. The solar wind flow subsequently pulls the solar wind portion of the open field line antisunwards into the "lobes" of the magnetotail. On field lines that have been open for more than about 15 min., plasma continues to enter the magnetosphere but is swept by the flow into the magnetospheric tail, rather than being precipitated into the ionosphere. However, there is no sharp poleward edge to the cusp, rather the precipitation evolves from "cusp" to "mantle" to "polar cap" as the field line moves antisunward [Lockwood, 1997]. The two nearly antiparallel lobe fields are separated by the cross-tail current sheet where they can reconnect, in a manner similar to the fields of the magnetopause. This reconnection re-closes the open field lines. Magnetic merging at the dayside and in the tail do not occur at singular points but rather along a line. Such a line is called an "X-line", since along this line the magnetic field lines have a topology resembling this letter in the plane perpendicular to the line. In the tail, the newly-connected geomagnetic field line has been stretched antisunward away from an equilibrium position and relaxes Earthward. The other side of the tail X-line the field lines are disconnected from the Earth and they, and the plasma frozen onto them, are ejected down the tail and ultimately rejoins the solar wind flow. This large-scale circulation of magnetic flux with its frozen-in plasma is called "convection" and was first proposed by Dungey [Dungey, 1961].

The oval region containing the footprints of the open field lines located between the reconnection points at the magnetopause and the magnetotail is one definition of the "polar cap" (there are several others that are easier to define in observations). The extent of the polar cap is defined by the open-closed field line boundary (OCB). The plasma convecting on the open field lines across the polar cap corresponds to a dawn-dusk electric field. Integrating that electric field over the dawn-dusk diameter of the polar cap gives a potential difference, known as the "transpolar voltage". The same open field lines map to a region in interplanetary space, which is called the "Stern gap", typically ~ 7.5 R_E wide in the y-direction (duskward). Figure 1.2 shows the antisunward footprint motion of these field lines in the polar cap. Magnetopause reconnection moves field lines from the closed to the open field line region on the dayside and the newly-opened field lines subsequently move antisunward under the combined action of the magnetic curvature force (the tendency for MHD flux tubes to straighten) and the solar wind flow. These motions are seen in the ionospheric field line footprints and the frozen-in F-layer ionospheric plasma as the motion into and across the polar cap towards the nightside. Tail reconnection causes the motion of open field lines on the nightside into the closed field line region, and field lines convect back sunward under the magnetic curvature force. This sunward convection of the field lines reconnected in the tail leads to a sunward convection of the footprints of these field lines at lower latitudes (outside the polar cap in the auroral oval). This leads to a two-cell convection pattern, the streamlines of which are equivalent to equipotential contours. This "steady state" picture of reconnection driven convection holds for southward IMF only. For northward IMF reconnection takes place at latitudes poleward of the magnetic cusp. Here IMF field lines, draped in the magnetosheath, connect with field lines in the tail lobes reconfiguring flux that is already open. Unlike the situation for southward IMF, no new open flux is generated.

An idealised view of reconnection assumes reconnection voltages that are the same at the dayside magnetopause and in the tail lobe, leading to a steady state of

convection. In reality the orientation of the upstream IMF is continually changing resulting in a constantly varying reconnection rate. The tail reconnection site can gain no information on these changes for at least several tens of minutes and thus equal magnetopause and tail reconnection voltages will be random, chance occurrences or due to the rare occasions when the IMF orientation remains steady. Thus an imbalance, a state of "non-steady" convection, is expected to be the normal behaviour of the magnetosphere. An example of "non-steady" state convection occurs when the IMF swings southwards after a period of northward IMF, generating what is called a "substorm". The magnetosphere does not generally evolve smoothly toward a new steady state of enhanced convection. The reconnection rate at the dayside increases; open flux is generated and transported to the tail. Because the tail reconnection does not instantaneously react to the build up of flux in the tail lobes, the magnetotail flares (grows wider) and the lobe field increases in the mid-tail region. The period of enhanced tail loading is called "growth phase". It typically lasts for about one hour. Because there is an imbalance in reconnection rates at the dayside and at the tail, the amount of closed flux returning to the dayside is reduced, causing the magnetopause to move inward due to a decrease in the dayside magnetic flux. This is called erosion. As the magnetic flux continues to accumulate in the tail, the cross tail current increases and eventually becomes unstable, triggering an increase in the rate of reconnection and releasing the stored up energy as the re-closed field lines snap back sunwards. This is known as the "expansion phase", which typically lasts 30 – 60 mins. This is followed by the "recovery phase" in which the magnetosphere returns to a quiet state. These phases make up a magnetospheric substorm, a process that is characterised by the cycle of energy storage and release, leading to enhancements in currents flowing in the polar ionosphere and associated disturbances in the strength of the high-latitude surface magnetic field.

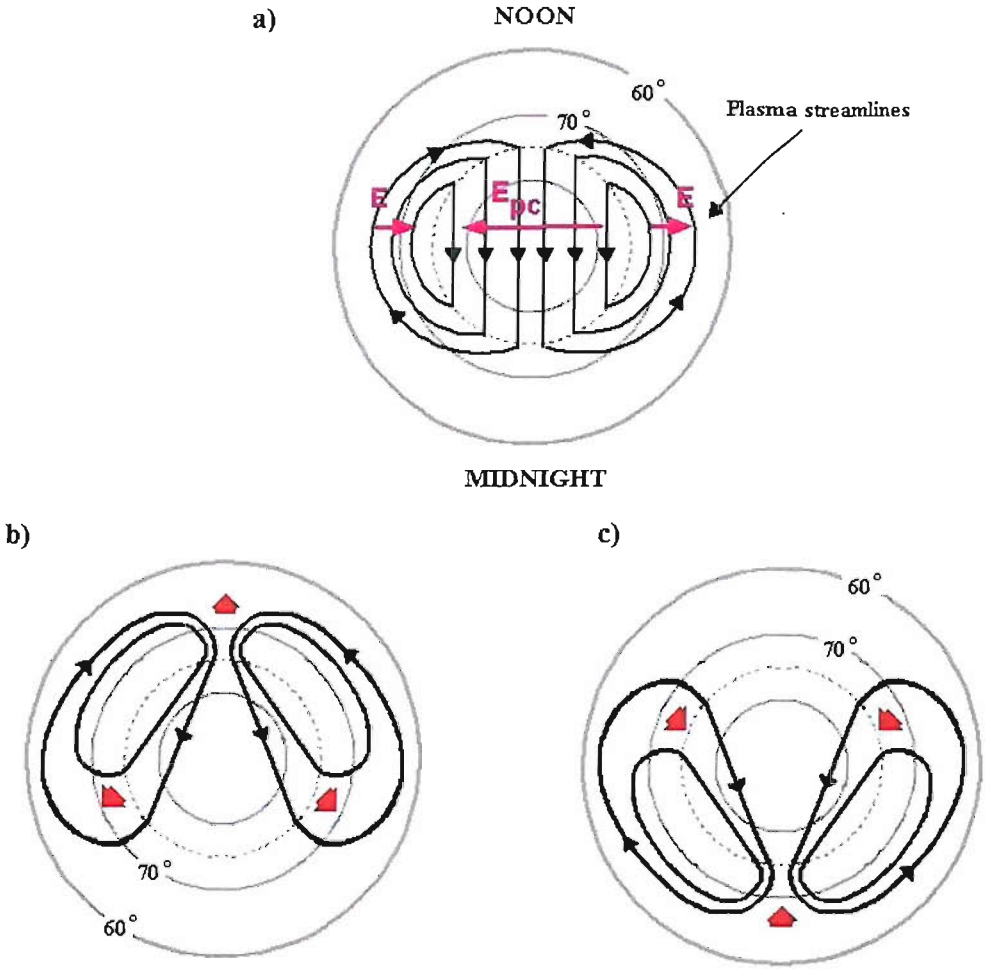

Figure 1.2 ***a)*** The two cell convection pattern translated into a two cell pattern of equipotential contours. This equipotential pattern is equivalent to an ionospheric electric field that is directed toward dusk in the northern polar cap. The polar cap is represented by the dotted line, this boundary is the open-closed field line boundary (OCB) . ***b)*** Dayside driven reconnection plasma flows (black arrows) with reconnection rate at the dayside being larger than the nightside reconnection rate, resulting in an expanding polar cap (red arrows). *c)* The opposite situation with the nightside reconnection rate being larger than the dayside reconnection rate, the polar cap contracts [Lockwood et al., 1990].

1.2 The Magnetosphere - Ionosphere System

1.2.1 The Magnetic Cusps

The motion of the magnetic field lines in response to reconnection-induced convection is communicated down to the high-latitude ionosphere. These field lines are also open to the solar wind and provide a path for magnetosheath plasma to enter the ionosphere through the magnetic cusps. Because of the field line motion, incoming particles are dispersed, an effect that is most noticeable in the slower ions, but can also sometimes be detected in the faster electrons. These regions, represented in Figure 1.1, are centred on local noon and extend approximately 2-3 hours in longitude and ~ 1° in latitude, thus forming funnels of open magnetic flux with a footprint of finite size in the ionosphere [Crooker et al., 1991]. In the ionosphere, the equatorward boundary of the cusp is defined as the projection of the dayside reconnection X-line. During periods of strong magnetopause reconnection, such as substorm growth phases, the inward erosion of the magnetopause is mirrored by equatorward erosion of the equatorward edge of the cusp. The position of the cusp is therefore strongly dependent on the IMF conditions, but lies at a nominal magnetic latitude of about 77°.

Equatorward of the cusp, and extending further towards dawn and dusk, is a region of sheath plasma precipitation called the "cleft" (or "low-latitude boundary layer"). The main distinction between the cleft/LLBL and the cusp is that the former contains a full or partial magnetospheric plasma population, whereas the latter does not. Traditionally, the cleft was seen as being on closed field lines and the presence of sheath precipitation was interpreted as being the result of a second type of injection process, other than reconnection, that moves sheath plasma onto closed field lines. However, a viable mechanism for doing this has not been defined. The alternative explanations involve reconnection: the cleft is either field lines that have been so recently opened that the magnetospheric plasma has not had time to escape into the

magnetosheath [Lockwood, 1997] or they are field lines that were open but have re-closed during northward IMF by reconnection at the sunward edge of the tail lobes in both hemispheres [Song and Russell, 1992].

Associated with the downward-flowing sheath plasma of the cusp/cleft is the "cleft ion fountain", from which plasma flows upward from the ionosphere into the magnetosphere, with the peak out flow occurring in the pre-noon sector [Lockwood et al.,1985]. The injection of magnetosheath plasma into the cusp has been found to be one of the mechanisms that heat the ionospheric plasma in the cusp/cleft region and thus drive the outflow of ionospheric plasma into the magnetosphere.

1.2.2 Field Line Particle Motions

The electric charge of particles couples them to the magnetic field line on which they are precipitating, affecting their motion. A charged particle in a magnetic field will move in a circular fashion about a point called the guiding centre. This gyroscopic motion has a constant frequency, the gyrofrequency ω_g, in a constant magnetic field and is given by:

$$\omega_g = \frac{qB}{m}$$

where q is the charge, B is the magnetic flux density and m is the particle mass. The direction of gyration depends on the sign of the particle charge and the radius of the gyration depends on its mass. The particles gyrate about the magnetic field, and will generally move at a constant speed along the magnetic field. The resulting motion is helical and the angle between the particle velocity and the magnetic field is known as the pitch angle, α:

$$\alpha = \tan^{-1} \frac{v_{\parallel}}{v_{\perp}}$$

where $v_{||}$ is the particle velocity parallel to **B**, and $v_{\perp}$ is the particle speed perpendicular to **B**.

The Earth's magnetic field is approximated to lowest order as a dipole field that changes in direction and magnitude both along and across the field. Each dipole field lines has a given "L-value" defined as $L = r/R_E$, where r is the geocentric distance to the equatorial crossing point of the field line in question and R_E is an Earth radius. In the real magnetosphere, the compression of the dayside makes the crossing point at $r < L\ R_E$ and the extended tail makes nightside field lines cross at $r > L\ R_E$. A related parameter is a form of magnetic latitude called "invariant latitude" defined as $\Lambda = \cos^{-1}(1/L)^{1/2}$.

The Earth's magnetic field has a field strength minimum at the equator and converging field lines in both hemispheres. In a converging magnetic field, a particle moving into regions of stronger field experiences a force directed away from the direction of the increasing field. This means that $v_{||}$ decreases to zero at some maximum field strength. As the motion along the field does not change the particle's energy, the $v_{\perp}$ must increase and $v_{||}$ fall, such that $v = (v_{||}^2 + v_{\perp}^2)^{1/2}$ is constant. The decrease in $v_{||}$ as the particle moves into converging field lines is described as being under the action of a "mirror force" that acts along **B**. When $v_{\perp}$ reaches the total velocity of the particle, $v_{||}$ goes to zero and reverses polarity i.e. the particle motion reverses at a "mirror point". The altitude in the Earth's magnetic field where a particle experiences the mirror point occurs depends on the particle's pitch angle as it crosses the geomagnetic equator. Particles of larger pitch angles mirror at higher altitudes in the Earth's magnetic field, while particles of lower pitch angles can penetrate further into the atmosphere. It is this mirroring mechanism that traps particles in a region of the Earth's dipole field called the ring current, as shown in Figure 1.1. Inside the ring current is a torus shaped region called the plasmasphere where the plasma co-rotates with the Earth rather than taking past in the solar wind-driven convection of the outer magnetosphere. The low-energy ionospheric plasma particles that populate this region therefore rotate with the Earth. This region extends

up to latitudes of approximately 60° [Cowley, 1977] and outwards to distances of about $4R_E$. The outer limit of the plasmasphere is called the plasmapause.

The overall motion of the charged particle is also affected by the electric field that is coupled with the magnetic field. Inside the plasmasphere that electric field is such that it causes co-rotation, outside it is such that it causes convection. The plasmapause is close to where the two balance out. The electrical force accelerates the particle during a part of each orbit and decelerates it during the remaining part of the orbit. Figure 1.3 shows that this causes a net displacement of a particle in a direction perpendicular to **E** and **B**, and independent of the sign of the charge. The drift in the guiding centre of a particle under the influence of an electric field is known as the **E** × **B** drift. In the absence of currents, all particles move with the same velocity and so the ion velocity $\mathbf{V}_i$ equals the electron velocity $\mathbf{V}_e$. The plasma velocity **V** is defined as the average of the ion and electron velocities, weighted by their mass:

$$\mathbf{V} = (\mathbf{V}_e m_e + \mathbf{V}_i m_i) / (m_e + m_i)$$

Thus in the absence of currents, $\mathbf{V}_e = \mathbf{V}_i = \mathbf{V}$. and for ideal MHD, the frozen-in theorem yields

$$V = \frac{E \times B}{|B|^2}$$

. Currents cause the ions and electrons to drift with different velocities (so $\mathbf{V}_e$, $\mathbf{V}_i$ and **V** are no longer all equal). Note that such currents need not be not a violation of the frozen in theorem which states that the field lines move with the plasma velocity **V**, not the individual species velocities $\mathbf{V}_e$ and $\mathbf{V}_i$. Other currents are caused by collisions between charged particles and neutral gas particles (see below) and these do constitute a breakdown in the frozen-in approximation, as the plasma velocity is no longer the same as the field line velocity [Richmond and Thayer, 2000].

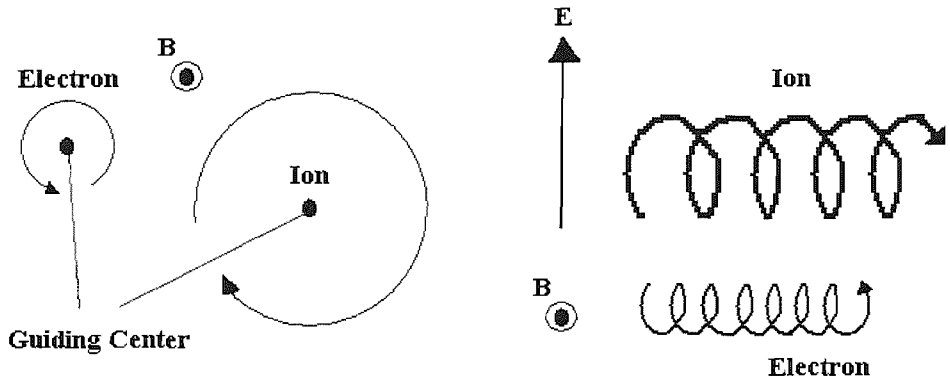

Figure 1.3 Gyration of charged particles around a guiding centre [Baumjohann and Treumann, 1997].

1.2.3 The Ionosphere

The ionosphere is the ionized component of the Earth's upper atmosphere. At subauroral latitudes, the primary method of ionization is photoionization, while in the auroral oval impact ionization by precipitating particles plays an important role in the production of ionospheric plasma. The varying dynamics and chemistry of the ionosphere is vertically structured into 3 layers that differ from one another in composition, density, ionization sources and degree of variability. These layers are known as the D (60 – 90 km), E (90 – 150 km) and F (150 – 800 km) layers. The dominant ions in the D and E regions are NO^+ and O_2^+, which are produced by extreme ultraviolet (EUV) radiation and energetic particle precipitation (exceeding about 1 keV). In the F region, where the bulk of the ionospheric plasma resides, O^+ dominates. Here the main sources of ionization are solar (UV) radiation and lower energy particle precipitation, as found in the cusp and cleft regions. Above the main F region is a region of exponentially decreasing density known as the "topside ionosphere".

1.2.4 The Ionospheric Current System

Collisions between the ionized particles and the neutrals in the ionospheric plasma are important and determine the electrical conductivity. At F region altitudes, the collision frequency is low and the plasma is free to drift with the $\mathbf{E} \times \mathbf{B}$ drift velocity. In the upper E region, the electrons can still drift with the $\mathbf{E} \times \mathbf{B}$ velocity due to the low electron-neutral collision frequency, however the ion-neutral collisions cause the ions to be diverted. In the lower E region, the higher frequency of collisions prevents any ion movement, relative to the neutral gas, whereas the electrons still move but are deflected and slowed by collisions with the neutrals. The ions and electrons are therefore moving with different velocities, resulting in current flow. In the E region Hall currents flow in the direction antiparallel to the ionospheric convection flows seen in the overlying F region (i.e. perpendicular to the electric field) and Pederson current flows in the direction of the electric field. Figure 1.4 is a schematic of the E region currents that flow in association with the Dungey cycle convection mapped into the F region. The Hall current flows in the opposite direction to the convection flows represented by the black arrows. The ionosphere is incompressible in the sense that the magnetic field is dominated by currents in the Earth's interior and approximately constant: this means that F region flow streamlines form continuous loops in the ionosphere with no sources and sinks. For a uniform ionospheric conductivity the same is true of the Hall currents, which therefore do not connect to field-aligned currents (FACs) in or out of the ionosphere (in reality Hall currents do connect to FACs to some extent at ionospheric conductivity gradients). The Pederson current flows in the direction of the E-field and so is also represented by the red arrows. Figure 1.4 shows that unlike the Hall current, the Pederson currents must require closure through a system of FACs. In the polar cap, the Pederson currents flow from dawn to dusk, here the "Region 1" field-aligned current system (green line) in the vicinity of the polar cap boundary closes the Pederson current circuit system by connecting the ionosphere to the "Chapman-Ferraro currents" in the magnetopause. Region 1 currents required are downward on the dawn flank of the polar cap and upward on the dusk flank. Equatorward of the polar cap, in the auroral oval, the

Pederson currents flow from dusk-to-dawn and are closed by a combination of the Region 1 currents and the "Region 2" currents (blue line) located on the equatorward edge of the oval. These Region 2 currents close via the "ring current" in the inner magnetosphere and are oppositely directed to the Region 1 currents at the same local time (i.e. upward at dawn, down at dusk)

1.2.5 Auroral Emissions

Precipitating particles do not only produce ionization. At higher latitudes where the geomagnetic field lines map to the plasma sheet region, located around the mid-plane of the tail shown in Figure 1.1, collisions between precipitating energetic particles and the neutral species also produces electromagnetic radiation with a range of different wavelengths; from ultraviolet to infrared. Radiation produced at visible wavelengths is known as the aurora and is seen at latitudes of about 70° inside a belt called the "auroral oval". Kinetic energy is converted into energy stored in the chemically excited states of atmospheric species, emitting photons of wavelengths determined by the energy transitions in the relaxation processes.

The auroral spectrum depends on the composition of the upper ionosphere and the precipitating population and energy spectrum. Auroral emissions are excited principally by electron precipitation. The commonly observed green colour in the aurora is due to the "auroral green line" of atomic oxygen at 557.7 nm, typically observed at altitudes between 100 and 200 km. The two-step process that produces this emission is:

$$O(^3P) + e \rightarrow O(^1S) + e'$$
$$O(^1S) \rightarrow O(^1D) + h\nu\ (557.7)$$

where e' has less energy than e. The $O(^1S)$ atom can also de-excite directly to the ground state $O(^3P_2)$ via the emission of an ultraviolet photon:

$$O(^1S) \rightarrow O(^3P_2) + h\nu\ (295.8)$$

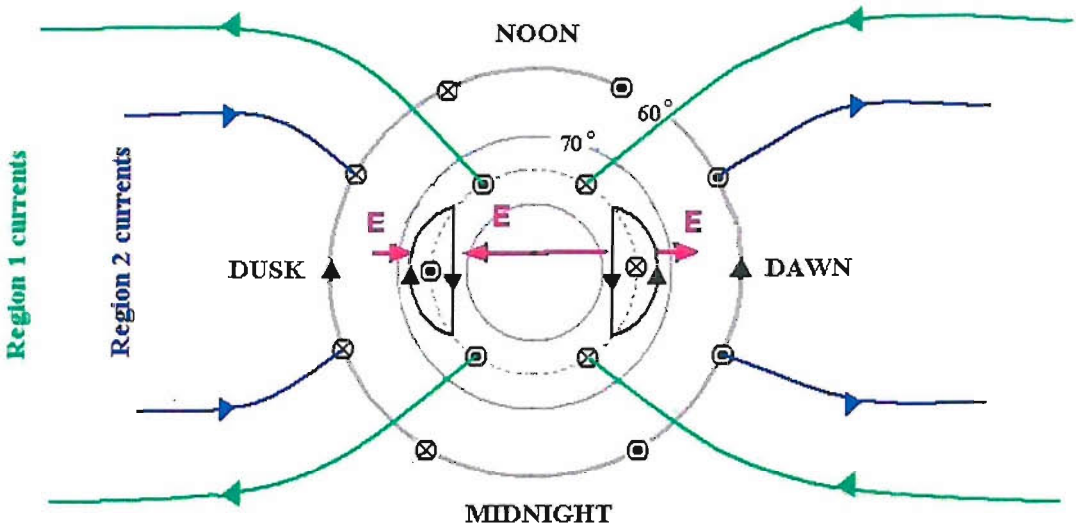

Figure 1.4 Schematic of the polar cap/auroral oval current system. The solid black lines represent the ionospheric convection streamlines, the black arrows representing the direction of these flows. The Hall current flows in the opposite direction to these arrows. The dashed grey line represents the polar cap boundary. The red arrows show the direction of the electric field, along which the Pederson currents also flow. The field-aligned Region 1 and 2 current systems are shown, with the sense of the currents being shown; dots are upward and crosses are downward.

At higher altitudes the "auroral red line" of atomic oxygen can be observed at 630.0 nm. It is created by "soft" low-energy electrons, which do not penetrate as deeply into the atmosphere. Such emission is caused by the precipitation of sheath electrons in the cusp and cleft regions

$$O(^3P) + e \rightarrow O(^1D) + e'$$
$$O(^1D) \rightarrow O(^3P_2) + h\nu\ (630.0)$$

Both lines represent so-called "forbidden lines". These excited energy states are metastable and under normal atmospheric pressure the excited atom would loose its energy by collisions with other particles rather than by light emission before de-excitation by emission (i.e. the emission is "quenched"). However in the rarified upper atmosphere this is not true, although the excited $O(^1D)$ state has such a long lifetime (110 seconds) that the red line is quenched by collisions at lower altitudes. Note that the existence of a $^3P_1$ state close to the ground state $^3P_2$ means that both the red and UV emissions are doublets (de-excitation to the $^3P_1$ from $O(^1D)$ and $O(^1S)$ giving 636.4nm and 297.2nm, respectively).

Ionized atoms and molecules also produce aurora. An example of these is ionized diatomic nitrogen (N_2^+1N), which produces a blue-line emission at 427.8 nm:

$$N_2 + e \rightarrow (N_2^+)^* + e' + e_n$$
$$(N_2^+)^* \rightarrow N_2^+ + h\nu\ (427.8)$$

The asterisk indicates that the molecular ion is created in an excited state. Ionized atomic oxygen (O^+) produces a red-line emission at 844.6 nm. These are prompt transitions and can be used to map the region of electron precipitation that produces discrete structures (as opposed to the forbidden transitions which allow motion of the excited atoms before emission).

Although auroral emissions are excited principally by electron precipitation, some are produced by precipitating protons (the "proton aurora"). Important hydrogen lines exist in the auroral spectrum [Vegard, 1939], each resulting from excited hydrogen atoms that are produced when energetic protons (H^+) interact with ambient neutrals in the atmosphere. The Balmer series involves transitions ending with the first excited state of hydrogen, the resulting photon emissions are in the visible spectrum. Examples of transitions in the Balmer series are: H_α (656.3 nm) and H_β (486.1 nm). The Lyman series involves transitions that end with the ground state of hydrogen, the resulting photon emissions are in the ultraviolet spectrum. An example of a transition in the Lyman series is: Lyman-α (121.8 nm), the mechanism for which can be written:

$$X + H^+ \rightarrow X^+ + H^*$$
$$X^* \rightarrow H + h\nu$$

Because these are charge-changing reactions, the incident proton beam penetrating the atmosphere becomes a mixture of protons and H atoms [e.g. Rees, 1989]. Because the hydrogen atoms retain the energy of the protons on charge exchange, the emissions of excited H atoms are Doppler-broadened and Doppler–shifted. The emitted photon has a Doppler displacement that depends on the velocity of the emitting hydrogen atom and the angle between the velocity vector and the direction of the photon [Omholt, 1971]. Observed from the ground along the magnetic zenith, the H emission profile is blue-shifted, because most of the energetic hydrogen atoms are moving downward. Multiple interactions with the atmosphere will produce a continuum of Doppler-shifted emissions at wavelengths extending from zero Doppler-shift to the maximum Doppler shift determined by the energy of the incident proton. Because neutral H atoms do not gyrate around the magnetic field lines they can move away from the field line down which the primary protons precipitated before emitting. Thus the proton aurora is spatially spread around the region of precipitation.

Electrons are also produced inside the proton beam through ionization and stripping reactions. These electrons, also called "secondary electrons", have low mean energy [Strickland et al., 1993] and are effective at exciting O atoms and N_2 molecule emissions. Significant fluxes of precipitating protons can, in fact, be an important contributor to the "electron aurora" [Frey et al., 2001, 2002; Galand, 2001]. All these interactions lead to electron and ion production, heating and excitation, and to the spectacular auroral emissions. Protons in the keV energy range deposit most of their energy in the E-region (100-160 km), whereas MeV proton energy deposition will occur at lower altitudes, typically in the D-region and below [Galand, 2001].

Aurora that is caused by proton precipitation is not as bright and spectacular as that caused by electrons. This does not, however, indicate that the effect of proton aurora on the ionosphere is negligible. The proton aurora is diffuse owing to the contribution of H atoms whose path, independent of the magnetic field configuration, produces spreading of the incident proton beam [Eather, 1967].

1.2.6 Identification of the Open/Closed Field Line Boundary and Region-1 Field-aligned currents

Auroral emissions are frequently used to try to identify the ionospheric footprint of the open/closed boundary (OCB). Because the near-noon OCB lies on the equatorward edge of the cusp precipitation it has become common practice to try to identify the dayside OCB using the 630.0 nm red-line emission of atomic oxygen. Rees and Luckey [1974] demonstrated the utility of the 630.0 nm red line emission rates when used in ratio with the 557.7 nm emission of atomic oxygen to determine the position of the OCB. A high 630.0/557.7 ratio indicates the low energy (soft) precipitation that characterises the cusp at ionospheric heights. It also signifies the lack of 557.7 nm emissions that occurs in the cusp region. (Note, however, that filamentary green line emissions are detected in transient events in the cusp region [Sandholt, 1988]. Observations from the ground show the 557.7 nm emission

reducing to background levels nearer the OCB and the 630.0 nm emission increasing at latitudes poleward of the boundary.

It is important to remember that because the 630.0 nm line is a forbidden line, the excitation point of the oxygen atom is most likely to be far from the emission point. Therefore the cusp auroral emissions in the red line occur sufficiently delayed from the excitation that they are well separated from the position inferred from a particle detector. (For example, during the 110 s mean radiative lifetime of the $O(^1D)$ state, the atom will move 55 km for a typical thermospheric wind speed of 0.5 kms^{-1} before emitting a red-line photon). For this reason the red line emission, and hence the 630.0/557.7 ratio, has limited uses in the study of fine structure in the cusp aurora, however it is a good indicator of the location of the dayside OCB when supplemented with other instrument observations.

In general, the high mobility of electrons, compared to ions, means that most of the field-aligned current is carried by electrons. Thus downward field-aligned currents are mainly caused by streams of up-going ionospheric electrons whereas the upward field aligned currents are predominantly carried by precipitating magnetospheric electrons. The latter is associated with auroral emission (particularly UV and green-line) whereas the former is not. If present within a broad region of precipitation, a filamentary downward FAC can sometimes be seen as the absence of the surrounding emission in the so-called "black aurora". On the other hand several studies have attempted to identify the upward Region-1 FACs of the dusk sector from UV and green-line emissions and associate the poleward edge of these emissions with the OCB. This approach has some validity on the dayside, but is unreliable on the nightside where there is frequently a considerable gap between the OCB and the poleward edge of the precipitation [Elphinstone et al., 1991].

1.3 Solar Wind – Ionosphere Coupling Mechanisms

Extensive studies have been carried out into the coupling mechanisms that allow the transfer of energy and momentum from the solar wind into the terrestrial environment. The various mechanisms that couple changes in upstream Interplanetary Magnetic Field (IMF) and solar wind to the Magnetosphere/Ionosphere system are examined in this section.

1.3.1 IMF Coupling Mechanisms

The phenomenon of magnetic reconnection has been successful in explaining most of the dominant features of the transfer of mass, energy and momentum across the magnetopause and has the potential to explain many of the remaining features. This process involves the coupling of the magnetized solar wind with the terrestrial field lines, discussed in Section 1.1.2, a process that results from a breakdown of the frozen-in approximation at the centre of thin current sheets to allow for the interconnection of these field lines. The breakdown of the frozen-in approximation is associated with the small spatial scale across a thin current sheet but may be aided by anomalous resistivity of the plasma, which allows the diffusion of field lines with respect to the plasma to become more important.

If the frozen-in theorem applied everywhere, there would be no mixing of the IMF and geomagnetic field. The two fields would be kept separate by the magnetopause current sheet between them. Figure 1.5 shows magnetic reconnection occurring at an x-type magnetic neutral line. The oppositely directed magnetosheath and magnetospheric field lines are separated by a thin Chapman-Ferraro current flowing in the magnetopause. In the centre a process of "magnetic merging" occurs, where field lines diffuse together and are reconfigured to generate field lines that thread the current sheet, in contradiction to the frozen-in theorem.

In order to understand this process more quantitatively, it is necessary to consider the general magnetic induction equation, which gives the rate of change of magnetic field **B**:

$$\frac{\partial \boldsymbol{B}}{\partial t} = \nabla \times (\boldsymbol{V} \times \boldsymbol{B}) + \frac{\nabla^2 \boldsymbol{B}}{\mu_0 \sigma}$$

This is obtained by combining the generalized Ohm's law with Faraday's and Ampère's law. The first term '$\nabla \times (\boldsymbol{V} \times \boldsymbol{B})$' is known as the "convection term", the second term '$\frac{\nabla^2 \boldsymbol{B}}{\mu_0 \sigma}$' is the "diffusion term": μ_o is the permeability of free space and σ the electrical conductivity and the product $\mu_o\sigma$ is sometimes called the "magnetic diffusivity". If the convection term is greater than diffusion term, the frozen-in approximation applies and the plasma will be transported by the magnetic field lines [e.g. Lockwood and Morley, 2004]. In plasma regions where this is the case, the effects of magnetic field diffusion can largely be neglected. Such regions can be identified by the "magnetic Reynold's number" R_m, which is the ratio of the convection term over the diffusion term and, from the induction equation, is of order $\mu_o\sigma V_c L_c$, where V_c and L_c, are the characteristic speeds and scale lengths of the plasma. Regions where R_m is very large are the solar wind and the Earth's magnetosphere, mainly because of the large-scale length. L_c. This is why the IMF is dragged out of the Sun by the solar wind and why they are mainly excluded from magnetospheric cavity which is filled with the geomagnetic field [Parks, 1991]. However in current sheets L_c is small and σ may be reduced by wave particle interactions ("anomalous resistivity") such that R_m approaches, or even falls below, unity. In these regions the diffusion term is significant, frozen-in breaks down and the field lines are able to diffuse through the plasma.

In Figure 1.5 the shaded region surrounding the x-line is the region within magnetic diffusion is important. The diffusion of the magnetic field lines into this region (from both sides of the current sheet) corresponds to an electric field called the reconnection

rate, which is the same everywhere in steady state (by Faraday's law $\nabla \times \mathbf{E} = d\mathbf{B}/dt = 0$). At the centre of the diffusion region the field lines can reconfigure so that they thread the current sheet. The newly reconnected field lines move away from the reconnection site under the magnetic curvature force (in steady state, the motion corresponding to the same electric field **E** as in the inflow region) and as plasma can flow along them they will be populated by a mixture of plasma from both sides of the current sheet to an extent determined buy the flight time of the particles. The conditions that facilitate reconnection are the subject of much debate. Regarding the field orientations required across the current sheet there are two main hypotheses: "component" reconnection and "antiparallel" reconnection. Component reconnection does not require the fields on the two sides of the current sheet to be antiparallel, just that they have magnetic field components that are antiparallel to each other [Gonzalez and Mozer, 1974], the perpendicular components have no effect on the reconnection itself. In this case, the X-line in the dayside magnetopause is thought of as remaining relatively close to the subsolar point and the reconnection rate varying with the magnetic shear across the current sheet (i.e. the magnetosheath field "clock" angle in the frame of the geomagnetic field). The antiparallel hypothesis however, requires that the reconnection field lines be close to antiparallel; changes in magnetosheath field angle relative to the interior field moves the X-line over the magnetopause to accommodate this condition [Crooker, 1979] and reconnection voltage changes are dominated by the changes in the length of the X-line. Figure 1.6 gives a schematic illustration of the two hypotheses. Figure 1.6a shows two different orientations of the sheath field (projections onto the l-m plane of the magnetopause are B_{sh} and B_{sh}') for component reconnection at a reconnection site X. Figure 1.6b shows the reconnection site X' and X'' needed to give antiparallel reconnection for the same sheath field orientations. In both cases, θ_{sh} is the sheath field clock angle where:

$$\theta_{sh} = \tan^{-1} \frac{|B_y|_{sh}}{|B_z|_{sh}}$$

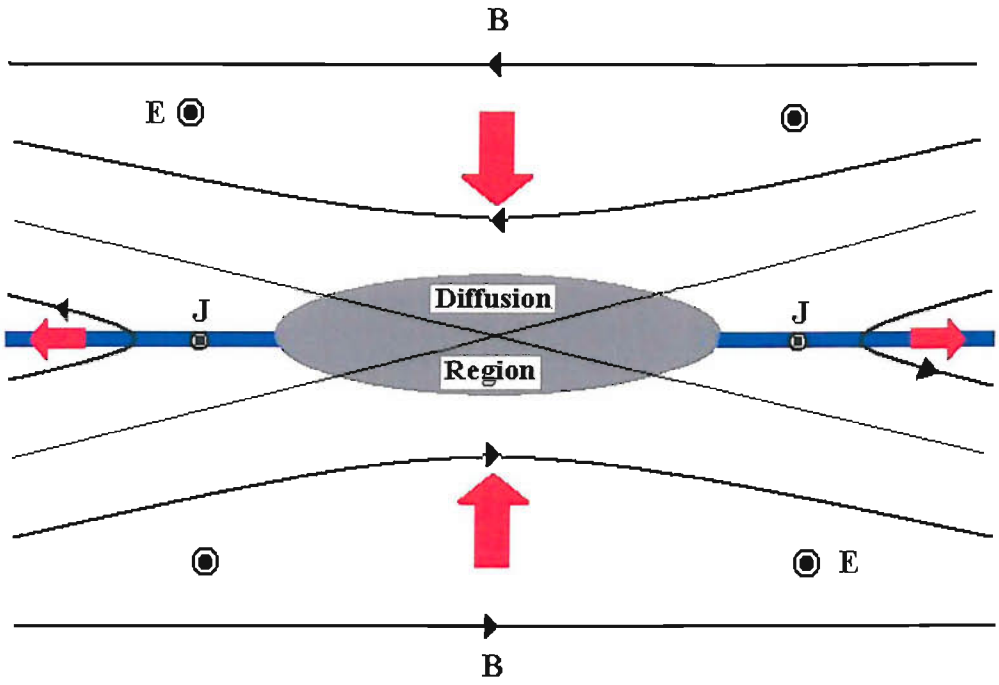

Figure 1.5 Schematic illustration of magnetic reconnection occurring at an x-type magnetic neutral line. Oppositely directed magnetic field lines, and the plasma attached to them, flow in from the top and bottom of the figure and flow out toward both sides. The flow directions are shown by the red arrows. Only in the shaded diffusion region, where the frozen-in theorem breaks down, is plasma not tied to the field lines and reconnection can take place. The separatices are marked by the light grey lines. The horizontal blue line marks the position of the current sheet. The current in the sheet points out of the page. In steady state the electric field is uniform throughout the region shown and also points out of the page.

Both hypotheses predict the same reconnection sites, behaviour and reconnection voltage for purely southward and purely northward IMF orientations. For purely southward IMF, $\theta_{sh} = 180°$ ($[B_z]_{GSM} < 0$, $[B_y]_{GSM} = 0$), the reconnection site will be equatorial. The newly-opened field lines evolve away from the reconnection site under the influence of the magnetic curvature ("tension") and the magnetosheath flow. As they are swept poleward, the injected ions are accelerated on crossing at the point where the field lines thread the magnetopause boundary. Ions of different energies injected simultaneously across the magnetopause onto any one field line, have different flight times along the field line. Hence they have different arrival times in the ionosphere, and as the field line is convecting, are spatially dispersed along the locus of the field line. The distribution function of these dispersed ions was predicted by Cowley [1982] to have a characteristic D-shape ("Cowley-D") and is described in more detail in Lockwood [1995a].

For purely northward IMF, $\theta_{sh} = 0°$ ($[B_z]_{GSM} > 0$, $[B_y]_{GSM} = 0$) reconnection will be poleward of one or both of the cusps on the sunward edges of the lobe. The most likely topology is with reconnection between the magnetosheath field and already open flux at the sunward edge of the lobe in one hemisphere. This gives reconfigured open field lines on the dayside [Crooker, 1992] and sunward convection of the lobe field lines reflected in the polar cap and shown schematically in Lockwood [1998]. In contrast to the situation of southward IMF, the curvature force of the field line is in opposition to the sheath flow and the field lines move more slowly; consequently a reversed ion dispersion signature is produced in the cusp [Reiff et al., 1980].

The differences in the two reconnection hypotheses occur for intermediate angles, for which the reconnection X-line is predicted to bifurcate and move into the pre-noon and post-noon sectors and to higher latitudes for the antiparallel case [Luhmann et al., 1984]. The key difference between the two hypotheses is that the angle between the magnetosheath field and the interior field is always close to 180° at the reconnection site for antiparallel reconnection but varies between 180° and 90° for component reconnection.

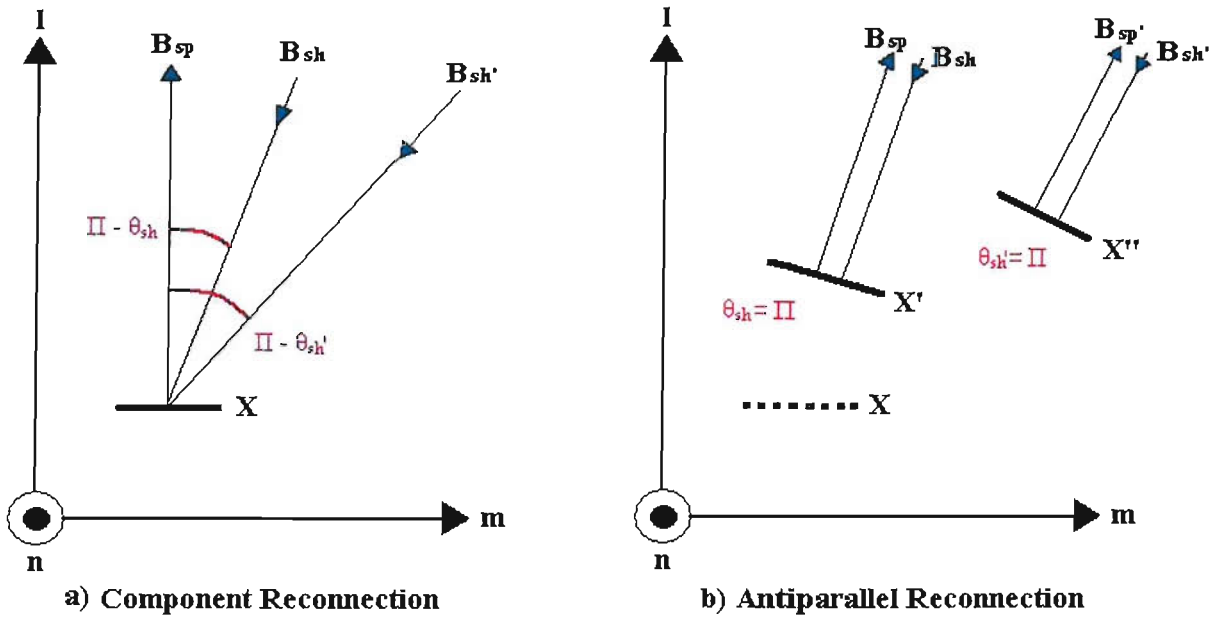

Figure 1.6 a) Two orientations of the sheath field clock angle: θ_{sh} and θ_{sh}' (projections onto the l-m plane are B_{sh} and B_{sh}') for component reconnection at a reconnection site X. *b)* shows the reconnection site X' and X'' needed to give antiparallel reconnection for the same sheath field orientations [Lockwood et al., 2003].

Both hypotheses are supported by observations, though no evidence to date is conclusive. Most of this evidence consists of in-situ measurements near the magnetopause. Fast flows consistent with the outflow from reconnection sites have been observed at the magnetopause at high latitudes, low latitudes, in the subsolar region, and on the flanks [e.g. Sonnerup et al., 1981; Paschmann et al., 1986; Kessel et al., 1996]. Also consistent with reconnection, magnetic fields with a finite component normal to the magnetopause have been observed at several locations on the magnetopause [Sonnerup et al., 1981]. These signatures are found in the outflow regions of reconnection sites, rather than at the site itself (see Figure 1.5). To discriminate between the two hypotheses in in-situ data requires us to identify that we are at an active reconnection site and then have two satellites, one each side of the boundary to measure the magnetic shear angle. Ground-based detection of ionospheric signatures to determine the nature of the reconnection lies with the reliance on mapping field lines from the ionosphere to the magnetopause using a model of the magnetospheric field and searching for the bifurcation discussed above. The work presented in this thesis combines both satellite and ground-based observations with the numerical cusp ion model of Lockwood and Davis [1996], described in Section 3.1, to provide a new test of the two hypotheses and examine the effects on cusp precipitation and the ionospheric signatures that result.

1.3.2 Solar Wind Coupling Mechanisms

Although magnetic reconnection is responsible for the majority of energy and momentum transfer, other solar wind processes also contribute; upstream solar wind pressure changes can influence the precipitation of charged particles into the upper atmosphere and cause characteristic transient FACs and ionospheric currents and flows.

It is widely accepted that the interaction of a pulse in the solar wind pressure with the magnetosphere leads to the generation of field-aligned currents, which manifest themselves in the high-latitude ionosphere. The number and direction of these current filaments can vary, but typically pairs of opposite polarity current filaments form and

propagate antisunward at subauroral zone latitudes with speeds of several kms^{-1}. These propagating currents are also known as "Travelling Convection Vortices" (TCVs). The pressure pulse signature in the low-latitude ionosphere and at geosynchronous orbit is seen as a sudden magnetic impulse (SI) [Sibeck, 1993; Trivedi et al, 2002].

A number of theories have been proposed to explain the generation of TCVs. These theories can be categorised into two types. In the first type, the impact of pressure variations close to the nose causes undulations on the magnetopause [Kivelson and Southward, 1991; Sibeck et al., 1989] that travel away from noon. These undulations produce vertical motion near the magnetopause, which generates FACs that map to the polar region. These paired field-aligned currents close in ionospheric currents that are recorded by the high-latitude magnetometers in the form of bipolar magnetic field perturbations. As illustrated in Figure 1.7, Pedersen currents and electric fields (dashed arrows) point inward toward a filamentary upward field-aligned current and outward from a filamentary downward field-aligned current. Hall currents (solid circles) flowing perpendicular to these induced electric fields produce magnetic field perturbations (also the dashed arrows) that point inward toward upward field-aligned currents, but outward away from downward field-aligned currents. As illustrated by Zesta et al. [2002], stations under the northern fringes of vortices produced by upward field-aligned currents observe southward magnetic field perturbations, while those under the southern fringes observe northward perturbations. Perturbations in the opposite sense occur during the passage of vortices associated with downward field-aligned currents. The second theory was based on the original ideas of Tamao [1964], who provided a foundation for further studies by Glaßmeier and Heppner [1992], Lysak et al. [1994] and Araki [1994]. These authors all pointed out that the compression of the magnetopause does not directly drive field-aligned currents, which can be mapped to the ionosphere. Instead they presented magnetohydrodynamic models to explain the propagating signatures seen on the ground. The solar wind density pulse is converted into a fast hydromagnetic (HM)

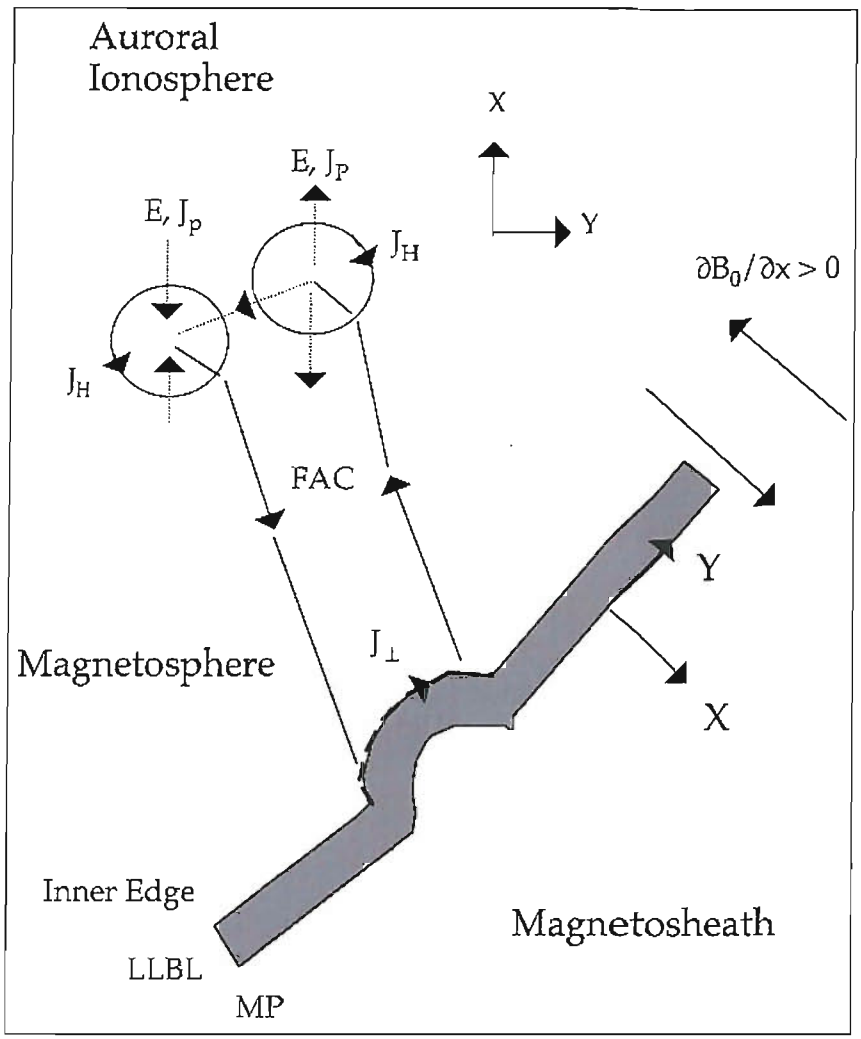

Figure 1.7 A schematic illustration of the generation of field-aligned currents at the magnetopause. The X-component points in the direction normal to the magnetopause, the Y-component points duskward (or azimuthally) along the magnetopause in the equatorial plane and the Z-component points northward parallel to B_0, B_0 being the zero-order magnetospheric magnetic field. Each transient compression generates a pair of oppositely directed field-aligned currents on the magnetopause. Hall current (J_H) vortices associated with the field-aligned currents generate the signatures observed by magnetometers in the high-latitude ionosphere, B_0. The direction of the Pederson currents are shown by the black arrows marked J_P [Sibeck et al., 2003].

compressional wave at the bow shock, which then propagates across the magnetosheath. Upon reaching the magnetopause, magnetosheath pressure variations drive magnetopause motion and launch compressional Alfvénic waves into the magnetosphere. The initial response in the ionosphere is seen on lower latitude field lines and not on field lines near the open-closed boundary. At high latitudes the waves couple and mode-convert into shear Alfvén waves at the point where the wave frequency matches the shear mode eigenfrequency of the field line [Southwood, 1974]. This establishes a short-lived resonance region inside the magnetopause. In the model reported by Lysak et al. [1994], the convection vortices form at locations where field line resonances occur, suggesting that the ground signatures of a pressure pulse at the magnetopause is the excitation of these resonances. A number of studies have shown that TCV events are frequently accompanied by resonances on field lines at lower than cusp latitudes [Potemra et al., 1996; Lühr et al., 1996]. The number of vortices generated is, however, under debate. The Glaßmeier/Heppner HM model [1992] predicts that a transient compression of the magnetosphere should generate a pair of oppositely directed field-aligned currents and vortices. Both the Kivelson/Southward [1991] and Lysak et al. [1994] models predict the generation of three vortices for a transient compression and relaxation with alternating current directions (a transient inward compression with no outward relaxation causes just two vortices in there theory). All the models concur on one point; the ionospheric events should only occur at local times where the transmitted solar wind variations apply pressure gradients to the magnetosphere.

The next chapter gives a description of the satellite-borne and ground-based instruments used in this study to observe the response of the global magnetospheric-ionospheric system to variations in upstream IMF and solar wind parameters.

Chapter 2.

Instrumentation

In the studies presented in this thesis, variations in upstream solar wind parameters are observed by a number of satellites that track their progression to the magnetopause. The changes at the magnetopause are communicated to the ionosphere and monitored by a range of ground-based and near-Earth satellite instruments.

2.1 Satellite-Borne Instruments

Using a combination of satellites situated at a variety of positions upstream and inside the magnetosphere it is possible to track features in the solar wind and study their interactions with the magnetospheric system. A multi-satellite study can provide plasma, energetic particle and magnetic field input for magnetospheric and ionospheric studies, determine the magnetospheric output to near-Earth solar wind, and investigate basic plasma processes occurring within the magnetosphere.

2.1.1 The ACE and WIND Satellites

Experimental observations of solar wind-magnetosphere coupling processes rely on measurements of the IMF and plasma parameters in the solar wind upstream of the magnetosphere. The Advanced Composition Explorer (ACE) orbits the L1 libration point, where the Sun and the Earth are in gravitational equilibrium, enabling it to monitor continuously the highly variable speed, composition and magnetic field of the solar wind as it propagates Earthwards. The WIND spacecraft has been moved between an L1 orbit and large "petal" orbits around the Earth. In either orbit, it provides interplanetary observations from a location well separated from that of ACE: when in the L1 halo orbit, these interplanetary observations are, like those from ACE,

continuous; when in the petal orbits the satellite spends part of the time within the magnetosphere.

The ACE spacecraft carries six high-resolution sensors and three monitoring instruments sampling low energy particles of solar origin and high-energy solar and galactic particles. With a semi-major axis of approximately 200,000 km, the elliptical orbit affords ACE a prime view of the Sun from which it performs measurements over a wide range of energy and nuclear mass, under all solar wind flow conditions and during both large and small particle events. In this study data, are used from two instruments: the Magnetometer instrument (MAG) which measures the local IMF direction and magnitude and establishes the large scale structure and fluctuation characteristics of the IMF upstream of Earth as a function of time, and the Solar Wind Electron, Proton and Alpha Monitor (SWEPAM) which measures the solar wind plasma electron and ion fluxes as functions of direction and energy. The data from these provide detailed knowledge of the solar wind conditions at a time resolution of 16 sec. The equivalent instruments on the WIND satellite are the Magnetic Field Investigation (MFI), and the Solar Wind Experiment (SWE) respectively. The WIND instruments have a lower time resolution of 32 sec.

This study uses data from the times when all four of these instruments observed solar wind and IMF variations in order to calculate their propagation time both between the two spacecraft and downstream to the magnetopause. The method used to calculate this propagation time is discussed in detail in Chapter 4.

2.1.2 The Geotail Satellite

The Geotail satellite is in an Earth orbit that takes it into the interplanetary medium at locations downstream of ACE and, usually, also of WIND. The satellite measures global energy flow in the near-Earth interplanetary medium and in the magnetotail in order to increase understanding of fundamental magnetospheric processes, including the physics of the magnetopause, the plasma sheet, and reconnection neutral line formation.

The satellite instruments used in this study are the Magnetic Field Measurements (MGF) and the Low Energy Particle (LEP). The MGF objective is to measure the magnetic field variation in the vicinity of the satellite at frequencies below 50 Hz. It consists of three fluxgate magnetometers that measure in both real-time and record modes. The LEP instrument objective is to observe plasma and energetic electrons and ions in the vicinity of the spacecraft. It consists of three sensors: the LEP-EA and LEP-SW that measure the three-dimensional velocity distributions of hot plasma and solar wind ions respectively, and an energetic ion mass spectrometer (LEP-MS) which provides three-dimensional determinations of the ion composition. All three sensors operate continuously and provide data from distances ranging from 8-200 Earth radii from the Earth. In this study these Geotail instruments are used to confirm the predicted downstream propagation time, measured by ACE and WIND, by examining the effect of the arrival of the solar wind feature on different magnetospheric boundaries.

2.1.3 The GOES Satellite

The Geostationary Operational Environmental Satellite (GOES) satellites, operated by the National Oceanic and Atmospheric Administration (NOAA) and NASA, circle the Earth in a geosynchronous orbit over the equator (altitude of 6.6 R_E, geographic latitude of 0°, and a fixed geographic longitude). This means they remain over a single position on the Earth's surface and monitor a point in the equatorial inner magnetosphere that moves around a full range of local times once every day.

The two GOES satellites used in this study are GOES-8 and GOES-10. The GOES-8 is located at 75W longitude above the equator and in the Atlantic sector. The GOES-10 is also located above the equator at 135W longitude and in the Pacific sector. In this study data from the Space Environment Monitor (SEM) onboard both GOES satellites is used to examine the effect of upstream features on the low-latitude magnetosphere. The SEM consists of three instrument groups: an energetic particle sensor (EPS) package, two magnetometer sensors, and a solar x-ray sensor (XRS).

The EPS measures the number of particles over a broad energy range, including protons, electrons, and alpha particles. The magnetometer sensors can operate independently and simultaneously measure the magnitude and direction of the Earth's geomagnetic field, detect variations in the magnetic field near the spacecraft. These geostationary craft provide information on the effect of sudden impulses that impact the magnetosphere, and assess the level of geomagnetic activity.

2.1.4 The LANL Satellites

Like the GOES satellites, the ten LANL satellites operate at geosynchronous orbit each with a nominal altitude of 6.6 R_E, geographic latitude of 0°, and a fixed longitude. These satellites carry an energetic particle instrument (SOPA) that measures electrons from 50 keV to 26 MeV, protons from 50 keV to >50 MeV and heavy ions at energies above 0.5 MeV. Typically data is received from 3-4 satellites simultaneously allowing an analysis of the reaction of the inner magnetosphere to the arrival of solar wind features as a function of local time.

2.1.5 The IMAGE Satellite

The Imager for the Magnetopause-to-Aurora Global Exploration (IMAGE) satellite is in a near-Earth elliptical orbit with apogee near 7.2 R_E, which enables it to take global images of the major plasma regions and boundaries in the Earth's inner magnetosphere. The latitude of apogee varies slowly with time such that images of the full auroral oval are possible in the northern and southern hemispheres alternately. These images are made simultaneously making it possible to relate processes occurring in one region to events observed in another region. Image cadence and exposure is set by the spacecraft spin, with ~ 5 sec exposures repeated every 2 min.

The main objective of the IMAGE mission is to improve the understanding of the interaction between the solar wind, magnetosphere, and ionosphere. One signature of this interaction is the occurrence of aurorae, which can be studied in three different spectral regions by the Far Ultraviolet (FUV) instruments on IMAGE [Mende et al., 2000]. The suite of FUV imagers provide global, simultaneous, and separate images

of the proton and electron aurora. The first of the two imagers used in this study is the Spectrographic Imager (SI12), which images Doppler-shifted Lyman-α emissions at 121.8 nm. These emissions are produced in the atmosphere by a charge exchange and de-excitation process previously discussed in Section 1.2.5. The SI12 channel is most sensitive to precipitating protons in the energy range 2-8 keV, with very little response to ions below about 1 keV [Gérard et al., 2000]. Proton precipitation is also a source of secondary electrons resulting from ionising collisions of the protons and hydrogen atoms of the neutral atmosphere (Section 1.2.5). These electrons have very low mean energy [Strickland et al., 1993; Lummerzheim et al., 2001] and are effective in exciting O atoms and N_2 molecules and thus producing OI (135.6 nm) and N_2LBH emissions seen by SI13 imager and Wide-field Imaging Camera (WIC) respectively.

Using data from the three FUV instruments, each of which study different spectral regions, allows us to differentiate between proton and electron precipitation at locations in the magnetosphere determined by the position of the satellite along its elliptical polar orbit. In this study we will look at the variations in auroral emissions stimulated by both proton and electron precipitation to see how they are each affected by changes in upstream solar wind conditions.

2.1.6 The DMSP Satellites

The Defence Meteorological Satellite Program operates several satellites (F11-F15) in low-Earth orbits (LEO). These DMSP satellites are three-axis stabilized in near sun synchronous, circular orbit. Each orbit is at an altitude of 840 km, with a period of 101 min and nominal inclination of 98.75° allowing a twice-daily coverage of along-track plasma densities, velocities, compositions and drifts in both polar regions.

In this study the DMSP/F2 and the DMSP/F4 satellites are used to obtain general information on magnetospheric topology by reference to ion and electron flux data from the SSJ/4 particle detectors, described by Hardy et al. [1985]. The data set consists of electron and ion particle fluxes between 30 eV and 30 keV recorded every

second, the energy spectra of which are used to infer the locations of the magnetospheric boundaries, in particular the dayside OCB defined as the poleward edge of the full magnetospheric population.

2.2 Ground-Based Instruments

Experimental observations of the ionospheric signatures of solar wind-magnetosphere coupling rely on the use of a range of ground-based instruments. The changes at the magnetopause are communicated to the ionosphere and monitored by a combination of radar, magnetic and optical instruments. This section gives a description of all the ground-based instruments used in this study.

2.2.1 Optical Instruments

The Spectrographic Imaging Facility (SIF) at Longyearbyen (LYR), Svalbard, is an optical platform jointly operated by the University of Southampton and University College London. The platform consists of the High Throughput Imaging Echelle Spectrograph (HiTIES), two photometers and a narrow angle auroral imager. The instruments on the platform are co-aligned and centred on the magnetic zenith. Since the ground-based instruments make continuous observations in a field-of-view around one location, this combination of instruments is well suited to discriminate between the spatial and temporal evolution of ionospheric optical features. The high latitude location provides a unique opportunity to study aurora almost 24 hours a day during the winter, including the cusp region.

The HiTIES spectrograph makes simultaneous measurements of different wavelength regions: H_β (484.4-487.6 nm), N_2^+1N (463.5-466.0 nm) and N_2^+1N (496.9-471.5 nm) in an 8° meridional slit centred on the magnetic zenith. This provides simultaneous measurements of both proton and electron precipitation over LYR. The data recorded to date have demonstrated that the imaging spectrograph is capable of measuring spatial changes in dynamic auroral structures with high spectral resolution and high time resolution.

The photometers on the SIF platform provide field-aligned intensities at wavelengths also measured by the spectrograph: H_β (486.1 nm) and N_2^+ (465.2 nm).

Each photometer has a field of view of 1° that is co-aligned with the centre of the slit of the spectrograph, providing high time resolution information on the signatures of precipitating protons and electrons which supplements the spectrograph data. A comprehensive description of the SIF has been provided by Lanchester et al. [2003].

Meridian Scanning Photometers (MSP) are also located at Longyearbyen and can therefore support the measurements made by the SIF instruments. The MSP, run by the University of Alaska, scans continuously along the magnetic meridian, monitoring the auroral line-of-sight intensities over a latitudinal range of approximately 70° – 80° MLAT, centred on LYR. There are five independent phototubes and counting systems each fitted with interference filters to isolate five spectral regions of interest. Data from three of the five spectral windows have been used to study ionospheric features at wavelengths: 630.0 nm, 557.7 nm and 486.1 nm [Sandholt, 1980; Sivjee, 1982]. The intensity ratio between the red-line 630.0 nm emission and the green-line 557.7 nm emission is used to identify the dayside open-closed field line boundary, the theory of which is outlined in Section 1.2.6, and the 486.1 H_β emission is used to detect proton precipitation at a range of different latitudes.

2.2.2 Radar

Ground-based radars are used to study ionospheric flow, and provide an ideal means of monitoring its temporal variations in a given region. In this study the EISCAT ESR, EISCAT VHF and SuperDARN radar observations are used to supplement the LYR optical instruments discussed above.

Situated at geographic coordinates of (78.2°N, 16.0°E), the EISCAT Svalbard Radar (ESR) is an incoherent scatter radar facility at LYR which is in an ideal position to study the dynamics of the upper atmosphere in the polar cusp region and the dayside polar cap [Cowley et al., 1990]. The ESR radar comprises of two dishes: the 32 m steerable dish and the 42 m dish which is fixed to point in the field-aligned direction.

In this study, the latter dish is used to observe a wide range of altitudes from the base of the D-region to the topside of the ionosphere at ~1000km. In the incoherent scatter technique, pulses of high power radio waves are scattered by thermal fluctuations in the plasma. The theory of incoherent scatter shows that, at the wavelengths employed, the total returned power depends on the number of electrons in the scattering area and gives an estimate of the ionospheric electron density; the width of the spectrum depends on the ratio of the ion temperature to ion mass and the overall shift of the spectrum corresponds to the bulk motion of the ions. The shape of the ion line spectrum is a function of the ratio of the electron and ion temperatures. With suitable assumptions about concentrations of different ions in the ionosphere, the basic parameters of electron density, electron temperature, ion temperature and line-of-sight ion velocity are routinely derived [Beynon and Williams, 1978].

In the studies presented here the EISCAT VHF radar at Tromsø (69.59°N, 19.23°E) provides observations from a range of different latitudes helping to differentiate between spatial and temporal variations in ionospheric signatures. The VHF radar is here employed with two beams: one pointed towards magnetic north (the western beam) that it is normal to the magnetic L-shells and the other (eastern) beam towards geographical north (north), giving a separation of 14.5° between the two beams. The radar records data with 10 sec integration periods, with range gates of length 75 km. Both beams are pointed at 30° elevation allowing the radar to observe a range of latitudes between 600 km and 1600 km, giving a coverage that extends beyond the latitude of the ESR field line (at a range of 1100km from Tromsø). Figure 2.1 shows the direction of both the VHF beams when mapped down along the magnetic field to 100 km altitude. In this study the eastern beam is used because it lies closest to the ESR radar allowing the ESR data to be placed in a wider latitudinal context. Using a combination of ESR and VHF radars, under favourable conditions, is well suited to studies of spatial and temporal variations in ionospheric flows and ionospheric plasma conditions.

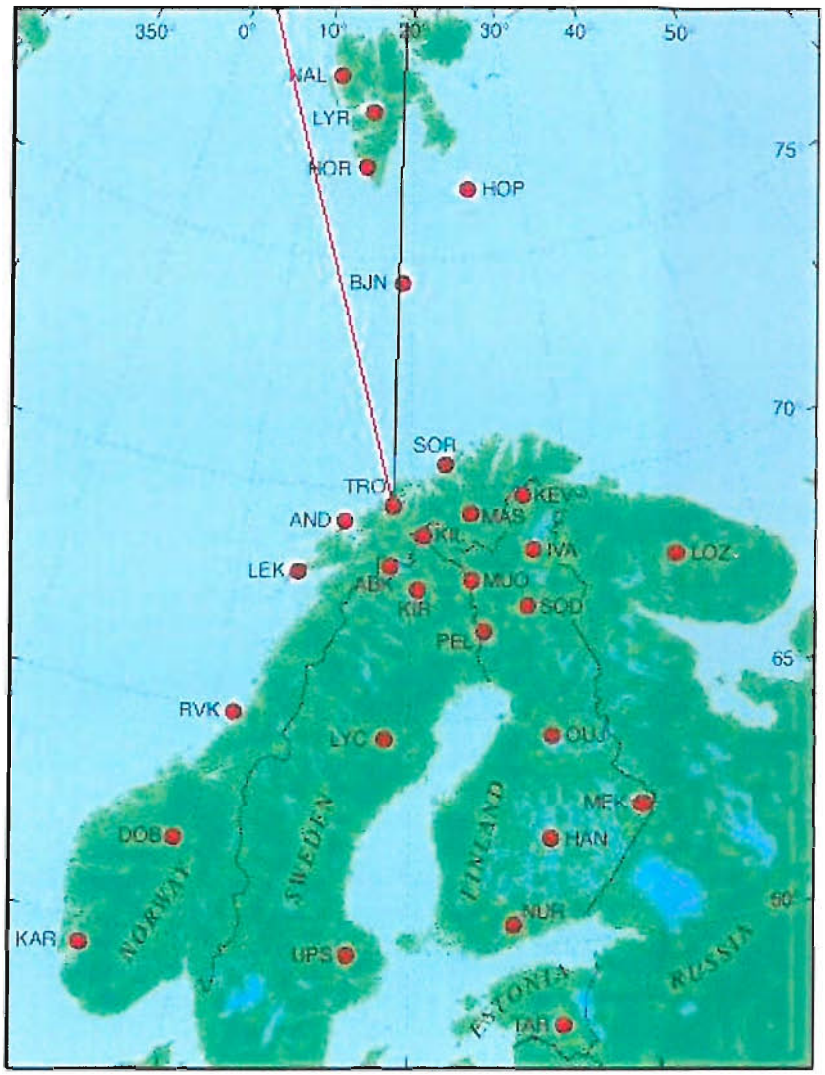

Figure 2.1 A map showing the directions of the VHF radar beams mapped down along the magnetic field to 100 km. [Østgaard et al., 2005]. The red line represents the radar beam that points towards magnetic north, the black line represents the radar beam that points toward geographic north. The red dots mark the locations of the instruments belonging to the IMAGE magnetometer network.

The detailed information on the state of the ionosphere provided by the incoherent scatter radar is supplemented by the broad study of the convection and morphology of the cusp precipitation region made by the HF radars [Baker et al., 1995]. The Super Dual Auroral Radar Network is a network of coherent scatter HF radar [Greenwald et al., 1995] which measures backscatter from field-aligned ionospheric irregularities. The radars transmit HF signals, which are refracted as they enter ionospheric regions with higher electron concentrations. If these regions contain sufficient coherent irregularities, of wavelength matched to the radar wavelength, the radar signals will be backscattered. These irregularities are generated by plasma drifts and density gradients [e.g. Fejer and Kelley, 1980; Villain, 1985] and are aligned along the magnetic field. The radars transmit power at a fixed frequency and from the returned signals, an estimate of the variation in backscatter power, line of sight Doppler velocity, and spectral width in the radar field of view is recorded. As many of the SuperDARN radars have overlapping fields of view, it is possible to combine line-of-sight velocities from the Doppler shifts observed at the two sites to derive the 2-dimensional field-perpendicular velocity vectors. In this study, SuperDARN radar data is used to monitor the bulk plasma motion of the ionosphere during events caused by the impact of a given set of upstream solar wind conditions. This provides information about the large-scale convection-related processes. These HF radars are therefore a very good diagnostic tool for studies of magnetosphere-ionosphere coupling.

2.2.3 Magnetometers

The International Monitor for Auroral Geomagnetic Effects (IMAGE) magnetometer network consists of 29 magnetometer stations covering a large range of latitudes from 59° to 79° in the Scandinavian longitude sector. Each station comprises a fluxgate magnetometer sampling the geographic X (north), Y (east) and Z (downward) components of the geomagnetic field every 10 sec with a resolution of 0.1-1 nT. A map showing the location of the instruments belonging to the IMAGE network is presented in Figure 2.1. The five high latitude stations of the IMAGE network: NAL, LYR, HOR, HOP and BJN, lie close to the VHF radar beam and thus

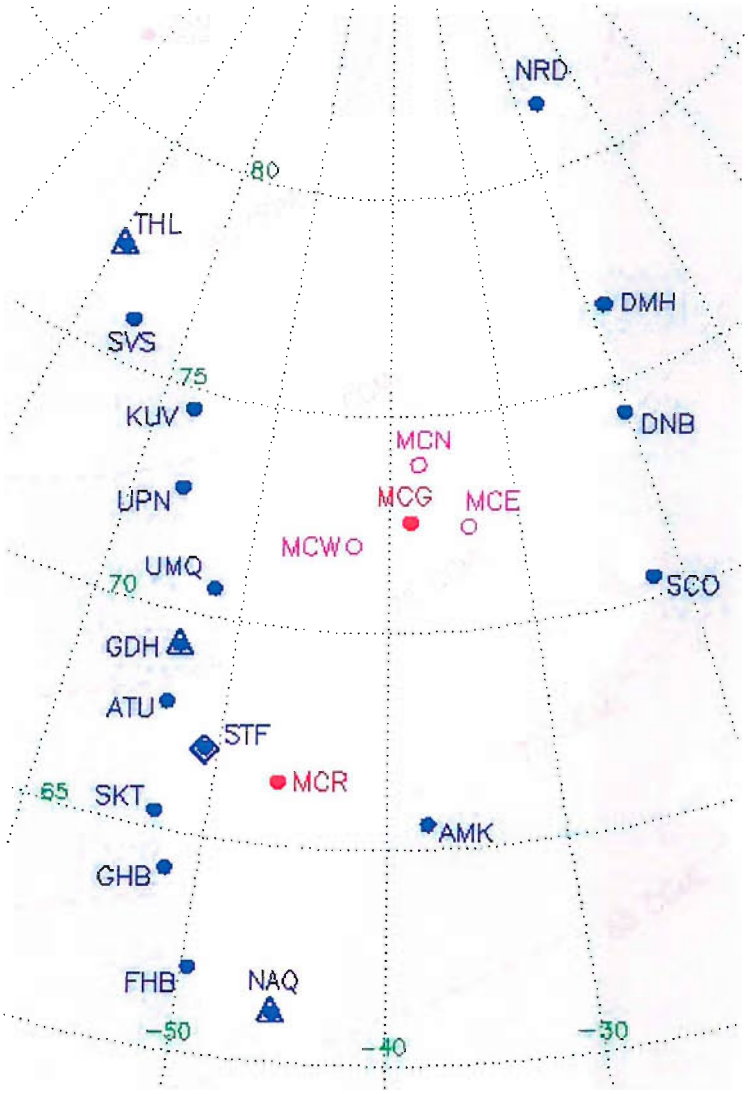

Figure 2.2 A map showing the location of the east and west magnetometer chains belonging to the Greenland network [http://web.dmi.dk/projects/chain/].

often observe features which are also detected by the radar. Together with other ground based recordings and satellite observations, IMAGE is an essential part in the investigations of high latitude magnetospheric-ionospheric physics.

The Greenland magnetometer array consists of two chains of seventeen magnetometer stations situated on the east and west coasts shown in Figure 2.2, which lie approximately 1000 km and 2300 km to the west of IMAGE. The 210MM magnetometer array lies to the east of IMAGE. The six stations used in this study, TIX, CHD, ZYK, MGH, ONW and KAG are shown in Figure 2.3. All the instruments, shown collectively in Figure 2.3, are fluxgate magnetometers that sample the geomagnetic X (north), Y (east) and Z (downward) components of the geomagnetic field every 20 sec with a resolution of 1 nT.

The low-latitude magnetometers of Hermanus in South Africa and Kourou in French Guiana are shown in Figure 2.3. With latitudes of -34.43° and 5.1° and longitudinal positions of 19.25° and 307.27° respectively, the stations are situated in a good position to study low-latitude ionospheric signatures that result from the impact of upstream features on low-latitude magnetic field lines.

The latitudinal and longitudinal spread of the IMAGE, Greenland, 210MM and low-latitude magnetometer stations supplies a means to observe the spatial and temporal evolution of different ionospheric signatures observations. IMAGE is an essential part in the investigations of high latitude magnetospheric-ionospheric physics.

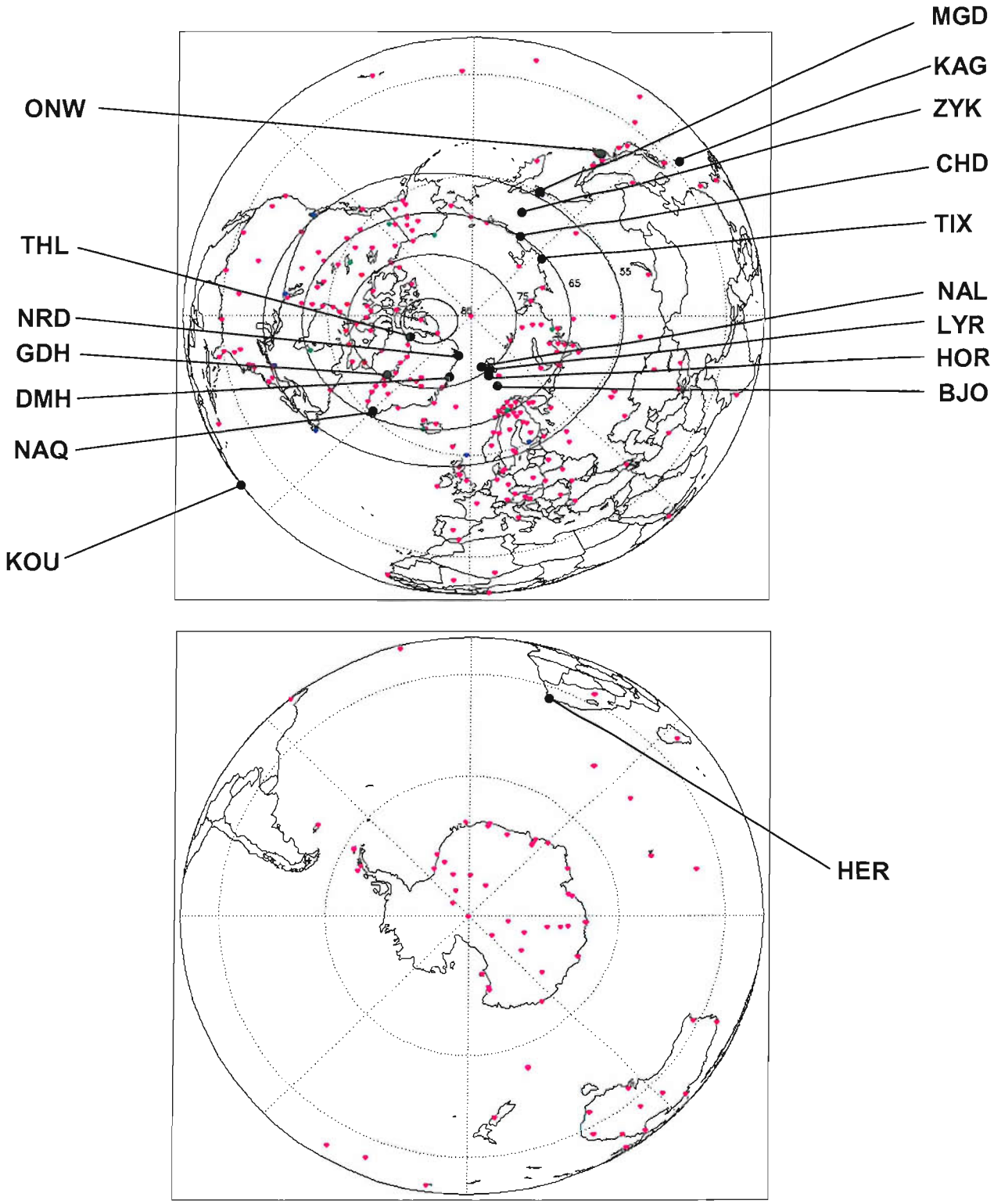
MGD
KAG
ZYK
CHD
TIX
NAL
LYR
HOR
BJO
ONW
THL
NRD
GDH
DMH
NAQ
KOU
HER
55
65
75
85

Figure 2.3 A map showing the locations of the global network of magnetometers (mauve points). Some of the key ones used in this study are shown in black (from WDC-C1's on-line instrument locator http://www.ukssdc.ac.uk/wdcc1/instruments.html).

Chapter 3.

Numerical Modelling of the Ionospheric Response to Dayside Reconnection

All the instruments described in the previous chapter are able to provide a good overview of solar wind/ionosphere connection, especially when used in combination with numerical model predictions. This chapter provides a description of the two numerical models that are used in this study: the Lockwood and Davis numerical cusp model [1996] and the Lockwood and Morley convection model [2004].

3.1 The Lockwood and Davis Numerical Cusp Model

The Lockwood and Davis cusp model uses the theory of cusp ion precipitation presented by Lockwood [1995] to simulate the dispersion of ions along newly-reconnected field lines during periods of southward IMF. This section provides an explanation of the theory behind the model and a description of the model itself.

3.1.1 Cusp Ion Precipitation

In Chapter 1 the subject of ion precipitation in the cusp due to dayside reconnection was introduced. During reconnection under southward IMF ($B_Z < 0$), the newly opened field lines allow magnetosheath particles to stream continuously across the dayside magnetopause into the cusp ionosphere [e.g. Lockwood and Smith, 1993; Onsager et al., 1993]. Each field line has a different orientation both sides of the magnetopause separated by a region of field rotation in the current sheet, known as a rotational discontinuity (RD). This change in magnetic field orientation causes acceleration of the incoming ions, which cross the magnetopause with sufficient electrons to maintain quasi-neutrality In Figure 3.1,

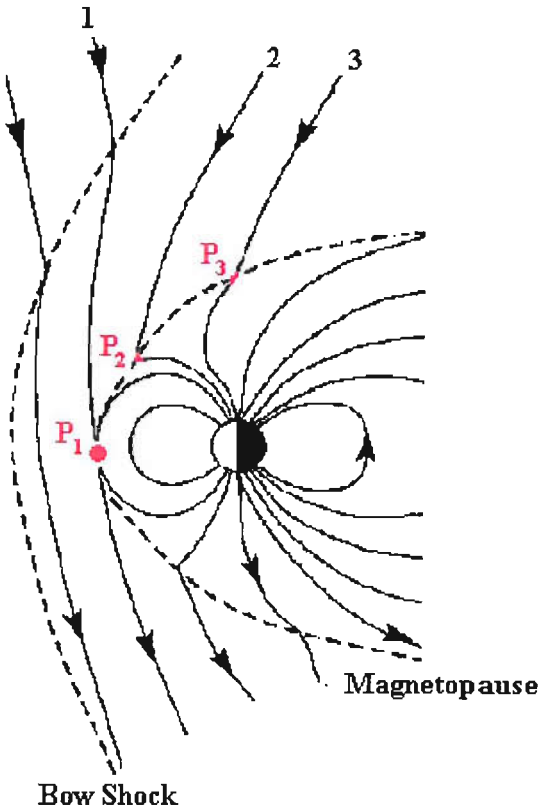

Figure 3.1 The evolution of newly opened field lines from a dayside magnetopause X-line into the tail lobe. Each field opened at any one point on the magnetopause line evolves through the positions marked *n*, in which it threads the magnetopause at point P_n. [Adapted from Lockwood, 1995]

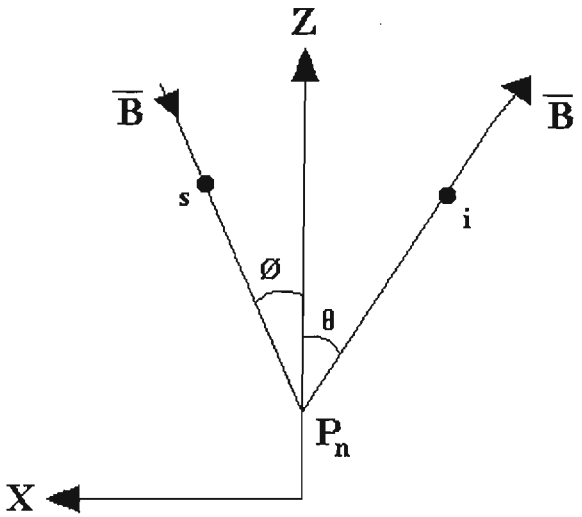

Figure 3.2 The rotational discontinuity (RD) formed by a newly opened field line at P_n which evolves along the magnetopause in the Z-direction at speed V_f in the Earth's frame of reference. The X-direction is the outward normal to the boundary. [Adapted from Cowley, 1982].

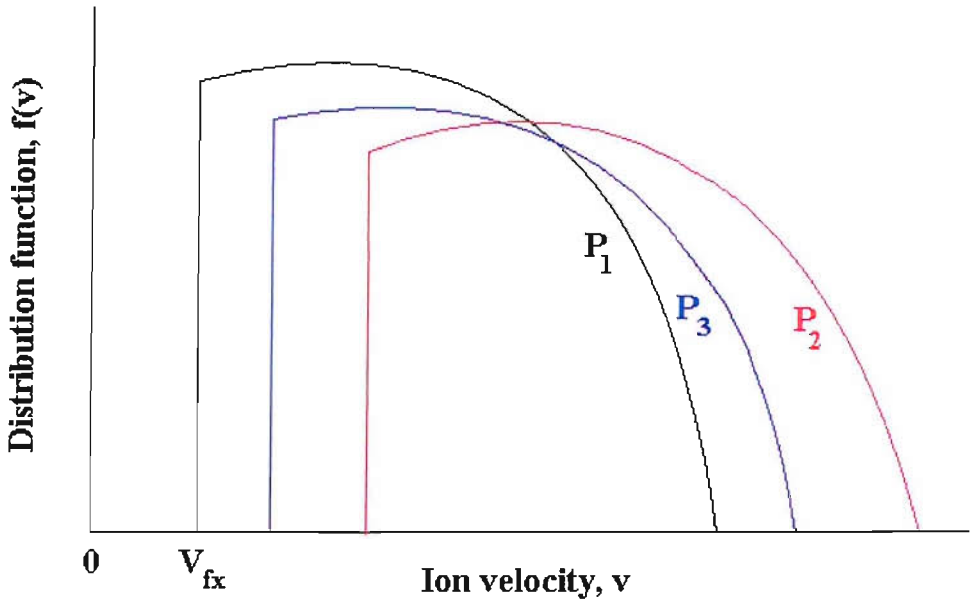

Figure 3.3 Field Parallel segments of the "Cowley-D" ion distribution functions of ions injected across the magnetopause at P_n in Figure 3.1. These distributions are shown as f(v) on log-linear axes. [Adapted from Lockwood, 1995].

a newly opened field line is shown in three positions (labelled 1-3) as it is convected away from the dayside reconnection site represented by a red dot. The points P_n are where the field line (in position n) threads the magnetopause at the RD. As the field lines convect away from the reconnection site the rotational angle and speed at the magnetopause change, altering the acceleration of the ions on crossing the boundary. Figure 3.2 shows the general situation at the RD formed by the newly opened field lines where they thread the magnetopause at P_n. The Z-axis points along the magnetopause in the direction of field line motion, and the X-axis is the outward normal to the boundary. The field line makes angles Ø and θ with the magnetopause on its magnetosheath and magnetospheric sides respectively. These angles increase with distance from the X-line as the field line straightens.

Figure 3.2 is in the de Hoffman Teller (dHT) frame of reference in which the field lines are at rest. In the Earth's frame of reference, both the dHT frame and the field lines move along the magnetopause in the Z-direction at speed V_f, which is typically 100-300 kms^{-1}, corresponding to a field perpendicular velocity of 10-30 kms^{-1} on the Earthward side of the RD [Aggson et al., 1983; Sonnerup et al., 1990]. The plasma will flow through the RD at the local Alfvén speed V_A, in the dHT frame [Hudson, 1970]. (Essentially, this is because in the plasma rest frame an RD propagates at the local Alfvén speed). Sheath ions approaching the magnetopause have $V_x < 0$ and $V_z < 0$, but once they have crossed the RD they have $V_x < 0$ and $V_z > 0$. About this bulk flow speed there is a thermal spread, and only ions with $V_x < 0$ will cross the magnetopause.

Figure 3.3 shows schematically the field-parallel velocity distribution function injected at position P_n, shown in Figure 3.1. We are only concerned with this near field-parallel part of the injected distribution as all other pitch angles are mirrored before reaching the ionosphere. The distribution functions have the truncated maxwellian D-shape distribution predicted by Cowley in 1992. The missing part of the injected distribution had velocity $V_x > 0$ in the magnetosheath and so never encountered the magnetopause. Near the X-line (P_1) the angle θ is sufficiently close to zero that the distribution cut-off velocity V_{min} is equal to the dHT (field line) velocity at this point, V_{fX}. The other two injection locations shown in Figure

3.1 are further removed from the X-line where, for subsolar reconnection, the magnetosheath temperature and density are both smaller [Spreiter et al., 1966]. Lockwood and Smith [1994] have shown that V_{min} increases as the field line accelerates away from the X-line, and these factors are reflected in Figure 3.3 for the distribution when the field line is at position 2, relative to that for position 1. However, as the field line straightens, V_{min} decreases. The distribution injected when the field line is in position 3 demonstrates that effect.

While the characteristics of the injected ion velocity distribution change with time as the field line is convected, the spectra of precipitating particles observed in the cusp are further complicated by the fact that ions of different field-aligned velocity, injected simultaneously across the magnetopause onto any one field line, have different flight times along that field line. For a southward IMF, newly opened field lines convect under the joint action of magnetic tension and shocked solar wind flow, causing lower-energy particles to arrive at successively higher latitudes [e.g. Rosenbauer et al., 1975; Shelley et al., 1976], which gives rise to a distinctive energy-latitude spatial dispersion [e.g. Reiff et al., 1977; Smith and Lockwood, 1996]. An observing low-altitude satellite will, at any time, detect ions with a range of energies precipitating into the ionosphere. Because the field line is convecting, any one single point on the magnetopause can only contribute one ion energy to the ion spectrum observed at a point at low altitudes. This means that a spread of energies at low altitudes reveals that particles must enter the magnetosphere over a range of injection locations. Note that this spread is an unique feature of injection by reconnection which allows particles to cross the magnetopause continuously once the field line has been opened. Further, as the field lines evolve tailward, the injected ions flow preferentially into the lobe rather than the cusp ionosphere. Thus high particle fluxes are restricted to the dayside polar cap region we class as cusp. A full discussion of cusp precipitation and dispersion following reconnection is presented by Lockwood et al. [1995a].

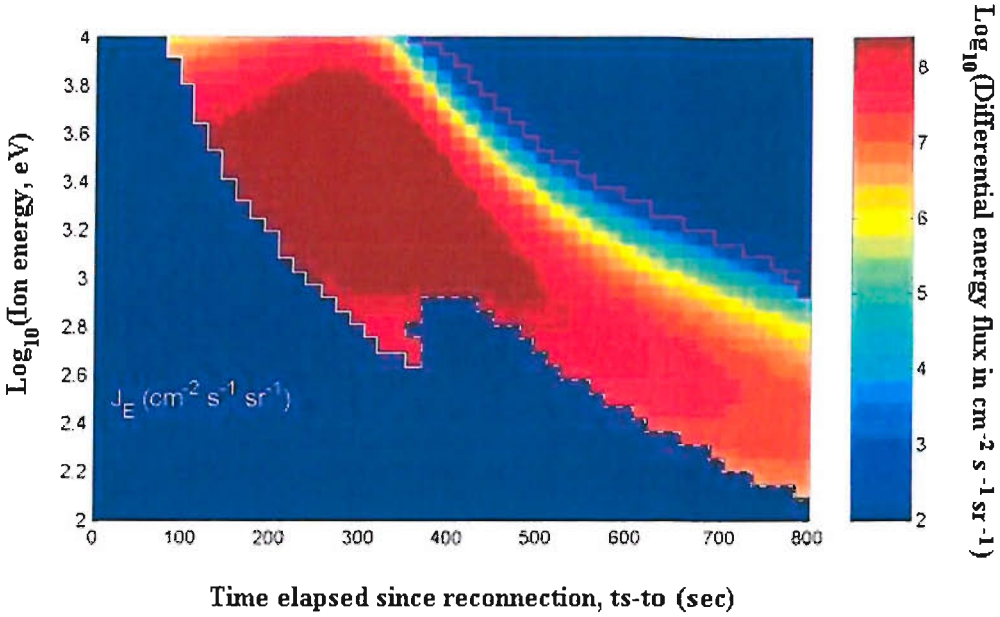

Figure 3.4 Modelled injected solar wind ions along a single evolving open field line. Differential energy flux of the ions is colour-coded as a function of energy and time elapsed since the field line was reconnected (t_s-t_o). The solid white line represents the low-energy cut-off energy, E_{ic}. The dashed white line shows the variation in the minimum energy, E_{min}, and the pale pink line shows the variations in the peak detected energy, E_{max}. Precipitation is modelled down to an altitude of 110km, an average emission altitude of the proton aurora [Lockwood et al., 2003].

3.1.2 Modelling the Cusp Ion Precipitation

Numerical modelling has been successful in reproducing the proton signatures of ion precipitation into the cusp ionosphere [Onsager et al., 1993; Lockwood and Davis, 1996b; Lockwood, 1997b, 1998]. In this study we employ the open magnetosphere model by Lockwood and Davis [1996b] to predict the ion dispersion characteristics for reconnection at a low-latitude magnetopause X-line. The model allows for the evolution of the continuous source population at the magnetopause for each open field line (as it migrates away from the reconnection site) and for the time-of-flight from the magnetopause to the ionosphere. The model assumes that the reconnection occurs at a fixed latitude, taken to be the magnetic equator. The velocity distribution of the injected plasma is a D-shaped distribution as predicted by Cowley [1982]. The field line velocity in the Earth's frame is such that the flow into the magnetosphere is at the local Alfvén speed $\mathbf{V}_A$ in the dHT frame ($\mathbf{V}_f - \mathbf{V}_{sh} = \mathbf{V}_A$). Input variations in magnetosheath density, temperature and the flow ($\mathbf{V}_{sh}$) along the magnetopause are taken from the gas-dynamic model of Spreiter et al. [1966], as described in Lockwood [1995a]. The magnetosheath field and the magnetospheric field are assumed to be co-planar, which is the case for antiparallel reconnection.

Figure 3.4 gives an example of the modelled differential energy fluxes of injected-and-dispersed solar wind ions seen in the ionosphere, predicted as a function of ion energy and time elapsed since the reconnection of the field line (t_s-t_o), where t_s is the is the time of observation and t_o is the time that the field line was opened. The solid white line represents the "lower cut-off" energy, E_{ic}. The decrease in the E_{ic} slope reflects the arrival of progressively lower energy, lower velocity ions in the ionosphere. These ions were injected at the reconnection site where $V_{min} = V_{fX}$. The dashed white line shows the variation in minimum ion energy, E_{min}, injected at distances increasingly further away from the reconnection site. The rise and fall of V_{min}, as discussed in Section 3.1.1, can be observed as the field line evolves away from the X-line. The pale pink line represents the peak detected energy, E_{max}.

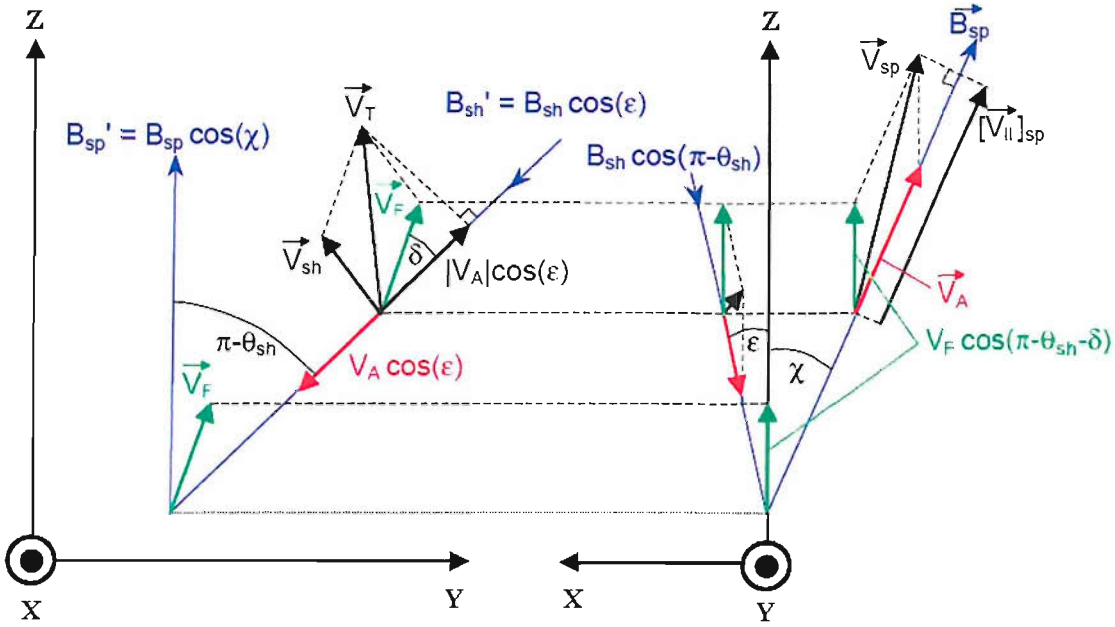

Figure 3.5. Geometry of newly-opened field lines at the dayside magnetopause. The left axis show the z-y plane of the magnetosphere, the right axis show a cross section of the magnetopause in the x-z plane, where x is the outward normal to the boundary, z lies in the boundary plane and aligned with the geomagnetic meridian in the northward direction and y lies in the boundary plane and makes up the right hand set. Both left and right axes give the geometrical projection of the magnetic field vectors onto the z-y and x-z planes, respectively needed to compute field line motion and the proton acceleration on crossing the magnetopause due to component reconnection [Lockwood et al., 2003].

The Lockwood and Davis model only considered the special case where the sheath field and the interior magnetospheric fields are coplanar i.e. the clock angle of the exterior magnetosheath field with respect to the interior magnetospheric field is 180°. The model therefore simulates antiparallel reconnection and also component reconnection for the special case of purely northward or southward IMF. The model result of Figure 3.4 is for a clock angle of 180°.

Lockwood et al. [2003] revised the model to allow for the study of ion precipitation over a range of clock angles, θ_{sh}. By replicating the effect of a varying clock angle on the acceleration of ions across the magnetopause, the model is able to reproduce the ionospheric signatures of component reconnection. The revised model is consistent with the hypothesis of component reconnection discussed in Section 1.3.1, in that it assumes that at all clock angles, reconnection occurs close to the magnetopause subsolar point. This is a fair assumption at clock angles, $\theta_{sh} < 90°$, however this is unlikely to be realistic in cases of northward IMF ($\theta_{sh} << 90°$) as the reconnection site has been shown to move to locations that give $\theta_{sh} \geq 90°$. However the assumption of a fixed reconnection site provides a method of distinguishing between the effects of variations in the location of the reconnection site from the effects of the angle θ_{sh}.

Figure 1.6a in Section 1.3.1 outlined the geometry of how the newly opened field line threads the magnetopause in the case of component reconnection, where: x is the outward boundary normal, z lies in the boundary plane and is aligned with the geomagnetic meridian in the northward direction, y lies in the boundary plane and makes up the right-hand set. The field inside the magnetosphere, B_{sp}, has no y component, but the magnetosheath field B_{sh} does, making an angle $(\pi-\theta_{sh})$ with B_{sp} in the z-y plane, as seen in figure 1.8a.

Figure 3.5 gives a detailed view of the field and flow vectors components projected onto the z-y and z-x planes respectively; only when a vector lies within the plane shown is it marked with a vector symbol, otherwise it is a component in that plane. The right hand axis is Figure 3.5 is the same basic geometry as

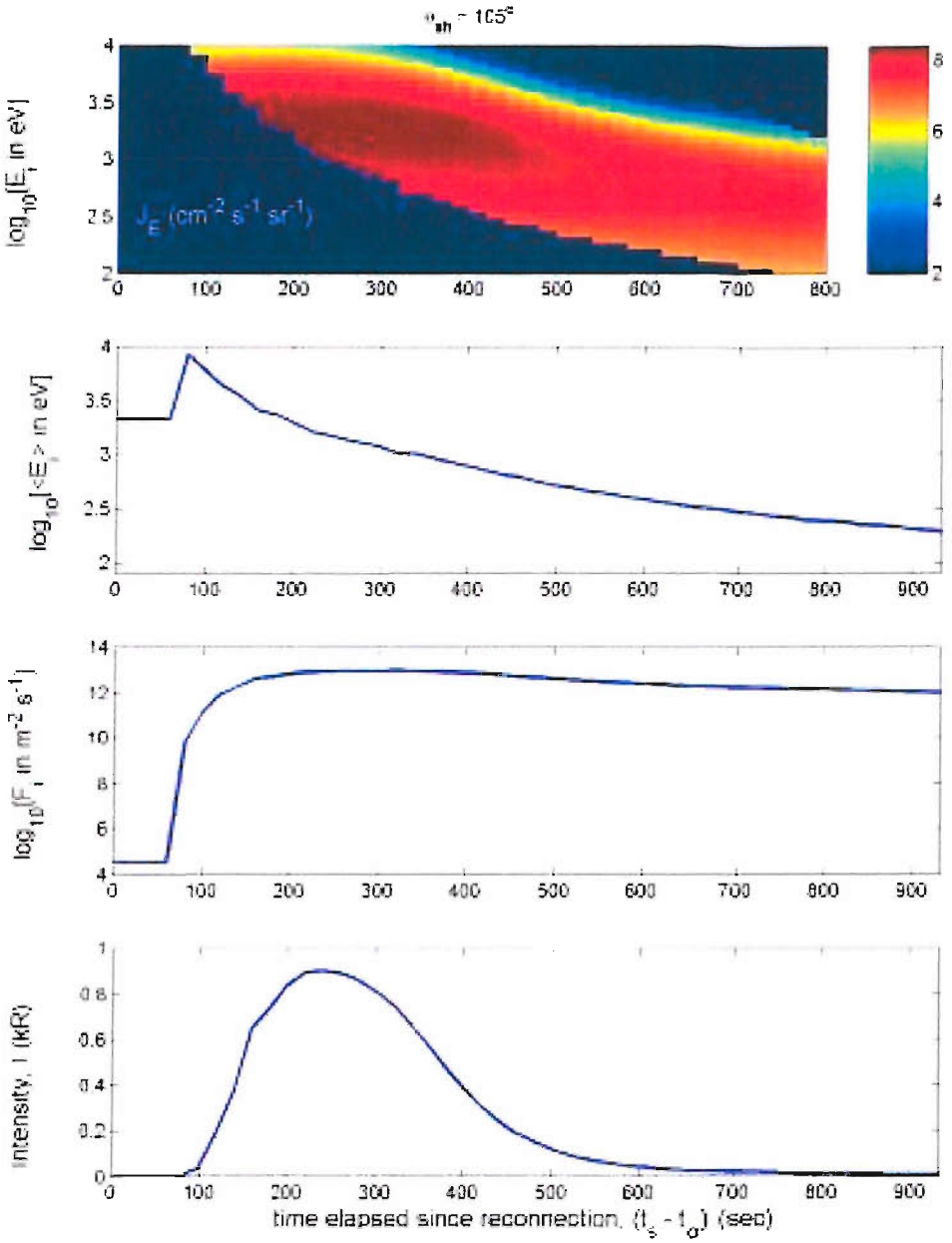

Figure 3.6 Modelled cusp ions as a function of time elapsed since reconnection (t_s-t_o) for a clock angle between exterior (sheath) and interior fields of θ_{sh} = 110°, using the model of Lockwood and Davis [1996], generalised to allow for $\theta_{sh} \neq 180°$. The simulation uses average proton concentration $\langle N[H^+] \rangle$ = 2.95×107m-3 and temperature $\langle T[H^+] \rangle$ = 3.3×105 K observed by ACE at 14:42-14:47 UT, with a subsolar reconnection site. ***a)*** The differential energy flux, J_E, colour-coded (using the scale to the left which shows $\log^{10}[J_E$ in $cm^{-2}s^{-1}sr^{-1}]$ and as a function of ion energy E_i and (t_s-t_o). ***b)*** The mean ion energy $\langle E_i \rangle$. ***c)*** The total precipitating ion number flux F_i. ***d)*** The Lyman-α emission intensity, I, as would be detected by the SI12/FUV instrument.

employed in the original theory of the ion acceleration by Cowley shown in Figure 3.2, but because the sheath field no longer lies in the z-x plane, some full vectors have now become components of that vector. The total flow over the boundary, V_T, is the vector sum of the sheath plasma flow V_{sh} and the field line velocity, V_F, such that the flow across the magnetopause RD is at the local Alfvén speed in the field line rest frame (dHT frame) as discussed above. The resultant field line velocity V_F makes an angle δ with the magnetosheath field in the z-y plane. From the geometric construction shown in figure 3.5a, the projection of the field line velocity onto the z-x plane is $V_F \cos(\pi-\theta_{sh}-\delta)$. For the anti-parallel case used by the original Lockwood and Davis model, this velocity was V_F, therefore this cosine factor was 1, valid for a purely southward IMF. However in the revised model the cosine factor falls to zero for $\theta_{sh} = 90°$ and is negative for $\theta_{sh} < 90°$ (northward IMF).

Figure 3.6 shows an example of the model results obtained for a sheath field clock angle of $\theta_{sh} = 105°$ i.e. component merging with southward IMF. The top panel shows the modelled ion dispersion along a single field line, showing the differential energy flux carried by the ions, as a function of their energy and the time elapsed since the field line was reconnected, (t_s-t_o). The second panel of Figure 3.6 shows the average ion energy, $<E_i>$ at each (t_s-t_o). This jumps up from the magnetospheric levels with the arrival of the first (highest energy) magnetosheath ions from near the reconnection site and then subsequently decays. This decay in $<E_i>$ is a result of two mechanisms; firstly the arrival of progressively lower energy ions in the ionosphere and secondly the decrease in ion acceleration at the magnetopause as the field line evolves away from the reconnection site. The third panel gives the downward number flux of ions, F_i, which rises with the arrival of the first sheath ions and the decays slowly as the cusp precipitation evolves.

3.1.3 Modelling the Lyman-α Emission Intensity in the Cusp

In the study presented in Chapter 5, the revised cusp ion model is used to investigate the relationship between the sheath field clock angle and variations in doppler-shifted Lyman-α emission intensity observed in the cusp region by the

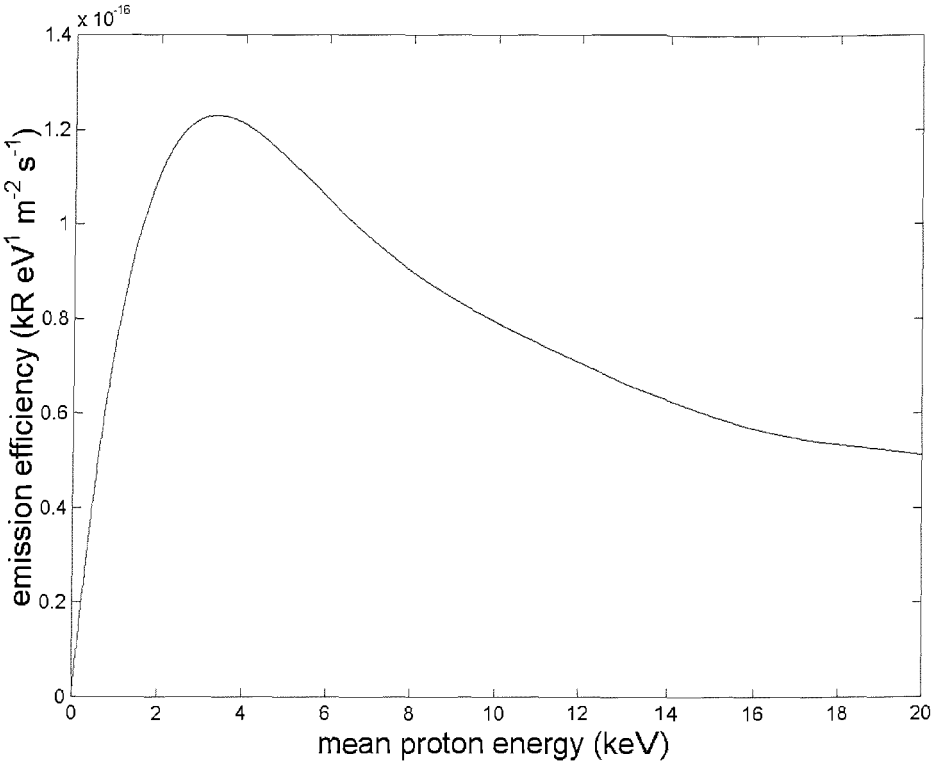

Figure 3.7 The variation of the Lyman-α emission efficiency, convolved with the SI12/FUV instrument response, as a function of the energy of precipitating protons [Gérard et al., 2001].

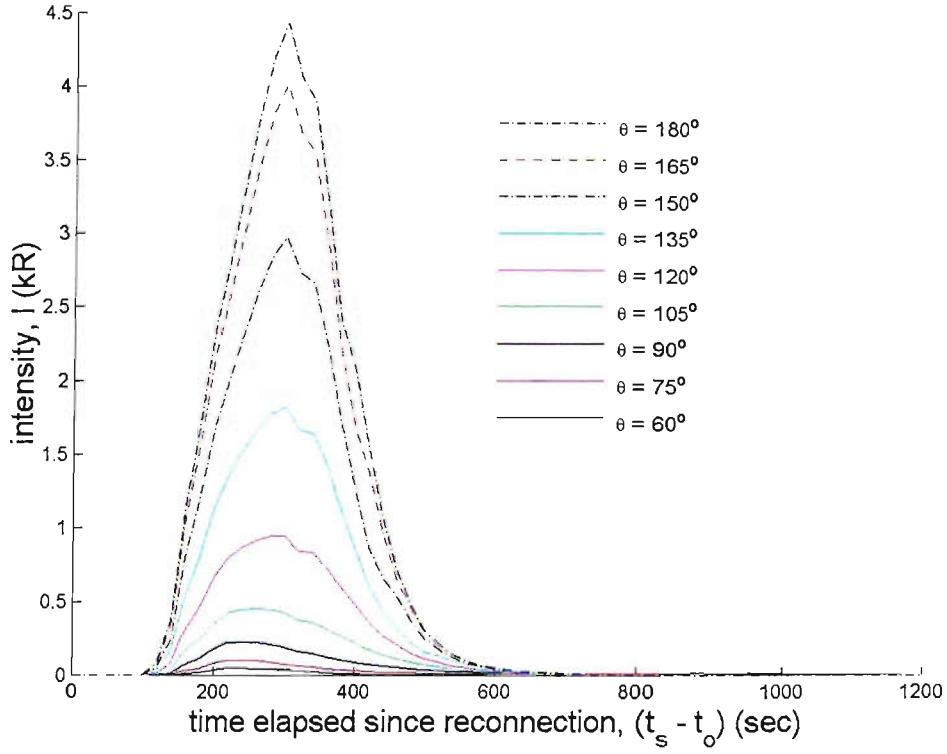

Figure 3.8 Modelled variations of the Lyman-α emission intensity, I, with time elapsed since reconnection (t_s-t_o) for a clock angle between exterior (sheath) and interior fields θsh between 60° and 180°.

IMAGE satellite. Because the IMF clock angle θ_{IMF} is largely preserved across the bow shock [Opgenoorth et al., 2001], the magnetosheath clock angle close to the magnetopause, θ_{sh}, can be considered interchangeable with the upstream IMF clock angle, θ_{IMF}. This means that the measured upstream θ_{IMF} can be used to drive the cusp model and replicate the effect on the ion dispersion along the newly reconnected field lines.

Lyman-α is produced by the precipitation of protons. In order to use the modelled ion spectrum to estimate the doppler-shifted Lyman-α emission along each newly-opened field line in the cusp region, the Lyman-α emission efficiency is required. In order to then make a comparison between the modelled Lyman-α emission and the observations made by the IMAGE satellite, the response function of the instrument is also needed. Figure 3.7 shows the variation of the Lyman-α emission efficiency convolved with the SI12/FUV instrument response as a function of the energy of precipitating protons [Gérard et al., 2001]. Below about 3.5 keV the instrument response falls off sharply. Above 3.5 keV the decay is due to the decrease in the efficiency of the emission production with ion energy.

The modelled doppler-shifted Lyman-α emission, resulting from the precipitating ion spectrum presented in Figure 3.6a is given in Figure 3.6d. It can be seen that peak Lyman-α emission, in this case, occurs at (t_s-t_o) near 250 sec. Before this peak, the intensity observed rises as the ion flux F_i rises. This is a time-of-flight effect. After the peak in the Lyman-α emission, the derived intensity decays rapidly because of the fall in the flux F_i and also, in particular, the fall in the ion energy, as indicated by $<E_i>$.

Figure 3.8 shows this variation of emission intensity with time elapsed since reconnection (t_s-t_o) for a variety of sheath field clock angles θ_{sh}. Two features are apparent. Firstly intensities are considerably enhanced when θ_{sh} approaches 180°. This is because the larger θ_{sh} gives more acceleration at the magnetopause RD and this lifts more ions towards the peak in the emission efficiency curve (Figure 3.7). Secondly, the time since reconnection of the peak emission increases to about 5 min for $\theta_{sh} = 180°$; this reflects the changing balance between the effects of ion energy and ion flux.

A full description of the revised model along with the method employed to compare modelled data with observational data are presented in Lockwood et al. [2003].

3.2 The Lockwood and Morley Convection Model

The Lockwood and Morley model [2004] predicts the evolution of the pattern of ionospheric convection flows in response to general time-dependent magnetic reconnection at the dayside magnetopause and in the geomagnetic tail. The model implements the Cowley and Lockwood theory of ionospheric flow excitation [1992]. This section provides a description of the theory and the model based on it.

3.2.1 The Cowley and Lockwood Theory

A number of observations have shown that the plasma flow in the Earth's polar ionosphere is driven by the solar wind-ionospheric coupling. The nature of this coupling and the resultant plasma flow in the high-latitude ionosphere depends on the orientation and strength of the IMF. Many studies have addressed how the convection responds to a change in the orientation of the IMF [e.g. Nishida, 1971; Lockwood et al., 1986; Etemadi et al., 1988; Saunders et al., 1992]. It was found that when the IMF points southward a twin-vortex flow is present, whose size and strength (as measured e.g. by the area of the polar cap and the voltage across it) both increase as the southward field increases. Dawn-dusk flow asymmetries are also present, opposite in opposite hemispheres, which are related to the IMF B_y component. As IMF B_z becomes small and turns northward, however, the flow system is typically contracted in size, the twin-vortex flows are less vigorous, and B_y dependent lobe circulation cells appear within the polar cap, which are believed to be driven by reconnection between the IMF and open lobe field lines. The evolution of the convection flow under slowly varying solar wind conditions is sufficiently described by the "quasi-steady" state picture described above. The way in which ionospheric convection responds to rapid changes in IMF direction however, is still the subject of much debate.

Originally, models of ionospheric convection had been inherently steady-state in nature, in that they predicted a given pattern of ionospheric convection for a given prevailing orientation of the IMF (e.g. Cowley, 1984; Heppner and Maynard,

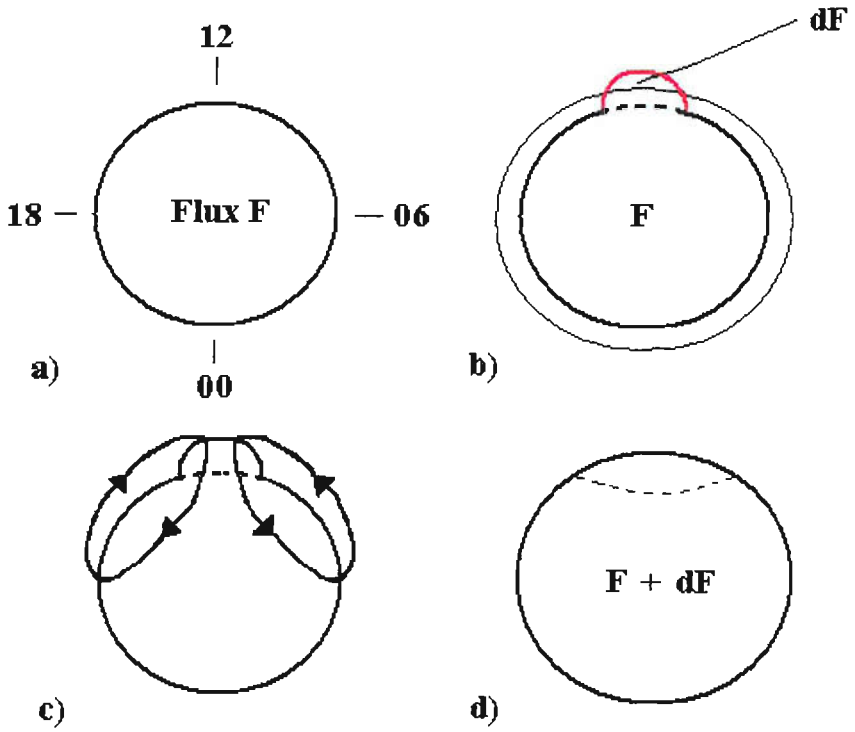

Figure 3.9 An illustration of the ionospheric response to the onset of dayside reconnection. The OCB is represented by the solid line. ***a)*** Shows the initial equilibrium configuration. ***b)*** Reconnection adds open flux, dF, to the polar cap perturbing the boundary. The thin line marks the new zero-flow equilibrium boundary, which contains an equal amount of open, F+dF. The dashed line marks the boundary of the newly-opened flux region. ***c)*** The twin-celled convection, which returns the system toward equilibrium. ***d)*** The system has reached the new zero-flow equilibrium configuration marked in ***b)***. [Cowley and Lockwood, 1992]

1987; Reiff and Burch, 1985; Weimer, 1995). Such models did not consider the previous history of the IMF and were not able to explain the behaviour of the convection flows under rapidly varying IMF conditions. Cowley and Lockwood [1992] developed a conceptual model of convection response on short timescales, which has been widely applied to the interpretation of convection responses observed on short timescales (meaning shorter than the typical duration of a substorm cycle). The picture of the flow response proposed by this model is illustrated in Figure 3.9, which combines together ideas on boundary motions and flows discussed previously by Siscoe and Huang [1985] and Freeman and Southwood [1988].

The basic idea behind this model is that if all magnetopause coupling is switched off, together with reconnection in the tail, then the near-Earth system will approach equilibrium and the flows will die away, even if open flux is still present. Subsequent reconnection at the magnetopause or in the tail perturbs the system away from this equilibrium, and excites flow, which carries the system towards a new equilibrium with the changed amount of open flux. The figure shows views of the northern polar ionosphere, and in Figure 3.9a the IMF has been northward for a significant interval such that there has been no dayside reconnection and the near-Earth flow has died away as the system approaches equilibrium, even though open flux, F, is present. For simplicity we do not include the effects of lobe or tail reconnection in this discussion, so as to isolate the effects of the magnetopause reconnection rate variations. The IMF then turns south at the subsolar magnetopause, and dayside reconnection starts. The first thing to happen is that the open-closed field line boundary moves equatorward in the noon sector, representing departure from equilibrium, as shown in Figure 3.9b, followed by the excitation of flow, Figure 3.9c, which appears first near noon and expands over the polar cap at a phase speed of several km s^{-1}. After 15-20 min the flow has expanded to cover the whole of the polar region and is accompanied by an expanding open-closed field line boundary at all local times. This corresponds to the situation analysed by Siscoe and Huang [1985]. The red line portion of the open-closed boundary, shown in Figure 3.9b, maps to the dayside reconnection region; the plasma crosses this boundary as the field lines become open. At the solid-line segments the boundary moves exactly with the plasma flow because

these do not map to active reconnection sites where flux crosses the boundary. The 15-20 min time scale for full flow excitation represents the time scale for open field lines to move from the dayside reconnection sites into the near-Earth tail, and for the near-Earth system to respond to these flux changes at Alfvénic propagation speeds. The thin black line in Figure 3.9b shows the equilibrium position of the open-closed boundary, which would contain the same amount of open flux, F+dF. If the IMF now turns northward once more and dayside reconnection ceases, then declining twin-vortical flow will be maintained until the open-closed boundary approaches the equilibrium position over an interval of ~20 min. After this, however, the flows will have died away to small values, as shown in 3.9d, and will so remain until further reconnection occurs either at the magnetopause or in the tail.

The Cowley and Lockwood model of flow excitation, therefore, predicts an immediate onset of convection in response to IMF changes, but that changes in the ionospheric flow will be smoothed by an inductive time constant of order 15-20 min, which is the time constant for the dayside magnetosphere-ionosphere system to come to equilibrium with the new amount of open flux that has been added to the polar cap. This polar cap expansion has been supported by various experimental studies. A study by Saunders et al. [1992] using the CANOPUS (Canadian) magnetometer array has shown the flow response was first initiated near the noon sector and spread towards the dawn and dusk sectors with longitudinal phase velocity of the order of 5 kms^{-1} consistent with the Cowley and Lockwood theory. Lockwood et al. [1993] showed that convection enhancements observed by the EISCAT radar, occurred in response to short-lived (minute-scale) pulses of magnetopause reconnection and Milan et al. [1999] have shown that flow responses observed by the CUTLASS SuperDARN radar are as predicted by the model.

3.2.2 Modelling the Convection Response to Dayside Reconnection

The Lockwood and Morley [2004] model is the numerical implementation of the Cowley and Lockwood conceptual model of ionospheric flow excitation described in the previous section. Lockwood and Morley use a number of initial

input parameters to drive their model, and hence the evolution of the convection flows and the motion of the open-closed boundary (OCB).

Figure 3.9a shows that the initial size of the polar cap is defined by an arbitrary amount of open flux, $F_{OCB}(t_s = 0)$. Establishing the initial position of the OCB, before the onset of reconnection, determines the value $F_{OCB}(t_s = 0)$ and therefore provides the first input to the model. Figure 3.9b shows that the onset of reconnection adds open flux to the polar cap. The reconnection voltage placed across the magnetosphere by magnetopause reconnection represents the rate of production of open flux added to the polar cap. The Lockwood and Morley model utilizes the fact that the reconnection voltage varies with the B_z component of the IMF [Reiff et al., 1981; Cowley, 1984a; Boyle et al., 1997], and hence the IMF clock angle, by the relation:

$$E_n = E_{no}\, \sin^4\left(\theta_{IMF}/2\right)$$

where E_n is the electric field tangential to the ionospheric x-line, which lies on the OCB, and is equal to the ionospheric projection of the reconnection rate, and E_{no} is the value of that electric field for purely southward IMF ($\theta_{IMF} = \pi$). This relationship means that it is possible to use the upstream IMF clock angle θ_{IMF} to drive the model by determining the amount of newly opened flux, ΔF_{pc}, to be added to the magnetosphere-ionosphere system in an interval Δt_m which is the sampling interval of the upstream data.

For an X-line footprint of prescribed length, this prescribes the distribution of potential around the OCB. It is assumed that the ionospheric conductivities are uniform over the polar regions and Laplace's equation is solved for inside and outside the polar cap separately to derive the spatial distribution of potential away from the OCB. An additional input parameter required is the latitude of the zero potential contour, equatorward of which the convection pattern is shielded out by the region 2 currents that connect to the ring current. In this way, the model

generates the streamlines of the full convection pattern. Figure 3.9 shows that because the model assumes that the equilibrium polar cap is circular in form, the OCB will expand equally at all MLTs. The equipotentials migrate away from noon as the polar cap voltage increases and flows intensify. The strength of the convection response (the density of the equipotential lines) is quantified by the transpolar voltage, Φ_{PC} (the voltage between the centres of the two flow cells) at any given time. The model provides a way of following the evolution of both the OCB in terms of latitudinal position, Λ_{OCB}, and the presence of open flux in the polar cap, ΔF_{PC}. The model allows studies of the evolution of the polar cap voltage, Φ_{PC}, as the convection pattern evolves, as opposed to the X-line voltage, Φ_{XL}, that is driven by the upstream IMF variation. Further details of the model and its application are given in Lockwood and Morley [2004] and Morley and Lockwood [2005].

In this thesis, the Lockwood and Morley model is used in combination with the Lockwood and Davis model to predict the spatial and temporal evolution of both ionospheric convection flow patterns and of the proton aurora in response to upstream solar wind and IMF data. These model predictions are compared to satellite-borne and ground-based observations in order to understand the underlying processes that produce ionospheric signatures characteristic of the cusp. In this way, the model results can be used to help separate ionospheric response to reconnection from the effects of ionospheric coupling with other upstream features.

Chapter 4.

Relating Upstream Features to Dayside Ionosphere Events

The main theme of this thesis is to couple upstream solar wind and magnetic field features, detected by the ACE and Wind satellites, to dayside ionospheric signatures observed by a range of ground-based and satellite-borne instruments. This study looks at two events that occurred on the morning and afternoon of the 26 November 2000, and a third event that occurred on the 29 December 2001.

4.1 26 November 2000

The Solar and Heliospheric Observatory (SOHO) observed a series of six solar flares and large eruptive events between 24 November and 27 November 2000 initiated by the activity of one active region (AR9236) located in the Sun's northern hemisphere [Solar-Geophysical Data, 2001]. A number of coronal mass ejections accompanying the flares were propelled in the direction of Earth, buffeting the magnetosphere from the 26 November onwards. The resulting geomagnetic activity on 26 November 2000 has been the focus of a number of different studies, which used the highly variable upstream solar wind conditions to explain a number of magnetospheric and ionospheric events [e.g. Yoshida et al., 2001; Pitout et al., 2002; Lanchester et al., 2003; Lockwood et al., 2003].

Figure 4.1 provides an overview of both the solar wind conditions and the resulting ground-based observations on 26 November 2000. The top two panels show the upstream variations in the B_z component of the IMF and the solar wind density, as

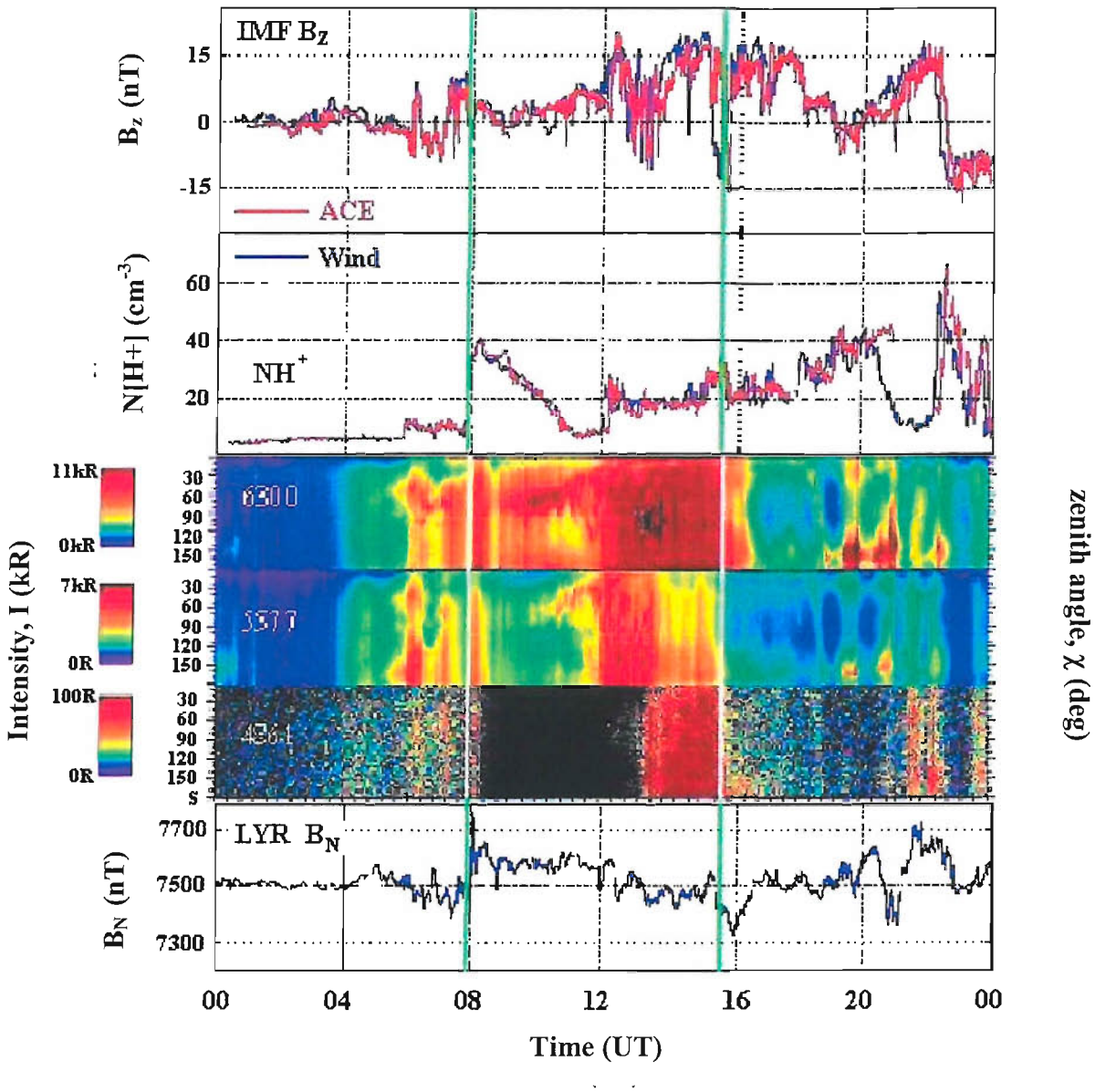

Figure 4.1 An overview of the solar wind and ground-based observations for the 26 November 2000. The top two panels show IMF B_z component and the solar wind proton number density, N[H+], both lagged by the predicted satellite-to-ionosphere propagation delay, as observed by ACE (in red) and Wind (in blue). Panels 3, 4 and 5 show the slant-path integrated intensity I of, respectively, 630nm (neutral atomic oxygen), 557.7 nm (neutral atomic oxygen) and 486.1 nm (neutral hydrogen (Balmer-beta) auroral emissions observed as a function of zenith angle by the meridian scanning photometer (MSP) at LYR. The bottom panel shows the northward component B_N of the magnetic field observed by the LYR magnetometer station. The two vertical green/white lines denote the times at which the two events, explored in this study, occurred.

monitored by both the ACE (red) and Wind (blue) satellites. In each case the data has been lagged by the average time it would take for each solar wind feature to have an initial impact on the ionosphere. Section 4.3 describes the method used to calculate this propagation time. Combining ACE and Wind data gives us the ability to lag the data more accurately by the propagation delay and the reduced uncertainty allows a direct comparison with ionospheric observations. The third, fourth and fifth panels show ionospheric observations made from the Meridian Scanning Photometer (MSP) at LYR. Both electron stimulated emissions (630.0 nm, 557.7 nm) and proton stimulated emissions (486.1 nm) were observed over a range of latitudes in response to the highly variable upstream conditions. The bottom panel shows the ground magnetic perturbations recorded by the magnetometer station at LYR during this period of heightened geomagnetic activity.

This study focuses on two events, which occurred on the morning and afternoon of the 26 November, marked in Figure 4.1 by two vertical green/white lines. Section 4.1.1 provides an overview of the afternoon event (starting around 15:20 UT) characterised by an increase in proton and electron cusp precipitation in response to a southward turning in the IMF which we infer triggered enhanced dayside reconnection. Section 4.1.2 provides an overview of the morning event (starting around 08:00 UT) in which enhanced cusp precipitation was detected in association with a distinct bipolar magnetic signature, as observed by magnetometers on the ground. We interpret these ionospheric features as the ionospheric response to the impact of a solar wind shock front, possibly due to a CME, accompanied by a brief southward IMF turning.

4.1.1 Event One: 26 November 2000 (PM)

The event on the afternoon of the 26 November was first reported by Lockwood et al. [2003] (hereafter LEA03). A double brightening of Lyman-α emission in the cusp occurred in response to a short-lived southward turning of the IMF during a period of enhanced solar wind plasma concentration. Combining data from the upstream ACE

and Wind satellites with cusp observations from the SI-12 channel of the FUV instrument on the IMAGE satellite revealed that the intensity of the cusp emission varied systematically with the IMF clock angle. This relationship was particularly striking when the intensity was normalised to allow for the variations in upstream solar wind proton concentration. The relationship between the upstream IMF clock angle, defined in Section 1.3.1, and the Lyman-α emission intensity reported in LEA03 is shown in Figure 4.2, along with the upstream solar wind proton concentration. The solar wind and IMF data has been lagged by the propagation time between the ACE satellite and the ionosphere allowing a direct comparison with the IMAGE FUV observations. Section 4.3 describes the method used to calculate the ACE-to-ionosphere propagation time: in particular, section 4.3.1 discusses how this method was applied to this particular event.

A detailed study of the 26 November afternoon event is set out in Chapter 5. It expands upon the original study made by LEA03 which used the numerical cusp model developed by Lockwood & Davis [1996], discussed in Section 3.1.2, to replicate the effect of the varying sheath-field clock angle on the acceleration of the ions injected across the magnetopause and hence on the consequent Lyman-α emission intensity. This study identifies a number of discrepancies in the original analysis in LEA03 and rectifies them in order to confirm and refine the findings of the LEA03 study, which concluded that the clock angle dependence of the Lyman-α emission was consistent with component reconnection.

The study presented here also reproduces the observed spatial distributions of this emission on newly-opened field lines by combining the Lockwood and Davis cusp model with the Lockwood and Morley numerical model of time-dependent ionospheric convection, discussed in Section 3.2. This allows a comparison of modelled magnetospheric and ionospheric parameters with those measured by a range of different instruments. Such a comparison provides a means of confirming quantitatively the concepts of ionospheric flow excitation by Cowley and Lockwood [1992] on which the model is based.

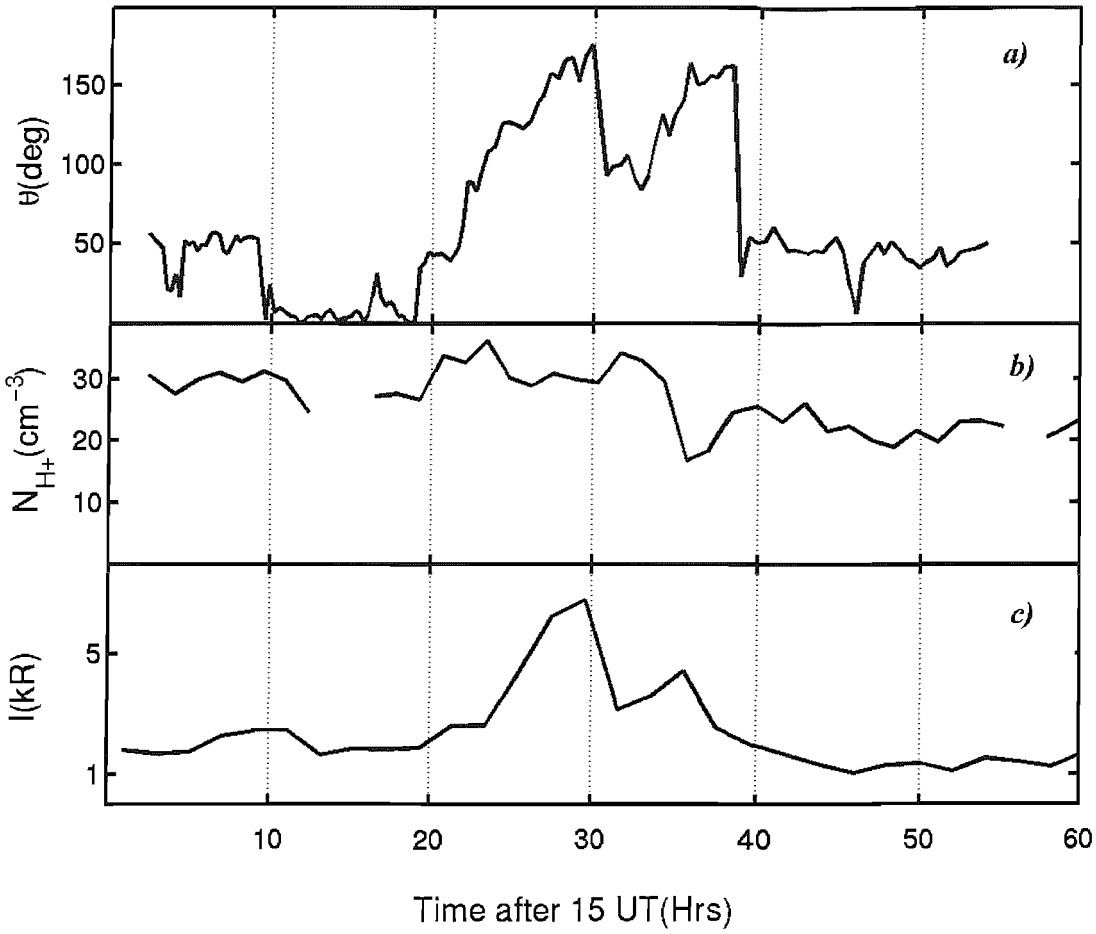

Figure 4.2 Variations of parameters observed during the brief intensification of the cusp proton aurora on 26 November 2000 (afternoon event), as reported by LEA03: ***a)*** the lagged IMF clock angle θ, and ***b)*** the proton concentration in the solar wind, as observed by ACE; ***c)*** I_o, the peak Doppler-shifted Lyman-α emission intensity in the cusp seen in FUV/SI-12 data. The solar wind and IMF data have been lagged by the propagation delay variation for this interval, as obtained by comparing Wind and ACE data.

4.1.2 Event Two: 26 November 2000 (AM)

The second event studied here occurred in the morning hours of 26 November 2000 around 8UT. The ground-based optical instruments on Svalbard measured a sudden increase in intensity of auroral emissions, resulting from both proton and electron precipitation. This is demonstrated by the top three panels of Figure 4.3, which show emissions in spectral windows associated with both electron and proton precipitation as detected by the MSP at Longyearbyen. At around the same time, a particularly distinct bipolar signature was seen in the magnetic recordings of the IMAGE, Greenland and 210MM magnetometer arrays, similar to those associated with a propagating vortical convection structure. The red line in the bottom panel of Figure 4.3 shows the LYR magnetometer data in which the bipolar structure is clearly apparent.

As discussed in the introduction, it is widely accepted that the interaction of a pulse in the solar wind pressure with the magnetosphere leads to the generation of field-aligned currents, which manifest themselves in the high-latitude ionosphere as propagating vortices known as TCVs. Examining upstream data reveals that both ACE and Wind measured a significant increase in the solar wind pressure during this event. However, determining whether this pressure increase is responsible for the observed ionospheric signatures is complicated by a simultaneous brief swing of the interplanetary magnetic field to a southward orientation. The brief pulse of reconnection that results from this southward turning, like a pressure pulse, produces transient field-aligned currents and associated flows, which expand away from noon. Figure 4.3 shows these upstream features lagged by the predicted ACE-to-ionosphere propagation delay, as calculated in Section 4.3.2.

Chapter 6 describes high- and low-pass filtering as a method of separating the effects of the reconnection pulse from the pressure pulse effects on the ground-based data, allowing the study of their individual impact on the magnetosphere-ionosphere

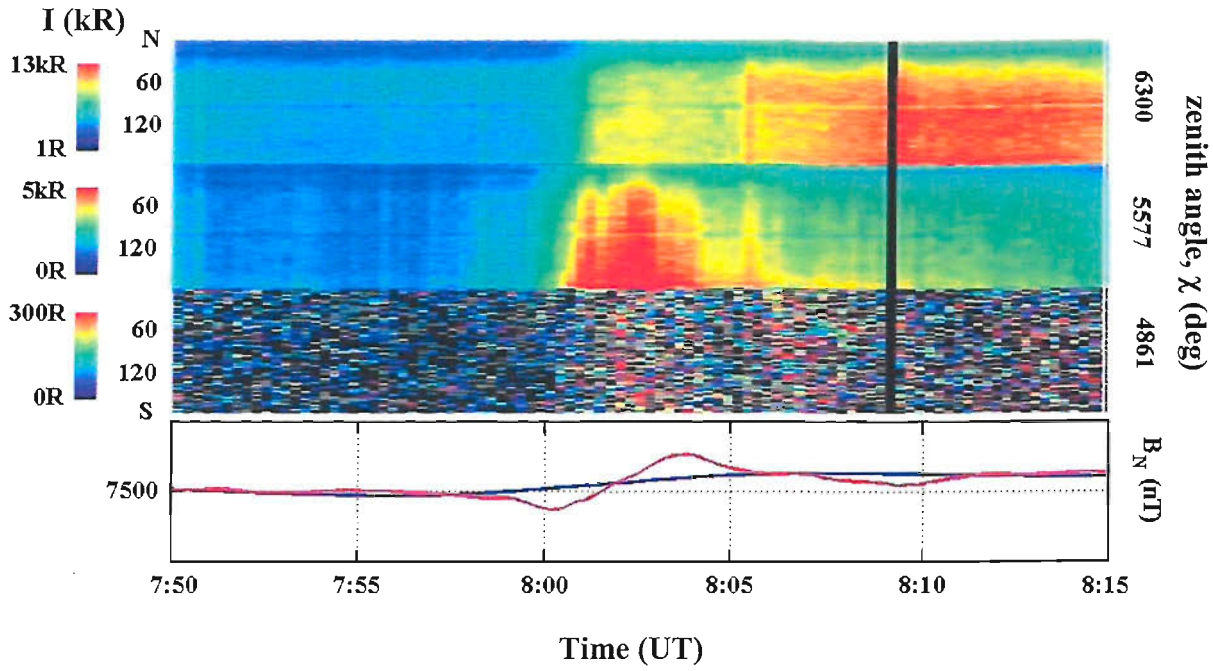

Figure 4.3 Data from the LYR MSP and magnetometer instruments during the 26 November 2000 morning event. The data and formats are the same as for the lower 4 panels of Figure 4.1. In the bottom panel the red line gives the unfiltered magnetometer data, while the blue line represents the low-pass filtered data.

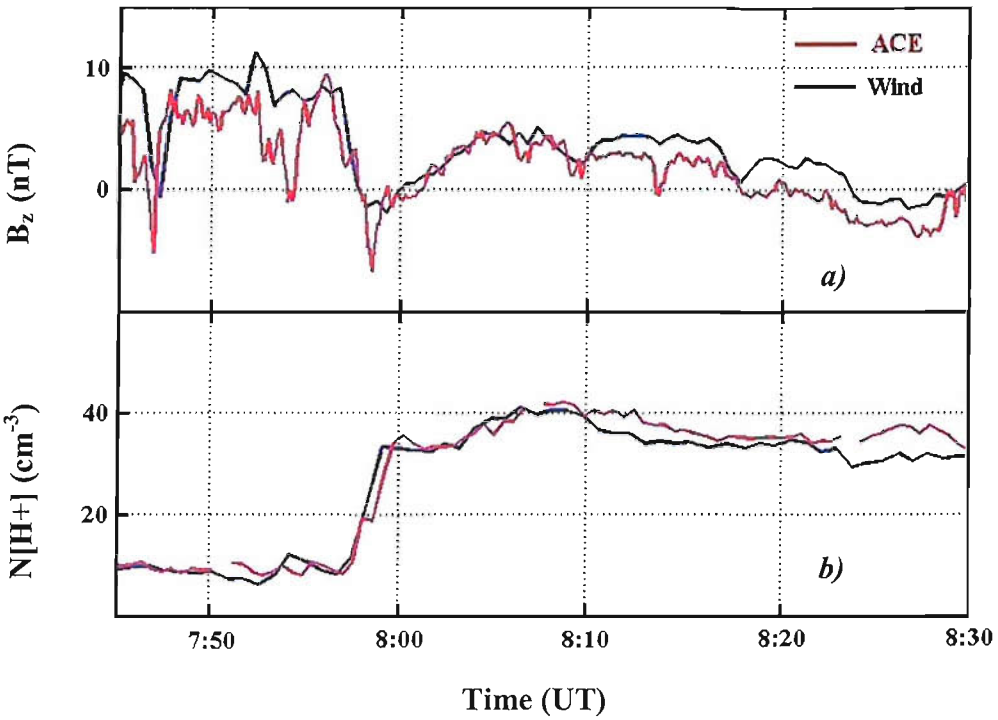

Figure 4.4 The variations in ***a)*** the B_z component of the IMF in GSM coordinates and ***b)*** the solar wind proton density; both observed by both the ACE (red) and the Wind (blue) satellites during the 26 November 2000 morning event. In each case the data has been lagged by the predicted propagation delay to the noon magnetopause.

system. The Lockwood and Morley convection model is here used to emulate the ionospheric flows triggered by the onset of dayside reconnection and provides evidence in support the filtering method as a way of separating the two class of effects. The position of the ground-based instruments at the time of the event made it possible to study both the reconnection and pressure pulse effects on the ionosphere near noon and to investigate the evolution of the temporally and spatially varying pattern of field aligned currents and flows associated with these effects.

4.2 29 December 2001

SOHO solar observations show that the twisted magnetic field above sunspot group 9747 erupted on the 26 December 2001. The blast triggered an hour-long solar flare and hurled a clear coronal mass ejection (CME) into space. The CME was not squarely Earth-directed but it did deliver a glancing blow to the magnetosphere on the morning of the 29 December 2001. The impact of the pressure shock front associated with the CME marked the start of low-level geomagnetic activity that continued throughout the day.

Figure 4.5 provides an overview of both the solar wind conditions and the resulting ground-based observations for the 29 December 2001. The vertical green/white line marks the time of arrival of the pressure front at the magnetosphere. The top two panels show the upstream variations in the B_z component of the IMF and the solar wind density as monitored by the ACE (red) and Wind (blue) satellites. In each case the data has been lagged by the average time it would take each solar wind feature to have an initial impact on the ionosphere. Section 4.3.3 describes the method used to calculate this propagation time. The third, fourth and fifth panels show data from the meridian scanning photometer (MSP) at LYR. Both electron-stimulated (630.0 nm, 557.7 nm) and proton-stimulated emissions (486.1 nm) were observed over a range of latitudes in response to the highly variable upstream conditions. The bottom panel shows the ground magnetic perturbations recorded by the magnetometer station at LYR during this period of heightened geomagnetic activity.

This study focuses on the interaction of the pressure front with the Earth's magnetosphere and the ionospheric signatures that result. This event is of particular interest as it occurs during a period of enhanced and consistently northward IMF, unlike the other two events, during which the IMF has at least a brief interval of southward IMF. This provides a means of testing the Lockwood and Morley convection model used to emulate the ionospheric flows in event one and event two.

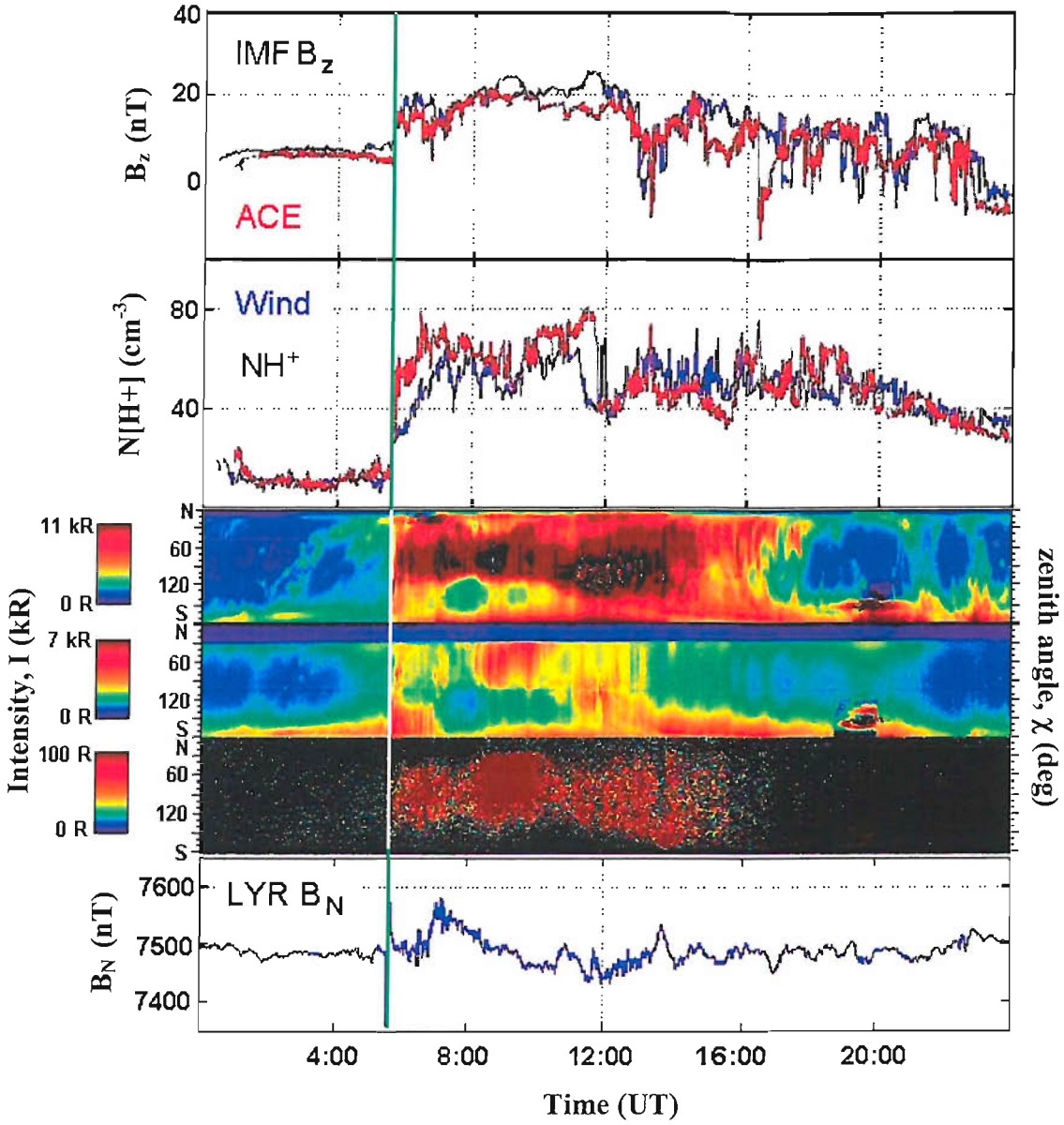

Figure 4.5 An overview of the solar wind and ground-based observations for the 29 December 2001. The data and formats are as for Figure 4.1

4.2.1 Event Three: 29 December 2001

During this event, a range of ground-based and satellite-borne observations revealed evidence of lobe reconnection accompanying auroral emissions resulting from the impact of the pressure front on the magnetosphere. These emissions were detected primarily in the noon sector by the IMAGE FUV instrument. Figure 4.6 shows images from the FUV/SI12 and FUV/SI13 instruments on IMAGE. The top three panels show the variations in proton-stimulated Lyman-α emission, the bottom three panels show variations in electron-stimulated OI emission over the period of interest. Enhanced auroral emissions are evident in the noon sector triggered by the arrival of the enhanced pressure front at 5:40 UT.

At the same time, a distinct signature is seen in the magnetic recordings of the IMAGE, Greenland and MM210 magnetometer arrays similar to those associated with the TCV in event 2. Figure 4.7 shows data from the LYR magnetometer station, along with and the lagged solar wind pressure monitored by the ACE and Wind satellites. There is a clear bipolar structure, which is linked, by the calculated ACE-to-ionosphere propagation time, to the solar wind pressure increase.

Chapter 6 uses the fact that this event is not accompanied by a southward IMF turning to test the filtering technique used in Chapter 5. Filtering the ground-based data should reveal no significant underlying convection and so the short period magnetic variations due to the pressure pulse should be seen in isolation.

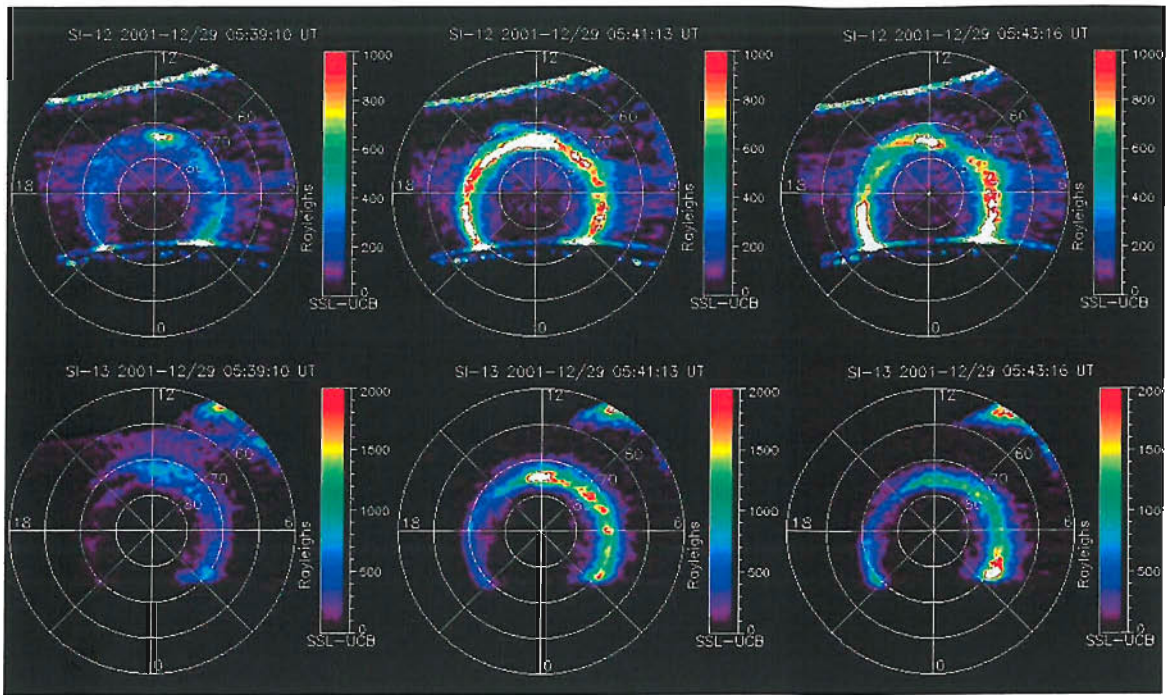

Figure 4.6 Images from the FUV/SI12 and FUV/SI13 instruments on IMAGE presented in and invariant latitude – magnetic local time (MLT) frame. The top three panels show the variations in proton stimulated Lyman-α emission, the bottom three panels show variations in electron stimulated OI emission over the period of interest. Both panels show an enhancement around 12 MLT just after the arrival of the solar wind pressure pulse at around 05:40UT.

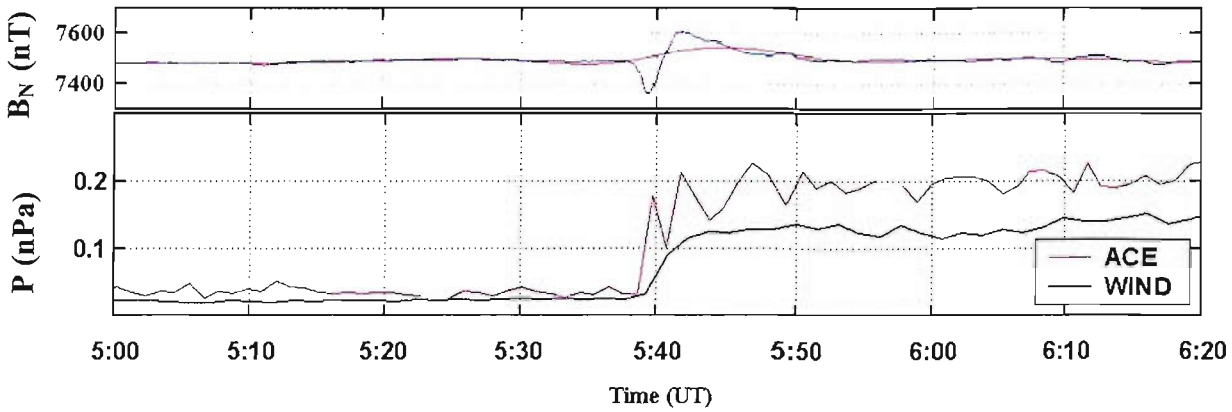

Figure 4.7 The top panel shows the filtered and unfiltered data from the LYR magnetometer station: the red line represents the unfiltered data, while the blue line represents the low-pass filtered data. The bottom panel shows the solar wind pressure at the ACE (red) and Wind (blue) satellites: in both cases the data has been lagged by the predicted propagation delay to the noon magnetosphere.

4.3 Calculating the Propagation Time of Upstream Events to the Dayside Ionosphere

Experimental observations of solar wind-magnetosphere coupling processes rely on measurements of the IMF and plasma parameters in the upstream solar wind. The ACE and Wind satellites' orbit enables them to monitor the highly variable speed, composition and magnetic field of the solar wind as it propagates Earthwards.

As a consequence of the spatial separation between an upstream monitor and the magnetopause (MP) coupling region, there is a propagation time t_p, for a solar wind signature to reach an assumed average MP coupling location (assuming that the structure has large enough spatial extent that it does indeed pass over both the spacecraft and the Earth). The propagation time t_p consists of two components: (1) the propagation time in the solar wind between arrival at the satellite and arrival at the subsolar bow shock; (2) the transit time across the subsolar magnetosheath to the MP coupling region. The propagation time of a feature between the spacecraft and the dayside cusp ionosphere has a third component which is the Alfvénic propagation of the effects of magnetopause processes along newly-opened field lines to the cusp ionosphere. Solar wind structures are often imagined to lie along a planar "phase front" that may be orientated at an arbitrary angle to the propagation flow. From a single spacecraft, we do not know this orientation and the resulting uncertainties can be large, even if the spacecraft is close to the Sun-Earth line. To obtain the lag with complete accuracy, we require 3 craft so that the phase front orientation is known in 3 dimensions; however, with two craft an improved estimate can be obtained because the craft are usually not far from the ecliptic plane. Figure 4.8 gives schematic illustrations of a single phase front in the X-Y plane when both ACE and Wind data are available (right) and when only ACE is monitoring the upstream conditions (left).

When only ACE is available, it is usually assumed that the phase front is perpendicular to the solar wind velocity vector, $\mathbf{V}_{xSW}$. This yields a propagation

delay to the bow shock (element 1 of the 3 that make up the satellite-to-ionosphere lag) of $(X_A\text{-}s)V_{xSW}$ (where s is the standoff distance of the bow shock) whereas for a real orientation angle of θ_f ,as shown, the lag would be $(X_A - s + Y_A \tan\theta_f)/V_{xSW}$, giving an error in the first estimate of $(Y_A \tan\theta_f / V_{xSW})$. For example, for a (small) Y_A of $30R_E$, a typical V_{xSW} of 400 km s^{-1} and θ_f of 45°, the error caused by the orientation assumption is 480 sec, which is comparable to the duration of many of the ionospheric impulse responses we wish to study.

The difference in arrival time of the front at ACE and Wind is used to determine the orientation of this front, θ_f, with respect to the Sun-Earth line. This calculation is made easier by the fact that both craft lie close to the ecliptic (X-Y) plane, simplifying this into a 2-D problem:

$$\tan\theta_f = \frac{Y_W - Y_A}{X_A - d - X_W}$$

The distance d can be computed from the lag δt_{AW} between a feature being seen at ACE and Wind and the observed solar wind speed, V_{xSW}, ($d = \delta t_{AW} \times V_{xSW}$). Once θ_f is known, the point at which it intercepts the Sun-Earth line, denoted by the red dot in Figure 4.8a, can be established. The transient time of the front along this line to the subsolar bow shock (BS) is then calculated using the mean observed solar wind speed, $\langle V_x sw \rangle$. Errors remain because of the unknown orientation in the X-Z plane: these are generally smaller because Z_A is generally smaller than Y_A.

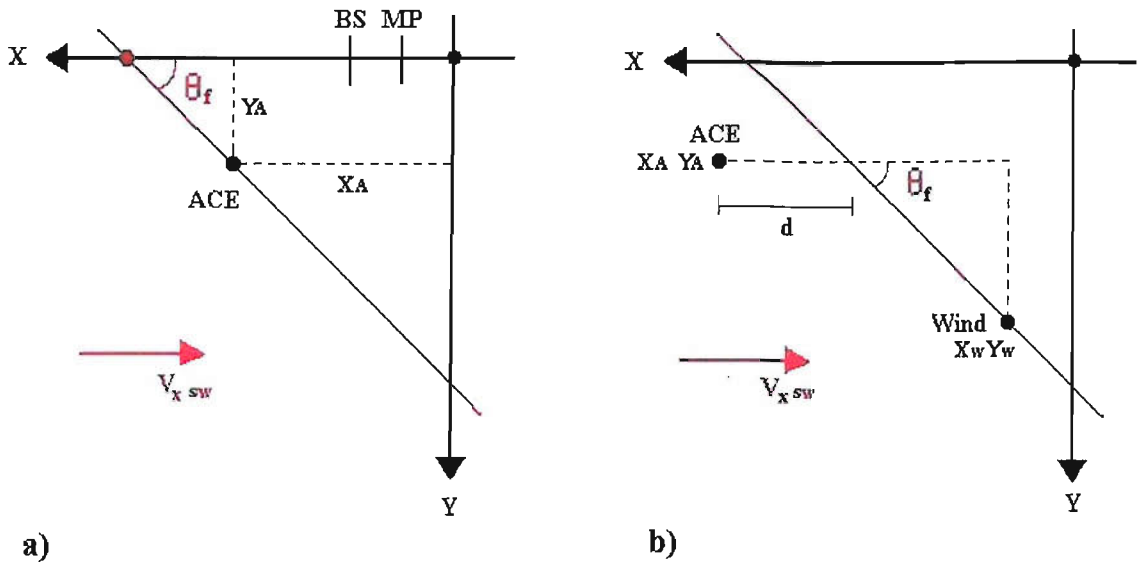

Figure 4.8 Schematic illustration of a single phase front in the X-Y plane. ***a)*** Shows the front orientation relative to the Sun-Earth line, 'θ_f', which passes across the ACE satellite situated at X_A, Y_A: X_A is its distance from the Earth along the Sun-Earth line and Y_A is its distance duskward of the Sun-Earth line. ***b)*** Shows the phase front passing across the Wind satellite (X_W, Y_W) and propagating toward ACE with a velocity of $V_x$sw.

The second element in calculating the propagation delay is the transit time across the subsolar magnetosheath, τ_{sh}. To estimate this, a model is required to locate the positions of the subsolar bow shock, 'R_{BS}', and the magnetopause, 'R_{MP}', and the variation of the plasma speed between them. The shock and magnetopause locations are here derived from the comprehensive empirical studies by Peredo et al. [1995] and Roelf and Sibeck [1993] respectively, as implemented by Khan and Cowley [1999]:

$$R_{BS} = \frac{\mathbf{162}}{\left[< n_{sw} > \; < V_{sw} >^2\right]^{1/6}} R_E$$

where '$<n_{sw}>$' is the average solar wind density (in cm^{-3}) and $<V_{sw}>$ is the average solar wind velocity (in kms^{-1}).

$$R_{MP} = \frac{\mathbf{111}}{\left[< n_{sw} > \; < V_{sw} >^2\right]^{1/6}} R_E$$

When the solar wind encounters the subsolar bow shock, its speed is suddenly reduced by a factor of ~ 4. According to gas dynamic models the speed continues to fall as the plasma traverses the magnetosheath and reaches the magnetopause. Accurate estimation of the overall transit time requires that these effects are taken into account.

The third element of the spacecraft-to-ionosphere delay is the Alfvénic propagation of the effects of magnetopause processes along newly-opened field lines to the cusp ionosphere. The transit time from the subsolar magnetopause to the ionosphere can then be determined because it is approximately one quarter of the period of fundamental mode eigenoscillations of the outer dayside field lines. Since these periods are typically found to lie in the range 5 – 10 min [Poulter et al., 1984], we have here taken the magnetopause-to-ionosphere transit time to be 2 min.

The accuracy of this calculation is limited by the assumptions that: 1) the upstream plasma conditions are spatially uniform over a few 10s of R_E, 2) the solar wind transients are parallel to phase fronts in the GSE x-y plane and/or Z_A is near zero, 3) the phase front is planar and 4) the phase front orientation does not change as it propagates.

In the studies presented here we use the GEOTAIL spacecraft, when it was available in a suitable location, to remove these uncertainties in events 2 and 3. Where necessary we make corrections for one or more of the above limitations separately. For example, for event 1 we find evidence for a linear variation in the orientation angle with time and use this to allow for effect 4).

This section has described the method used to calculate the ACE-to-ionosphere propagation time. Sections 4.3.1, 4.3.2 and 4.3.3 show how this method is applied to the three individual events.

4.3.1 Event One: Calculating the ACE to Ionosphere Propagation Time

The first event, discussed in Section 4.1.1, showed strong signatures in the solar wind and subsequent proton precipitation. A double brightening appeared to occur in response to two short-lived southward turnings of the Interplanetary Magnetic Field (IMF), during a period of strongly enhanced solar wind plasma concentration. Because the variations in the cusp Lyman-α emission were short-lived, the propagation delay of the upstream features needed to be accurately determined before the controlling influence in the IMF could be verified.

The upstream solar wind parameters are shown in Figure 4.9. Figure 4.9a, b and c show the three components of the Interplanetary Magnetic Field (IMF) in the GSE frame of reference, as seen by ACE (in red) and Wind (in blue). The data is plotted as a function of time at Wind with the ACE data shifted by $\delta t_{WA} = t_W - t_A$, where t_W is the time at which a certain feature in the IMF variation was seen at Wind and t_A is the time that the same feature was seen at ACE. Similar, but not identical, IMF variations were seen by the two craft over the time period shown in Figure 4.9. From shortly after 13 UT to after 17 UT the IMF was northward except for the brief southward excursion during which both $[B_x]_{GSM}$ and $[B_y]_{GSM}$ changed polarity indicating a crossing from away to toward sectors with the IMF in garden-hose orientation. Figure 4.9d shows the solar wind speed seen by ACE, which was enhanced at about 11:30 UT and remained high throughout the period of interest although it fell somewhat (from about 630 kms^{-1} to 560 kms^{-1}) around the time of the return of the IMF to a northward orientation.

Figure 4.9c shows that a time lag of δt_{WA} = 12 min has been used to align the southward IMF turning seen by both craft. However, this lag clearly does not apply to the subsequent return to northward IMF just after 15:00 UT which is seen by both craft but with an increased lag of δt_{WA} = 16 min. A factor in this change of the lag is the decrease in solar wind speed but this is far from sufficient, showing that the

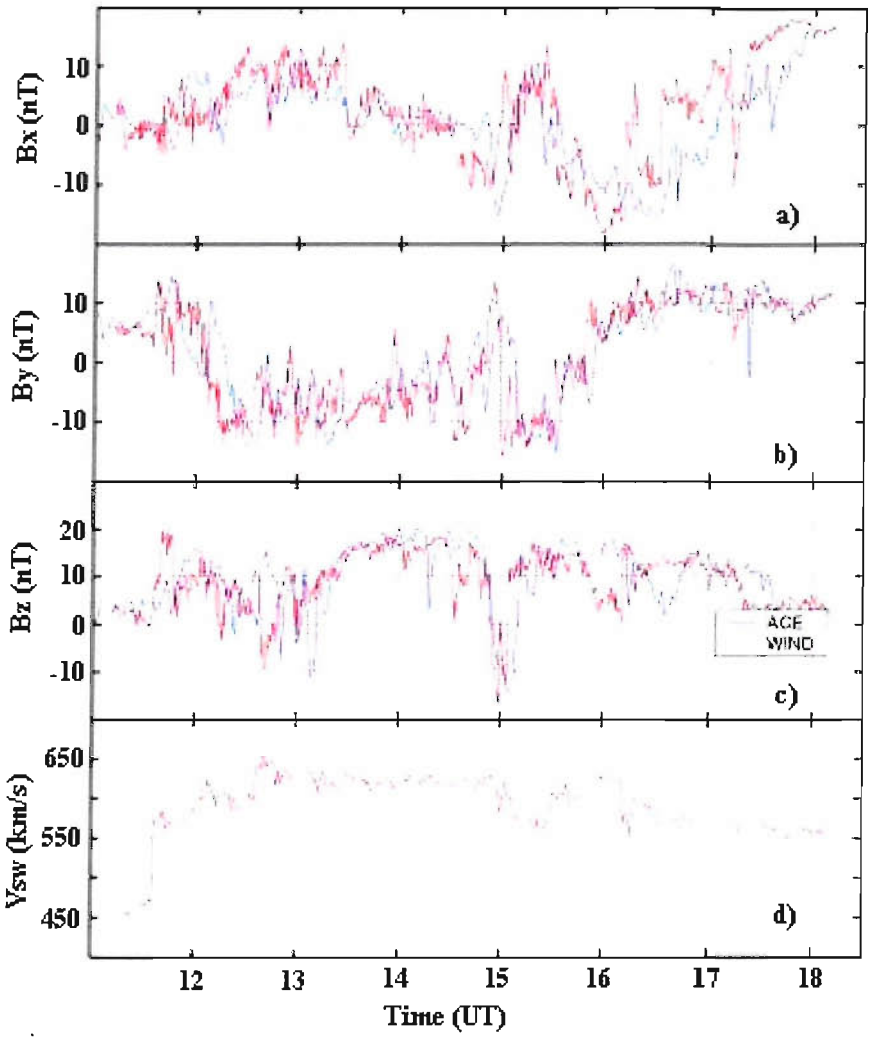

Figure 4.9 Interplanetary conditions on 26 November 2000, as detected by the ACE and Wind satellites (red and blue lines, respectively). The top 3 panels give the three components of the IMF in GSE coordinates. The bottom panel gives the solar wind speed observed by ACE. The ACE data are shown as a function of the predicted time at Wind, $t_{WA} = t_A + \delta t_W$, for a constant propagation lag δt_{WA} of 12 min. which aligns the southward turning seen by the two craft at t_W near 14:54 UT.

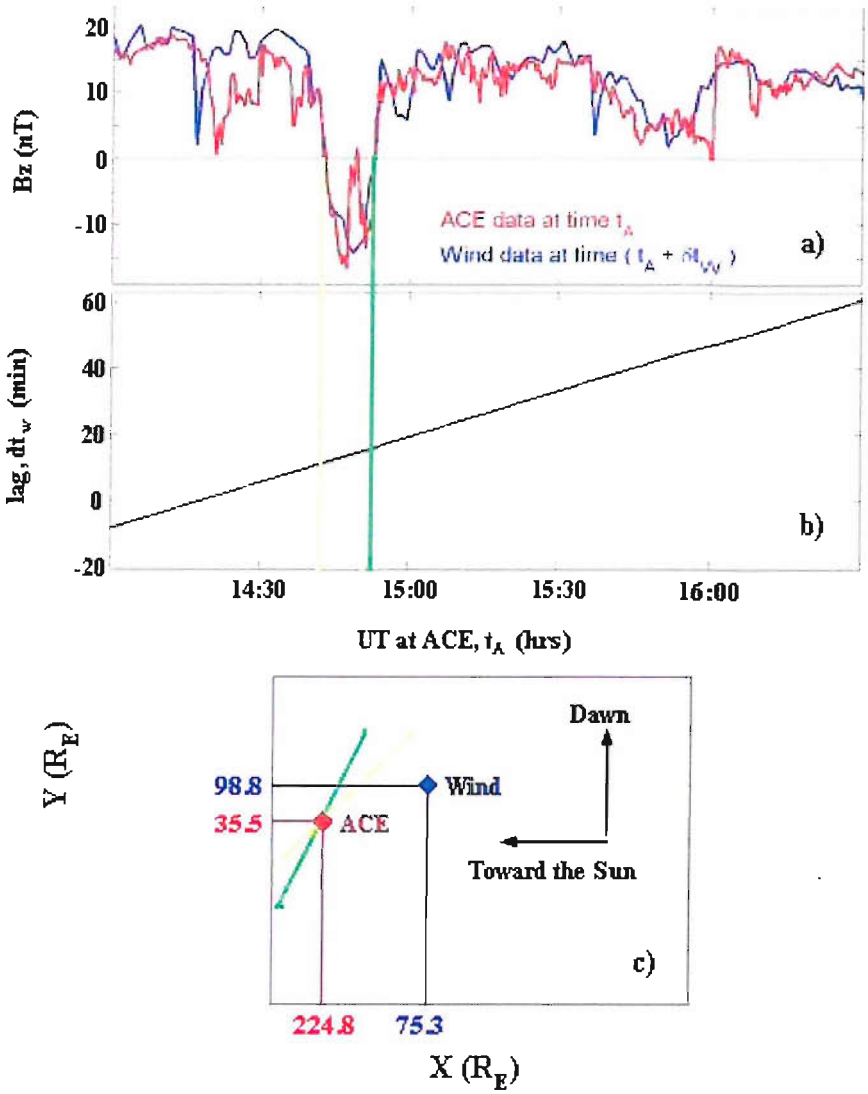

Figure 4.10 a) The northward IMF component (in GSE coordinates, $[B_Z]_{GSE}$) as a function of time at ACE t_A, as observed by ACE (red) and Wind (blue) for the linearly varying lag $\delta t_W = t_W - t_A$, shown in *b)*. *c)* shows the inferred orientations of the southward (yellow) and northward (green) turnings of the IMF in the GSE (X-Y) frame. The phase front associated with the southward turning (yellow line) is at an angle of $\theta_{fS} \approx 39.3°$ to the Sun-Earth line, whilst the phase front associated with the northward turning (green line) has increased to an angle of $\theta_{fN} \approx 49.3°$.

orientation of the IMF phase front must also have changed between the southward and northward turnings.

Figure 4.10a shows that if we use a linear extrapolation of these lags for the southward and northward turnings (Figure 4.10b) to later times we continue to get a very good agreement between the $[B_z]_{GSE}$ variations seen by ACE and Wind. A slightly more rapid linear variation of δt_{WA} with time would be needed to match the data before the southward turning. However, the features of interest in this event all occurred during and after the southward IMF turning and thus the errors in δt_{WA} before this are not relevant and we adopt the simple linear lag variation shown in Figure 4.10b.

We therefore need to evaluate the geometry of the orientation of the southward and northward IMF turnings to estimate the corresponding ACE-to-Earth propagation lags, δt_{ES} and δt_{EN}. These are deduced from the ACE and Wind data, and are shown in Figure 4.10c. These fronts are propagated to the bow shock at the observed solar wind speed, and then additional lags of 5 min and 2 min are applied to allow for the traversal across the bow shock and along the cusp field lines to the ionosphere. This gives δt_{ES} = 40 min and δt_{EN} = 46 min and thus we predict the southward and northward turnings should be seen in the ionosphere at 15:22 UT and 15:39 UT respectively [Lockwood et al., 2003a]. From this we can associate the changes in these IMF features with the observed double brightening of Lyman-α in the dayside cusp.

4.3.2 Event Two: Calculating the ACE to Ionosphere Propagation Time

The second event, discussed in Section 4.1.2, included a sudden increase in intensity of auroral emissions, resulting from both proton and electron precipitation. A particularly distinct ionospheric signature is seen in the magnetic recordings of the IMAGE, Greenland and MM210 magnetometer arrays, similar to those associated with a TCV. In order to link these signatures to upstream solar wind features the upstream interplanetary satellites ACE, Wind and Geotail have been used to track the pressure front and the southward turning as they propagate between the craft.

Figure 4.11f show ACE and Wind situated at $X_A = 224.7\ R_E$, $Y_A = 35.3\ R_E$ and $X_W = 76.5 R_E$, $Y_W = 95.8\ R_E$. Figure 4.11 show the variations in the components of the IMF and the solar wind density and velocity at the two satellites. Similar, but not identical, features are seen at both craft and with a constant time delay of $\delta t_{WA} = 31$ mins. A good correlation between ACE and Wind data is obtained. In Figure 4.11 both datasets have been lagged by the predicted propagation delay to the noon ionosphere, calculated using the procedure described in Sections 4.3 and 4.3.1. The inferred orientation of the phase front in the X-Y plane is at an angle $\theta_f = 76.10°$) (see Figure 4f), and the solar wind velocity of ~ 490 kms^{-1} at the time of the event yields ACE-to-ionosphere and Wind-to-ionosphere time delays of 53 min and 22 min, respectively. This implies that an ionospheric response to the arrival of the two features would be expected at 7:57 UT, as shown in Figure 4.11. Figure 4.12 displays data from the Geotail satellite lying downstream of both ACE and Wind, close to the region of dawnside magnetosheath. Figure 4.12a and 4.12b shows the electron and proton fluxes measured over a range of energies. Figure 4.12c shows the magnitude of the magnetic field and Figure 4.12d, 4.12e and 4.12f show the variations in all three components of the magnetic field in the GSE reference frame. Figure 4.12g shows the position of Geotail with respect to the bow shock (BS) and the magnetopause (MP) between 7:00 and 8:30 UT.

During the period of relatively low solar wind density (~10 cm^{-3}) preceding the pressure front, Geotail lay close to the bow shock in the solar wind. This is depicted in Figure 4.12g. Figure 4.12a and 4.12b shows that at 6:20 UT, over half an hour before the arrival of the pressure front, the satellite orbit took it into the foreshock, a region sunward of the bow shock that is characterised here by an increase in both electron and proton flux (generated at the bow shock and propagating upstream against the solar wind flow) seen in all the energy channels. The most noticeable increase was in the proton and electron energy channels (1×10^4 – 2×10^4) eV and ~1×10^2 eV shown in Figure 4.12a and 4.12b. At 6:40 UT, Geotail remerged from the foreshock and travelled Earthwards, the inclination of its orbit bringing it briefly into contact with the foreshock again at 6:50 UT. At 7:40 UT, the satellite entered a region of increased ion flux and magnetic field strength giving a clear change in all five panels of Figure 4.12. These plasma and field enhancements reflect the satellite crossing the bow shock into the hot and dense plasma of the magnetosheath denoted by a red star in Figure 4.12. This can be verified by studying the variations in the magnetic field components displayed in Figure 4.12c, 4.12d and 4.12e. When the satellite enters the magnetosheath, the component of the IMF that is perpendicular to the expected bow shock orientation is enhanced [Opgenoorth et al., 2001]. Because of the general orientation of the shock in the GSE frame, this magnetic field enhancement is here reflected in all three IMF components. At 7:45 UT, the craft briefly re-emerged from the magnetosheath (giving a decrease in particle flux and magnetic field strength), before crossing the bow shock for a second time at 7:50 UT. At 7:57 UT, Figure 4.12 shows Geotail leaving the magnetosheath for a second time, as the bow shock is forced earthwards across the satellite. The reaction of the bow shock to the impact of the front is consistent with a compression of the magnetosphere.

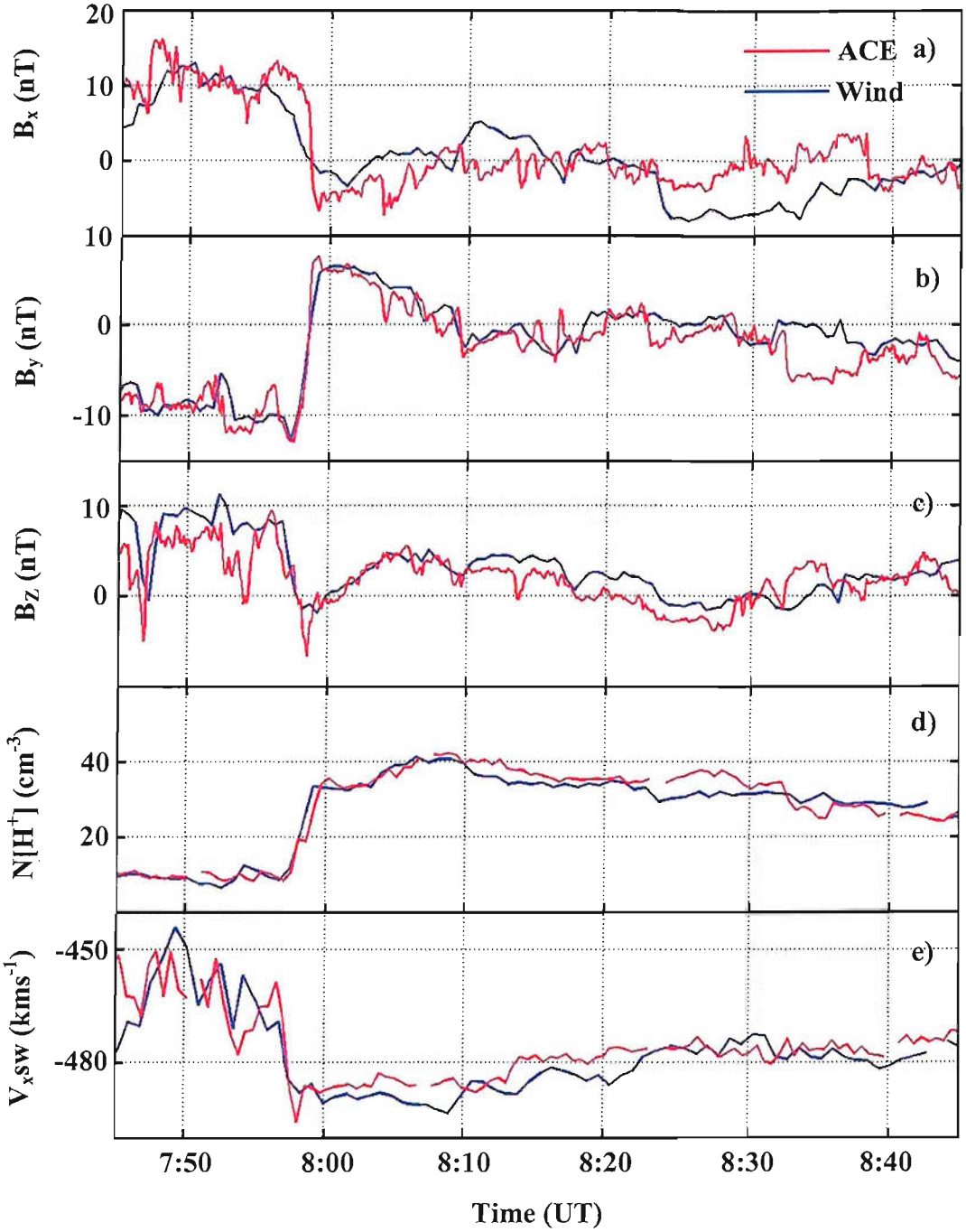
ACE
Wind
a)
b)
c)
d)
e)
B_x (nT)
B_y (nT)
B_Z (nT)
$N[H^+]$ (cm^{-3})
$V_x$sw (kms^{-1})
20
10
0
10
0
-10
10
0
40
20
-450
-480
7:50
8:00
8:10
8:20
8:30
8:40
Time (UT)

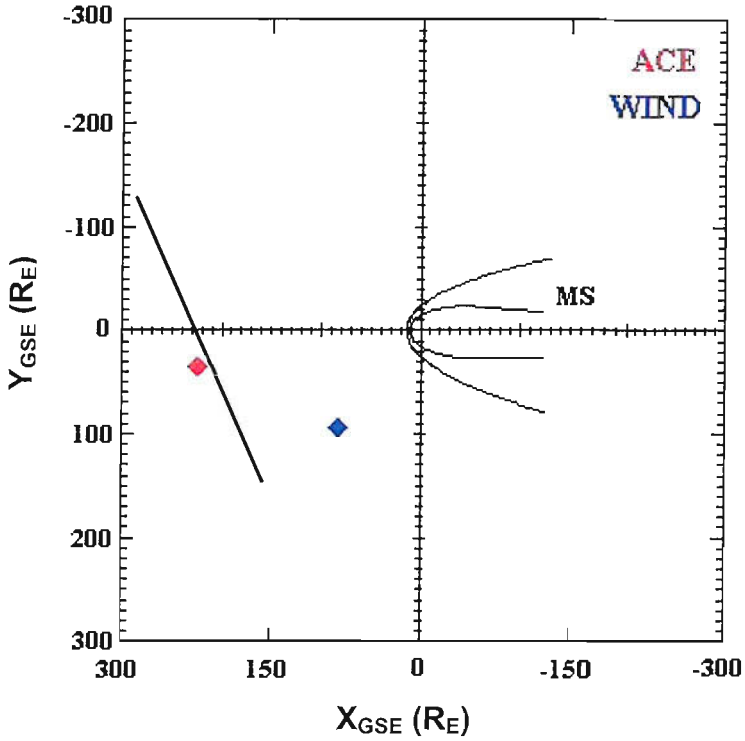

Figure 4.11 The variations on 26 November 2000 (Event 2) in ***a)*** the B_x component, **b)** the B_y component and **c)** the B_z component of the IMF in GSM coordinates, ***d)*** the variations in solar wind density and **e)** the x-component of solar wind velocity at the ACE and Wind satellites. In each case the data has been lagged by the predicted propagation delay to the noon magnetosphere: 53 min and 22 min for ACE and Wind respectively. **f)** shows the positions of ACE (X_A,Y_A) and Wind (X_W,Y_W) respectively upstream of the Earth's magnetosphere (MS). The thick black line represents the inferred pressure front at an angle of θ_f to the Sun-Earth line in this plane.

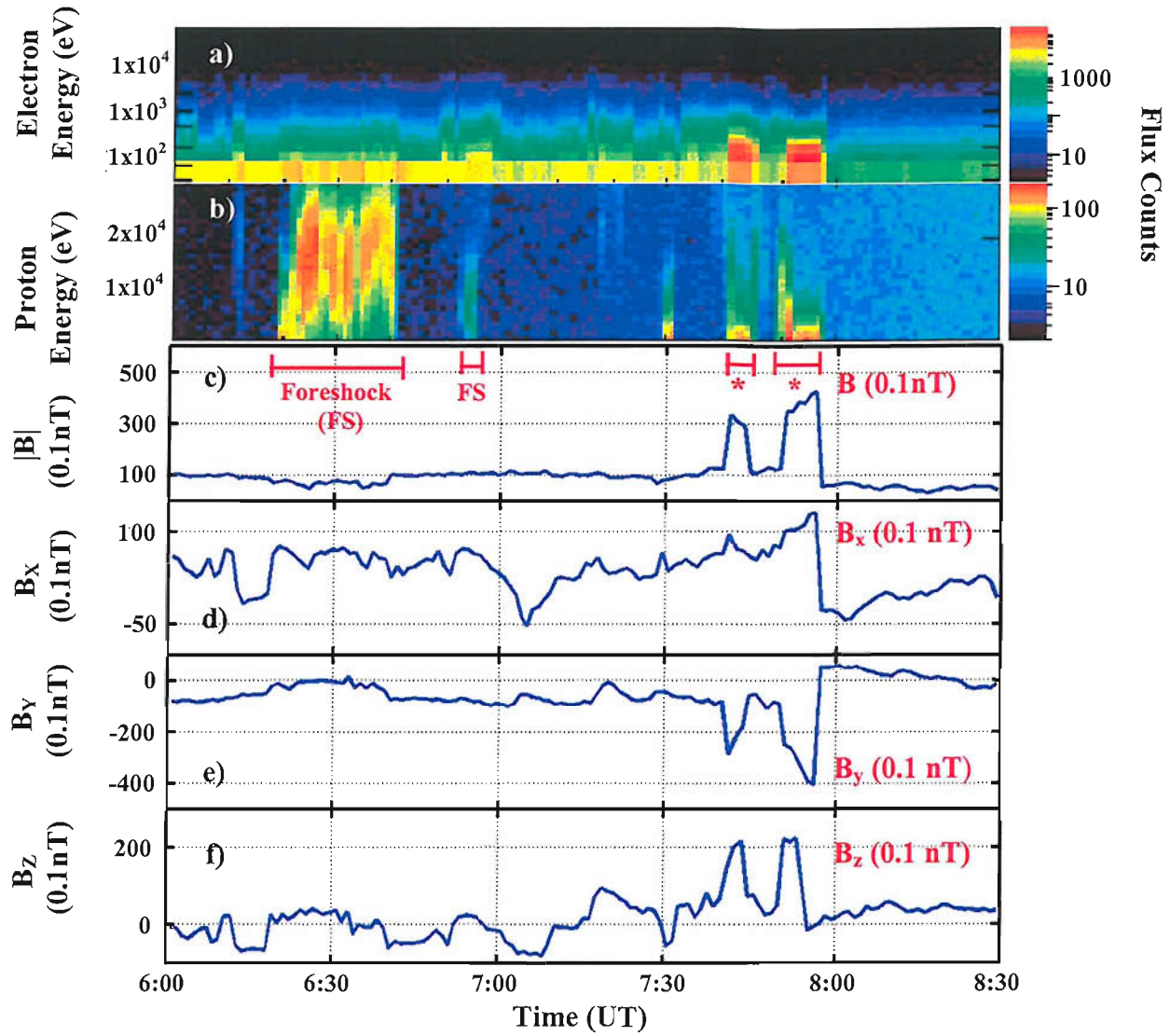

Figure 4.12 Particle and magnetic field data recorded by the Geotail satellite on 26 November 2000 (Event 2) lying close to the bow shock. ***a)*** and **b)** show the proton and electron count rate (proportional to differential energy flux) as function of energy and time whilst panels ***c)***, ***d)***, ***e)*** and ***f)*** show the components of the magnetic field in the GSE reference frame. ***g)*** (below) shows the position of Geotail, with respect to the bow shock (BS) and the magnetopause (MP). The green line shows the path of the satellite both before and after 8UT. Red stars highlight times when the satellite is in the magnetosheath, Earthward of the bow shock.

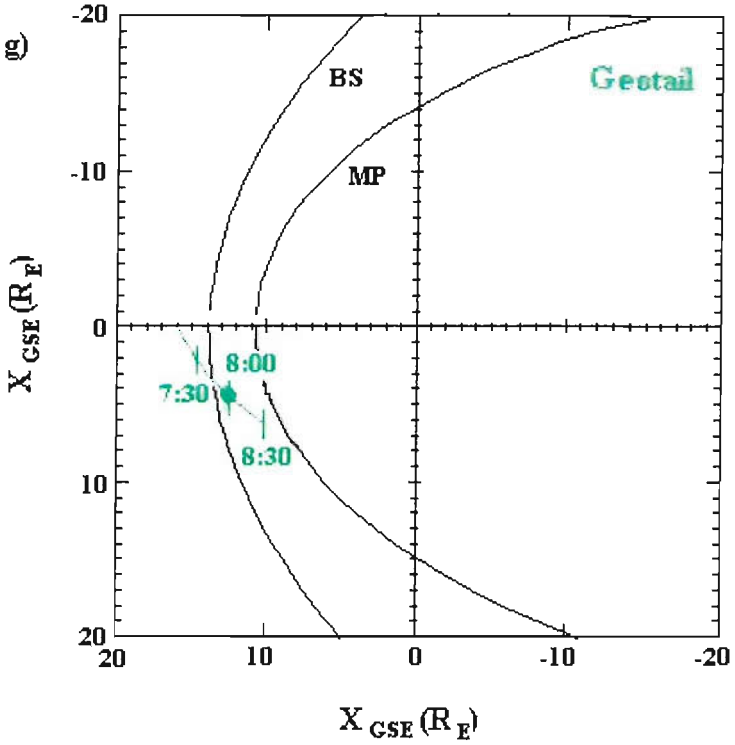

The time Geotail experiences the first effect of the pressure pulse at the bow shock is the time at which the propagation calculation predicted the pressure pulse effects would reach the ionosphere (rather than the magnetopause). The reason for this slight time discrepancy could be due to any of the assumptions discussed in Section 4.3. However, the estimation of the propagation time, within the experimental error of ± 2 min, enables us to relate effectively the upstream IMF and solar wind features to the auroral emissions and ionospheric signatures seen on the ground.

4.3.3 Event Three: Calculating the ACE to Ionosphere Propagation Time

The third event, discussed in Section 4.2.1, also resulted in bursts of auroral emissions at 12 MLT, from both proton and electron precipitation accompanied by a distinct bipolar signature seen in the magnetic recordings of the IMAGE, Greenland and MM210 magnetometer arrays. Data from three upstream interplanetary satellites ACE, Wind and Geotail have been used to track solar wind features as they propagate between the craft, in order to conclusively linking them to the ionospheric observations.

Figure 4.13f shows ACE and Wind situated $X_A = 241$, R_E, $Y_A = 12.1$ R_E and $X_W = 48.81$ R_E, $Y_W = 243.9$ R_E. Figure 4.13 shows the variations in the components of the IMF and the solar wind density and velocity at the two satellites. Similar, but not identical, features are seen at both craft with a time delay of $\delta t_{WA} = 28$ mins. As with the second event a constant extrapolation can be used to lag the ACE dataset, showing a good correlation with Wind. In Figure 4.13 both datasets have been lagged by the predicted propagation delay to the noon ionosphere, calculated using the procedure described in Sections 4.3 and 4.3.1. Due to the position of the satellites within the X-Y plane a similar method can be adapted to this event. Having calculated the angle of the phase front, $\theta_f = 76.5°$, and with knowledge of the solar wind velocity, which increased to ~ 500 kms^{-1} at the time of the event, ACE-to-ionosphere and Wind-to-ionosphere time delays of 52 min and 24 min respectively were calculated. This implied that an ionospheric response to the arrival of the two features would be expected at 5:39 UT, shown in Figure 4.13.

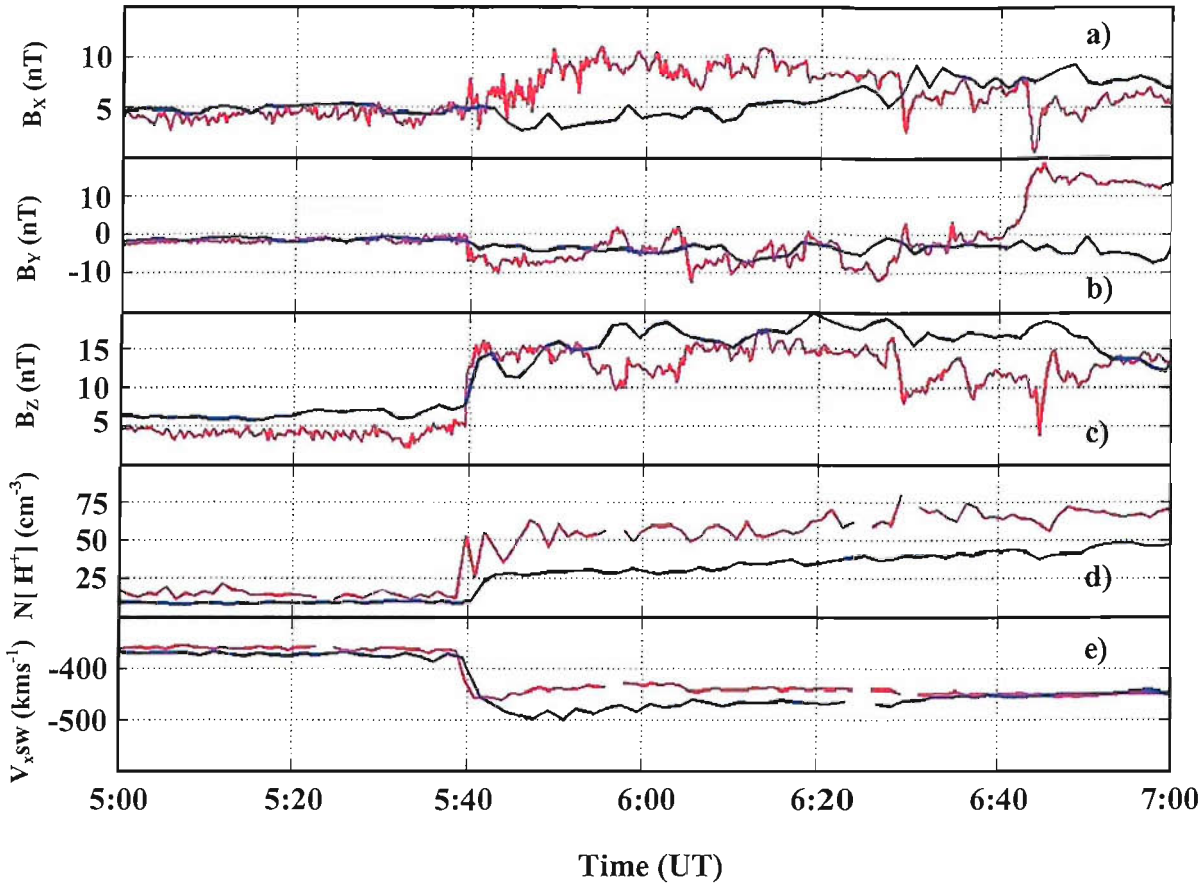

Figure 4.13 The variations during Event 3 on 29 December 2001 in ***a)*** the B_x component, ***b)*** the B_y component and ***c)*** the B_z component of the IMF in GSM coordinates, ***d)*** the variations in solar wind density and ***e)*** the x-component of solar wind velocity at the ACE and Wind satellites. In each case the data has been lagged by the predicted propagation delay to the noon magnetosphere: 52 min and 24 min for ACE and Wind respectively. ***f)*** shows the positions of ACE (X_A,Y_A) and Wind (X_W,Y_W) respectively upstream of the Earth's magnetosphere (MS) and the inferred orientation of the event phase front.

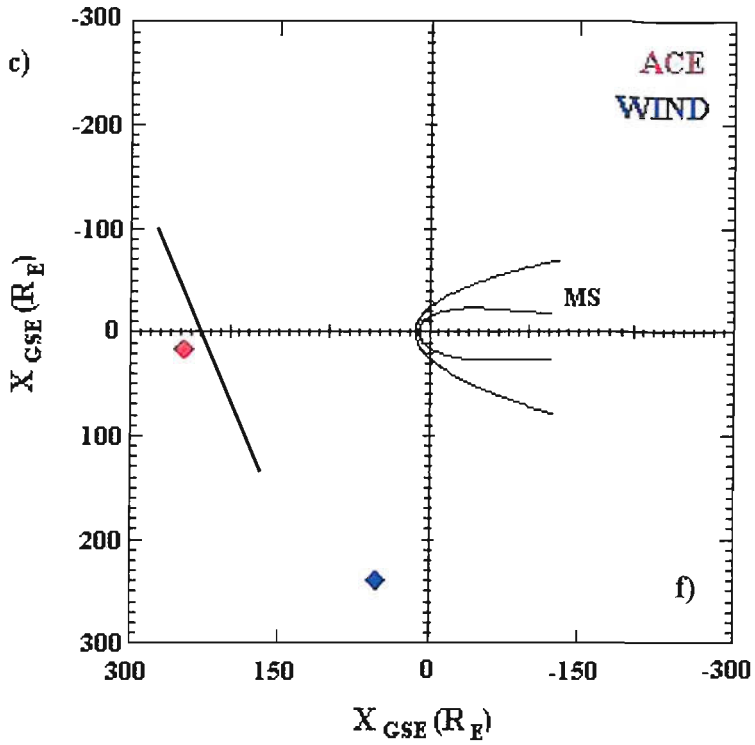

Figure 4.14 displays data from the Geotail satellite lying downstream of both ACE and Wind, close to the region of dawnside magnetosheath. Figure 4.14a and 4.14b shows the electron and proton fluxes measured over a range of energies, Figure 4.14c shows the magnitude of the magnetic field and Figure 4.14d, 4.14e and 4.14f show the variations in all three components of the magnetic field in the GSE reference frame. Figure 4.14g shows the position of Geotail with respect to typical bow shock (BS) and magnetopause (MP) locations between 4:30 and 5:00 UT. During the period of interest, Geotail is in the process of moving from the magnetosphere, across the magnetopause into the magnetosheath. This is characterised by an increase in both the density of the plasma and the strength of the magnetic field. The magnetopause crossing takes place at the time of the predicted impact of the front at 5:40 UT, indicating a compression of the magnetopause which forces it earthward across the

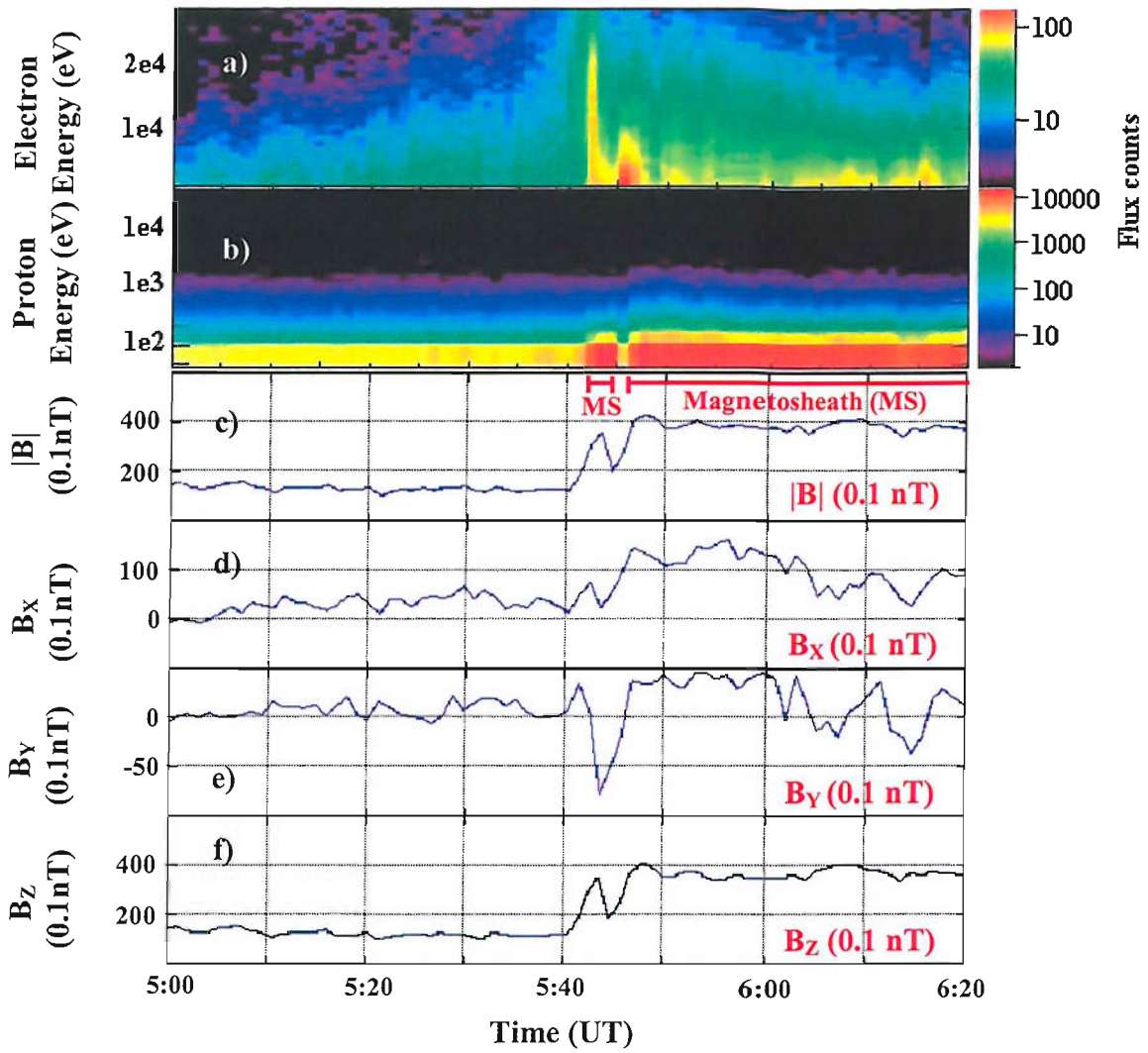

Figure 4.14 Particle and magnetic field data recorded by the Geotail satellite on 29 December 2001 (Event 3) when lying close to the Magnetopause. The data and plot format is the same as Figure 4.12.

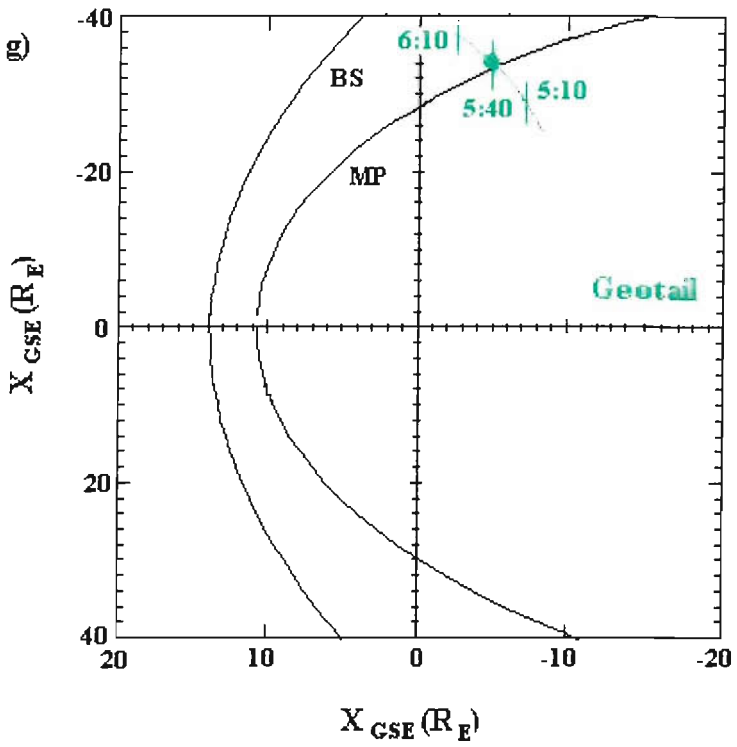

satellite, moving Geotail out into the more dense plasma of the magnetosheath. The satellite then remains within the magnetosheath except for a small interval around 5:45 UT. In this period the ions return to a magnetospheric-like spectrum which implies a brief return to the magnetosphere and hence an oscillatory motion of the magnetopause. However, the electrons show considerable enhancement and the magnetic field components (particularly the Y) are completely different to their pre-event magnetospheric values: this implies that the bow shock was also briefly compressed over the craft, putting it in the upstream solar wind before it was returned to the sheath by an outward relaxation of the bow shock. Before and after these boundary crossings high energy (>10keV) electrons are seen, which are likely to be accelerated at the propagating shock front. For either interpretation of the Geotail

data, they reveal a compression, followed by an oscillation of the magnetopause as a result of the impact. The time Geotail experiences the first effect of the pressure pulse is in good agreement with the predicted propagation time from ACE and Wind. Using the estimated propagation delay, we are able to relate the upstream IMF and solar wind features to the auroral emissions and the distinct ionospheric signature seen in the magnetic recordings on the ground.

The following chapters investigate the response of the global magnetosphere-ionosphere system to specific variations in upstream solar wind parameters that characterised these three different events, which occurred on the 26 November 2000 and 29 December 2001. This chapter has briefly introduced the three events and described the method of identifying the solar wind parameters that were responsible for the ionospheric signatures associated with each. The next three chapters will consider the various coupling mechanism that govern energy transfer from the solar wind to the magnetosphere in response to the specific upstream features observed on these days.

Chapter 5: Event One

Modelling of the Observed Proton Aurora and Ionospheric Convection in Response to Changes in the IMF Field Clock Angle.

Observations made on 26 November 2000 have been the focus of a number of studies that used upstream solar wind condition to explain a different ionospheric signatures. Kabin et al. [2001] studied the effect of several hours of steady southward IMF on this day on ionospheric convection, whilst Pitout et al. [2002] used EISCAT ESR and DMSP observations to study simultaneous high- and low-latitude reconnection during an interval of predominantly northward IMF. Lockwood et al. [2003] (LEA03) reported the response to a brief period of southward IMF on the afternoon of 26 November 2000, in particular studying the response of the proton emissions in the cusp.

The advent of space-based imagers observing the Earth in Doppler-shifted Lyman-α emissions has drawn attention to the use of the global distribution of proton aurora to identify newly-opened field lines generated by magnetopause reconnection. Precipitation of solar wind electrons and ions, guided along newly reconnected field lines into the cusp region, cause the excitation of auroral emissions. While not the main source of particle energy flux associated with these emissions, protons have relatively long flight times and, as a result, they carry information about the recent history of the reconnection process. In addition, the precipitation of electrons is greatly influenced by the proton flux as quasi-neutrality is maintained along the field lines [Burch, 1973].

The afternoon event on 26 November 2000, first introduced in Section 4.1, is characterised by a double brightening of doppler-shifted Lyman-α observed by the SI12 channel of the FUV imager on the IMAGE spacecraft. LEA03 showed that this double brightening occurs in response to two short-lived southward turnings of the Interplanetary Magnetic Field (IMF), during a period of strongly enhanced solar wind plasma concentration. Section 4.3.1 described how the application of derived propagation lags, confirms the relationship between the upstream IMF and cusp emissions as well as revealing that the emission intensity varies systematically with the upstream IMF clock angle. This association is demonstrated in panels a) and c) of Figure 5.1, which compares interplanetary and ionospheric conditions during this event. The solar wind and IMF data has been lagged by the propagation time between the ACE satellite and the ionosphere, as derived in Section 4.3.1. Figures 5.1a and 5.1b show that the agreement of the IMF clock angle with peak Lyman-α intensity is strong, especially when the latter is normalised to allow for the variation in the solar wind concentration, $N[H^+]$, shown in Figure 5.1b. The vertical red lines mark the first and last changes of the IMF clock angle θ_{IMF} associated with the southward and the northward turnings, respectively. The vertical black line shows the brief return of θ_{IMF} to near 90°. It can be seen that the peak proton emission varies with θ_{IMF}. The intensity of the second peak is not proportionally as great as the first but this is, in part, caused by the variation in the solar wind proton concentration $N[H^+]$ which shows a minimum at this time (Figure 5.1c).

Figure 5.1e shows the latitudinal motion of this peak intensity derived from IMAGE FUV data. This is obtained by integrating the IMAGE data into 48 MLT sectors, each 30 min wide, to give latitudinal profiles. Figures 5.2a and 5.2b show emissions in the 12:00-12:30 MLT sector; the intensity is plotted as a function of latitude and time. The two cusp brightenings can be identified and also coincide with equatorward motion of both the peak emission and of the latitudinal band of emission (roughly delineated by the yellow lines, which show the smoothed variation of a chosen value of the latitudinal intensity gradient). Figure 5.2b is the doppler-shifted Lyman-α emission at 121.8 nm excited by proton precipitation, Figure 5.2a is the

corresponding plot for the 135.6nm doublet of oxygen OI emissions, observed by the SI13 channel of FUV. Figure 5.2 shows the OI emission has many similar features to the proton emission.

The similarities between the variations in Lyman-α and oxygen OI emissions become more evident when the peak emission intensities of the Lyman-α and oxygen OI emissions are plotted as a function of time, as shown in Figure 5.3. The red line is the peak doppler-shifted Lyman-α proton intensity, the blue the peak oxygen OI emission and the green is the OI emission at the latitude of peak proton emission. Because the peaks at the two wavelengths are at very similar latitudes (compare Figures 5.2a and 5.2b), the last two variations are very similar. The bottom panel of Figure 5.3 shows the ratio of the Lyman-α to the oxygen OI intensities at the latitude of peak Lyman-α. Similar variations in all intensities are observed with the double brightening noted above. However the bottom panel shows that the ratio of Lyman-α to OI intensities increased, particularly during the first brightening. The variation of the OI emission is, at least in part, explained by emission caused by secondary electrons produced by ion precipitation, discussed in Section 1.2.5.

Figure 5.2c shows the northward IMF component in the GSM frame of reference, $[B_z]$GSM. Both Figure 5.1e and Figure 5.2 show that the cusp aurora begins to migrate southward (velocity of motion of peak $V_{max} < 0$) when θ_{IMF} begins to increase, and then relaxes poleward ($V_{max} > 0$) as soon as the clock angle returns to small values with the northward turning. The peak emission intensity is also clearly enhanced when the lagged IMF points southward. The equatorward and subsequent poleward migration of the cusp in response to the lagged θ_{IMF}, is consistent with the erosion of the dayside magnetopause and the corresponding cusp migration; it also confirms the lag variations used and indicates ongoing magnetopause reconnection. Figure 5.1d shows the effect of this reconnection on the transpolar voltage derived from the SuperDARN HF radar data. The voltage rises a few minutes after the first response of the proton aurora (in latitude and intensity). It subsequently peaks at 15:37 and decays with roughly the same constant with which it rose.

The changes in the spatial distribution of proton aurora during the event are shown in Figure 5.4. Superposed on the proton aurora images are the convection flow streamlines deduced using a convection model and line-of-sight velocities observed by the network of northern hemisphere SuperDARN radars. These streamlines are derived by fitting the convection model to the observed line-of-sight velocities [Ruohoniemi and Baker, 1998]. The model is driven by the upstream IMF conditions and thus it is very important to quantify correctly the ACE-to-ionosphere lag for these high resolution response studies. The radar scan used is at the time closest to the FUV image, the start time of which is given above the top right corner of each frame, along with the propagation lag in parentheses. The lagged values are as used in Figure 5.2c. Flow streamlines are 6 kV apart in each panel.

At 15:19:24 UT the ionospheric flow is weak and disorganised, but begins to respond with a highly localised flow vortex at 15:21:26 UT around the brightening cusp proton aurora spot near noon. This appears to be in response to the clock angle increase but the lagged IMF is still northward at this time. By 15:23:29 UT the localised vortex has grown into a larger-scale southward IMF flow pattern, dominated by the dusk cell and with westward flow from a reconnection site that appears to be in the afternoon sector: this is consistent with the positive IMF B_y at the time of the southward turning (Figure 4.7). The westward flow poleward of the proton cusp gradually decays and becomes weakly eastward over the interval 15:25:32-15:37:48 UT, consistent with the IMF B_y change to negative during the period of southward IMF and the migration of the proton aurora (thought to be close to the reconnection site) towards the morning sector [Cowley et al., 1990]. In this time, the flow was enhanced but lagged behind the brightening of the cusp aurora. The flow within the cusp region had an extended peak between 15:37:48 UT and 15:41:53 UT, whereas the proton aurora peaked at 15:30:00 UT. Thus the dayside flows respond to the IMF changes in the way expected, but follow after the brightness fluctuations of the cusp proton aurora. The effects of the magnetic curvature force giving IMF B_y-dependent

eastward or westward flow is seen poleward of the proton cusp aurora, as would be expected because the proton emissions are seen at small elapsed times since reconnection, close to the merging gap.

The aurora and flows are very much as predicted by the model of ionospheric flow excitation by Cowley and Lockwood [1992], discussed in Section 3.1, and therefore provide a demonstration of the model. The high solar wind concentration in this event allowed the production of newly-opened flux to be monitored by the FUV/SI12 instrument on IMAGE using the proton aurora produced by magnetosheath ions precipitating into the ionosphere. Figure 5.1 shows that a number of things happened when the effect of the onset of the increase in IMF θ_{IMF} reached the ionosphere (at 15:19 UT). Specifically, the aurora (seen in both Lyman-α proton and oxygen OI emissions) began to migrate equatorward near noon; the proton aurora began to intensify and, shortly after, the convection flows began to increase (as quantified by in the transpolar voltage Φ_{pc}). Figure 5.4 shows that at this time, the brightening of the cusp proton aurora was restricted to a spot near noon but that this grew in longitude and moved equatorward over the interval (15:19-15:27 UT). The data presented here clearly show a modulation of the intensity of cusp proton emission with IMF θ_{IMF}.

The LEA03 study combined a model of cusp ion precipitation by Lockwood and Davis [1996] and Lockwood [1997b] with theoretical considerations of the excitation of Lyman-α emissions, convolved with the IMAGE SI12/FUV imager response shown in Figure 3.7. The model, discussed in Section 3.1, was adapted to replicate the effect of a varying sheath-field clock angle on the acceleration of the ions injected into the magnetosphere as they cross the current layer of the dayside magnetopause. The original model of Lockwood and Davis allowed only for the special case where the sheath-field and interior magnetospheric fields were coplanar (i.e. the sheath field clock angle, $\theta_{sh} = 180°$), known as "anti-parallel reconnection" [Crooker, 1979]. The revised model used by LEA03 allows for a range of clock angles, θ_{sh}, equivalent to assuming that "component reconnection" could be responsible for the variations seen.

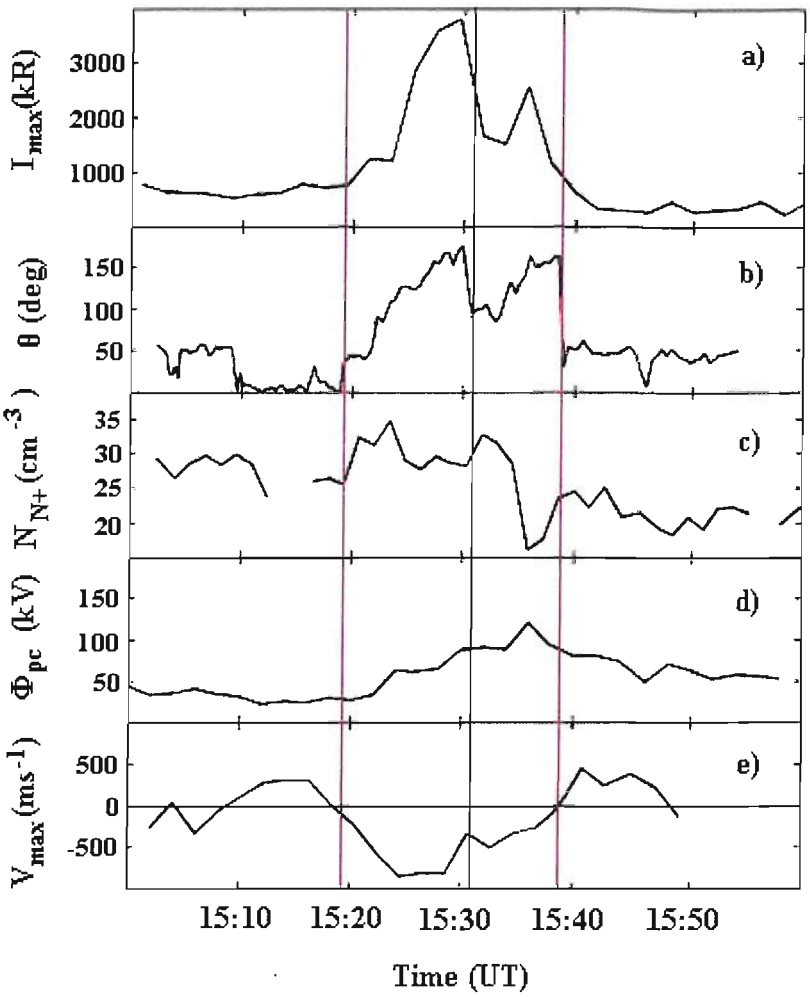

Figure 5.1 Variations of parameters observed during the brief intensification of the cusp proton aurora on 26 November 2000 reported by LEA03: ***a)*** I_o, the peak Doppler-shifted Lyman-α emission intensity seen in FUV/SI-12 data; ***b)*** the lagged IMF clock angle θ, ***c)*** the proton concentration in the solar wind, as observed by ACE, $N[H^+]$; ***d)*** the transpolar voltage from the SuperDARN radar data; and ***e)*** *V*max, the meridional phase velocity of motion of the peak Lyman-α emission. All ACE data have been lagged by the derived ACE-to-Earth propagation delay.

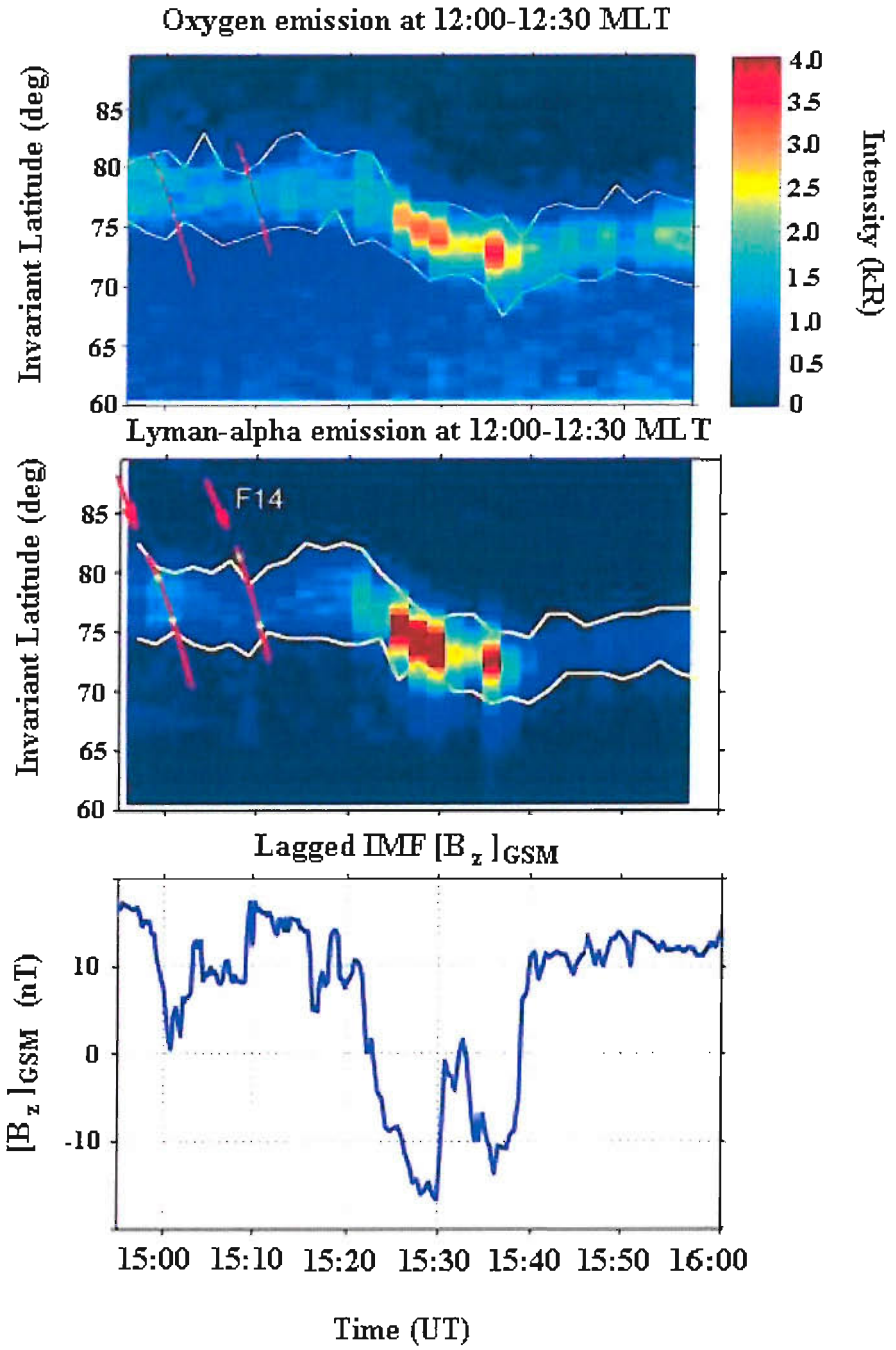

Figure 5.2 Keograms of ***a)*** the oxygen (135.6nm) and ***b)*** the doppler-shifted Lyman-α (121.8nm) emission intensities seen by the FUV instrument in the 12:00-12:30 MLT sector. ***c)*** Shows the IMF Bz component in GSM coordinates, lagged by the predicted ACE-to-Earth propagation lag.

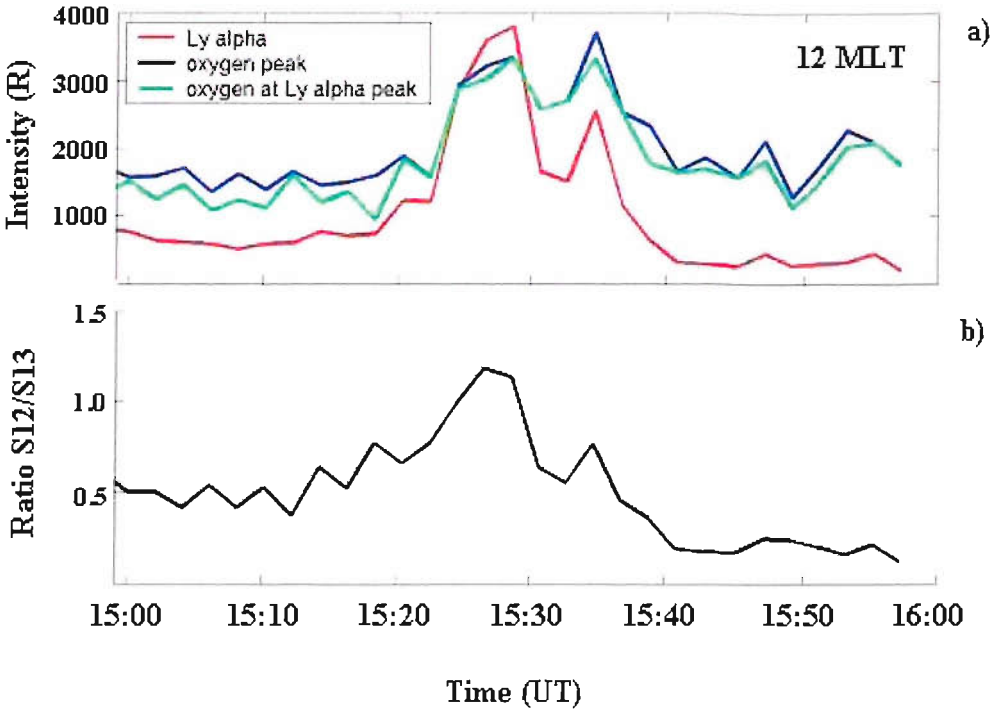

Figure 5.3 a) The time variations of the peak Lyman-α emission (red), the peak oxygen emission (blue) and the oxygen emission at the location of the peak Lyman-α emission (green). ***b)*** The ratio of the peak emission intensities: Lyman-α/oxygen OI at the Lyman-α peak. All are shown for integrations over 12:00-12:30 MLT.

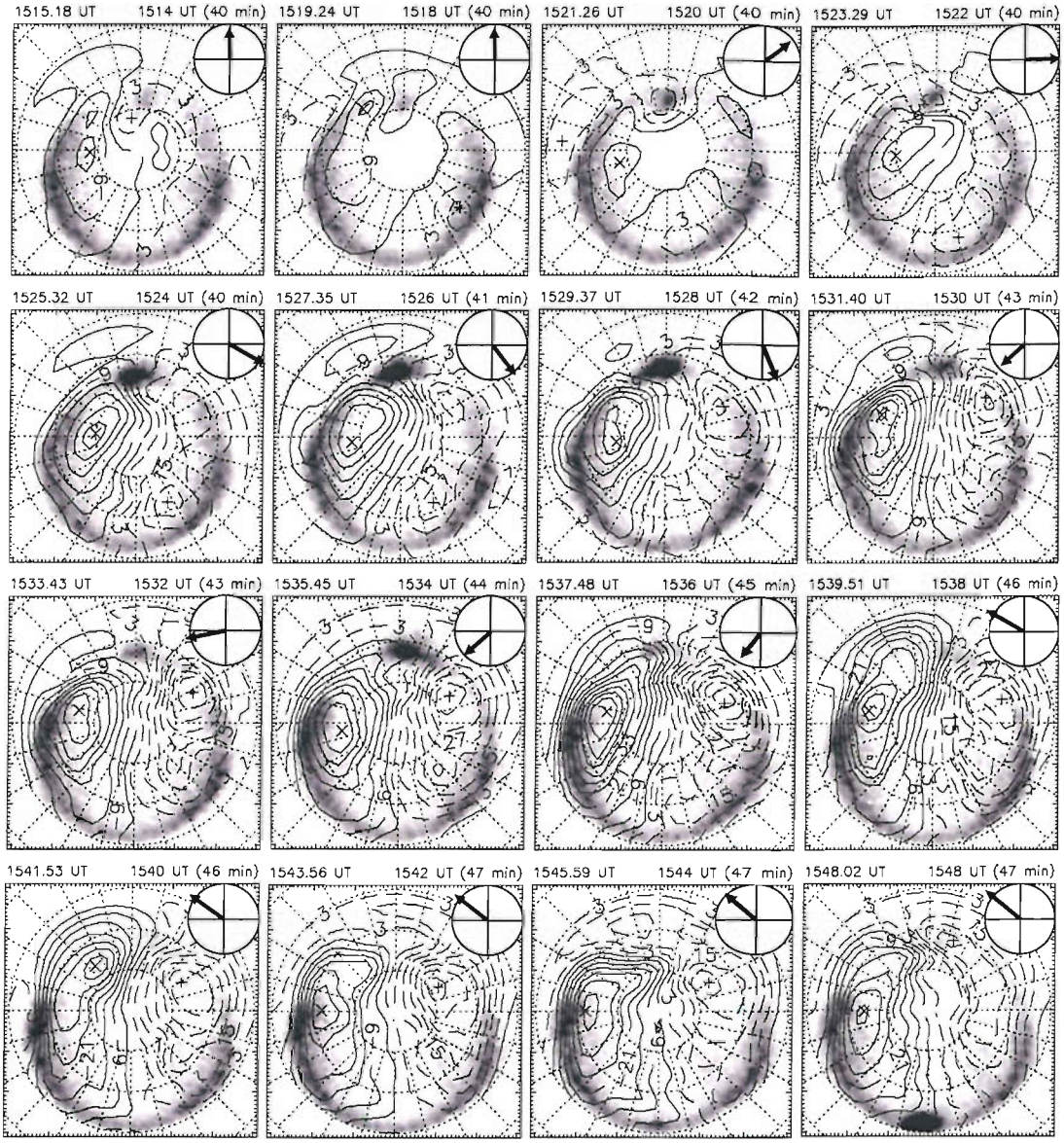

Figure 5.4 Global images of the doppler-shifted Lyman-α emission seen by the SI-12 channel of the FUV instrument on the IMAGE spacecraft, with superposed convection potential contours derived from observations by the SuperDARN HF coherent radar network. The images are 5-s integrations, taken once every 122 s. The intensity scale is the same in each frame (absolute intensities are given by the scale in Figure 5.8. The convection patterns are produced by the mapped-potential technique in which a model is fitted to all line-of-sight velocity observations, the model used being determined by the IMF orientation seen by ACE for best estimates of the ACE-ionosphere lag, δt_E. For each image, the closest 90-second radar scan has been employed. Streamlines are 6kV apart. Above each frame is given the time of the FUV image, the start time of the radar scan, and (in parentheses) the lag δt_E employed. The vector in the top right of each frame is the lagged IMF in the $[B_Z]_{GSM}$ (up the page) - $[B_Y]_{GSM}$ (to the right) frame, the circle corresponding to a magnitude of 15 nT.

By assuming that the clock angle is preserved across the bow shock (so $\theta_{sh} = \theta_{IMF}$, see Opgenoorth et al., 2001), the LEA03 study was able to reproduce the observed variation of the Lyman-α intensity with the IMF clock angle θ_{IMF}, by changing only the sheath field clock angle θ_{sh}, whilst keeping all other variables fixed. This implied that the clock angle dependence was consistent with component reconnection at a fixed reconnection site.

The observed variations in Lyman-α intensity could also be produced by moving the reconnection site, as the N_{sh}/N_{sw} ratio will vary. However, this would mean that changes in the oxygen emission intensity would be expected to match those in the Lyman-α, such that the ratio of the two would remain constant. Figure 5.3c shows the ratio of the Lyman-α to the oxygen OI intensities at the location of the peak Lyman-α intensity. Rather than remaining constant, the ratio shows that the variation with IMF θ_{IMF}, is greater in the proton precipitation than in the electron precipitation (indeed, due to the effect of secondary electrons produced by proton precipitation, it is likely to be present only in the proton precipitation). This means that, although a relevant factor, plasma concentration changes caused by motion of the reconnection site can not explain the clock-angle dependence of the Lyman-α emission reported in this paper. The comparison of the Lyman-α intensities with oxygen OI emission intensity supports the theory that clock angle dependence is consistent with component. reconnection. The data offers an opportunity to test the antiparallel hypothesis.

This chapter expands upon the original study of LEA03, identifying a number of discrepancies in the original analysis and rectifying them, but nevertheless confirming the findings of the Lockwood study. The present study also reproduces the observed spatial distributions of this emission on newly-opened field lines by combining the Lockwood and Davis cusp model with the Lockwood and Morley numerical model of time-dependent ionospheric convection. This allows a comparison of modelled magnetospheric and ionospheric parameters with those measured by a range of different instruments. Such a comparison provides a means of

confirming quantitatively the concepts of ionospheric flow excitation by Cowley and Lockwood [1992] on which the model is based.

5.1 Re-Analysing the Data

One problem with the original analysis was that it did not take the time-of-flight of the ions from the magnetopause to the ionosphere into consideration. This means that, in effect, the intensity does not respond instantaneously to clock angle changes, nor to changes in the solar wind concentration $N[H^+]$. Further complications arise from the dispersed effect of such changes on the precipitating ion spectrum and the fact that the efficiency of proton aurora excitation is a function of ion energy [Gérard et al., 2001]. In addition, the IMAGE FUV instrument resolves proton aurora from geocoronal emissions by accepting only Doppler-shifted Lyman-α, making the instrument response also highly dependent on ion energy. One result is that the delay of observed peak emission after reconnection is a function of clock angle. This is because the ion acceleration on crossing the magnetopause depends on the clock angle, as discussed in section 3.1.1, and thus, for example, during a period of low $N[H^+]$ and reduced θ_{sh}, the peak intensity observed may be higher than expected, resulting from field lines opened at an earlier reconnection time when $N[H^+]$ and θ_{sh} were higher. In this chapter we repeat the analysis of LEA03 allowing for these effects. This is achieved by predicting the variation of intensity on all newly-opened field lines in response to the observed changes in $N[H^+]$ and θ_{sh}. The peak emission, I_m, is then compared with the peak measured by the SI12 instrument. Thus the simulation exactly parallels the production of the measured intensity data. These results will be discussed in Section 5.2.

This study also investigates the implications of this analysis on observing pulsed reconnection effects during southward IMF conditions. Recently, Frey et al. [2003] have presented observations by FUV/SI-12 showing persistent, and quasi-steady, proton aurora during prolonged (~10 hours) periods of northward IMF. These observations are placing limits on any periods of zero reconnection rate under these conditions, which are considerably tighter constraints than for the corresponding emissions caused by cusp electron precipitation. Cusp electrons are usually undispersed and persist down each newly-opened field-line for an extended period

following reconnection as the field line evolves from the reconnection site into the tail lobe. In particular, the much-studied 630 nm emission is thermally excited by enhanced ionospheric temperature caused by cusp precipitation and has a long ($\sim$ 2 min) de-excitation time. These factors result in this "red-line" emission persisting for the order of 10 min around the footprint of each newly-opened field-line; the effects of pulsed reconnection will be smoothed with such a time constant [Lockwood and Davis, 1995; Davis and Lockwood, 1996]. The proton emission, on the other hand, requires the more energetic of the (dispersed) cusp ions, which persist for shorter intervals on each newly-opened field line, and thus periods of zero reconnection should be easier to detect. In Section 5.4 we compute the time constants for the growth and decay of proton emission intensity, as seen by FUV/SI-12 and consider how this affects the detection of pulsed reconnection.

The third part of this study, presented in Section 5.3, uses the numerical model of Lockwood and Morley (LM03), outlined in Section 3.2, to predict the evolution of ionospheric convection flows and the distribution of the proton aurora emission, effectively generating model simulations of the data shown in Figure 5.4. This is done using a novel application of the LM03 model in which the magnetopause reconnection rate, an input to the model, is specified by the observed upstream IMF conditions. As well as predicting the convection, the model predicts the variations in the latitude of the open-closed field-line boundary, Λ_{OCB}, and variations in transpolar voltage, Φ_{PC}. These predicted model variations are then compared to observations by the IMAGE satellite and the SuperDARN radar network respectively and shown in Figure 5.1d and Figure 5.1e.

The equatorward erosion of the dayside OCB following magnetopause reconnection is well documented in the literature. It is observed in statistical surveys of the equatorward latitude of cusp precipitation [Burch, 1973; Newell and Meng, 1989; Stubbs et al., 2001], as well as time series data on the equatorward edge of the 630 nm ("red-line") cusp aurora [Eather, 1985; Horwitz and Akasofu, 1977; Sandholt,

1988; Leontyev et al., 1992]. In addition, the effect has been observed in radar observations of flows and ionospheric gradients associated with the OCB [Freeman and Southwood, 1988; Lockwood et al., 1993; McCrea et al., 2000; Milan et al., 2003; Moen et al., 2003; Lockwood et al., 2003]. In order to compare the model variations in OCB with observations, the latitude of the equatorward edge of cusp precipitation (close to the OCB) is derived from the OI "electron" emission observed by the SI-13 channel of FUV. This latitude has also been estimated using the equatorward edge of the cusp proton aurora observed by SI-12/FUV. Both these estimates agree very well with the OCB location inferred from particle observations during overpasses of DMSP (Defence Meterological Satellite Program) spacecraft.

The transpolar voltage is also affected by magnetopause reconnection, rising in response to southward turnings of the IMF. This effect was also first noted in statistical surveys of satellite data [e.g. Reiff et al., 1981; Wygant et al., 1983] and then in time series data from inversion of observations from global networks of magnetometers [Lu et al., 1989; Ahn et al., 1992; Knipp et al., 1993; Ridley et al., 1997, 1998]. These inversions have generally employed the AMIE (Assimilative Mapping of Ionospheric Electrodynamics) technique. The effect has also been observed in data from the SuperDARN network of HF radars [Ruohoniemi and Greenwald, 1998; Ruohoniemi et al., 2002; LEA03]. The transpolar voltage Φ_{PC} is calculated from SuperDARN line-of-sight velocity data using the method of Ruohoniemi and Baker [1998] in order to compare it with the model predictions.

5.2 *The Peak Intensity of the Proton Aurora*

The Lockwood and Davis model calculates the energy spectra of the precipitating proton population as a function of time since the field line was reconnected, and from these, makes estimates of the resulting Lyman-α emission intensity, convolved with the IMAGE SI-12 instrument response [Gérard et al., 2001]. Figure 5.5a and 5.5b show the modelled precipitating cusp ion differential energy flux, J_E, on each newly opened field line as a function of the time elapsed since reconnection and ion energy, E_i, for two specific clock angles between the reconnecting magnetosheath and magnetospheric field lines, $\theta_{sh} = 120°$and $\theta_{sh} = 180°$. All other inputs to the model are the same in the two cases. Comparison of these two cases reveals the effect of θ_{sh}, via its effect on the acceleration at the magnetopause and hence ion energy E_i. Time elapsed since reconnection is $(t_s - t_o)$, where t_s is the time of observation or, in this case, simulation, and t_o is the time that the field line was reconnected. Panels c and d of Figure 5.5, show the intensity of the Doppler-shifted Lyman-α emission that would be detected by the FUV/SI-12 on IMAGE, also as a function of $(t_s - t_o)$. Details of the procedure used to derive the differential energy flux spectra, $J_E(E, t_s - t_o)$ and the corresponding intensity variation, $I(t_s - t_o)$, are given in Section 3.1.

Figure 5.5 shows that the peak intensity is reached at $(t_s - t_o)$ near 300 sec in both cases. Before this peak, the intensity increases as the precipitating ion flux increases; this is the effect of ion time-of flight from the magnetopause to the ionosphere. After the peak, the intensity decays as both the flux and energy of the ions decrease due to a combination of the time-of-flight effects, magnetosheath spatial structure and the decline in magnetopause ion acceleration caused by the field line straightening as it evolves into the tail lobe. The cusp ion fluxes at the highest energies depend on the clock angle because of its effect on the ion acceleration on crossing the magnetopause and it is these fluxes which determine the proton emission intensity.

In general, the draping of the IMF behind the bow shock means that the orientation of this magnetosheath field, for a given IMF clock angle θ_{IMF}, is a complicated

function of position on the magnetopause [Kobel and Flückiger, 1994]. However the fact that the clock angle is preserved across the nose of the bow shock means that the clock angle over much of the dayside, θ_{sh}, is the same as that seen in interplanetary space, θ_{IMF} [Opgenoorth et al., 2001]. Hence for reconnection that is not too far removed from the nose, the variation with sheath clock angle of the modelled peak Lyman-α intensities, demonstrated by comparison of Figure 5.5c and 5.5d, can be compared to the observed variation of peak intensity (normalized to allow for the variations in the upstream solar wind density) as a function of IMF clock angle.

Figure 5.6a shows modelled variations of intensity, I, with $(t_s - t_o)$ for constant θ_{sh} angles between 60° and 180° in steps of 10°. For each clock angle, the times of peak intensity ($I = I_{peak}$) and when $I = e^{-1}I_{peak}$ are evaluated and hence the growth and decay time constants between I_{peak} and the $e^{-1}I_{peak}$ level are evaluated; these are shown by the dot-dash and dashed lines in Figure 5.6b. The duration for which the intensity exceeds this threshold $e^{-1}I_{peak}$ level, Δt, is the sum of these two time constants and is shown in Figure 5.6b by the solid line. It can be seen that Δt peaks at 4.8 min near $\theta_{sh} = 100°$ and falls to just over 4 min near $\theta_{sh} = 180°$.

We here consider field lines reconnected at times t_o that are 15 seconds apart, the resolution set by the IMF observations. Using the lagged ACE data, calculated in Section 4.4.1, we know the solar wind proton concentration $N[H^+]$ and clock angle θ_{sh} of the field line reconnected at that time t_o. The propagation delays required are from the solar wind monitor to the reconnection site and so are smaller than those attaining its peak value, I_{peak}. At a later time t_s, the elapsed time since reconnection is $(t_s - t_o)$ for that field line and the intensity is computed as in Figure 5.5a, 5.5d and 5.6a. This gives the family of curves shown in Figure 5.7a for the interval containing the observed brief swings to southward IMF. Since the model results are to be compared with the intensity of the brightest pixel recorded by the SI-12 instrument, I_o, an envelope has been drawn around these curves to give I_{max}, the brightest emission present at every 15 sec time step in t_s.

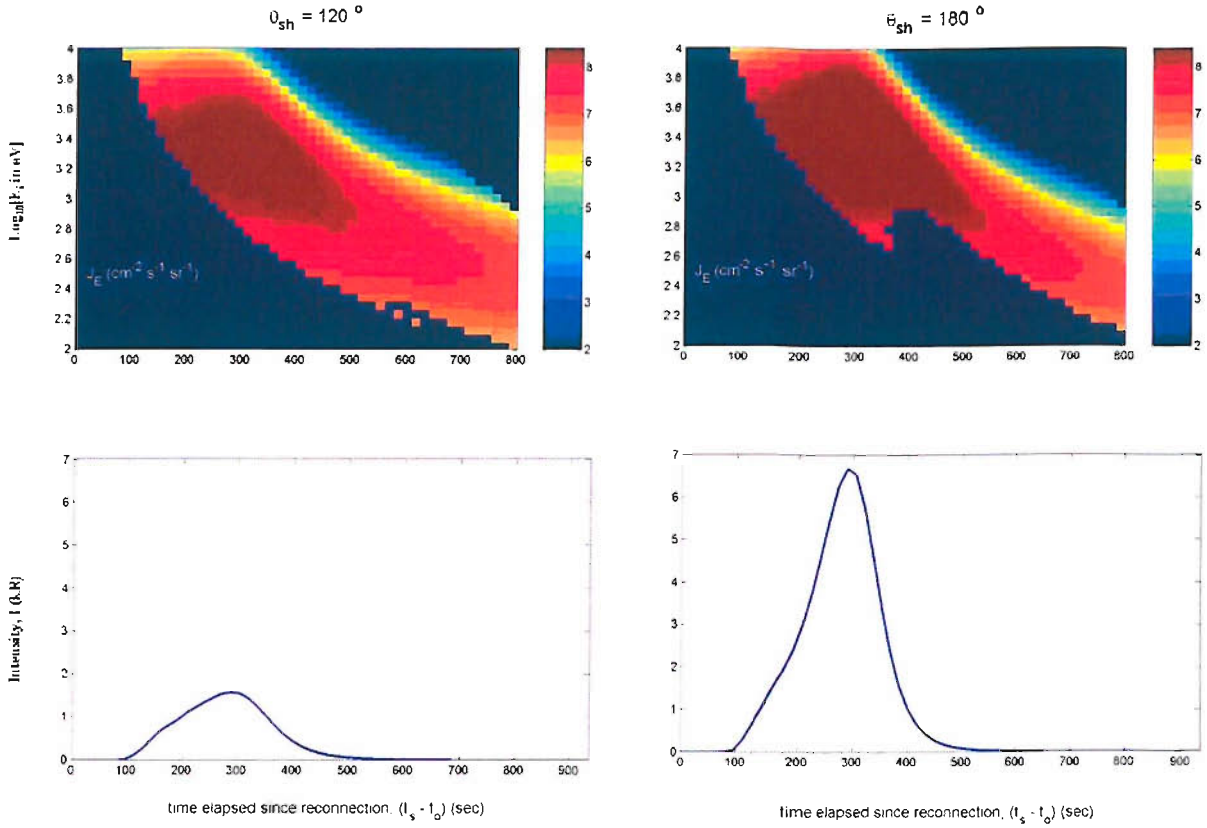

Figure 5.5 Modelled variations of cusp ion precipitation down a single opened field line, showing the differential energy flux, $J_E(E_i, t_s\text{-}t_o)$ in spectrogram format, grey-scaled as a function of ion energy E_i and time elapsed since reconnection ($t_s - t_o$) for sheath field clock angles θsh, of ***a)*** 120° and ***b)*** 180°. ***c)*** and ***d)*** show simulated variations of the Doppler-shifted Lyman-α emission intensity *I* that would be seen at the ionosphere footprint of that field line by the SI-12 imager channel of the FUV instrument on IMAGE.

The lower panel of Figure 5.7 shows $[t_s - t_o]_\rho$, the time since reconnection of the field line for which $I = I_{max}$. If a given field line continues to be the one generating the peak intensity, $[t_s - t_o]_\rho$ ramps up as that open field line ages. The drops in $[t_s - t_o]_\rho$ seen in Figure 5.7b occur when the intensity of what was the brightest field line is exceeded by the intensity of a more recently reconnected field line. Highlighted examples of such drops can be seen at times: t_1, t_2 and t_3. The steady rise (with unity slope) seen between the times shows that a single field line governed the peak intensity, and thus the shape of the envelope, during the intervening periods. The drop at time t_3 is considerably larger than the other highlighted steps. Before this, during a period of northward IMF, the intensity generated on the opened field lines failed to exceed the intensity on a field line opened previously while the IMF was southward. Only when the IMF turned southward again was sufficient intensity generated to exceed it and a large step in $[t_s - t_o]_\rho$ resulted. This panel serves to illustrate that the I_{max} envelope in Figure 5.7a represents the most intense field line, irrespective of where and when it was reconnected, and that the variation of the peak observed intensity reflects the effects of the proton emission time constants shown in Figure 5.6b.

An initial comparison of the modelled and observed intensities shows a clear dependence of emission intensity on the IMF clock angle, as found in the previous study by LEA03. As discussed above, the modelled peak intensity sequence I_{max} is at time resolution 15s. To make a quantitative comparison, we have sampled the I_{max} at the same rate as the FUV observations (every 122s) and found the cross correlation coefficient of the resulting sampled sequence, I_m, with the observed peak intensity variation, I_o. The lag was incremented in 15-second steps for ± 20 min about the nominal value before I_{max} was sampled and so the data sequence I_m is not precisely the same for every lag. The results are shown in the correlogram in Figure 5.8a. In this figure, positive lag corresponds to I_o leading I_m and a lag of zero corresponds to the predicted ACE-to-ionosphere propagation delay calculated in Section 4.3.1. The peak correlation is very high (0.91), showing that the modelling is reproducing the observations closely.

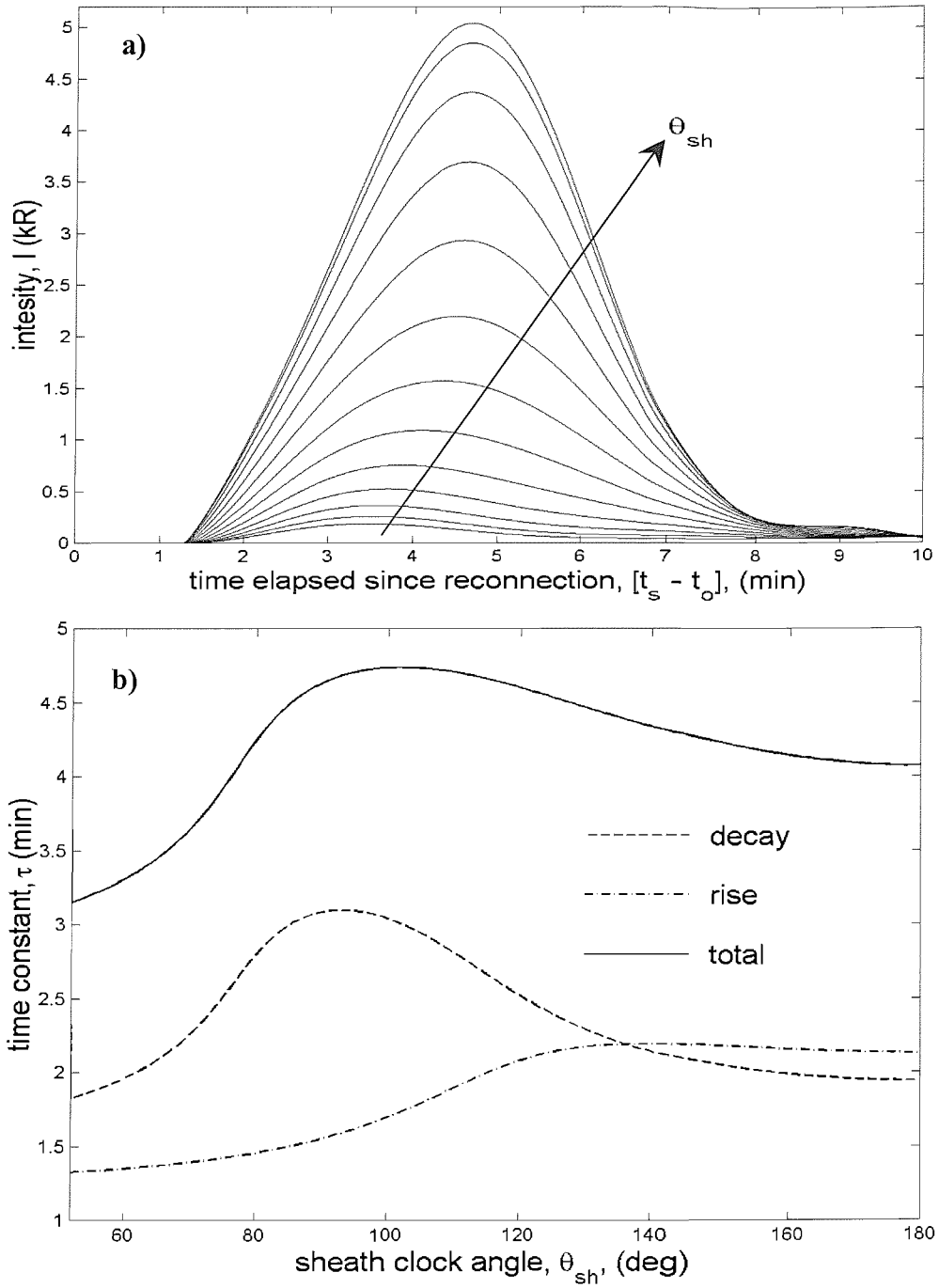

Figure 5.6 ***a)*** Modelled doppler-shifted Lyman-α intensity I, convolved with the response of the SI-12 channel of the IMAGE FUV instrument, as a function of time elapsed since reconnection (t_s - t_o), for sheath field clock angles θ_{sh} between 60° and 180° in steps of 10°. ***b)*** The rise and decay time constants of the curves in ***a)*** defined by the $e^{-1}I_{peak}$ level, where I_{peak} is the peak of each curve (see Figure 5.3d). The solid line is the sum of the rise and the decay times.

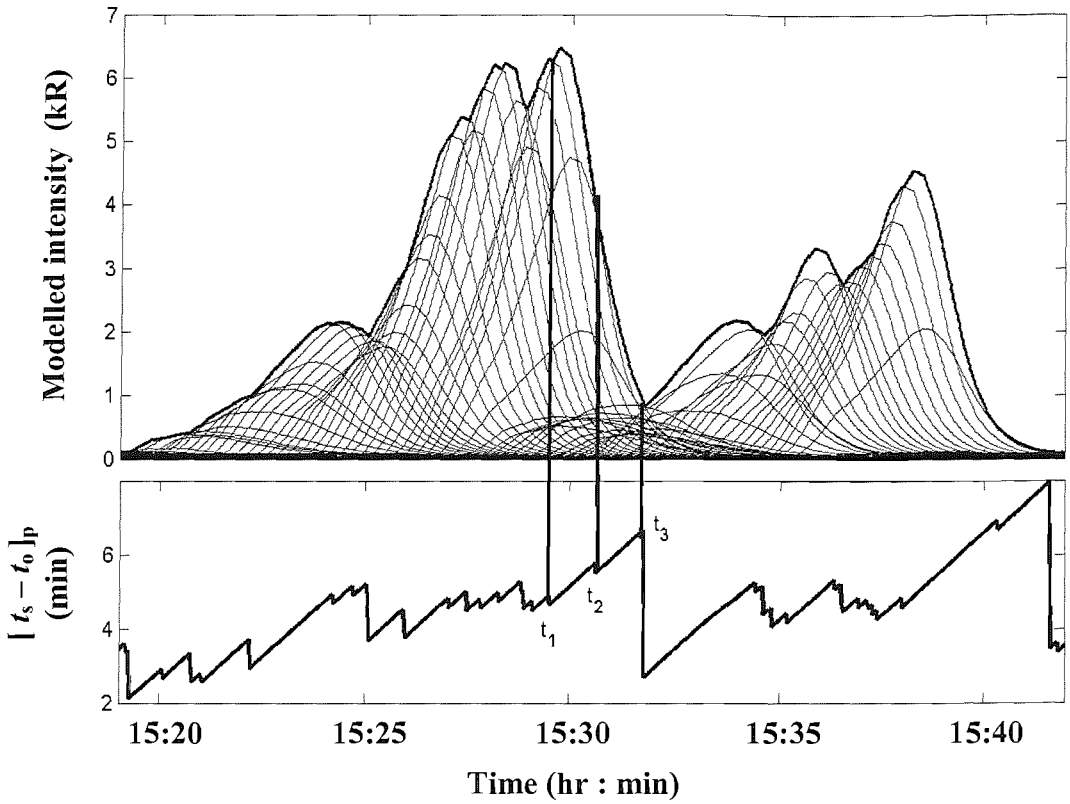

Figure 5.7 a) Temporal variations of the Doppler-shifted Lyman-α intensity modelled on newly-opened field lines that are reconnected at times t_o that are 15s apart, for the solar wind concentration $N[H^+]$ and IMF clock angle θ observed by ACE at (t_o - δt), where δt is the predicted ACE-to-magnetopause propagation delay. The thick line is I_{max}, the envelope of the various light curves for these newly opened flux tubes. ***b)*** The time elapsed since reconnection $[t_s - t_o]_p$ of the field line giving the peak intensity: times t_1, t_2 and t_3 are examples of downward steps in $[t_s - t_o]_p$ caused by a more recently reconnected flux tube surpassing an older open flux tube in intensity.

Using the autocorrelation functions of I_o and I_m to allow for the persistence in the data series (Appendix B), we find that this correlation is significant at the 98% level. The peak correlation is at a lag of 312s which is almost all attributable to the fact that peak intensity is reached roughly 300s after the field line is opened (see Figure 5.5); the nominal lag of Section 4.3.1 was between the IMF variations seen at ACE and the peak cusp aurora seen in the ionosphere, δt_E. This is roughly 300s greater than the ACE-to-magnetopause lag δt required to generate the I_{max} and I_m modelled sequences. Thus the peak correlation at 312s (5.2 min) in Figure 5.8 confirms the propagation lag variation determined in Section 4.3.1 is accurate. Part b) of Figure 5.8 analyses the uncertainty in the lag by looking at the significance S of the difference of the correlation at a given lag and the peak correlation, evaluated using the Fisher-Z test of the difference between two correlations (see Appendix B). By definition, S is zero at the peak correlation but increases as the correlation falls away from the peak. Figure 5.8b shows that S exceeds 90% at lags less than 3.6 min and exceeding 8.0 min. Thus the uncertainty in the lag (at the 90% confidence level) is ±2.2 min.

The linear regression fit between I_m and I_o is shown in Figure 5.9 and can be used to scale the best fit model variation to the observations, the results being shown in Figure 5.10. It is noticeable in Figure 5.9 that the best regression fit is not a line of unity slope; although the larger I_o and I_m values are comparable, I_o consistently exceeds I_m at low values. LEA explained this as the effect of lobe reconnection and the consequent northward-IMF cusp spot. Figure 5.10 shows that the model predicts a comparable peak intensity before and after the southward turnings of the IMF but that the measured peak Lyman-α intensities are slightly larger prior to the event. This disparity might be explained by a corresponding change in polarity of the B_x component of the IMF, during the event. Lockwood and Moen [1999] have postulated that the IMF B_x component can modify the tendency for lobe reconnection to take place in the summer hemisphere [Crooker and Rich, 1993]. Before the event, $B_z > 0$ and $B_x > 0$ and Lockwood and Moen [1999] postulate that lobe reconnection occurs preferentially antisunward of the northern hemispheric cusp for this IMF

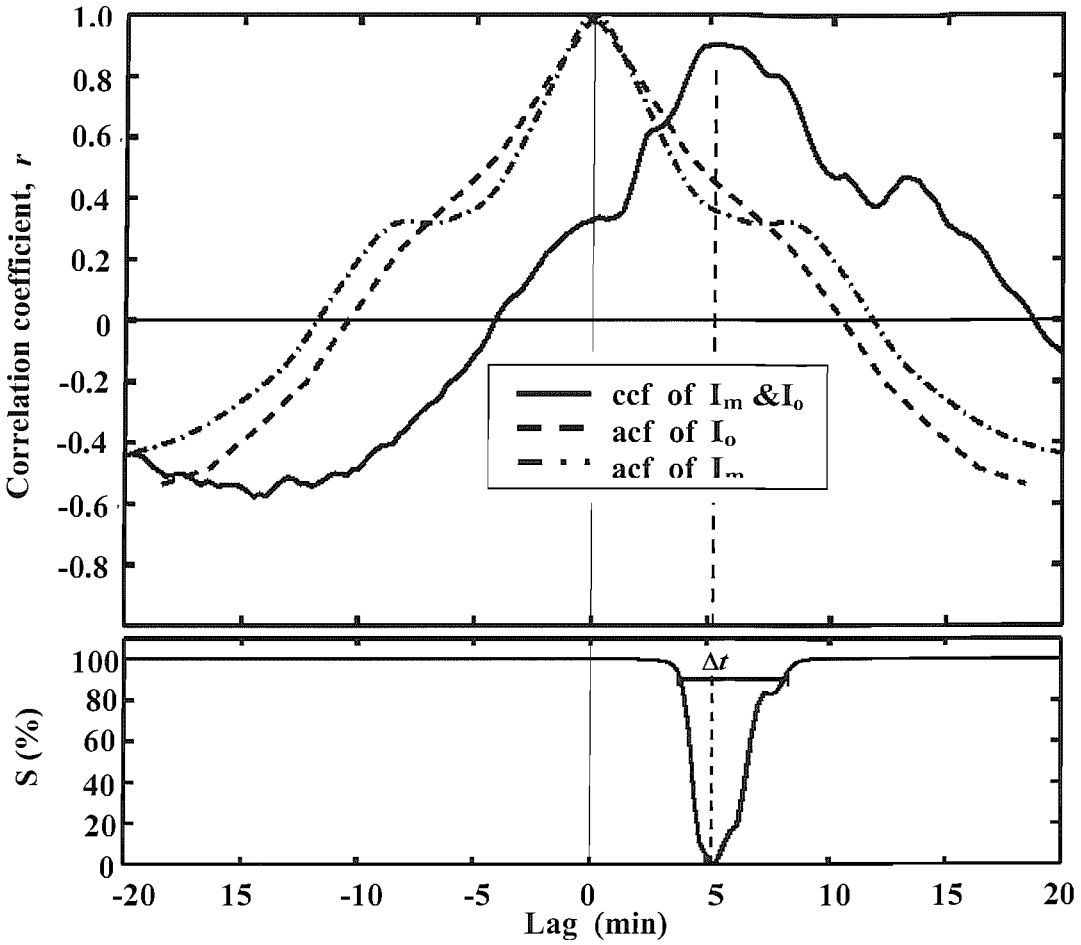

Figure 5.8 ***a)*** Correlation analysis of the observed (I_o) and modelled-and-sampled (I_m) variations of peak intensity. I_m is the variation I_{max} shown in Figure 3.7a, sampled every 122s, the same interval as for the observed peak intensity, I_o. The solid line shows the cross-correlation coefficient (ccf) as a function of lag , the dashed line shows the autocorrelation function (acf) of I_o, and the dot-dash line shows the acf of I_m. ***b)*** The significance S of the difference between a correlation at a given lag and the peak correlation.

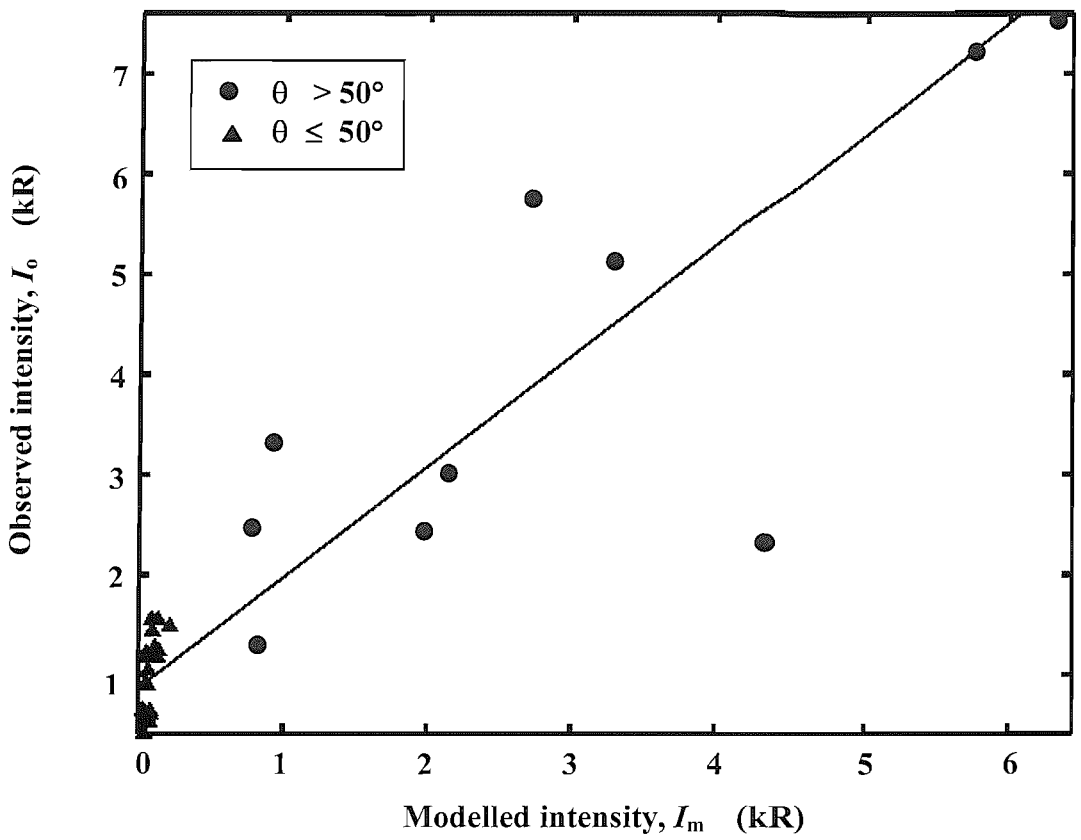

Figure 5.9 Scatter plot of *I*o against I_m for the lag giving peak correlation shown in Figure 5.8 and the best-fit linear regression fit. Symbols differentiate between data taken when the IMF clock angle is smaller than or exceeds 50°.

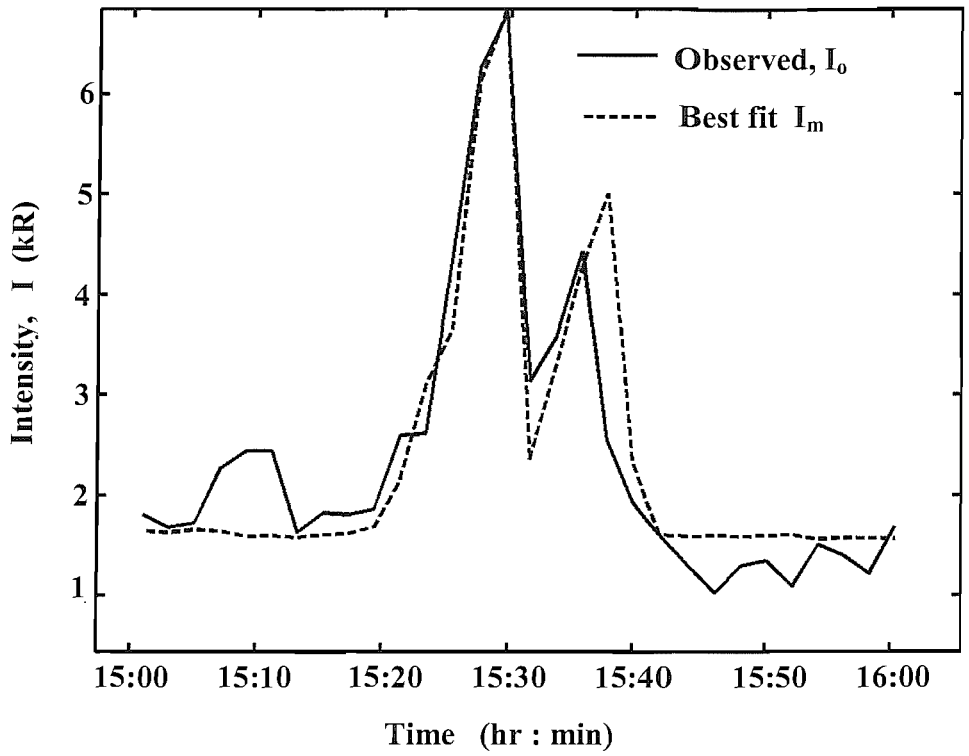

Figure 5.10 Comparison of peak Lyman-α intensity observed by the IMAGE FUV instrument, I_o (solid line) with the best-fit modelled variation, I_m (dashed line). I_m is the variation I_{max} shown in Figure 5.7, sampled every 122s like the observations, at times which give the peak correlation shown in Figures 5.10 and 5.11.

orientation, even during northern hemisphere winter. After the event, $B_z > 0$ and $B_x < 0$, an orientation for which lobe reconnection is most likely to take place just antisunward of the southern hemisphere cusp. Thus in the former case, the reconnection would be in the same hemisphere as the IMAGE observations, whereas in the latter case it would be the opposite hemisphere. This difference could be the origin of the lower intensity seen after the interval of southward IMF.

5.3 *The Spatial Distribution of the Proton Aurora*

In this section we use the numerical model of Lockwood and Morley (LM03), outlined in Section 3.2, to predict the evolution of ionospheric convection flows and the distribution of proton aurora emission, effectively producing model simulations of the data shown in Figure 5.4.

As discussed in Section 3.2, the Lockwood and Morley model (LM03) of ionospheric convection is based on the theory of the excitation of time-dependent ionospheric convection of Cowley and Lockwood [1992 and 1997]. It predicts the pattern of ionospheric convection for general variations in reconnection rate, in both time and space in both the low-latitude magnetopause and the cross-tail current sheet. Section 3.2.2 explained how the dayside reconnection rate, an input to the model, is calculated from the lagged IMF clock angle θ_{IMF} using an empirical relation, which generates a value for the electric field tangential to the dayside ionospheric merging gap, E_n, at a given MLT and simulation time t_s. This is the magnetopause reconnection rate mapped down field lines to the noon merging gap. E_{no} is initially set at 114 kV, in order that E_n later matches the observation.

The Lockwood and Morley model assumes a circular polar cap, the size of which is defined by the amount of open flux present at time t_s, $F_{OCB}(t_s)$, which is determined by the initial open flux, $F_{OCB}(t_s = 0)$, and the integrated difference between the magnetopause and tail reconnection voltages over the time interval $t_s = 0 - t_s$. The initial open flux, $F_{OCB}(t_s = 0)$, is an input to the model. As newly opened flux, ΔF_{pc}, is added to the system, the OCB erodes equatorward at the footprint of the magnetopause X-line. This perturbation propagates tailward at a speed which is also an input to the model. In this way the polar cap expands to a new equilibrium position at lower latitudes at all local times. This evolution represents the response of the

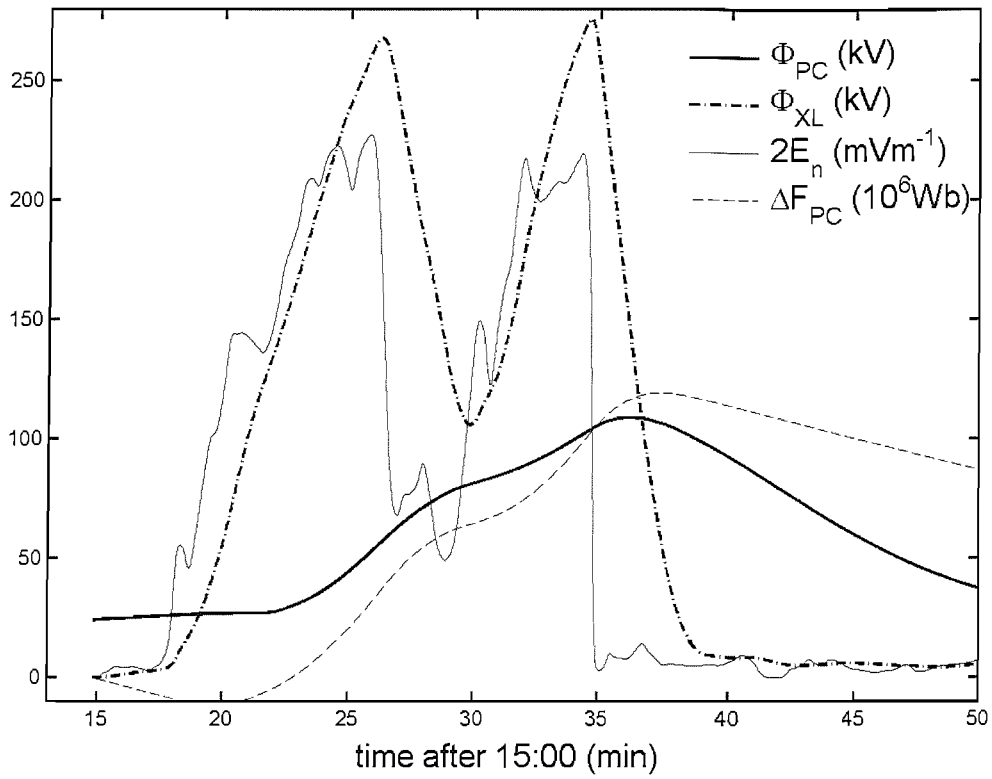

Figure 5.11 Inputs to and outputs from the LMO3 model of ionospheric convection applied to 26 November 2000. E_n (thin solid line) is the electric field at noon tangential to the ionospheric OCB, in its own rest frame (proportional to the magnetopause reconnection rate), specified by the lagged IMF clock angle observed by ACE. (Note that $2E_n$ has been plotted to best exploit the common y-axis scale). The integrated voltage along the entire X-line at any one instant is, Φ_{XL}, is shown by the dot-dash line. The thin dashed line gives ΔF_{PC}, the difference in F_{PC} with respect to the initial value $F_{PC}(t_s=0)$. The transpolar voltage generated by the model is Φ_{PC} shown by the thick solid line.

boundaries to newly opened flux being transported into the tail lobes through the action of the solar wind.

At each time-step (Δt_s = 1s) the spatial distribution of the reconnection rate is updated as are the OCB and equilibrium boundary locations. From the velocity with which the OCB is tending back towards the equilibrium latitude, the distribution of potential around the OCB is obtained; from this the transpolar voltage is derived and solving Laplace's equation (by assuming a uniform spatial distribution of ionospheric conductivity) yields the convection pattern. To match the observations, the model is run here with a constant reconnection voltage of 28 kV along a fixed X-line in the cross-tail current sheet.

The inputs to, and some of the outputs from the model are shown in Figure 5.11. The thin line shows the electric field along the ionospheric merging gap, $E_n(t_s)$. The value of E_{no} employed (114 mVm^{-1}) gives the best fit of the peak modelled transpolar voltage to that observed by the SuperDARN radar network. The variation of E_n shown in Figure 5.11 applies at noon; reconnection rate changes propagate away from noon and we here use the same propagation speed as LM03, namely 1 hr of MLT per minute. This propagation continues to MLTs of 09:00 and 15:00, on the dawn and dusk flanks respectively. These MLTs are determined from the MLT extent over which the proton aurora is detected on the newly-opened field lines by the FUV/SI-12 instrument, as shown in Figure 5.4. This assumes that the solar wind concentration is high enough to reveal all newly-opened flux in the SI-12/FUV images, even if it is produced on the magnetopause flanks where sheath concentrations are lower than at noon. The simulations shown in Figure 5.12 indicate that this is valid.

The variation in the total merging gap voltage Φ_{XL} which results from the propagation of the E_n variation along the merging gap, is shown by the dot-dash line in Figure 5.11. The thin dashed line in Figure 5.11 shows the variation in the polar cap flux, ΔF_{PC}. When Φ_{XL} is zero, the decline in ΔF_{PC} reveals the effect of the

constant tail voltage of 28 kV and when $\Phi_{XL} > 28$ kV, ΔF_{PC} increases because the rate of production of open flux outstrips the rate at which it is lost. Lastly, the thick solid line shows the variation of the transpolar voltage Φ_{PC} generated by the model. Note that the Φ_{PC} variation is effectively the input Φ_{XL} variation that has been inductively smoothed.

Convection streamlines are generated by the model from the potential distribution around the OCB by solving Laplace's equation. The convection patterns derived are shown in Figure 5.13, evolving over a period of 30 mins. Each pattern employs the same equipotential contour levels spaced 3 eV apart. Expansion of the convection pattern arises as the active merging gap expands longitudinally and the equatorward erosion of the OCB expands towards midnight. The model therefore allows us to follow the evolution of both the OCB in terms of its latitudinal position, Λ_{OCB} (MLT, t_s), and the transpolar voltage Φ_{PC}.

In order to compare model results with observations made on 26 November 2000, initial conditions need to be matched to those prevailing on this day. As the latitude of the OCB, Λ_{OCB}, determines the amount of open flux present in the polar cap, the initial polar cap flux $F_{PC}(t_s = 0)$ is set to match observations made by the IMAGE FUV instrument. Figure 5.14 shows how a circular OCB can be fitted to the highest intensity dayside Doppler-shifted Lyman-α emissions (using a threshold high enough to remove sunlight background) seen by SI-12/FUV at 15:22 UT. The thick solid line places the northward- IMF cusp "spot" on open field lines and the main proton aurora at all other local times on closed field lines. Also shown in Figure 5.14, as thick black lines, are segments of DMSP passes where the ions and electrons are consistent with open field lines. These passes all took place during the interval 14:36-15:20 prior to the swings to southward IMF.

Close to midnight, the poleward edge of the proton aurora detected is considerably equatorward of this circular boundary. This may show that the polar cap is not

circular; however, the existence of this sub-visual closed field line region outside the polar cap has often been inferred for quiet intervals and substorm growth phases

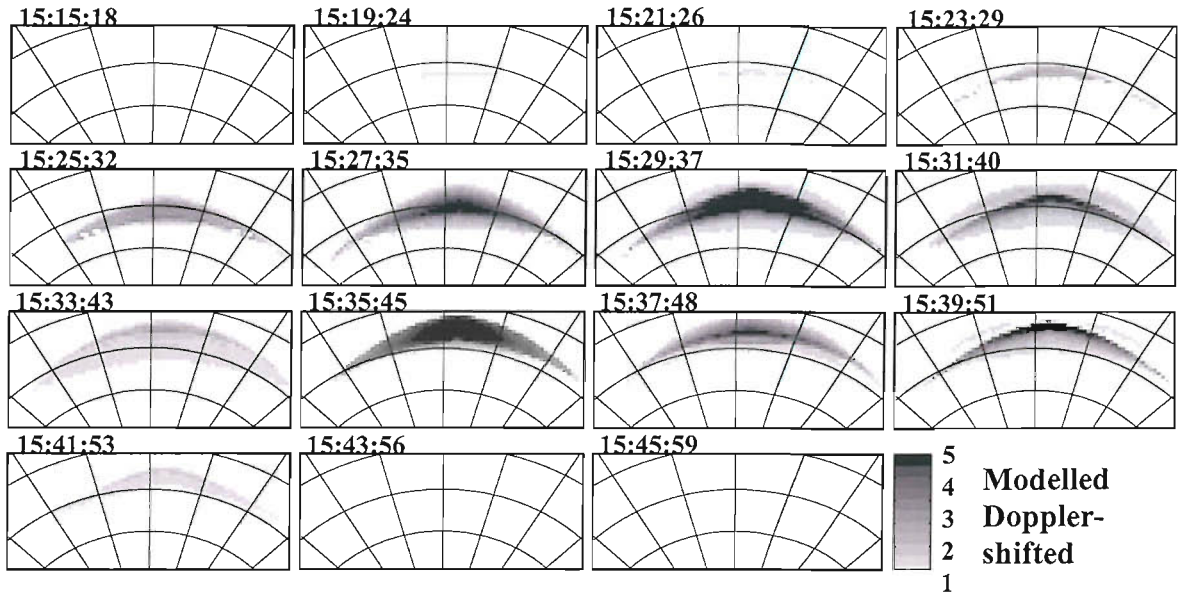

Figure 5.12 Simulated maps of the Doppler-shifted Lyman-α emission intensity *I* that would be detected by the SI-12 channel of the IMAGE FUV instrument. Panels are for 15:16-15:46 and are for the same times as the SI-12 images presented in Figure 5.4. The radial lines are for constant MLT, 1 hour apart with 12 MLT up the page; invariant latitudes of 75°, 70° and 65° are shown.

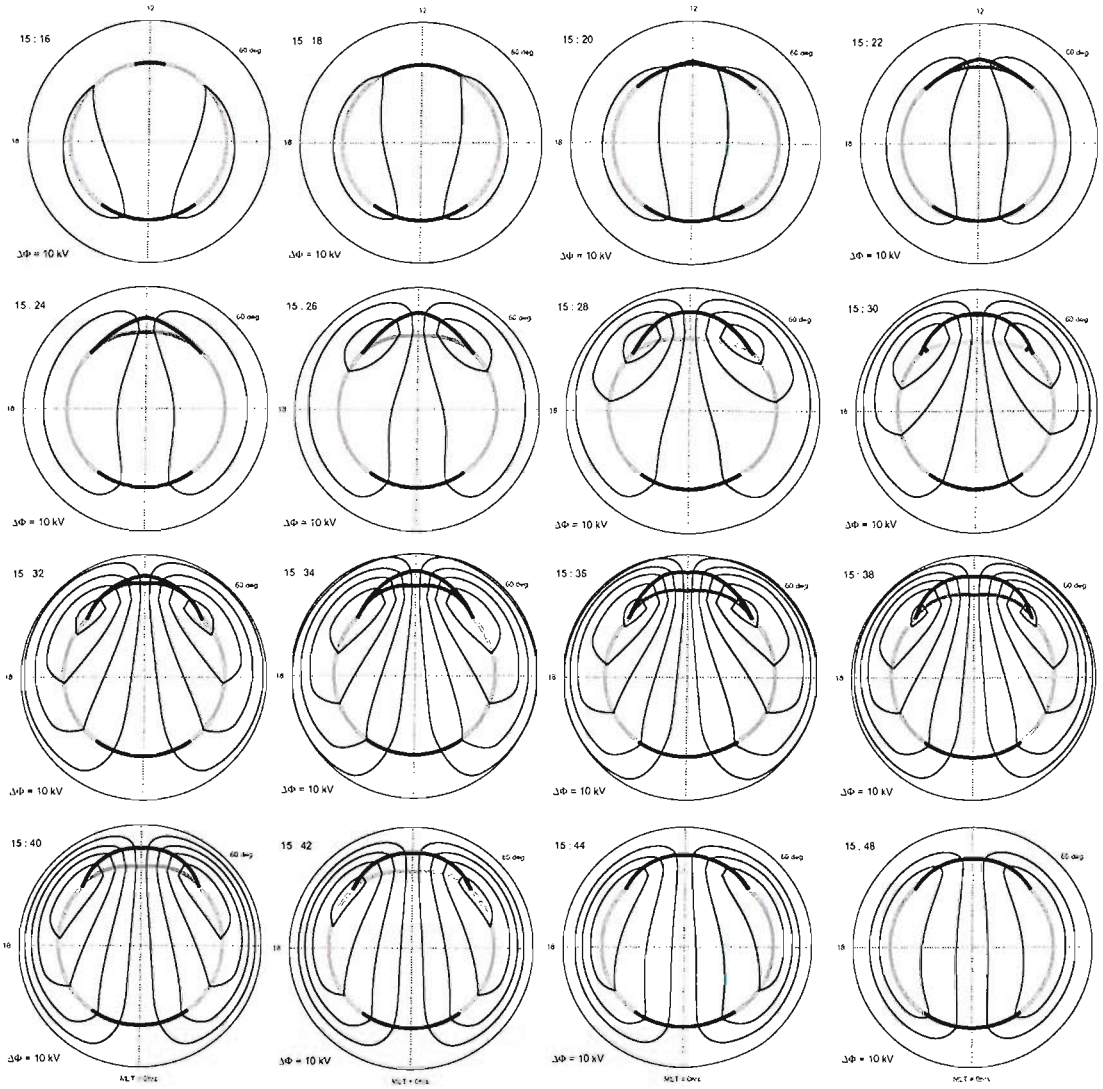

Figure 5.13 Model convection patterns for the same times as the SuperDARN data shown in Figure 5.4. The ionospheric projections of the dayside and tail reconnection X-lines are shown as thick black lines and the "adiaroic" (non-reconnecting) open-closed boundary segments by thinner lines. The broadly east-west grey lines poleward of the dayside merging gap show field lines opened at the onset of the two swings of the IMF clock angle, θ_{IMF}, to larger values. Patterns are 2 min apart and are for 15:18 –15:48 UT. The convection patterns are for the optimum estimates for $\tau_{OCB} = 9.7$ min and $E_{no} = 108$ mV m^{-1}.

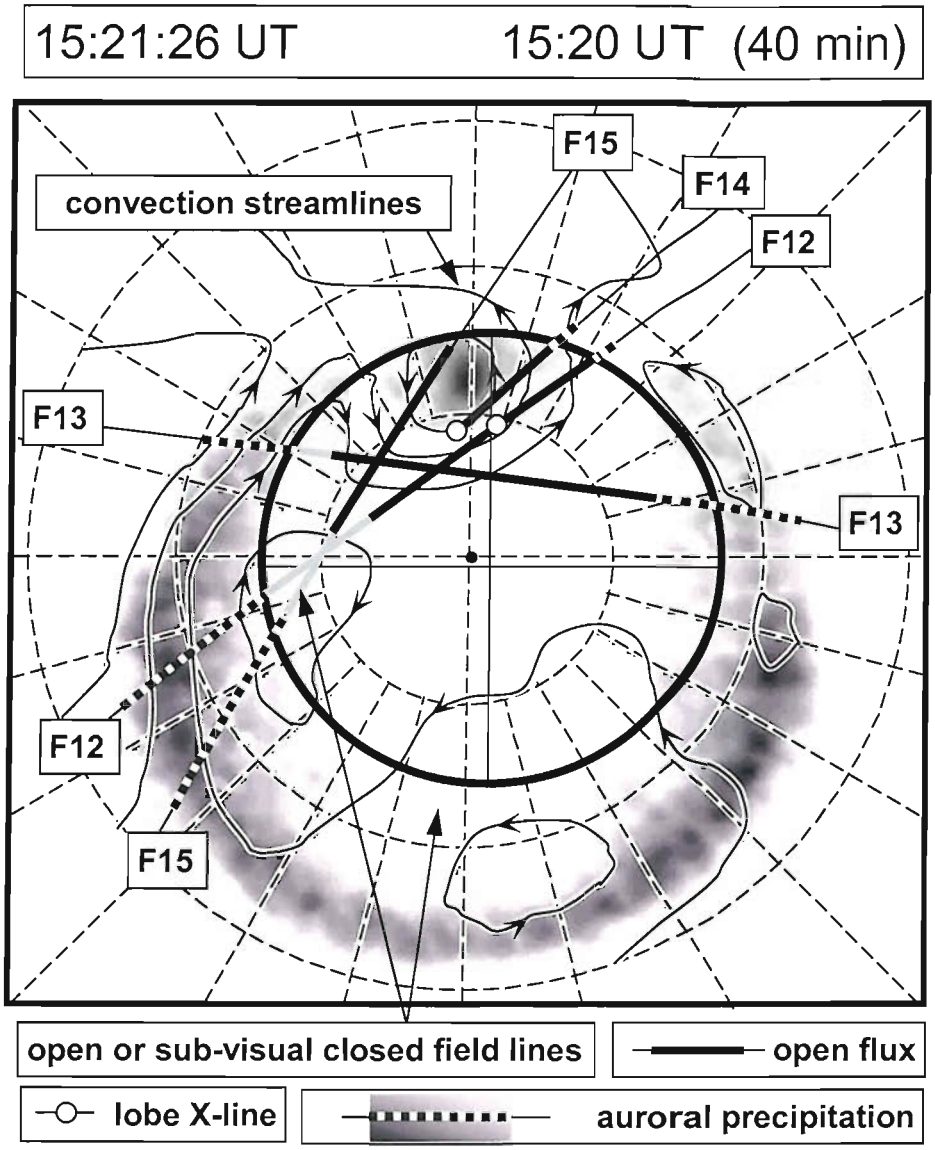

Figure 5.14 Image of the doppler-shifted Lyman-α emission seen by the SI-12/FUV instrument on the IMAGE spacecraft at 15:22 UT, with superposed convection flow streamlines for the SuperDARN radar scans commencing at 15:20: these are derived using the "mapped-potential" technique with an predicted ACE-to-ionosphere lag of 40 min. The thick solid line is a circular estimate of the dayside OCB location which places the northward-IMF cusp "spot" and lobe cell sunward flow on open field lines and the main nightside proton aurora on closed field lines. This would imply a region of sub-visual precipitation on closed field lines in the midnight sector (22 - 03 MLT). The OCB circle shown has a radius of 16° and is offset from the magnetic pole towards the nightside by 0.7° of invariant

latitude and toward dawn by 1.2°. This sets the initial polar cap flux $F_{PC}(t_s=0)$ of 6.1 $\times 10^8$ Wb, and places the noon OCB at a latitude $\Lambda_{OCB}(t_s=0)$ of 74.7°. Across this invariant latitude-MLT map of the polar cap are traced northern hemisphere passes by DMSP satellites F12, F14 and F15 and a southern hemisphere pass by F13: because the F13 pass is in the southern hemisphere is has been mirrored in MLT about the noon-midnight axis to reproduce dawn-dusk hemispheric asymmetries associated with the IMF B_y. The segments marked by thick black lines are where particle precipitations observed imply open field lines and the black and white dashed segments are where auroral oval precipitation was observed. The segments shaded grey are where the precipitation observed implies either open field lines or sub-visual closed field lines. The open circles show observed ionospheric footprints of lobe reconnection sites. These passes were all during the interval before the image was taken and while the IMF was northward. The times of the polar cap traversals (i.e. poleward of the auroral oval) for F12, F13 and F15 are 14:39:00-14:47:50, 14:58:33-15:05:00 and 14:53:42-15:00:42. F14 entered the polar cap during a data gap but left it at 15:10:24.

[Elphinstone et al., 1991; 1992; Samson et al., 1992]. If this region contains open, rather than the sub-visual closed flux inherent in the circular OCB adopted, then the only effect on the analysis presented here is that open flux estimates are consistently too small. The OCB estimate in Figure 5.14 has a radius of 16° and has a centre that is offset from the magnetic pole towards the nightside by 0.7° and toward dawn by 1.2°. This sets the initial polar cap flux $F_{PC}(t_s=0)$ of 6.1 $\times 10^8$ Wb and places the noon OCB at a latitude of 74.7°.

To summarise these inputs: $F_{OCB}(t_s = 0)$ is set at 7.65×10^8 Wb to match Λ_{OCB} at noon at $t_s = 0$ (15:15 UT); E_n is set by the observed (lagged) IMF clock angle with a value of E_{no} which is adjusted so the modelled voltage peaks at 105 kV, the value observed by the SuperDARN radar network. A constant tail reconnection voltage of 28 kV is applied (between 21 and 03 MLT) to match the observed polar cap contraction when Φ_{XL} is near zero. Lastly, the maximum extent of the ionospheric merging gap is set at 09 - 15 MLT to match the observed extent of cusp proton aurora. All other inputs to the model are as employed by LM03.

Figure 5.13 presents model flow patterns for this event, which reveal the evolution of patches of newly-opened flux. These patches are associated with equatorward erosion of the dayside OCB, caused by enhanced magnetopause reconnection and are highlighted in more detail in Figure 5.12, which shows the predicted intensity of Doppler-shifted Lyman-α on these newly-opened field lines. The LM03 convection model allows us to track the motion of all the newly-opened field lines, opened at time t_o, so that their locations at every simulation time, t_s, are known. Thus the model generates maps of time elapsed since reconnection $\{t_s - t_o\}$ in the MLT-Λ frame. From the solar wind clock angle θ_{IMF} and plasma concentration $N[H^+]$ on the field line reconnected at time t_o, the proton aurora intensity can be estimated for all $t_s > t_o$, as in Figure 5.7.

The longitudinal structure in the magnetosheath means that the plasma concentration and temperature crossing the magnetopause are functions of MLT. In order to reproduce the consequent longitudinal structure in the proton aurora we need to map this sheath structure down the field lines to the ionosphere. In general, the mapping of the magnetopause X-line into the ionospheric merging gap depends upon the amount of open flux present [Crooker et al., 1991]. We here define the mapping factor by setting an upper limit to the magnetopause reconnection rate E_X of 1 mVm^{-1} and, because field lines evolve away from the X-line at speeds V_F exceeding 250 kms^{-1}, this sets an upper limit to the boundary-normal field of $B_n = E_X/V_F \leq 4nT$. We obtain the mapping factor by comparing this with the peak electric field in the ionosphere, $E_{no} = 114$ mVm^{-1}. (The length dl_X along the X-line which corresponds to dl_i along the ionospheric merging gap is given by $E_X dl_X = E_{no} dl_i$). For a magnetopause at a geocentric distance of $12R_E$ and a merging gap at invariant latitude $\Lambda = 75°$, the resultant mapping factor means that 1 hr of MLT along the ionospheric merging gap maps to approximately 2.5hrs of MLT along the X-line. Because the model can only be run for IMF $B_y = 0$, the nose of the magnetosphere is predicted to map to the centre of the merging gap. This is a limitation in the model, and one that should be

addressed in the future. We then use the gas dynamic predictions of the source magnetosheath plasma as a function of MLT [Spreiter et al., 1966].

It can be seen from Figure 5.10 that the model is reproducing the general behaviour of the SI-12/FUV observations, with the first intensification reproduced exceptionally well. The largest discrepancy is at 15:36, and this corresponds to the worst mismatch in the time series, where the observed second peak in I_o is slightly earlier and weaker than that in the model prediction, I_m. This point is also the one major outlier in the scatter plot in shown in Figure 5.9. This difference may, at least in part, be caused by the polarity change in the IMF B_y component and the observed shift of the proton aurora peak towards the morning sector. The LM03 model in its present form deals with the transfer of magnetic flux into and out of the open field line polar cap by low-latitude reconnection; it does not include effects taking place within the polar cap. Thus the east-west flows on newly-opened field lines, caused by the Svalgaard-Mansurov effect and associated with the Y-component of the IMF, are not included nor is any stirring of polar cap caused by high-latitude (lobe) reconnection in one hemisphere.

Figure 5.15 presents a comparison of the model output with the observations. Figure 5.15a shows the modelled OCB latitude at noon, Λ_{OCB}, plotted with the equatorward edge of the Lyman-α emissions generated by cusp ion precipitation as scaled from the IMAGE FUV instrument data. The figures shows that the model matches closely the equatorward erosion of the OCB inferred from the proton aurora images. In Figure 5.15b, the modelled transpolar voltage, Φ_{PC}, is compared with results from the SuperDARN radar network. The observed voltages Φ_{PC} are derived using the "mapped potential" model fit to the SuperDARN data. The convection flows seen in Figure 5.4, are derived by fitting the convection model to the observed line-of–sight velocities made by the Northern hemisphere SuperDARN network. The model is driven by the upstream IMF conditions and unlike the LM03 model, it makes no allowances for the time history of the IMF, and therefore the evolution of

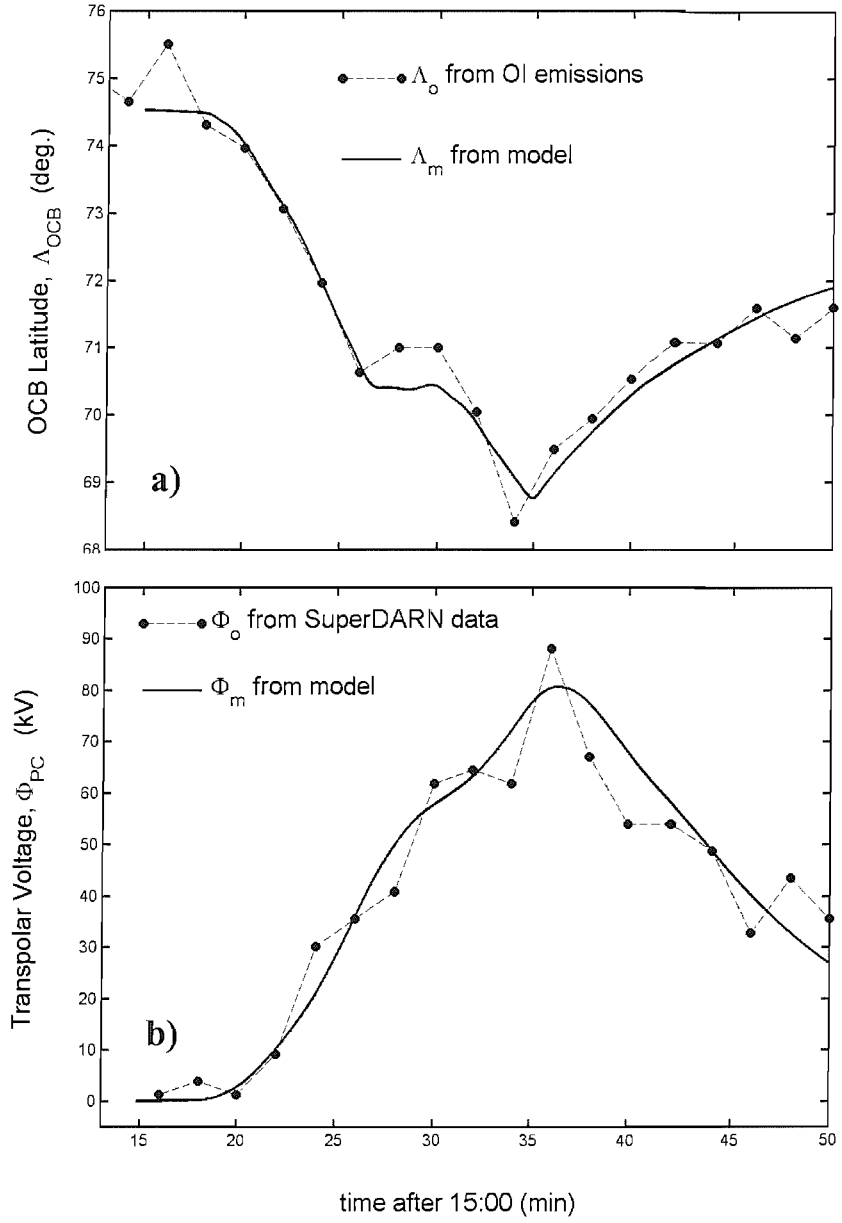

Figure 5.15 Observations (solid lines) compared with model variations (dashed lines). Figure ***a)*** shows the modelled transpolar voltage θ_{PC} compared with observations by the SuperDARN radar network. Figure ***b)*** shows the modelled open-closed boundary latitude Λ_{OCB} at noon compared with the equatorward edge of OI auroral emissions by cusp electron and ion precipitations, as observed by the IMAGE FUV instruments.

the newly-opened flux added to the polar cap in response to time-varying reconnection. In other words, the model assumes a steady state and will suppress features that are associated with the OCB expansion, which itself is a non-steady state feature. Despite this limitation a comparison of the flows shown in Figure 5.13 shows that the model reproduces the growth, decay and shape of the convection regions well, especially considering the model cannot reproduce the effects of the y-component of the IMF and the east-west flows on newly-opened flux that this component generates.

5.4 The Time Constants of Proton Emission

The above study of the response of the Doppler –shifted Lyman-α emission also allows an investigation of the implications on observing pulsed reconnection effects during southward IMF conditions. This has been of recent interest because Frey et al (2003) used persistent proton aurora emission to infer continuous reconnection, but did not take the time constants for the change in the emission into account. In this section, we use the time constants for the growth and decay of proton emission intensity, as seen by FUV/SI-12 and consider how this affects the detection of pulsed reconnection.

The autocorrelation function (acf) of the observed intensity I_o is shown by the dashed line in Figure 5.8a and reveals a correlation time of order 10 min. However, this may be set by the persistence (the tendency for it to remain constant) of the emission, but could also reflect the persistence of the controlling IMF conditions. Figure 5.1 shows that I_o decays with a time constant of about 5 min following the abrupt decrease in IMF clock angle (seen at about 15:40 in Figure 5.1). This is a better estimate of the persistence of the emissions and is close to the decay times predicted in Figure 5.6b. This and the good match between the modelled and observed peak intensities shown in Figure 5.10, along with the general reproduction of the spatial pattern of proton aurora in Figure 5.12, gives great credence to the modelled variations of Doppler-shifted Lyman-α intensity, as shown in Figure 5.6a, and the rise and decay times shown in Figure 5.6b. As discussed in Section 5.2, these time constants smooth the effect of reconnection rate variations in the proton emissions. In this section, we investigate the limits that this places on the detection of reconnection pulses. The observations presented in the previous section show two clear brightenings and expansions of the cusp proton aurora in response to two reconnection pulses. However, these pulses were directly driven by southward swings of the IMF and, for component reconnection, the effect of the reconnection rate pulse is convolved with the clock angle effect on the ion acceleration at the magnetopause.

LEA03 discussed how anti-parallel reconnection would require motions of the reconnection site (to locations where the magnetosheath ion concentration and temperature are different) to generate the same effect. In this section, we use the model to investigate the effect of reconnection pulses at various constant IMF clock angles.

In general, the reconnection rate will show variations over a background level. Decreases of the rate to a low background value will cause steps in the cusp ion dispersion [e.g. Lockwood and Davis, 1996] and several observed examples of cusp ion steps have been interpreted in terms of such temporal variations because they are associated with poleward-moving events and because the step propagates with the convection flow [Lockwood, 1995]. If the reconnection rate falls to a low, but non-zero value, the step is not instantaneous, although it may appear to be if the ion spectra are not sampled sufficiently rapidly.

If the reconnection does fall to zero between the pulses, the step is instantaneous, whatever the resolution of the ion data. If the reconnection rate does not fall to zero between any pulses, newly-opened field lines are always being generated. The intensity of the proton aurora produced at the ionospheric footprint of each of these field lines will then evolve as shown in Figure 5.6a, and for constant IMF clock angle $\theta_{IMF} = \theta_{sh}$ and solar wind concentration $N[H^+]$ the peak intensity I_{max} (and hence the sampled peak intensity I_m) will be constant. However, because the amount of newly-opened flux present will vary, the area of the proton aurora patch will vary. Thus detection of reconnection rate pulses over a steady background will require resolution of changes in the area of the proton aurora patch.

On the other hand, if the reconnection rate does go to zero between pulses, the peak proton aurora intensity I_{max} is not constant and will start to show minima. We here investigate the depth and duration of these minima in order to evaluate if, and when, they could and should be detected. Figure 5.5d defines the time Δt for which the

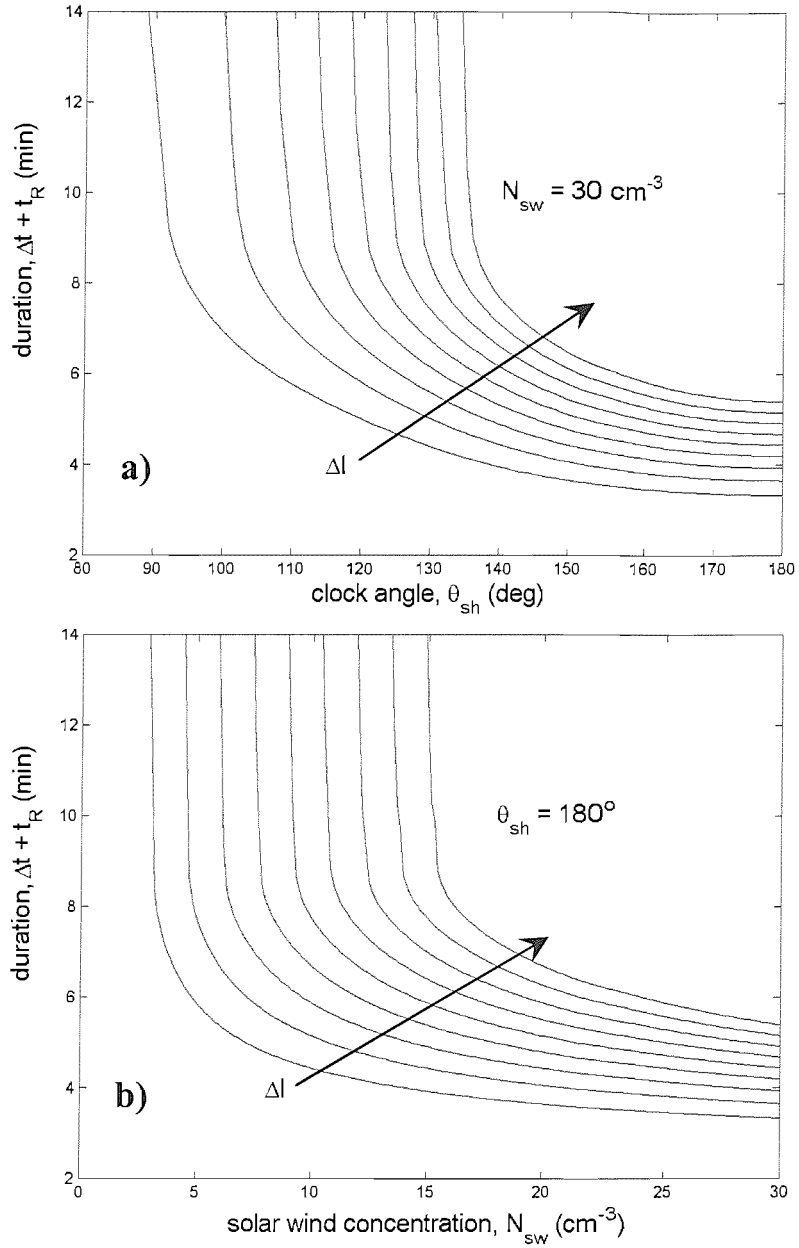

Figure 5.16 Modelled variations of $(\Delta t + t_R)$ for ΔI between 0.5 kR and 2.0 kR, in steps of 0.25kR, where Δt and ΔI are defined in Figure 5d and t_R = 2min. ***a)*** As a function of sheath field clock angle θ_{sh} for constant solar wind concentration N_{H+} of 30 cm^{-3}. ***b)*** As a function of N_{H+} for constant θ_{sh} of 180°.

intensity on a given field line exceeds a threshold that is the peak intensity, minus a difference ΔI. If we can detect a decrease in intensity greater than or equal to ΔI we will see the effect of an interval of zero reconnection rate, provided that it exceeds $(\Delta t + t_R)$ in duration. The additional time t_R is the sampling interval of the data and must be added to Δt to ensure that at least one data point is obtained when the intensity is below the threshold. We here use t_R = 122s, appropriate to the FUV instrument. Figure 5.16a shows the predicted variation of $(\Delta t + t_R)$ with sheath field clock angle θ_{sh} for a very high solar wind concentration ($N[H^+]$ = 30 cm^{-3}) for ΔI between 0.5 and 2.0 kR (in steps of 0.25 kR). It can be seen that $(\Delta t + t_R)$ values decrease as ΔI decreases and as θ_{sh} increases. Thus, for example, if we can detect intensity changes ΔI of 2 kR and greater, then for this $N[H^+]$ we can detect periods of zero reconnection of duration 5.5 min or greater at θ_{sh} of 180°. If the intensity resolution available is ΔI of 0.5 kR, this value is reduced to 3.5 min. Note for component reconnection, with a lower θ_{sh}, these durations are increased. Figure 5.16b shows the dependence of $(\Delta t + t_R)$ as a function of $N[H^+]$ for a constant θ_{sh} of 180° (anti-parallel reconnection) for the same ΔI values. It can be seen that $(\Delta t + t_R)$ increases as $N[H^+]$ decreases. For the most common value of $N[H^+]$ of 5 cm^{-3} [Hapgood et al., 1991] only ΔI of 0.5 kR and 0.75 kR will allow detection of the intensity changes and only for intervals of zero reconnection exceeding 5.5 min and 7.5 min, respectively. Nevertheless, periods of zero reconnection between pulses should be detectable at high sheath field clock angles and high solar wind concentrations and Figure 5.16a and 4.16b provide a means of evaluating when pulsed reconnection should be detected.

5.5 *Discussion*

The excellent agreement shown in Figure 5.10 between I_o, the peak Lyman-α intensity observed by the IMAGE FUV instrument, and I_m, the best-fit modelled variation, highlights the clock angle dependence of the emission intensity seen in the cusp region. In LEA03, this dependence was discussed by showing the intensity of the cusp aurora as a function of the simultaneous inferred sheath clock angle θ_{sh} and solar wind proton density $N[H^+]$. We have improved these findings by allowing for: the evolution of the Doppler-shifted Lyman-α emission with time since reconnection, the variation of that evolution with θ_{sh} and $N[H^+]$, and the limited sampling by the FUV instrument. The results presented here are generally similar to those of LEA03 but the scatter in the data is reduced and the correlation increased by the improved procedure adopted.

The southward turning of the IMF reaching the ionosphere triggered the migration equatorward and intensification of the proton aurora near noon. As the polar cap expanded, the convection pattern intensified and the equipotentials migrated away from noon as the polar cap voltage, Φ_{PC}, increased. The dayside bulge in proton aurora is replicated by the model and is caused by the equatorward erosion of the OCB at the footprint of the magnetopause X-line. Figure 5.13 predicts in detail how the bulge evolved, growing in longitude and expanding equatorward. The double nature of the intensification, caused by the IMF clock angle variation, is clear and is well reproduced by the model, although it predicts a slightly larger and later second peak than is actually observed.

The success of the model in explaining the evolution of the cusp proton aurora, in peak intensity, location and extent gives strong support to the rise and decay times of the emission predicted by the model and the persistence of proton emission of each newly-opened field line. From this, we have studied the conditions required to

observe pulsed magnetopause reconnection using the SI-12/FUV instrument during southward IMF conditions.

If the reconnection voltage is pulsed over a non-zero background level, for constant solar wind and IMF conditions, the peak proton emission intensity will not vary with time and the only signature will be lagged variations in the area of the patch of proton emission with the same periodicity as the reconnection voltage variation. If the reconnection rate falls to zero between the pulses, decreases in the peak emission will be observed in addition to the area changes, again with the periodicity of the reconnection variations. This "blinking" of the cusp proton aurora should be detectable in the case of anti-parallel reconnection if the solar wind plasma concentration is high. If we take an intensity difference of 1 kR to be resolvable above noise fluctuations, Figure 5.12b shows that, for a very high solar wind proton concentrations of $N[H^+] = 30$ cm^{-3}, intervals of zero reconnection exceeding 4 min should be detected. For lower solar wind concentrations, intervals of zero reconnection will need to be longer if they are to be detected; for $N[H^+] = 10$ cm^{-3}, intervals would need to be at least 6 min in duration and for the mode $N[H^+]$ of 5 cm^{-3}, no intensity variations would be detected at all. Figure 5.16a shows that for component reconnection, smaller clock angles between the reconnecting field lines would mean that only longer intervals of zero reconnection would be detected. Thus the SI-12/FUV instrument allows us to place limits on intervals of zero reconnection between pulses. It should be stressed that this analysis is for southward IMF conditions. As pointed out by Frey et al. [2003], the same sort of considerations would apply to lobe reconnection during northward IMF, when the reversed ion dispersion often observed can have otherwise very similar characteristics to those during southward IMF [Woch and Lundin, 1993]. However, the relevant time constants and the limits placed would be different because of the differences in the location of the reconnection site and because the evolution of the recently-reconnected field lines would be different.

This study has also used the combination of global imaging of the ionospheric convection pattern and of the proton aurora (by the SuperDARN radar network and the SI-12/FUV instrument of the IMAGE satellite) to demonstrate quantitatively the concepts of ionospheric flow excitation proposed by Cowley and Lockwood [1992]. The response of dayside OCB and the flows observed and modelled in this event show that the equation of Section 3.2.2 provides a reconnection voltage that serves as a realistic input to the model. It is also a clear confirmation of the Cowley-Lockwood [1992] flow excitation model. The accuracy with which the LM03 numerical model reproduces the response in both Λ_{OCB} and transpolar voltage shows that the Cowley-Lockwood theory is also quantitatively correct, using the time constant of 15 minutes for newly-opened flux to be appended to the tail lobe (as implemented in the model by LM03 and as assumed here).

This study is the first time that the LM03 model has been applied to observations. The next chapter will compare observations from the morning of the same day with LM03 model results in order to determine the coupling mechanisms responsible for the dayside ionospheric signatures seen by a range of different instruments.

5.6 *Event Summary*

We employed the Lockwood and Davis model of cusp ion precipitation and proton aurora emission to fit variations of the peak Doppler-shifted Lyman-α intensity observed on 26 November 2000 by the SI-12 channel of the FUV instrument on the IMAGE satellite. The major features of this event appeared in response to two brief swings of the interplanetary magnetic field (IMF) towards a southward orientation. The simulations were based on the observed variations of the solar wind proton temperature and concentration and the interplanetary magnetic field clock angle. They also allowed for the efficiency, sampling rate, integration time and spatial resolution of the FUV instrument. The good match (correlation coefficient 0.91, significant at the 98% level) between observed and modelled variations confirmed the time constant (~ 4 min) for the rise and decay of the proton emissions predicted by the model for southward IMF conditions. The implications for the detection of pulsed magnetopause reconnection using proton aurora were discussed for a range of interplanetary conditions.

We also reproduced the observed spatial distributions of this emission on newly-opened field lines by combining the Lockwood and Davis cusp model with the Lockwood and Morley numerical model of time-dependent ionospheric convection. The latter model required an input magnetopause reconnection rate variation, which was here derived from the observed upstream IMF clock angle, θ_{IMF}. This reconnection rate was mapped to an ionospheric merging gap, the MLT extent of which was revealed by the doppler-shifted Lyman-α emission on newly-opened field lines, as observed by the FUV instrument on the IMAGE spacecraft. To match the observed convection patterns, a small and constant tail reconnection voltage was applied until the onset of the subsequent substorm expansion. We reproduced the observations by adopting a θ_{IMF}-dependence of the magnetopause reconnection electric field, mapped to the ionosphere, of the form $E_{no}\sin^4(_{IMF}/2)$. We here estimated the peak value E_{no} by matching the variations of both the latitude Λ_{OCB} of the dayside

open-closed field line boundary (as inferred from the equatorward edge of cusp proton emissions seen by FUV) and the transpolar voltage Φ_{PC} (as derived using the mapped potential technique from SuperDARN HF radar data). The analysis confirmed quantitatively the concepts of ionospheric flow excitation by Cowley and Lockwood [1992] on which the model is based.

Chapter 6: Event Two

The Magnetospheric-Ionospheric Responses to a Simultaneous Pressure Front and Southward Turning of the IMF

The multi-instrument study presented in this chapter uses data from 26 November 2000. The event, first introduced in Section 4.2, is the first of a series of events on that day, another of these events being the subject of the previous chapter. During the event studied here ground-based optical instruments on Svalbard measured a sudden increase, commencing at about 08:00, in the intensity of the auroral emissions resulting from both proton and electron precipitation. A particularly distinct ionospheric bipolar signature was seen in the recordings of the IMAGE, Greenland and MM210 magnetometer arrays similar to those associated with a propagating vortical structure.

It is now widely accepted that the interaction of a pulse in the solar wind pressure with the magnetosphere leads to the generation of filamentary field-aligned currents (FACs), which manifest themselves in the high-latitude ionosphere as propagating convection vortices known as TCVs, each FAC being at the centre of the corresponding vortex and its direction (up or down) determining the sense of the vorticity. The possible mechanisms for the generation of the FACs are discussed in Section 1.3.2. Examining upstream data reveals that both ACE and Wind did indeed see a significant increase in the solar wind pressure. Determining whether this pressure increase is responsible for the observed ionospheric signatures is complicated by a simultaneous brief swing of the interplanetary magnetic field southwards accompanying the pressure increase. Figure 4.11 shows these upstream features lagged by the predicted ACE-to-ionosphere calculated in Section 4.3.2.

The impact of the southward turning on the ionosphere is predicted by the Lockwood and Cowley [1992] theory of flow excitation discussed in Section 3.2. Following the onset of reconnection, the theory predicts a pair of filamentary field-aligned currents which elongate and expand away from noon to eventually establish the large scale Region-1 current system associated with magnetosphere-ionosphere convection. Thus a brief pulse of reconnection, like a pressure pulse, produces transient, filamentary field-aligned currents and associated flows with expansion away from noon. The similarity in the way both features impact on the ionosphere means that separating the effects of a reconnection pulse from a pressure pulse effect is not straightforward. In theory, the effects can occur in isolation, in practice however, the effects of the two are often convolved and interact with each other because the driver gas giving the pressure pulse frequently causes IMF direction swings [Hapgood et al., 1991].

This chapter describes filtering as a method of separating the effects of the reconnection pulse from the pressure pulse effects on the ground-based data, allowing the study of their individual impact on the magnetosphere/ionosphere system. In this way, filtering gives an estimate of the relative contributions of the two upstream features on energy transfer and deposition in the magnetosphere and ionosphere. The validity of the filtering method is here found to be supported by the Lockwood and Morley convection model, introduced in Section 3.2, which is used to emulate the ionospheric flows triggered by the southward turning.

The position of the ground-based instruments made it possible to study both the reconnection and pressure pulse effects on the ionosphere near noon and investigate the evolution of the temporally and spatially varying field aligned currents associated with these effects. The results put forward in this chapter show the existence of two trains of vortices forming near noon and propagating around the morning and afternoon sectors. Evidence for the existence of field line resonances (FLRs) are present in both the magnetometer and radar data at lower than cusp latitudes. Resonances in the Pc5 range are seen to predate the arrival of the pressure front and remain present for a few hours afterwards. This study considers the two theories outlined in Section 1.3.2 in order to determine the

mechanisms behind the generation and propagation of these vortical flows and FLRs.

The observations from all instruments, space and ground-based, are presented in Section 6.1. A description of these instruments has been given previously in Chapter 2. The analysis of the event, presented in Section 6.2, involves the separation of the effects of the pressure pulse from those resulting from convection using a low pass filter. The Lockwood and Morley convection model is used to emulate the ionospheric flows triggered by the onset of dayside reconnection and provide support for the use of filtering as a way of separating the low frequency convection data from the high frequency pressure pulse effects. Section 6.3 discusses the interpretation of the data and examines the implications of the methods used to analyse these results.

6.1 Observations

It is expected that the solar wind density pulse will be converted into a fast hydromagnetic (HM) compressional wave at the bow shock, which will then propagate across the magnetosheath. Upon reaching the magnetopause, magnetosheath pressure variations drive magnetopause motion and launch compressional Alfvénic waves into the magnetosphere, generating signatures at geosynchronous orbit. As shown in Figure 6.1, signatures were indeed recorded by the onboard magnetometer of the GOES-8 satellite situated on the nightside, as shown in Figure 6.1d. The satellite observed Pc5 oscillations in all three components of the magnetic field commencing just before 8 UT when a major change in the magnetic field strength is seen. Figure 6.1a, 6.1b and 6.1c show the three components of the magnetic field from GOES-8; ten full oscillations were observed between 08:05 and 08:45, giving a mean period of 4 min. The initial decrease in field strength is due to the compression of the magnetotail by the pressure front, which moves the satellite on to a higher L-shell.

6.1.1 Optical Observations

The Spectrographic Imaging Facility (SIF) at LYR, consisting of a number of ground-based optical instruments including the High Throughput Imaging Echelle Spectrograph (HiTIES) and two photometers, is described in Section 2.2.1. Since these ground-based instruments make continuous observations at one location, the combination of instruments is well suited to discriminate between the spatial and temporal evolution of the ionospheric features caused by the reconnection and pressure pulses over LYR.

The top panel of Figure 6.2 shows the proton and electron induced emission intensities recorded by the SIF photometers. Starting just before 8 UT, an oscillation of period about 5 minutes was observed in both the H_β and the N_2^+ emissions. The initial cycle was followed by two subsequent cycles in H_β but in the nitrogen emission the oscillations cease abruptly at 8:07 UT.

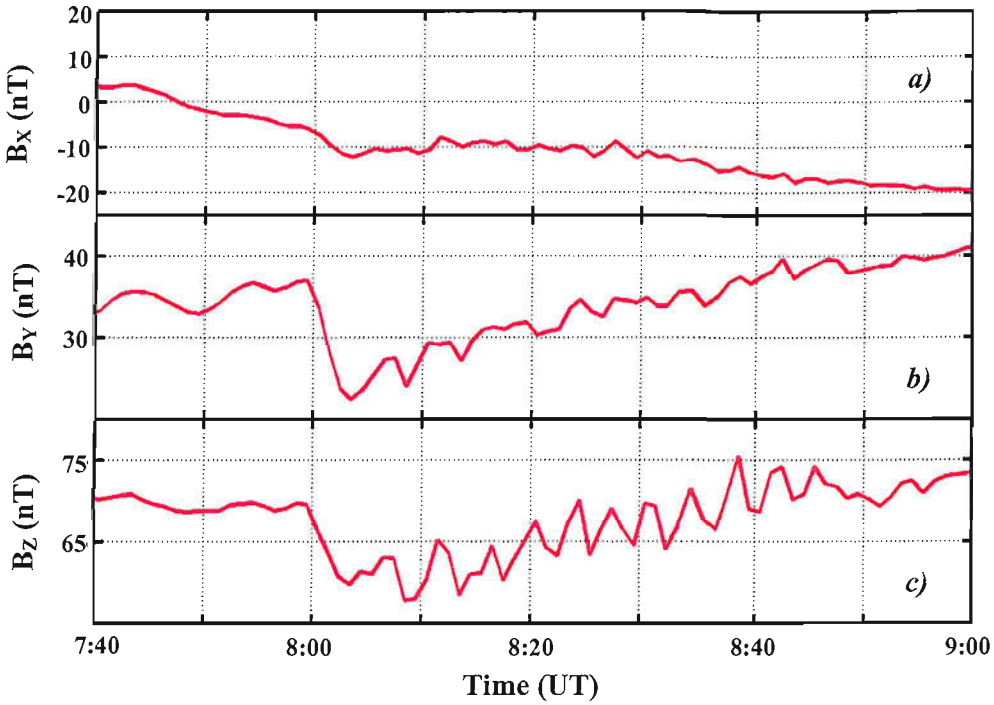

Figure 6.1 a), b) & c) Respectively, the B_X, B_Y and B_Z magnetic field components, measured by the GOES-8 onboard magnetometer. ***d)*** The position of the satellite over the period of interest from 7:30 – 9:00 UT.

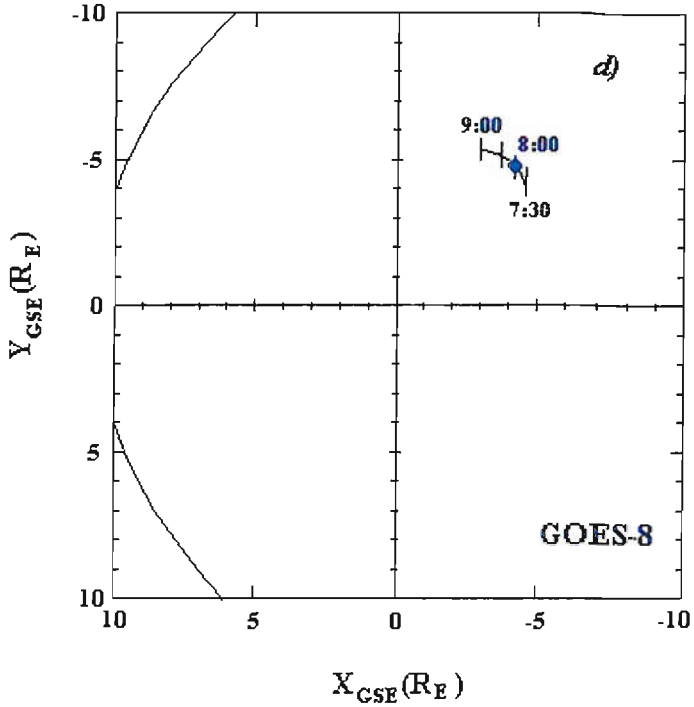

The lower panel shows the magnetic field variations from the magnetometer station situated at LYR. Both the photometer and magnetometer data has been filtered to remove the low frequency convection changes, revealing similar variations in the magnetic data and the intensity of the hydrogen emissions due to the pressure front. The nitrogen emission intensity initially varies along with the hydrogen emission intensity until 8:05 UT, when the correlation breaks down. The magnetometer and photometer data will be discussed in detail in Section 6.3.

The SIF and magnetometer observations are supported by those from the Meridian Scanning Photometers (MSP). The precipitation and subsequent emissions associated with both the arrival of the pressure front and the southward turning were observed in all the associated spectral windows at a range of latitudes. Figure 6.3 shows the MSP plots for the electron induced 630.0 nm and 557.7 nm emissions and the proton induced 486.1 nm emission around the time of the event.

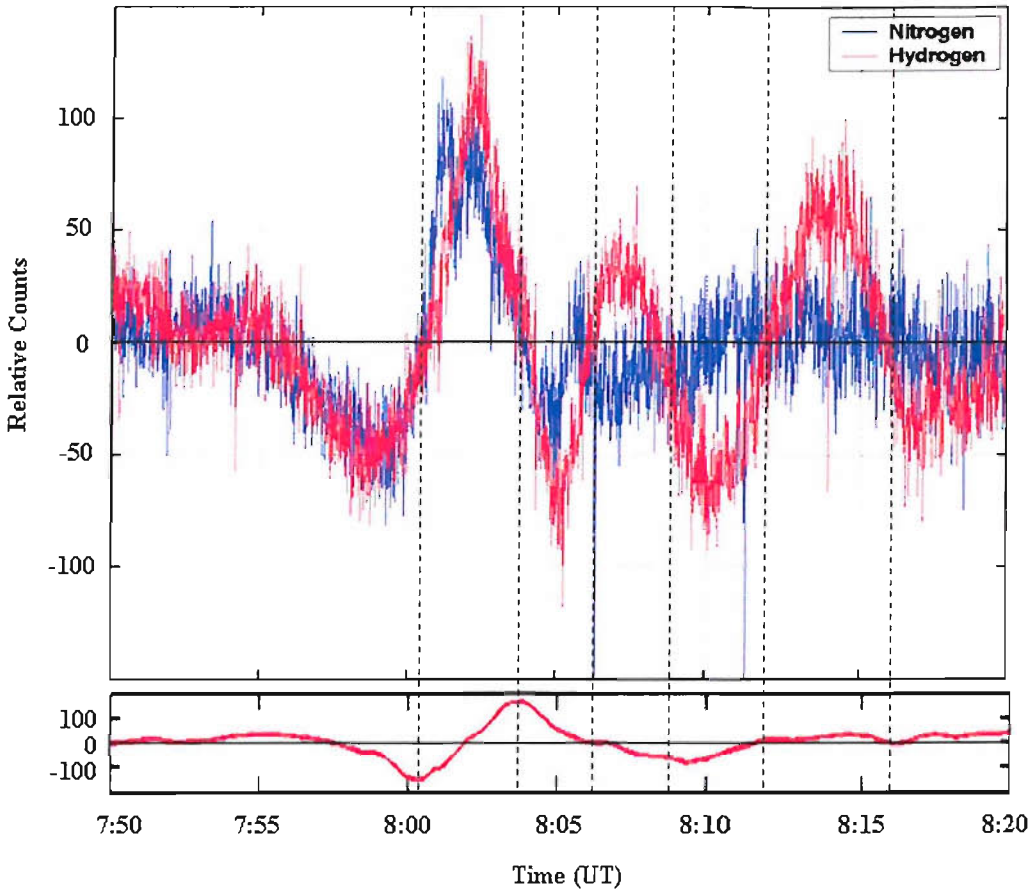

Figure 6.2 The top panel shows the variations in the intensity of proton (H_β) and electron (N_2^+) induced emissions recorded by the narrow-band photometers at LYR. The bottom panel shows the northward (B_N) component variations observed at the LYR IMAGE magnetometer station. Both the photometer and magnetometer data have been filtered to remove the low frequency variations, revealing similar variations in the magnetic data and the emissions resulting from the impact of the pressure front.

Figure 6.3c shows that three weak pulses of H_β (486.1nm) emission were observed, centred at approximately 8:02 UT, 8:07 UT and 8:14 UT, corresponding to the peaks of the oscillations seen by the SIF photometers. In Figure 6.3b an increase in the oxygen (557.7 nm) emission is observed, initially at the southernmost edge of the field of view but then expanding rapidly to cover zenith angles 30-180°. This is simultaneous with both the first pulses in hydrogen and nitrogen emission seen by the SIF photometer. The northward limit of this enhanced emission then moves progressively equatorward, except at 8:05 UT, when a second, very brief, burst of 557.7 nm emission is detected over much of the field-of-view. This second pulse corresponds to a sudden increase in the oxygen (630.0 nm) emission shown in Figure 6.3a, which lasts for approximately 12 mins. Such an increase in the 630.0/557.7 intensity ratio could indicate the passage of LYR from closed field lines onto open field lines (Section 1.2.6). One way of confirming this boundary motion is with the use of satellite data. However, the FAST and DMSP satellites are not in suitable positions to provide information on the particle boundaries for this event. Note that the increase in the 630.0/557.7 intensity ratio occurs simultaneously over a range of latitudes and so no equatorward motion is detected. This is most likely caused by scattering from cloud at this time, which also may have extended the latitudinal extent of the brief burst of 557.7 nm emission at 8.05 UT.

6.1.2 Radar Observations

The EISCAT incoherent scatter radar (ESR) situated at LYR provides measurements of ion temperature, electron temperature, electron density and line-of-sight plasma velocity over a wide range of altitudes. During the period of interest, the ESR system was running with a field-aligned beam and the TAU0 modulation experiment, which utilises two alternating code signals allowing complete coverage from the E-region to topside at a time resolution of 6.4 sec.

Figure 6.4 shows that just after 8:02 UT, there was an enhancement lasting about 5 mins in F-region ion temperature accompanied by a small increase in electron temperature at altitudes above 400 km. This period is delineated by the two black lines at 8:02 UT and 8:07 UT.

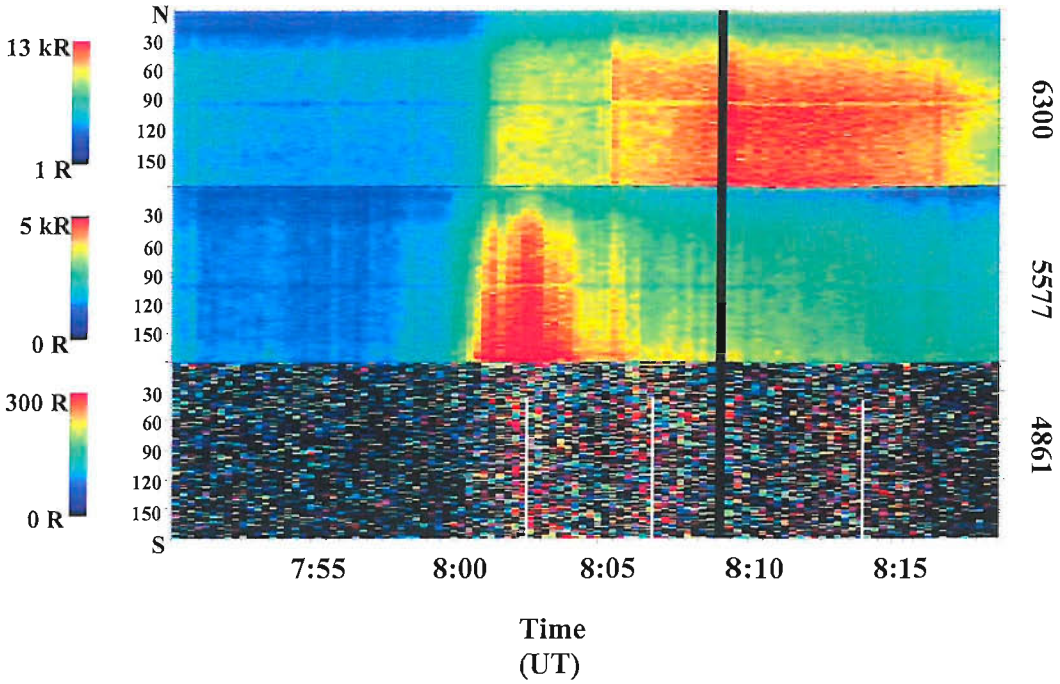

Figure 6.3 The MSP measurements for 630.0 nm (neutral atomic oxygen), 557.7 nm (neutral atomic oxygen) and 486.1 nm (neutral hydrogen, Balmer-beta) emissions around the time of the event. The white lines mark the peaks of the three oscillations in H_β emission.

This temperature enhancement is marked by a trough in electron density, consistent with either enhanced local plasma loss rate caused by the enhanced plasma velocities and/or a change of convection pattern which brought lower-density plasma into the field of view. At 8:07 UT, the time at which the ion temperature enhancement decreases, a gradual increase in electron density is detected over a period of 2 mins, followed by a more rapid increase at 8:09 UT, denoted by the third black line. These changes are shortly after the large increase in the 630.0/557.7 intensity ratio at 08:06, as discussed in the previous section. The overall enhancement lasted for 12 mins and was accompanied by an increase in electron temperature denoting soft electron precipitation characteristic of the cusp. There was also an upwelling of ions, a characteristic of cleft ion fountains which supply low-energy ions from the ionosphere to the polar magnetosphere at times of strong anti-sunward convection [Lockwood et al, 1985].

A wider view of the event is provided by the EISCAT VHF radar at Tromsø which views a range of latitudes around the ESR. The black line in Figure 2.1 shows the orientation of the VHF radar beam used in this study. Figure 6.5 shows data from this beam for several hours around 8 UT. Figure 6.5d shows that the radar detected an alternating sequence of away (red) then toward (blue), ion plasma velocity oscillations along the direction of the radar beam, over an invariant latitude range of 70.5° – 75.5°. Due to the elevation of the radar beam, the increase in latitude is accompanied by an increase in altitude from ~ 200 km to ~ 900 km. These 5-minute velocity oscillations are clearly present for several hours before 8 UT and last for a couple of hours after the arrival of the pressure front and the southward turning. Figures 6.5a, 6.5b and 6.5c show enhancements in the electron density and the ion and electron temperature just after 8 UT. The temperature enhancements are seen to move to lower latitudes, before returning poleward. This equatorward and poleward motion takes approximately 20 mins.

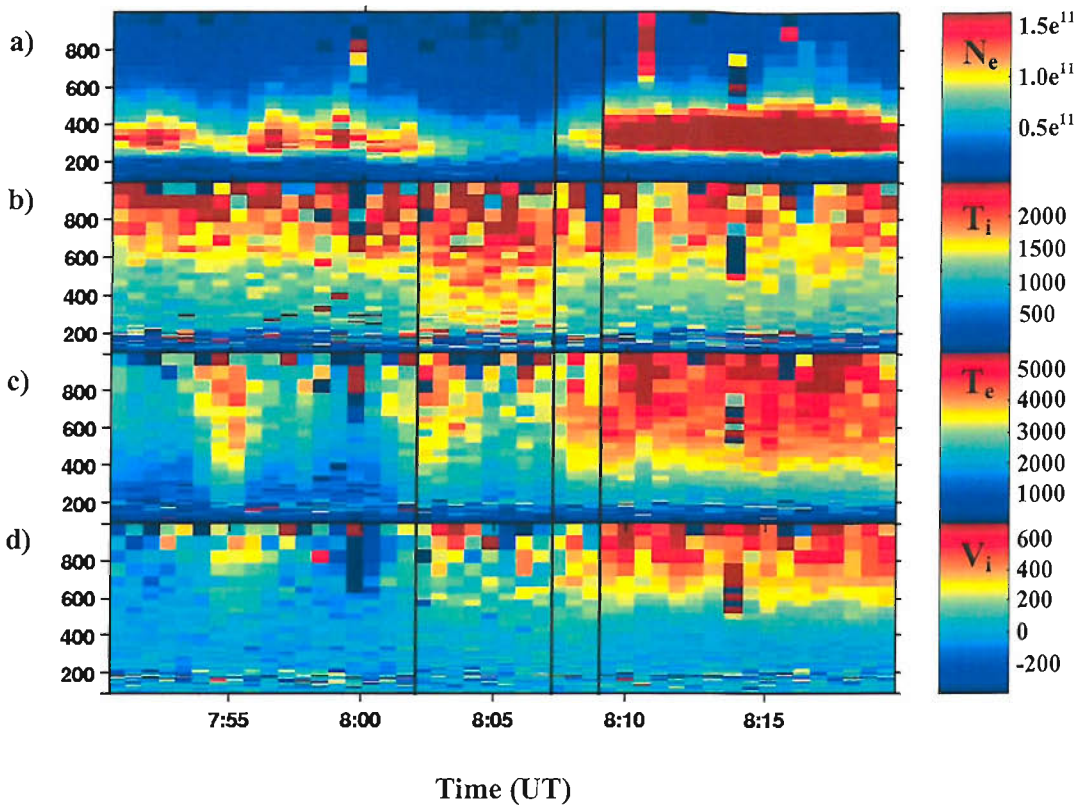

Figure 6.4 Data from the field aligned ESR radar at LYR shown in altitude-time spectrogram format. Panel ***a)*** shows the electron density (cm^{-3}) at a range of altitudes, ***b)*** shows the ion temperature (K), ***c)*** the electron temperature (K) and ***d)*** the field aligned ion velocity (kms^{-1}) over the period of interest. Each parameter is colour coded as a function altitude and time.

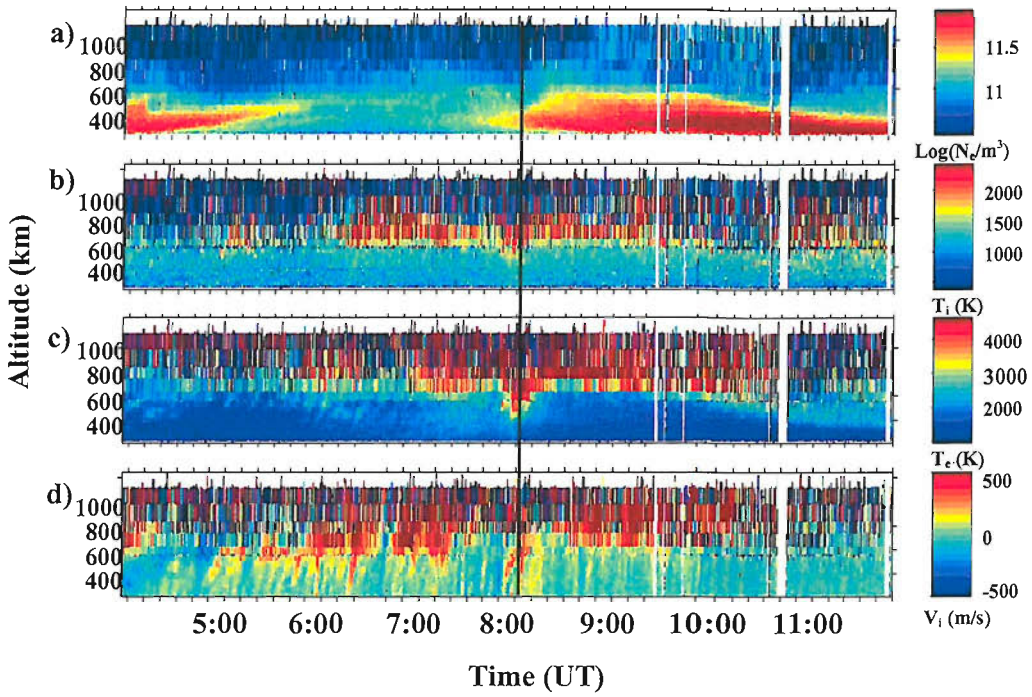

Figure 6.5 EISCAT VHF data for several hours around 8 UT in altitude-time spectrogram format. Panel ***a)*** shows the electron density (cm^{-3}), ***b)*** the ion temperature (K) ***c)*** the electron temperature (K) and ***d)*** the line-of-sight ion velocity (kms^{-1}) which is seen to vary in an oscillatory manner both before and after the 8 UT event. The black line marks the time at which ion and electron temperature enhancements were observed just after 8 UT. Each parameter is colour-coded as a function of altitude and time: because the VHF beam is at low elevations to the north, the altitude scale also covers a range of invariant latitudes: for the closest range gate at 200 km altitude the invariant latitude is $\Lambda = 70.7°$, whereas for the furthest range gate at 1200 km altitude, the invariant latitude is $\Lambda = 78.5°$.

6.1.3 Magnetic Observations

The IMAGE magnetometer network covers a large range of latitudes, thereby providing a way of discerning the latitudinal variation of the response to an interplanetary structure impacting the magnetosphere. In the study presented here, this provides a valuable link between the instruments at Longyearbyen and the VHF radar. The five high-latitude stations of the IMAGE network (NAL, LYR, HOR, HOP and BJN) are close to the VHF radar beam and thus often observe the same features that are detected by the radar. Figure 2.1 show the positions of the IMAGE stations, relative to the VHF radar beam.

Figure 6.5 demonstrates that oscillations were seen by the VHF radar before the impact of the pressure pulse and remained present for a few hours afterwards. Power spectral analysis presented in Section 6.2.2 of this chapter (Figures 6.19a and 6.19c) shows that the same is true of the IMAGE magnetometer data. Further evidence of these pre-existing field-line oscillations are seen by the lower latitude east and west chain stations in Greenland which, as well as registering the initial impact of the pressure pulse, also observe the long-lived resonances seen by the IMAGE network.

Analysis of the magnetometer records from both the IMAGE and Greenland chains also reveals an isolated magnetic field variation, bipolar in structure, typical of a TCV. Figure 6.6 shows the magnetometer traces from the five highest latitude IMAGE stations. Figure 6.7 shows the magnetometer traces from four stations on the west coast of Greenland.

This chapter will present detailed analysis of data from stations with the larger longitudinal separation of these two networks. This analysis revealed a triple vortical structure travelling westwards across the morning sector. A subsequent investigation (Section 6.2.2) of the MM210 magnetometers that lie to the east of the IMAGE chain also revealed a second set of vortices travelling eastwards around the afternoon sector.

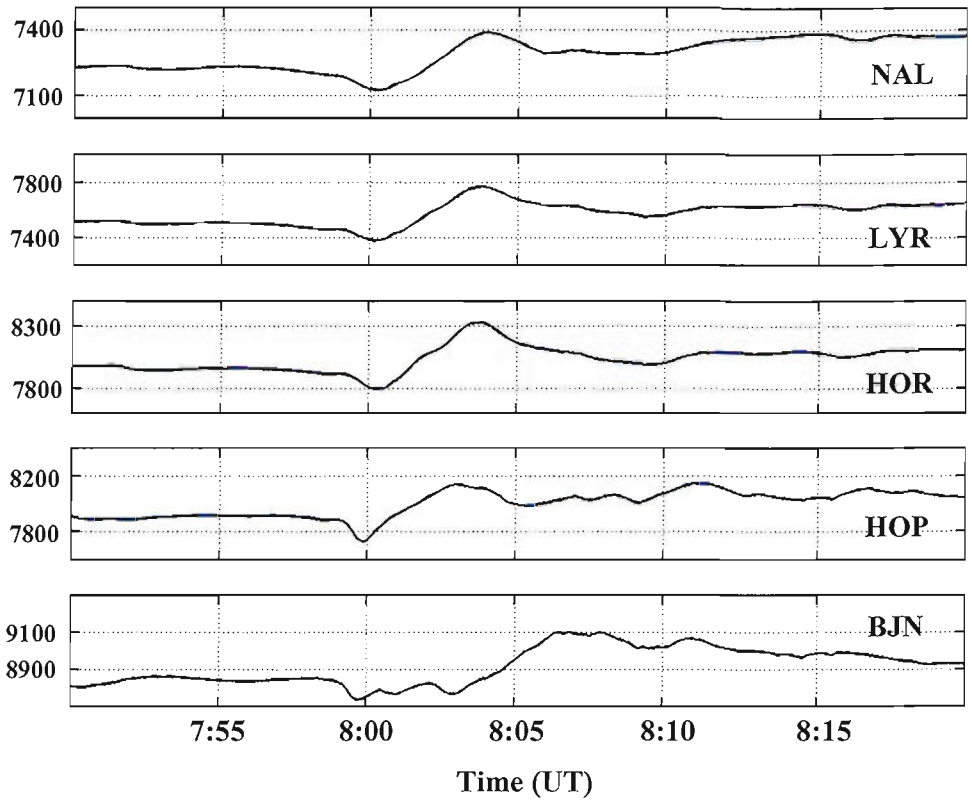

Figure 6.6 The northward (B_N) component (nT) of the magnetic traces from the five highest IMAGE magnetometer stations. The main bipolar signature is clearly apparent starting just before 8 UT.

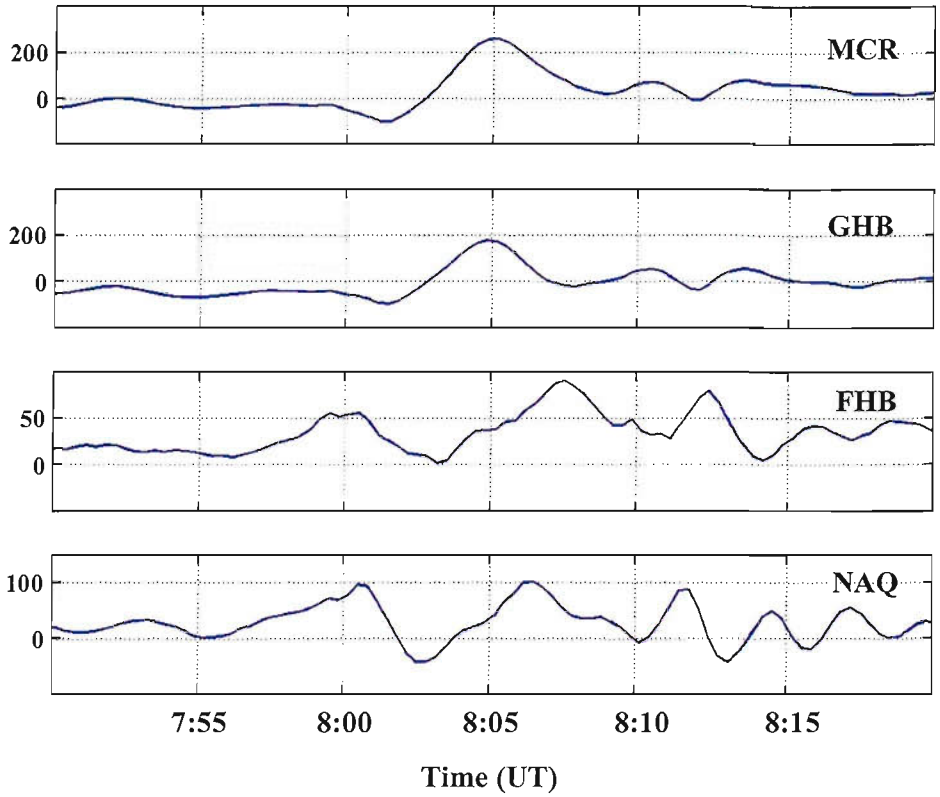

Figure 6.7 The northward (B_N) component (nT) of the magnetic traces from the four west coast Greenland magnetometer stations. The main bipolar signature is clearly apparent starting just before 8 UT.

The low latitude magnetometer of Hermanus (HER) has a latitude of -34.3° and longitudinal position of 19.2°. The KOU magnetometer has a altitude of 5.1° and longitudinal position of 302.7°. The fast mode waves seen by GOES-8 in geosynchronous orbit propagate across the magnetospheric magnetic field lines, such that their effects reach the low-latitude ionosphere. Sibeck [1990] reported examples of pressure pulse events in which both equatorial and mid-latitude ground magnetograms displayed simple transient step functions in the H-component. Such an impulsive increase is evident in both the Hermanus and KOU data shown in Figure 6.8a and 6.8b respectively.

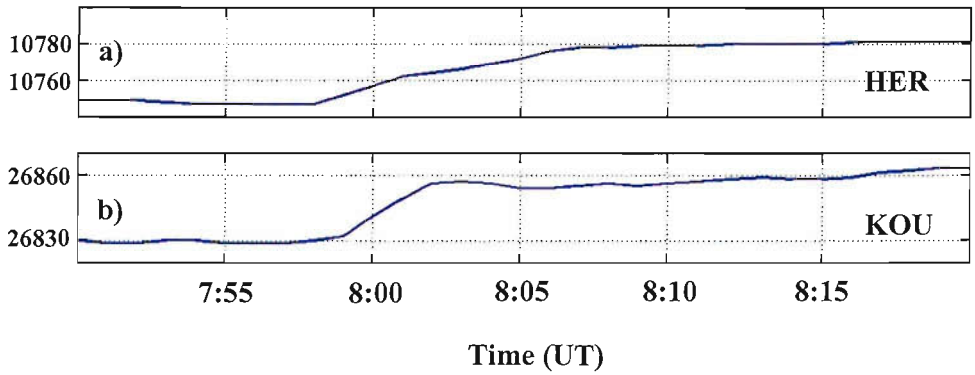

Figure 6.8 The northward (B_N) magnetic trace for the low-latitude ***a)*** Hermanus and ***b)*** KOU magnetometers.

6.2 *Analysis of the Combined Datasets*

The upstream solar wind and IMF observations during this event reveal a significant increase in the solar wind pressure accompanied by a brief turning southwards of the B_z component of the IMF (see Section 4.1.2). In this chapter we attempt to use a low pass filter to allow us to separate, at least to some extent, the slow convection variations (low frequency) from the higher frequency pressure pulse effects, and hence to examine their individual impact on the magnetosphere/ionosphere system. The properties of the filter are given in Appendix C. The cut-off frequency of the filter was varied to study the effect on separation of the two sets of features, but was found to be most effective at 15 min., as expected from the Cowley-Lockwood [1992] flow excitation theory which predicts a response time for the whole convection pattern of this order, consistent with observations [Todd et al., 1988, Etemadi et al, 1988; Kahn and Cowley, 1999].

6.2.1 *Convection Effects*

Figure 6.9 shows both filtered and unfiltered data from the five highest latitude IMAGE magnetometer stations. The blue line is the unfiltered data, while the red line is the low frequency data separated by the filter as discussed in the previous section. The low frequency data vary over periods greater than 900 seconds. This is thought to be the increase in flow associated with the onset of dayside reconnection. Figure 6.9 shows that the bipolar signature evident in the unfiltered data and commonly associated with pressure pulse effects is removed in the low frequency data which shows a slower rise commencing at the time of the bipolar signature. The residual flows are also vortical at the IMAGE chain, albeit very slightly, with a brief, weak negative B_N deflection, followed by a long, strong positive one. To determine the origin of the convection flows that cause this slowly-varying feature, the Lockwood and Morley convection model [2003] is used to emulate the ionospheric flows triggered by the onset of dayside reconnection. The model is a numerical implementation of the Cowley-Lockwood

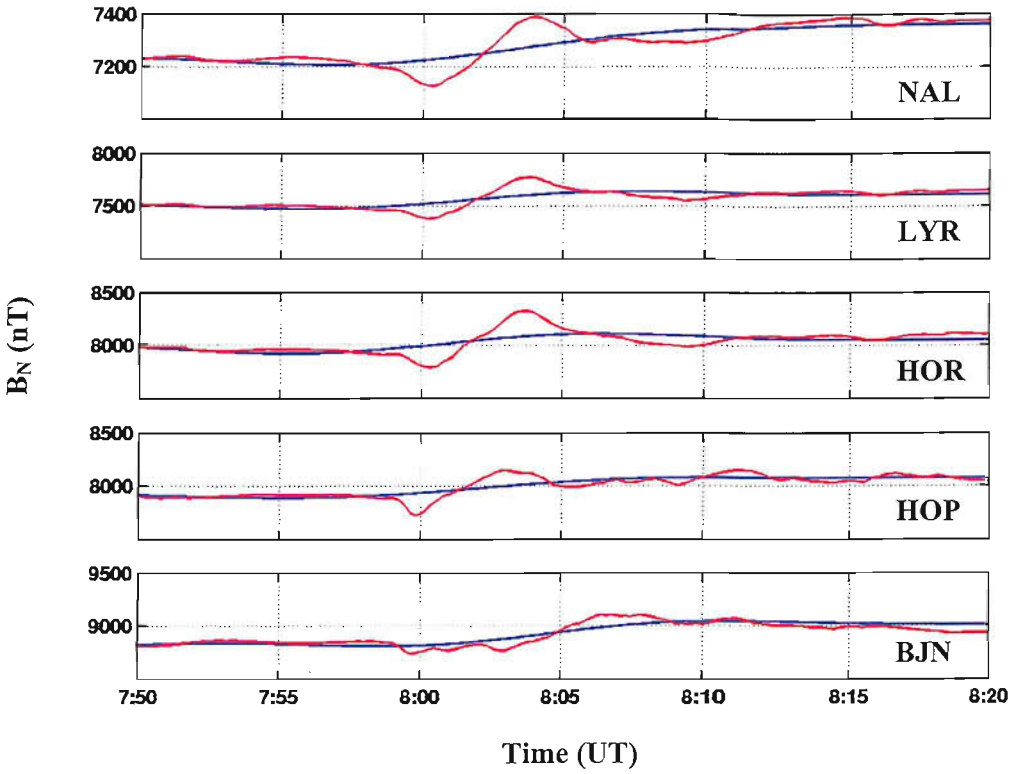

Figure 6.9 Filtered and unfiltered data from the 5 highest latitude IMAGE magnetometer stations. The red line represents the unfiltered data, while the blue line represents the low frequency filtered data.

conceptual model [1992] and was discussed in Section 3.2. It was developed to predict quantitatively the ionospheric convection in response to time-dependent magnetopause reconnection. The main input to the model is the reconnection rate variation and here the lagged ACE IMF data are used to generate the model flow patterns in response to a B_z southward turning.

Figure 6.10 shows the evolution of the derived convection flow patterns in response to the upstream IMF clock angle. The switch in direction of the IMF from northward to southward causes an enhancement in the open flux production at the magnetopause, that open flux is then transported into the tail lobes by the action of the solar wind. The addition of open flux to the polar cap causes the open-closed boundary (OCB) to expand towards a new equilibrium position at lower latitudes at all local times. The model calculates the convection streamlines (equipotentials) throughout the polar cap associated with that expansion from the distribution of potential around the OCB.

Figure 6.10 shows a series of plots separated by 5 min and spanning a 25 min interval around the time of the southward turning. The positions of the three magnetometer chains are shown by coloured dots: IMAGE (red), Greenland (blue) and MM210 (green). The ionospheric projection of the dayside reconnection X-line is represented by a thick black line and lies dawnward of magnetic noon, centred at 10 MLT and extending 3 MLT in both directions. The "adiaroic" OCB segments are represented by the thick grey lines and the thinner grey lines are the flow streamlines showing the motion of plasma and frozen-in field lines as they progress through the convection cycle.

Figure 6.10 shows that at 7:55 UT, 2 mins before the effects of the southward turning impinge on the ionosphere. The initial OCB location as a function of MLT, input into the model, is chosen to ensure flow directions are as seen by the magnetometers, and that boundaries cross the sites at the times observed. These initial conditions ensure that the Greenland stations all lie on open field lines, with the most southern station (NAQ) lying close to the OCB. On the duskside, the two MM210 magnetometers were situated to the south of the OCB, as were three of the five magnetometers (HOR, HOP and BJN) of the IMAGE chain. The

relative positions of these magnetometer stations with respect to the OCB remained the same throughout the 25 min, with the exception of the two highest latitude IMAGE stations of NAL and LYR. At 7:57 UT the OCB migrated equatorward, due to the onset of dayside reconnection, causing NAL to pass from closed field lines onto open field lines. This expansion to lower latitudes brought LYR into close proximity to the reconnecting boundary, where it remained for the rest of the 25 mins. This is consistent with the OCB location inferred from the optical observations described in Section 6.1.

Figure 6.12, Figure 6.13 and Figure 6.14 show the predicted and observed variations in the northward magnetic field component, associated with the convection flows, at IMAGE, Greenland and MM210 chains respectively. These predictions assume that the spatial distribution of ionospheric conductivity is uniform. As the convection vortices expanded over the stations, the model quantitatively predicts the convection flows at each magnetometer. The model output is given by the green line, the low frequency filtered convection data by the blue line and the unfiltered data by the red line.

As the cells of the convection patterns expand over the stations, they cause an increase in magnetic field strength which depends on their positions relative to the OCB. However it is evident from Figures 6.12, 6.13 and 6.14 that some discrepancies do exist between the model and the data. Figure 6.12 shows that at IMAGE, the model progressively overestimates the strength of the convection flows with decreasing latitude. The reasons for this could be the proximity of the Region 2 (R2) current and/or the position of the zero potential line with respect to the lower latitude stations. In the model the R2 current system, found at the equatorial edge of the auroral oval, is used to confine the convection poleward of a fixed latitude set arbitrarily. This means that at progressively lower latitudes, the modelled convection flows become increasingly influenced by the R2 currents. In reality the latitudinal position of the R2 current would not be constant but vary depending on auroral activity. During periods of strongly southwards IMF, as in this case, the R2 current would expand equatorward, away from the magnetometer stations, and would therefore have less of an influence on convection flows detected by them. This would explain why the actual current flows in Figure 6.12

are weaker than the modelled current flows and why the modelled current flows strength increases with decreasing latitude.

The model assumes that the convection flows are symmetric about the centre of the X-line where the potential is zero. In this case, the X-line is centred at 10 MLT, in the sector favoured by positive B_y IMF as discussed in Section 3.2. If the actual zero potential were to be closer to /further away from that in the model (which is the centre of the merging gap), the flows and magnetic deflections would be, respectively, stronger/weaker at IMAGE. Indeed the SuperDARN observations (discussed below) suggest that the zero potential contour may move considerably in MLT during the period of interest. However, no attempt has been made here to improve the fit by adjusting these additional parameters; the Lockwood and Morley model has sufficient free parameters that little would be learned with any certainty from obtaining a good fit in this manner. What can be seen from Figures 6.12-6.14 is that both the main features and the character of the slowly-varying filtered component of the data are plausibly reproduced by the model.

The low-latitude Greenland magnetometer stations and the two MM210 stations are situated close to adiaroic OCB segments, and so are not complicated by localised effects around the dayside reconnection X-line. Figure 6.13 and Figure 6.14, however, still show slight discrepancies in the strength of the convection flows generated by the model (green) and the low frequency data (blue). These discrepancies could be due to the assumption in the model that the conductivity is independent of position. In reality the conductivity is enhanced by regions of strong precipitation, which would be expected during periods of southwards IMF. Such a limitation in the model could explain the inconsistencies in the magnitude of the convection flows when comparing the modelled and actual data of Figure 6.13 and Figure 6.14. This could also be another factor contributing to the discrepancies of Figure 6.12.

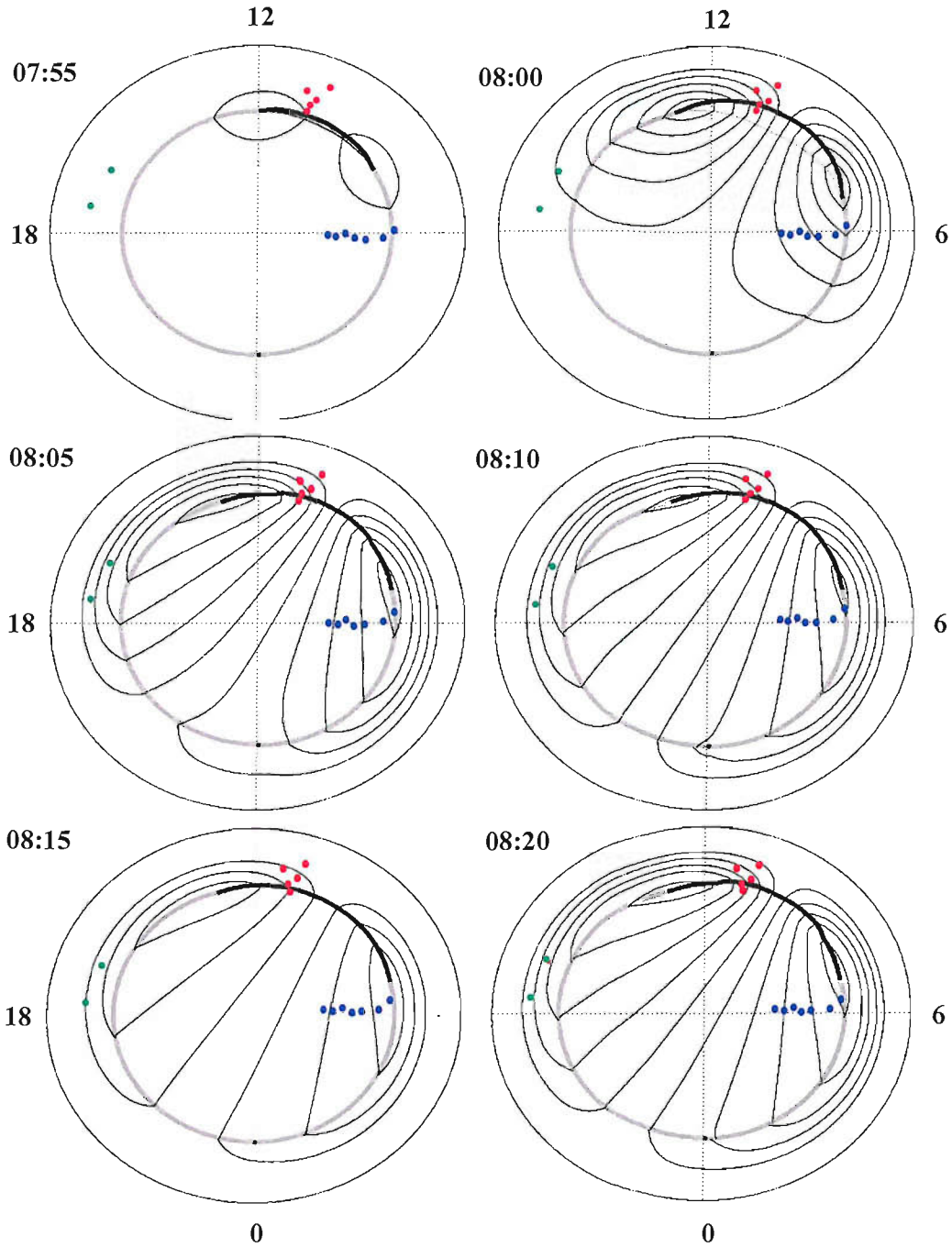

Figure 6.10 The evolution of the convection flows in response to the upstream IMF clock angle. The ionospheric projections of the dayside and tail reconnection X-lines are shown as thick black lines and the "adiaroic" (non-reconnecting) open-closed boundary segments by thinner lines. The positions of the three magnetometer chains are shown by coloured dots: IMAGE (red), Greenland (blue) and MM210 (green). The patterns are 5 mins apart and are for 7:55 - 8:20.

Due to the lack of satellite data, the initial model conditions cannot be set to match observations, instead the location and extent of the X-line and the latitude of the OCB at the start of the model run were chosen so that the time at which the convection vortices expanded over the magnetometer stations gave as good a fit as possible to the low frequency data (in particular, the times of the reversal of ΔB_N from weakly negative to positive as the centre of the convection cells passes through the MLT of the station). Any difference between the time at which the effects of dayside reconnection are apparent in the model and the low frequency data is almost certainly due to the placement of the X-line, rather than reflective of the calculated time at which the southward turning impinges on the ionosphere. The SuperDARN mapped potential plots for the interval are shown in Figure 6.11. Note that these data have not been filtered and so will contain both the effect of the southward IMF and the effect of any transient filamentary field-aligned induced by the pressure pulse. Considering the mapped potential procedure, the latter are likely to be heavily damped but may have introduced some vortical structures into the derived convection patterns. Comparing these plots with Figure 6.10, reveals the convection enhancement and decay predicted by the model; the major difference in this respect is at 08:20 when the model is predicting the start of a second rise in convection, whereas the SuperDARN data reveal a continuing decline. The other major difference was alluded to above, namely the motion of the zero-potential contour (which separates the dawn and dusk cells). The mapped potential SuperDARN plots indicate that this was in the afternoon sector originally (near 15MLT), but moved west to enter the morning sector between 08:02 and 08:04 UT, being at 10-11 MLT thereafter. It must be remembered that the mapped potential plots are produced by fitting a model convection pattern to the data and the model is driven by the upstream IMF data. Thus the change in the mapped zero potential contour is undoubtedly due to the change in the IMF B_y component from negative (at lagged time 07:55) to positive (after lagged time 08:01). The key question is whether the shift is driven by the radar flow observations or by the fitted flow model. It is therefore instructive to note that at 08:01 the IMF B_y polarity has already shifted but the zero potential contour is still in the afternoon sector.

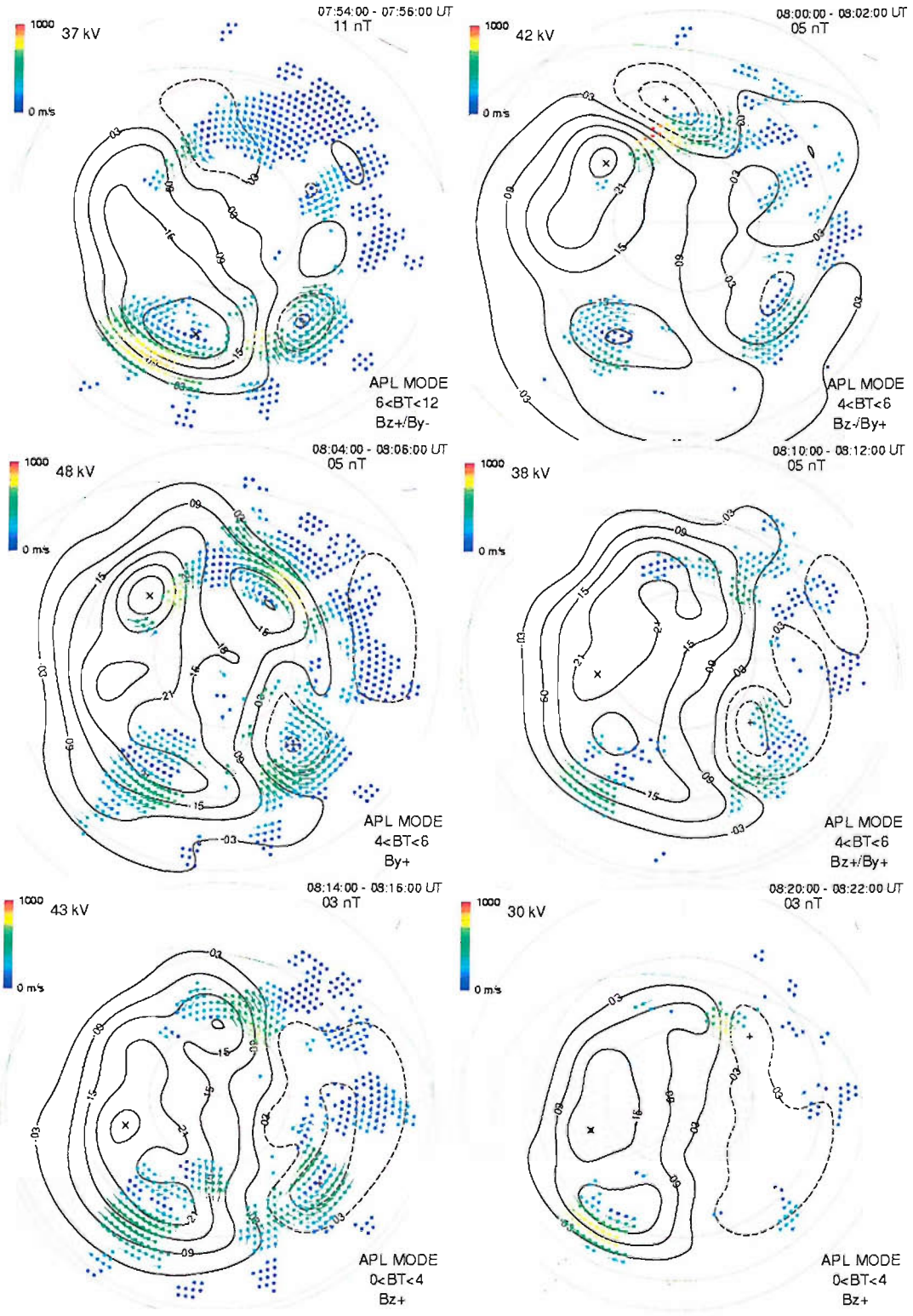
07:54:00 - 07:56:00 UT
11 nT
1000
37 kV
0 m/s
APL MODE
6<BT<12
Bz+/By-
08:00:00 - 08:02:00 UT
05 nT
1000
42 kV
0 m/s
APL MODE
4<BT<6
Bz-/By+
08:04:00 - 08:06:00 UT
05 nT
1000
48 kV
0 m/s
APL MODE
4<BT<6
By+
08:10:00 - 08:12:00 UT
05 nT
1000
38 kV
0 m/s
APL MODE
4<BT<6
Bz+/By+
08:14:00 - 08:16:00 UT
03 nT
1000
43 kV
0 m/s
APL MODE
0<BT<4
Bz+
08:20:00 - 08:22:00 UT
03 nT
1000
30 kV
0 m/s
APL MODE
0<BT<4
Bz+

Figure 6.11. Mapped potential plots in the MLT-invariant latitude frame (with noon at the top), derived from the data from SuperDARN radars in the northern hemisphere during this event. The equipotential contours are from a model that is driven by the upstream IMF orientation and then fitted to the line-of-sight velocities observed by the radars. The vectors are also from the model fit and so are based on the observed line-of-sight components and the model fit to the beam-perpendicular components. Vectors are colour coded according to their magnitude. *(Plots courtesy of Dr. G. Provan, Leicester University).*

This strongly suggests that the effect is real and not just a consequence of the potential mapping procedure. Thus motions in the zero potential contour are likely to be the main cause of the discrepancies between the modelled and observed magnetic deflections at IMAGE (Figure 6.12).

With these caveats in mind, the overall good agreement between the model and the low frequency data at all three magnetometer convection flow variations illustrated in Figure 6.12, 6.13 and 6.14 therefore support filtering as a way of separating the low frequency convection data from the high frequency pressure pulse effects. However, the longitudinal motions of the dayside X-line in MLT, as detected by the SuperDARN radars but not included in the model, limit the extent to which detailed comparisons can be made.

6.2.2 Pressure Pulses Effects

The previous section provides evidence that although the convection flows produced by dayside reconnection following a southward excursion of the IMF dominate the magnetometer data, this longer period effect can be removed by filtering. The shorter period effects of the pressure pulse are then clearly visible, and can be used to investigate the subsequent evolution of ionospheric flows generated by its arrival. It was noted above that the Travelling Convection Vortices (TCVs) generated were superimposed on pre-existing oscillations in the magnetic field, measured as currents by ground magnetometers and as ionospheric flows by the EISCAT VHF radar. A study of these oscillations is set out later in this section.

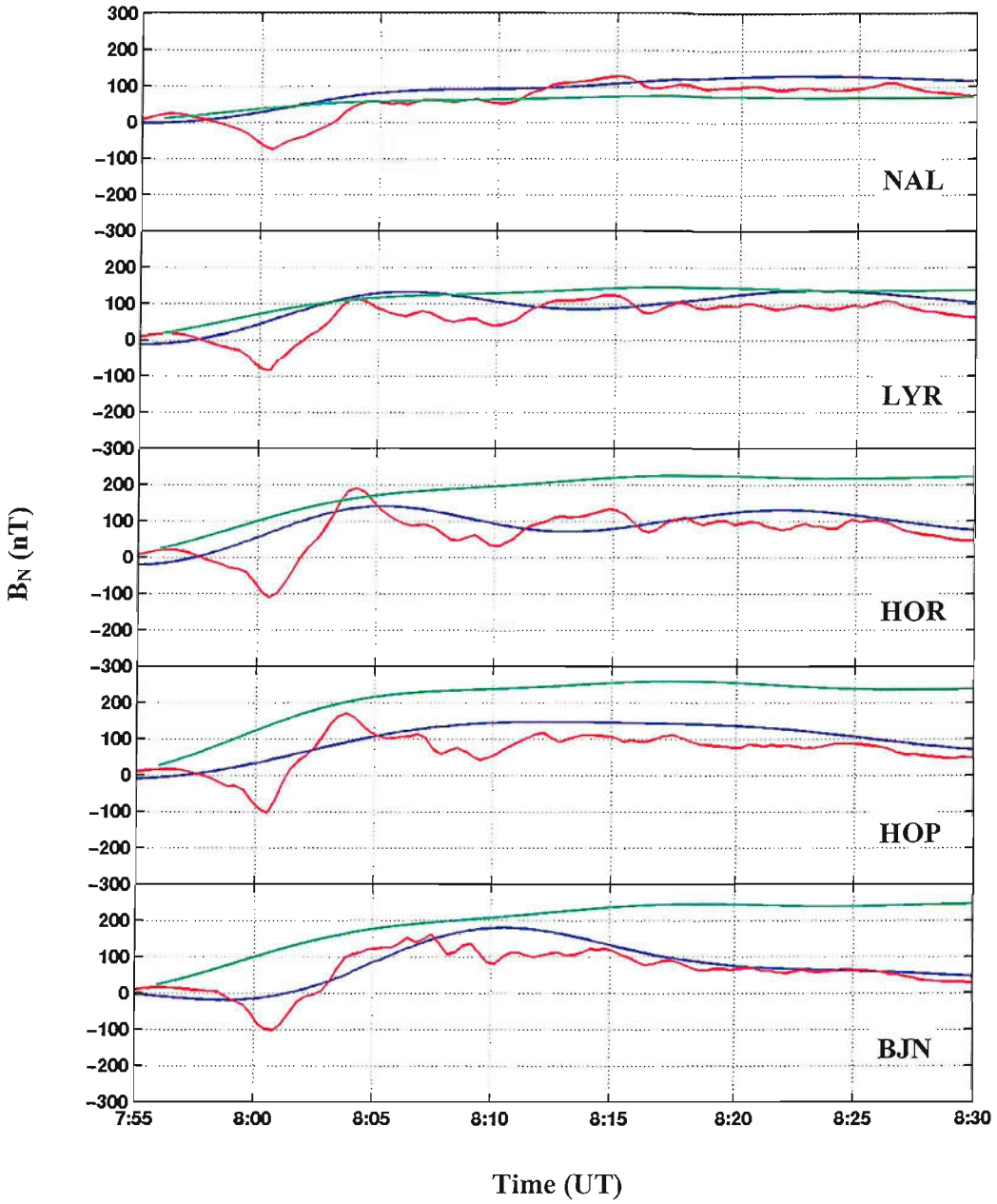

Figure 6.12 The variations in the magnetic field strength associated with the convection flows for the 5 highest latitude IMAGE stations. Initial conditions were chosen so that the model output represented by the green line was as good a match as possible to the low frequency filtered magnetometer data represented by the blue line. The red line represents the unfiltered data.

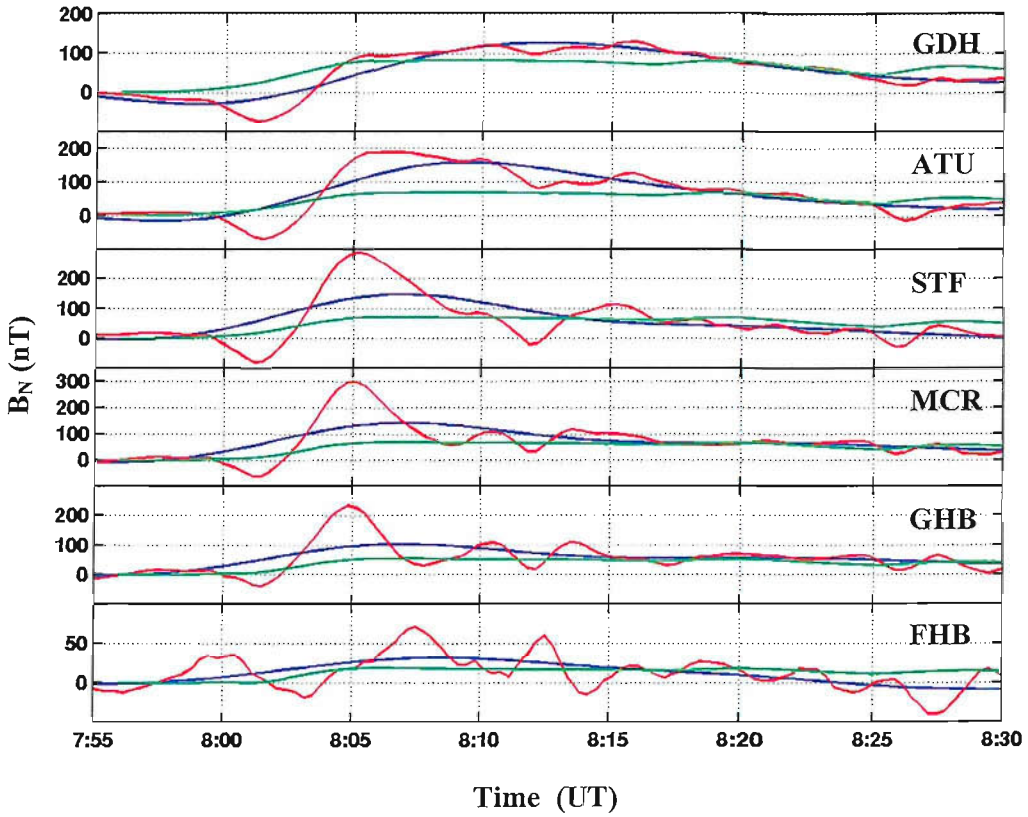

Figure 6.13 The variations in the magnetic field strength associated with the convection flows for six of the Greenland magnetometer stations. The model output is represented by the green line, the low pass filtered data by the blue line. The red line represents the unfiltered data.

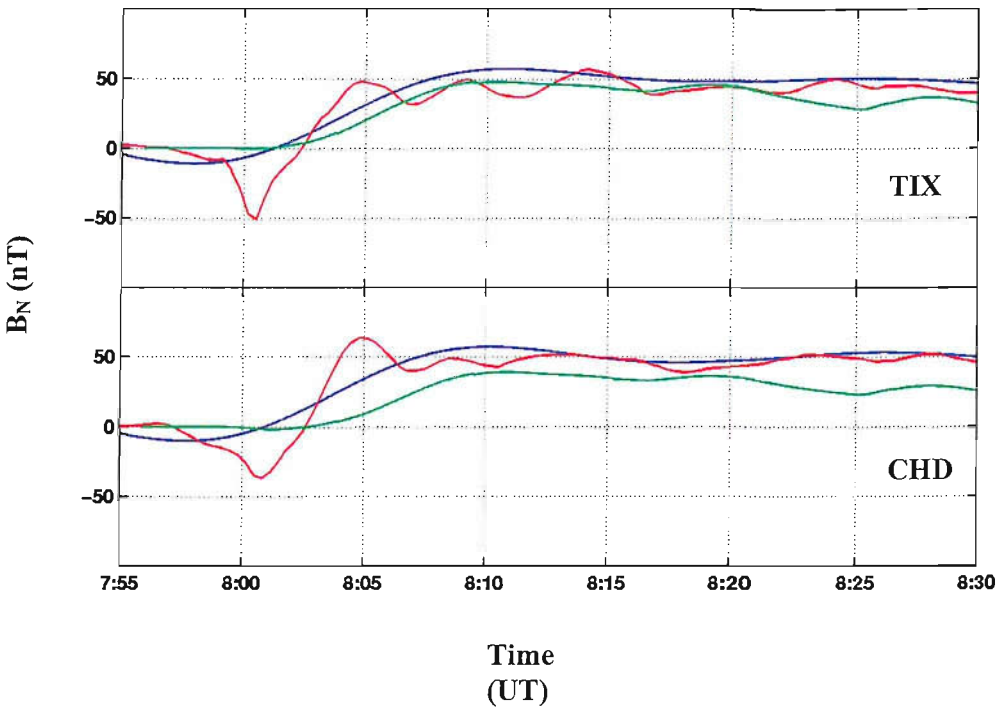

Figure 6.14 The variations in the magnetic field strength associated with the convection flows for the two MM210 magnetometer stations. The model output is represented by the green line, the low pass filtered data by the blue line. The red line represents the pre-filtered data.

Figure 6.15 shows a stacked plot of the B_N component data for the ten highest-latitude stations of the IMAGE array, with the highest latitude station at the top. This data has been filtered to remove longer periods, as discussed in Section 6.2.1. The four highest latitude stations observed a negative-to-positive deflection in the magnetic field B_N component, accompanied by a negative deflection in the B_E component (not shown). The five lowest latitude stations measure a reversed positive-to-negative deflection in the B_N component, but the same negative excursion in B_E. All ten stations show an approximate 90° phase shift between B_N and B_E. The bipolar variation in B_N accompanied by a single excursion in B_E is consistent with a pair of oppositely directed currents passing over the stations. The 90° phase difference in both components is the signature of the ionospheric vortical flows associated with these field-aligned currents [Zesta et al, 2002].

The orientation of the upstream pressure front, shown in Figure 4.11, means that it hits the duskside magnetopause at approximately 13 MLT. In response, a set of TCVs are expected to propagate in a westward direction away from the point of impact, towards the IMAGE magnetometer array situated at 11:30 MLT. (A matching set is also expected to propagate eastward into the afternoon sector). The direction of propagation of this chain of vortices is confirmed by the times of arrival of the signature at each of the IMAGE stations. The data presented in Figure 6.15 reveal that the TCV signature is first seen at the station of Hopen (HOP), situated to the east of the other stations at a longitude of 115°.

Figure 6.15 also reveals the latitude along which the centre of the vortical flows travel. This is marked by a reversal in polarisation between the stations of HOP and KEV, which shows that the path of the centre of the field-aligned current associated with the TCV lies between magnetic latitudes of 73° and 66°. Between these two stations is BJN at 71.5°, which has the maximum peak to peak disturbance in the horizontal field magnitude of 300 nT, suggesting that the centre of the vortex passes closest to this station. At the start of the event at 7:55 UT, the BJN B_N component trace follows the magnetic variations of the stations situated at higher latitudes. At about 8 UT, it switches to more closely resemble the traces

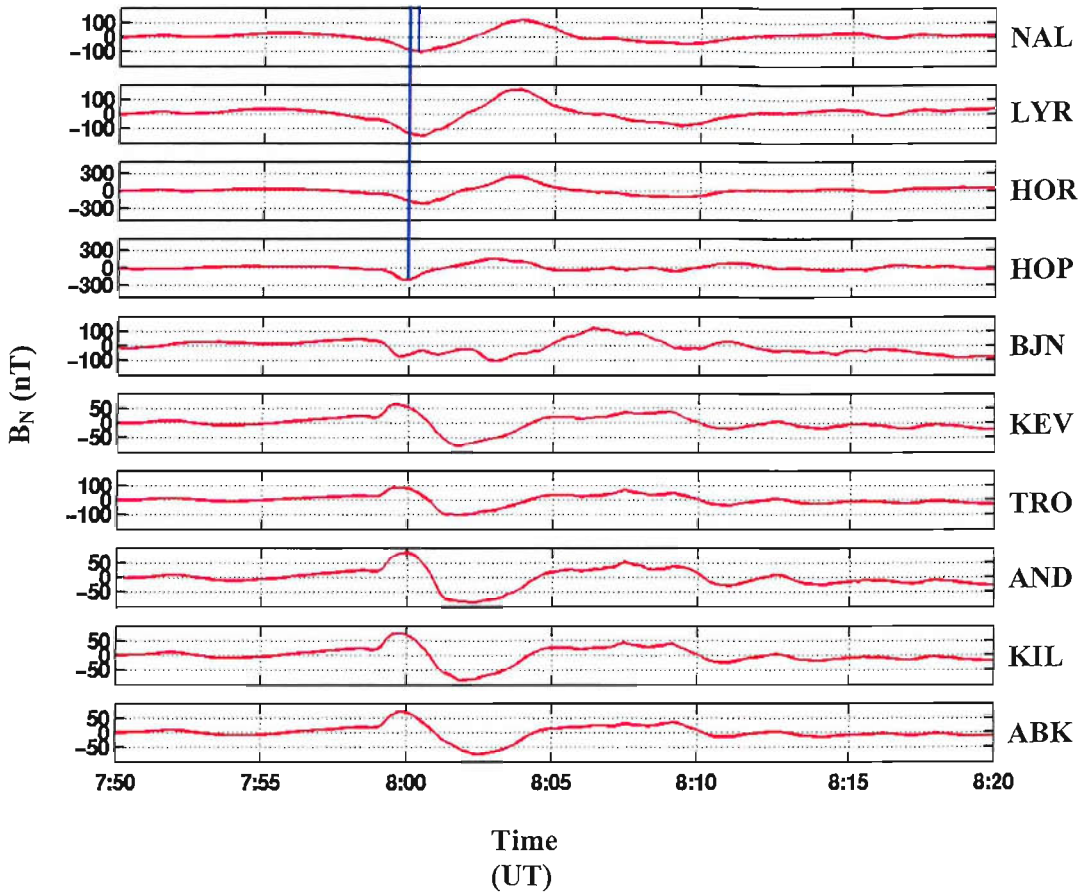

Figure 6.15 A stacked plot of B_N component variations observed at the ten highest-latitude stations of the IMAGE array. These data have been filtered to remove the lower frequency variations. The two vertical blue lines compare the times of the peak negative magnetic deflections at the NAL and HOP magnetometers caused by the longitudinal motion of the TCV.

of the lower latitude stations. This behaviour suggests that either the centre of the TCV passes poleward over BJN at around 8 UT, or that the line connecting the two vortices is tilted relative to the direction of motion with the centre of the leading vortex situated to the south of BJN and the centre of the trailing vortex situated to the north.

Figure 6.16 offers a way of determining the structure and motion of the vortices as employed by Friis-Christensen et al. [1988]; Glaßmeier et al. [1992] and Lühr et al. [1996]. If we assume that the ionospheric conductivity is horizontally uniform over the event, the magnetic field deflections recorded by the magnetometers are solely due to the Hall current system (Fukunishi's Theorem). This means the magnetic field vectors recorded by the magnetometers can be rotated by 90° anticlockwise to be consistent with the convection direction and speed. Without uniform conductivity this would not be the case, as regions of enhanced precipitation, expected during periods of southward IMF, would contribute to the magnetometer readings.

The sequence of vectors from each station can then be lagged to allow for the phase motion of the event so that it lines up with those from the other stations [Kunkel et. al, 1986]. Figure 6.16 shows that the application of this method produces a train of three vortices each with east-west scale lengths of ~ 2500 km moving anti-sunward with a westward phase motion of ~ 9 kms^{-1} and a southward phase motion of ~ 2 kms^{-1}. Figure 6.16 shows that the central vortex lies slightly to the south of the leading and trailing vortices and that the central vortex is considerably larger than those before and after.

Figure 6.16 gives a form of "snapshot" of the TCV as it passes over the IMAGE chain. However its evolution at other longitudes is harder to determine. Having determined the E-W and N-S velocity of the TCV as a way of explaining the temporal variations of the associated current system, data from the magnetometer chains lying to the west of IMAGE must be used to track its progression over time.

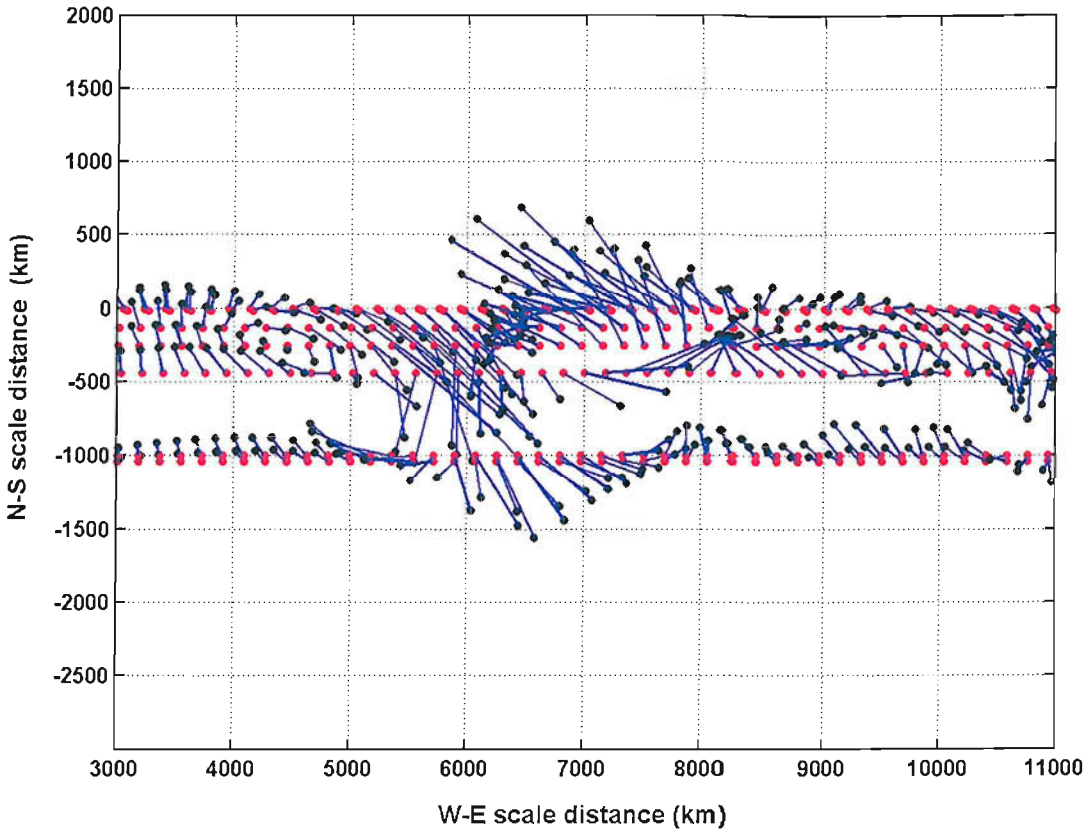

Figure 6.16 The IMAGE magnetometer data presented using the procedure developed by Friis-Christensen et al. (1988); Glaßmeier et al. (1992) and Lühr et al. (1996) in which the magnetic perturbation vectors are lagged and rotated by 90° anticlockwise (see text for details). A train of vortices with east-west scale lengths of ~ 3000 km moving anti-sunward at a westward speed of ~ 9 kms^{-1} and a southwards speed of ~ 2 kms^{-1} is revealed. The figure also provides evidence for the existence of a third vortex not evident in the Figure 6.15 time series plots. The individual blue vectors represent the convection flow direction at that particular point in a reference frame moving with the TCVs.

The Greenland magnetometer array consists of two chains of seventeen magnetometer stations situated on the east and west coasts, approximately 1000 and 2300 km to the west of IMAGE. Figure 6.17 shows the high-pass filtered B_N component magnetic traces from seven of the Greenland magnetometer stations. The east chain stations are represented by a red line, the west coast stations by a blue line. Analysis of the 20-sec resolution data revealed that the bipolar structure representing the TCV was observed in both chains. Its progression from east to west is revealed by the delay of the bipolar signature between the two chains and its latitude from the reversal in the polarity between two consecutive stations along each chain. In the eastern chain this reversal is seen between the DNB and AMK magnetometers situated at magnetic latitudes of 75° and 69° respectively. At the western chain it is seen between the stations of GHB and FHB at latitudes of 70° and 68°. The magnitude of the magnetic deflections at each of these stations provides another way of estimating the path of the TCV. Figure 6.17 shows that on the east coast, the magnitude of the B_N component at DNB is twice that of AMK suggesting that the centre of the vortices pass closer to the higher latitude station at ~ 75°. This method also reveals that at the west coast stations, the TCV passes closer to the more northerly station of GHB at a latitude of ~ 70°. It is possible to calculate the speed at which it is travelling along this line of propagation. This is done by lagging the B_E component magnetic field data of the three stations identified as lying closest to the path of the centre of the vortices: HOP, DNB and GHB of the IMAGE, Greenland east and Greenland west chains respectively. The B_E component of a TCV event is effectively the signature of the strong southward or northward Hall current between successive vortices, and is therefore a better indication of the location of the TCV structure. Lagging the B_E component traces revealed a 120 (± 15) sec time delay between HOP and DNB and a 230 (± 15) sec delay between HOP and GHB. These time delays translate into an along-path velocity of 9 (± 1) kms^{-1} between IMAGE and the east coast of Greenland, which increases to 16 (± 1) kms^{-1} in order to reach the west coast of Greenland.

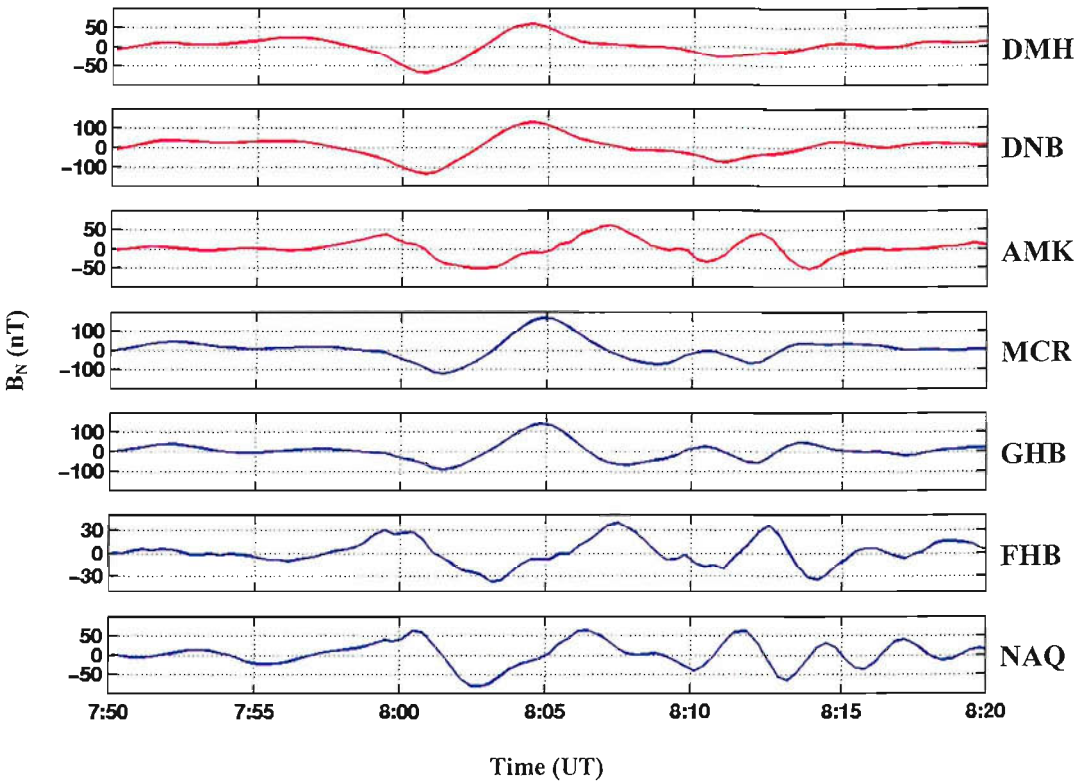

Figure 6.17 The B_N component magnetic traces from seven of the Greenland magnetometer stations. The east chain stations are represented by the red lines, the west coast stations by the blue lines. These data have been filtered to remove the lower frequency variations.

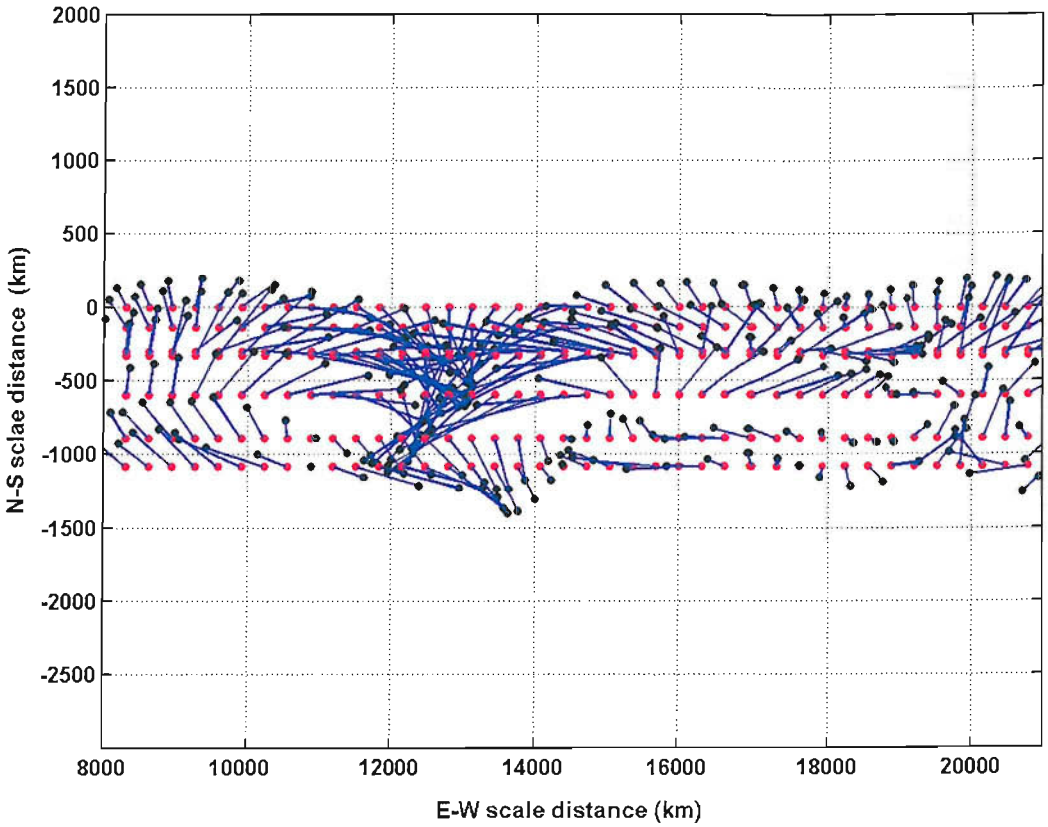

Figure 6.18 The image of the TCV derived by the same method as used in Figure 6.16 for data from the Greenland West magnetometer chain. Event phase motion with speeds of ~ 16 kms^{-1} westward and ~ 2 kms^{-1} southward are inferred.

Figure 6.18 shows the snapshot of the TCV as it passed over the west stations at Greenland, produced by rotating the magnetic perturbation values by 90° anticlockwise and lagging them according to a consistent event phase motion, as in Figure 6.16. Speeds of ~ 16 kms^{-1} west, ~ 2 kms^{-1} south, consistent with the along-path speeds calculated above, were used to shift the individual current patterns in such a way as to reproduce the vortical flow initially observed over IMAGE. Due to the increase in speed, the vortices appear to get progressively more elongated in the E-W direction over time as the TCV travels between Svalbard and Greenland. This is evident when comparing Figure 6.16 and Figure 6.18. The TCV also appears to be more twin-vortical in nature, the third vortex being less apparent in these data.

An investigation was also made of data from magnetometers lying to the east of the IMAGE chain in the afternoon sector. Figure 6.19 shows the B_N component magnetic traces from TIX and CHD of the 210MM magnetometer array situated at latitudes of 65.67° and 64.67° respectively. At 8 UT the chain is located at 18 MLT in the afternoon sector. The figure reveals that the bipolar signature is present in the data. Comparing the B_E component magnetic traces from both stations revealed that the TIX magnetometer responded 2 mins before CHD which lies 15° further to the east. This suggests that a current structure is travelling eastwards across the stations, the leading vortex rotating with the opposite sense to the corresponding vortex in the westward moving TCV seen at IMAGE and Greenland. Due to the lack of data from high latitude stations in the afternoon sector, the sense of rotation of the easterly moving TCV is a conjecture and only holds true if both TIX and CHD lie to the south of the vortical system; however, this is likely to be a valid assumption considering that both these stations are located several degrees south of typical TCV latitudes [Zesta et al., 2002].

A number of studies have shown that TCV events are frequently accompanied by resonances on field lines at lower than cusp latitudes [Potemra et al., 1996; Lühr et al., 1996]. Evidence for the existence of these field line resonances (FLRs) is present in both the magnetometer and radar data for the 26 November event.

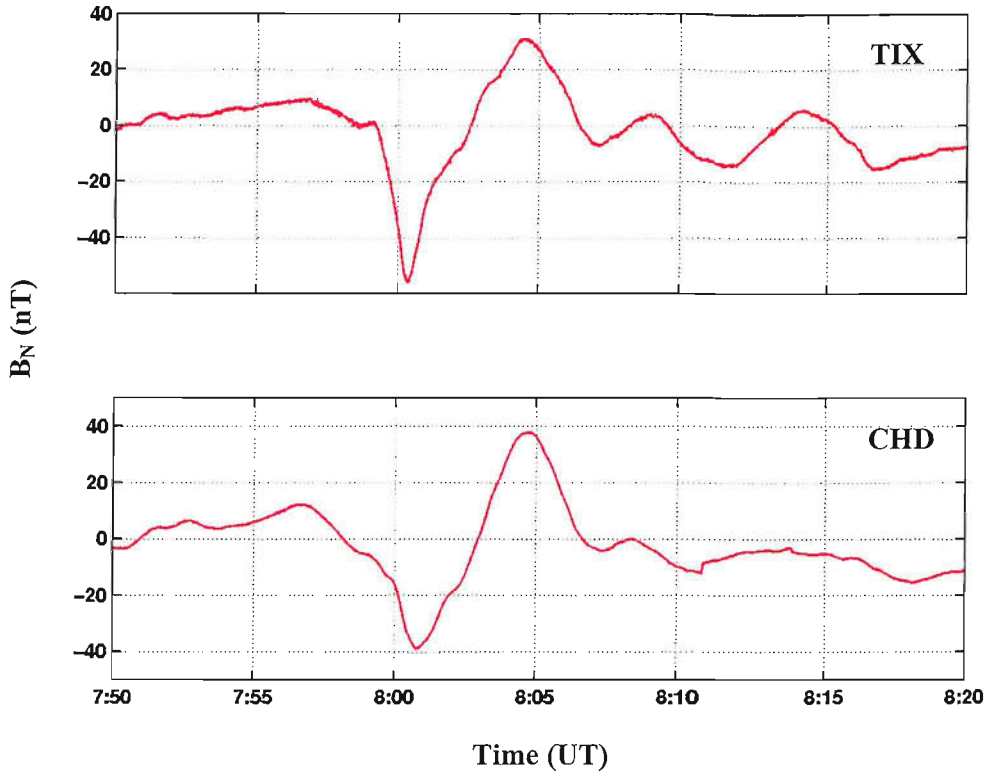

Figure 6.19 The B_N component magnetic traces from TIX and CHD of the 210MM magnetometer array. These data have been filtered to remove the lower frequency variations.

Resonances are seen to exist before the arrival of the pressure front and remain present for a few hours afterwards.

Figure 6.5 shows the VHF data for several hours around 8 UT. The lowest panel shows that the line-of-sight component of the ion velocity varies in an oscillatory manner, starting before 5 UT and continuing for several hours. The trigger for this velocity modulation is unclear and is not evident in the upstream satellite data. The effect of the pressure pulse on these oscillations can be studied by comparing the radar data with magnetometer readings from the same location. Because the radar is pointing to the north at 30° elevation, this line-of-sight component largely reflects north-south flow with only a small contribution from field-aligned flows. This north-south flow is also recorded by the magnetometers as variations in the B_E component of the magnetic traces.

Figure 6.20a shows the power spectra of the ten IMAGE magnetometers for the 30 mins preceding the arrival of the pressure front at 7:57 UT. The most distinct feature in this interval is the continuous 330 sec oscillation seen at all the stations, corresponding to a wave in the Pc5 frequency range. The strength of the oscillation peaks at BJN and decreases on moving to higher and lower latitudes. A second weaker feature is present at a period range of 200-250 sec observed at all the IMAGE stations.

Figure 6.20c shows the power spectra of the ten magnetometers for 30 mins after the arrival of the pressure pulse (08:10-08:40UT). The 330 sec feature is once more present at all the stations, but the peak amplitude of the oscillation has shifted to HOP, again decreasing at higher and lower latitudes. The second feature, evident in Figure 6.20a, is not present after the pressure front has hit. Figure 6.20b shows the power spectrum of the VHF radar data over the entire time interval covered by both Figure 6.20a and 6.20b (07:30-08:40 UT). Both the 200-300 sec and the 330 sec features are clearly present over a latitudinal range of ~ 71°-75° magnetic, corresponding to the stations of BJN, HOR and LYR that lie close to the radar beam. The station of NAL lies at an invariant latitude of

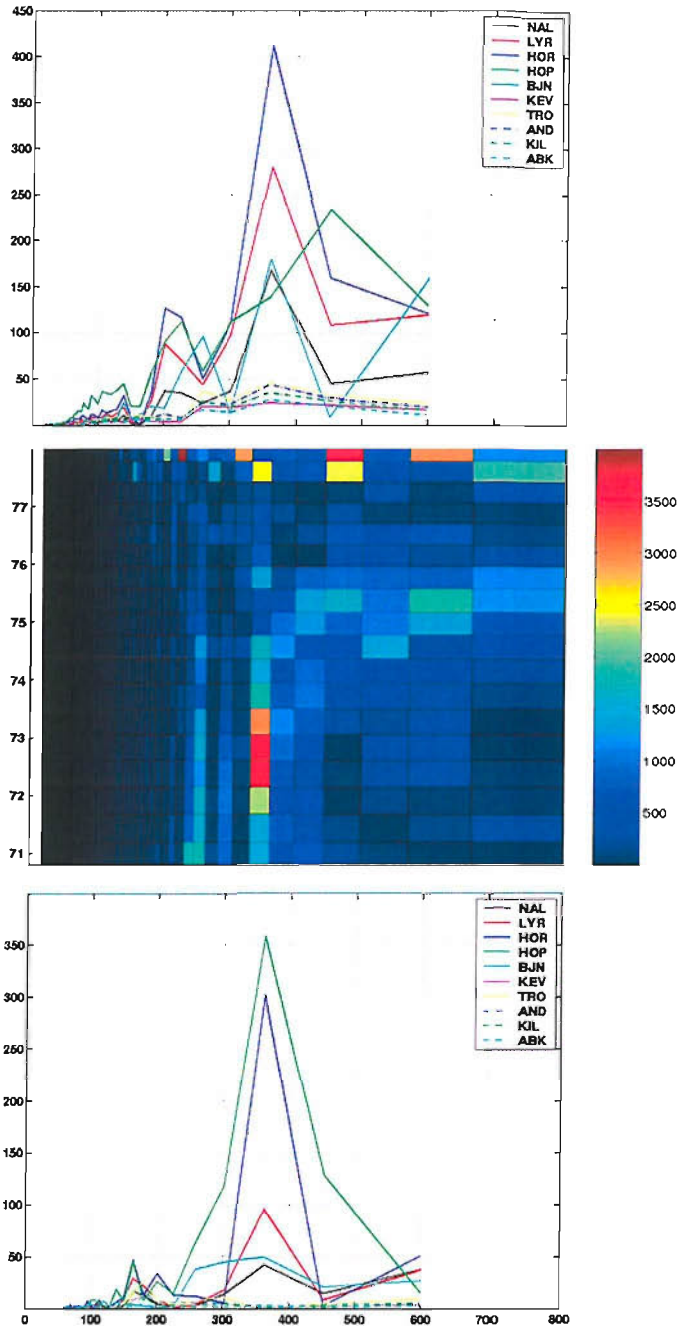

Figure 6.20 ***a)*** The power spectra of the ten magnetometers for the half an hour proceeding the arrival of the pressure front at 8 UT. The most distinct feature in this interval is the continuous 5.5-minute oscillation seen at all the stations, corresponding to a wave in the Pc5 frequency range. There is also a weaker resonance feature at around 200 sec. ***b)*** The power spectrum of the VHF radar data over time interval of 7:30 - 8:40 UT. The resonant features are clearly present over a latitudinal range of ~ 71°-75° magnetic, corresponding to the stations of BJN, HOR and LYR that lie close to the radar beam. ***c)*** The power spectra of the ten magnetometers for the time interval of

8:10 - 8:40 UT. The high period resonance is still evident although the power of the lower period resonance has decreased.

75.25°, slightly north of the feature, supporting the model findings of Section 6.2.1 that proposed that NAL lies poleward of the OCB for most of this time period.

6.3 Discussion

Several ground-based instruments and satellite measurements have been used to separate the effects of a simultaneous pressure front and a southward turning of the IMF co-incident on the magnetosphere/ionosphere system. The ground-based instruments were in an excellent position to measure the effects of the pressure pulse near noon and to measure the passage of the OCB over them due to dayside reconnection. The evolution of the pattern of ionospheric convection in response to reconnection and the formation of a field-aligned current system due to the impact of the pressure pulse were both found to contribute to a bipolar ionospheric signature observed in the magnetic recordings of the IMAGE magnetometer array, but the predominant bi-polar feature was associated with the pressure pulse. The low-pass filtered data reveal magnetic deflections that are broadly consistent with the predictions of a convection model based on the IMF clock angle. The agreement is far from perfect, which is to be expected considering the simplified inputs to the model (in particular that the merging gap is at a fixed MLT and does not move during the event). That the overall trends and character of the model output and the filtered data are similar strongly suggests that the low-pass filter has isolated the effects of the reconnection pulse caused by the swing of the IMF to southward. Removing these slower variations with a high-pass filter with the same frequency cut-off has been found to help to isolate the pressure pulse effects from the reconnection effects.

As discussed in the introduction to this chapter, the solar wind pressure front impacts on the bow shock, the energy of which is converted into a fast (HM) compressional wave that propagates across the magnetosheath. Upon reaching the magnetopause, the magnetosheath pressure variations drive magnetopause motion and launch compressional Alfvén waves into the magnetosphere. The ionospheric effects of this wave propagation are first observed by magnetometers at equatorial latitudes. The compressional waves observed by GOES-8 in geosynchronous orbit propagate inward across the magnetic field lines to the equatorial ionosphere where the Hermanus magnetometer is situated (19.2°S, 124.4° E). At high latitudes, it is expected that the waves couple and mode-convert into shear Alfvén

waves at the point where the wave frequency matches the shear mode eigenfrequency of the field line [Lysak et al., 1994]. Usually this establishes a short-lived resonance region inside the magnetopause; however, in this case, the VHF radar and magnetometer data show that it causes an enhancement in power of a resonance region already established there. We reach this conclusion from spectral analysis of the high latitude IMAGE magnetometer traces displayed in Figure 6.20a and 6.20c, which show the existence of a 330 sec resonance feature both before and after the arrival of the pressure front at 7:57 UT. The strength of this resonant oscillation peaks at a magnetic latitude between 71.5° (BJN) and 73° (HOP), decreasing away at lower and higher latitudes. This finding is supported by the VHF radar data in Figure 6.20b which shows the 330 sec feature clearly present over a magnetic latitudinal range of 71° -75°, peaking at around 72° – 73°.

Magnetohydrodynamic modelling of the effects of a pressure front, have predicted the formation of convection vortices at locations where these field line resonances occur, suggesting that TCVs are solitary enhancements of the pre-existing oscillations. This theory is supported by the IMAGE magnetometers which observed two trains of oppositely directed field-aligned currents forming at a latitude matching that of the resonance region, and propagating tailward across the morning and afternoon sector. The structure of the convection vortices associated with these field-aligned currents is closely tied to the wavelength of the field line oscillations. This is revealed by the oscillations seen in the optical data at LYR as well as by the magnetometer data.

High-latitude optical data shows that the existence of these wave oscillations also influences the behaviour of the particles precipitating down the field lines. Both the MSP and field-aligned photometers co-located at LYR detected pulses of proton induced H_β emission which exhibit the same spectral features as the VHF and magnetometer data. This suggests that field-aligned proton precipitation is being modulated by the same field line oscillations that modulate the N-S ion flows recorded by the VHF radar and IMAGE magnetometers. Figure 6.2 reflects the strong correlation between the optical signature of the field-aligned photometers and the oscillating magnetic trace of the LYR magnetometer which contributes to the structure of the TCV of Figure 6.16. This supports the

magnetohydrodynamic model that proposes that the spatial structure of the TCV is governed by the characteristics of the oscillating wave modes present on the field lines.

The latitudinal and longitudinal spread of the ground-based instruments allow us to witness the temporal evolution of the TCV as it propagates away from noon. The progression of the westward-moving TCV across the morning is tracked by the IMAGE and Greenland magnetometer chains located at 11:30 and 06:00 MLT respectively. As the TCV moves tailward, its velocity is seen to increase from 9 kms^{-1} at IMAGE to 16 kms^{-1} at Greenland. This increase in propagation velocity shows that the train of vortices accelerate on their way from noon to earlier morning hours, a characteristic previously reported by Sibeck [1991] and Lühr [1994,1996]. The velocity at which the TCVs travel is governed by the propagation of the HM wave in the magnetosheath. As the TCV moves tailward the sheath speed accelerates and hence the TCV appears to accelerate. After reaching its maximum velocity the TCV is expected to slow again at around 0800/1600 MLT because beyond this, although the sheath speed is near the solar wind speed and its velocity down the tail is constant, the field lines are being stretched tailward so the unit length on the magnetopause maps to increasingly smaller lengths in the ionosphere.

The motion of the TCV tailward is also marked by a decrease in amplitude. Zesta [2002] carried out a statistical study of TCV events. She reported that the largest events, those with amplitudes of the order of ~300 nT, generally occur in the late morning sector just before noon and decrease in amplitude as they move tailward. In the case presented here, the peak-to-peak amplitude reduces to a third its original size as it moves between IMAGE and the east coast of Greenland. If the spatial structure and temporal evolution of the TCV is governed by the characteristics of the oscillating wave modes present on the local field lines, as it propagates away from the resonance region a reduction in wave power and hence amplitude would be expected.

The latitudinal spread of the magnetometer stations of both the IMAGE and Greenland arrays allowed the detection of a shift to lower latitudes of the TCV as

it moved tailward. This latitudinal motion corresponds to an equatorward velocity of 2 kms^{-1}. Past studies have shown that the majority of TCV events show some poleward or equatorward motion [Murr et al, 2002]. Gussenhoven et al. [1983] offer an explanation for this in terms of the latitude of the OCB as a function of MLT. The motion of a TCV will be affected by the position and motion of the OCB. The fact that the distance between the auroral oval boundaries and the geomagnetic pole in the invariant latitude-MLT frame increases with MLT away from noon means that TCVs moving around the oval on resonant field lines would be expected to move equatorward. This equatorward motion is reflected in the 2 kms^{-1} southward velocity measured at both IMAGE and Greenland.

In addition to the OCB and auroral oval latitude affecting the TCVs motion, the TCV has an effect on the latitudinal motion of the OCB. This is because the TCV induces flow that is poleward and equatorward in the vicinity of the TCV but no local reconnection is taking place. This means that the non–reconnecting ("adiaroic") boundary must be moved poleward and equatorward with the induced plasma flow. The relative motion of the OCB due to the ongoing convection is as predicted by the Lockwood and Morley model in Figure 6.10. It is assumed that the OCB is situated at the point were the ionospheric convection reverses, the "convection reversal boundary" (CRB). In reality, the CRB and OCB can differ because of: any viscous-like momentum transfer onto closed field lines, transit times of Alfvén waves and/or field-aligned currents induced at conductivity gradients. The OCB is therefore thought to lie close to, but somewhat poleward/equatorward, of the CRB, outside/inside from the reconnection merging gap [Lockwood, 1997]. Figure 6.21a shows the latitudinal motion of the CRB, as predicted by the convection model, at an MLT centred on the IMAGE stations. This panel reveals the effect of the predicted reconnection rate variation due to the observed IMF clock angle changes. As the model responds to the addition of open flux to the polar cap, the CRB/OCB reacts by expanding equatorward to a new latitude. The commencement of reconnection at 7:57 UT causes the boundaries to expand to lower magnetic latitudes, before relaxing back poleward. In the case of the CRB a shift equatorward from 77.8° to 75.4° is predicted, followed by a poleward shift back to 75.9°. The position of the CRB predicted by the model is supported by the B_N and B_z (vertically downwards) components of

the IMAGE magnetometer traces, which reveal a reversal in current direction between NAL and HOR, indicating the presence of a convection reversal boundary between magnetic latitudes of 76 and 74°.

As discussed above, in addition to being influenced by a dayside reconnection pulse, the position of both the CRB and OCB are affected by the convection flows inherent to the train of vortices, the centres of which move longitudinally just equatorward of the boundary. The N-S flow reversals that separate the individual vortices, shown in Figure 6.16, either move the boundaries poleward or equatorward.

Figure 6.21b shows the effects these vortical flows have on the latitudinal position of the CRB/OCB, assuming that there are no other external factors acting on it. The ionospheric conductivities are not known, so to scale the magnetometer deflections in terms of flow velocities at the boundary, the maximum line-of-sight (northward) velocities observed by the VHF radar were compared to the corresponding maximum east-west magnetometer deflection. Ideally the value for the peak flow used would be from a latitude equivalent to the TCV, however the VHF data at this latitude are noisy and so it was necessary to employ a value from a lower latitude, noting that the velocities and deflections were not a strong function of latitude.

At 8 UT a reversal in flow from north to south between the leading and second vortices, results in an equatorward shift of the CRB/OCB. This reversal is marked by an increase in the ion temperature (due to field-perpendicular flows) observed by the ESR radar at LYR. The result of combining the shift of the boundary due to the TCV with the corresponding shift due to reconnection (Figure 6.21a) is shown in Figure 6.21c. This boundary motion could represent either the motion of the CRB or the OCB lying to the south.

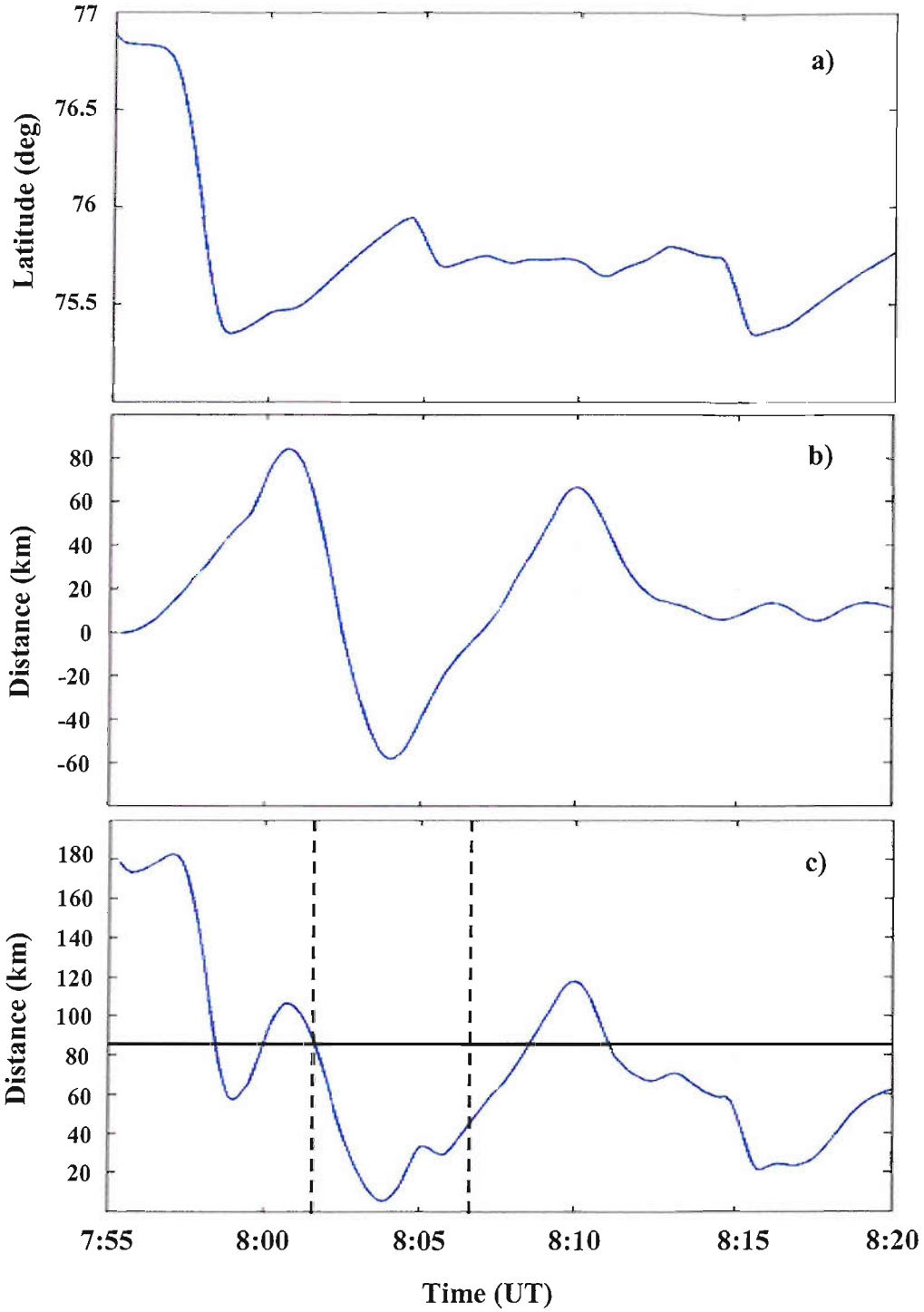

Figure 6.21 ***a)*** Modelled latitudinal motion of the convection flow reversal boundary (CRB) at an MLT centred on the IMAGE stations: these motions are due to the variation in the magnetopause reconnection rate). ***b)*** The effects of the vortical flows on the latitudinal position of the CRB, assuming that there are no other external factors acting on it. ***c)*** The predicted combined effect of reconnection and the passage of the TCV on the latitude of the boundary. The position of LYR relative to the predicted boundary location is represented by the solid black line.

As discussed in Section 6.2.1, comparisons between the SuperDARN mapped potential patterns and the model predictions suggest that that there may have been a considerable shift in the MLT of the merging gap which would have reduced both the speed and the amplitude of the equatorward motion of the boundary (by increasing the longitudinal extent of the region in which there is equatorward erosion of the OCB). Figure 6.22 shows the CRB latitude at 11-12 MLT, derived from the mapped potential SuperDARN plots shown in Figure 6.11. In this plot, the CRB starts to move equatorward at 07:56 UT, roughly the same time as derived from the model (Figure 6-21a), and moves equatorward by about one degree of invariant latitude in the interval 07:56-08:15. This is the shift as deduced from the model, but occurs over about 19 mins, instead of the 4 mins for the model predictions. This smoothing out of the erosion could be explained by the longitudinal motion of the merging gap. An additional factor is that within the merging gap, flows are predominantly northward and the CRB and its motions may be difficult to detect from the potential patterns.

If we assume that the TCV effects are completely smoothed out by the mapped potential model fitting procedure, the motions shown in Figure 6.22 are all due to reconnection and so correspond to the model predictions in Figure 6.21a. We can therefore add the predicted effect of the TCV, as shown in Figure 6.21b to the motions shown in Figure 6.22 to get a different estimate if the OCB /CRB motion in this event under the combined action of the reconnection pulse and the TCV. The result is shown in Figure 6.23.

Because of the lack of global imager data or in-situ particle precipitation data for this event, the only data with which we can compare Figures 6.21c and 6.23 come from the Svalbard optical experiments. The MSP at LYR observes a sudden increase in 630.0 nm emission at 8:07 UT, which lasts for approximately 12 mins shown in Figure 6.3. Rees and Luckey [1974] demonstrated the usefulness of the red line emission when used in ratio with the 557.7 nm emission of atomic oxygen. A high ratio indicates the low energy precipitating flux which characterises the cusp and an increase in this ratio indicates the passage of the

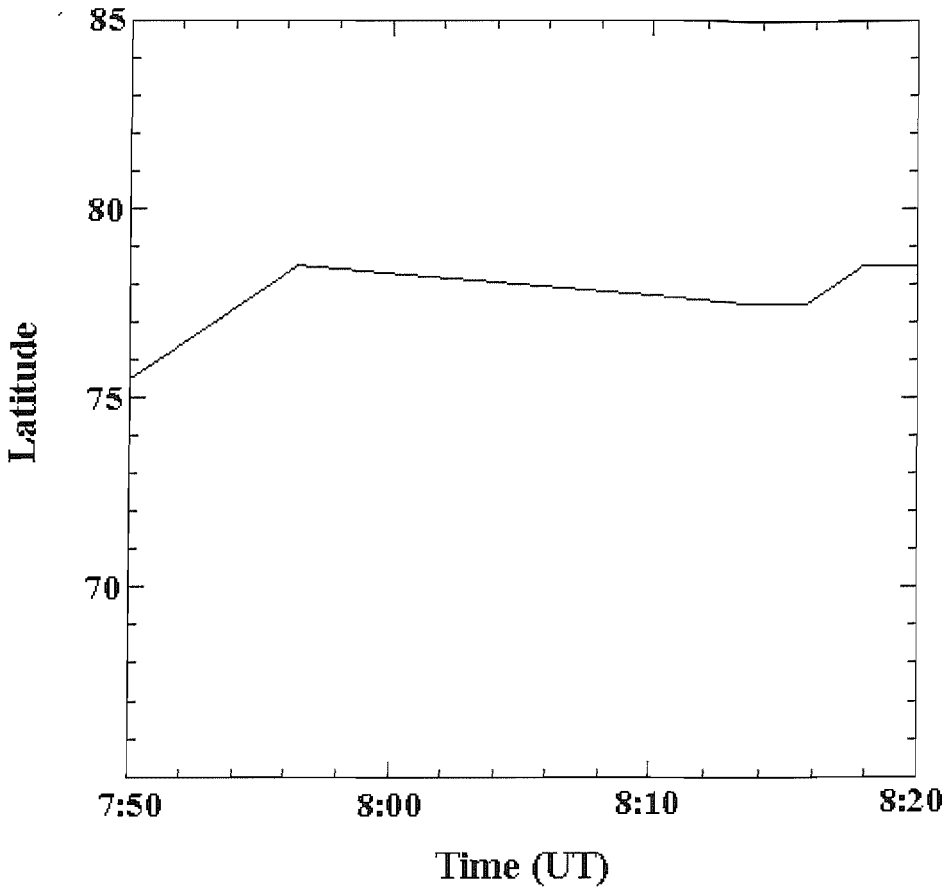

Figure 6.22 The convection reversal boundary latitude derived from the SuperDARN mapped potential plots shown in Figure 6.11, for the 11-12 MLT sector of the IMAGE magnetometer chain.

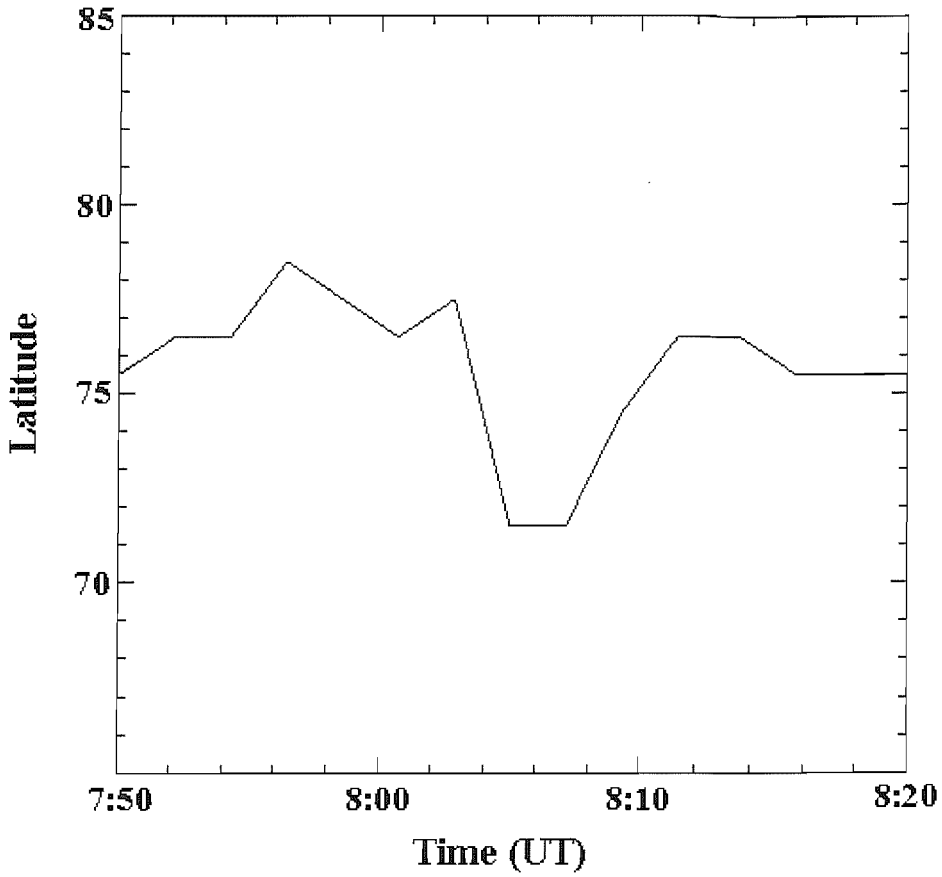

Figure 6.23 An estimate of the relative motion of the CRB due to the combined effects of the dayside reconnection and the passage of the TCV.

OCB equatorward over LYR. Thus this increase in the 6300/5577 ratio could indicate a rapid motion of the OCB equatorward at this time.

The expanding boundary is inferred from the optical signatures of electron precipitation observed by the field-aligned photometer shown in Figure 6.2. The same field line oscillations that modulate the protons also controls the behaviour of the electrons. However at 8:07 UT the pulsations in the electron emissions stop abruptly, marking the passage of LYR from oscillating closed field lines onto open field lines. The passage of the OCB over LYR does not have the same effect on the modulation of the proton precipitation. This is to be expected because, unlike electrons that are bound to their associated field lines, proton dispersion through charge exchange, as discussed in Section 1.2.5, means that the LYR instruments are able to detect the modulations in proton emissions on closed field lines even after the equatorward motion of the OCB has placed them on open field lines.

The equatorward motion of the OCB is also inferred by both the EISCAT VHF and ESR radar. The OCB motion is marked by an equatorward progression of ion and electron enhancements in the VHF radar data. These enhancements subsequently return poleward after 12 mins supporting the MSP observations that LYR remains in the cusp for this amount of time. The timing of the OCB motion across LYR is supported by the ESR, which at 8:07 UT saw an increase in the electron density and temperature, characteristic of soft electron precipitation in the cusp, lasting for approximately 12 mins. This gradual increase in precipitation reflects the evolution of particle flux down newly reconnected field lines, suggesting that LYR passes over a reconnecting boundary [Davis, 1996]. This supports the positioning of the X-line in the vicinity of the IMAGE magnetometer stations in the convection model of Section 6.2.1.

Figures 6.21c and 6.23 show two different estimates of the relative motion of the CRB due to the combined effects of the dayside reconnection and the passage of the TCV. Because there can be an offset between the CRB and the OCB, we do not know exactly where to place LYR if we take the variation shown to be that of the OCB. The solid black line represents the position for LYR which gives the

closest agreement with the ground-based data and for which the OCB would be crossed at 08:07. However, for the model predictions (Figure 6.21c) there is a discrepancy, with the model moving LYR onto open field lines at 8:02 UT whereas the main equatorward motion is between 07:57 and 08:04. This problem remains for the locations derived from SuperDARN data (Figure 6.23), but is slightly less severe, in that the main equatorward motion is between 08:03 and 08:05 UT. The cause of this discrepancy could be one of a number of factors. The time-of-flight of the full flux of charged particles (determined by the ion flight times) down the newly reconnected field lines into the ionosphere could account for 1-2 mins of this time difference, which could be sufficient for Figure 6.23, but another mechanism needs to be called upon to explain the larger difference in Figure 6.21a. An additional unexplained feature of both sets of OCB prediction is that a return to closed field lines is expected at around 08:10 UT, but there is no such feature in the optical emissions which imply that once in the polar cap, LYR remained there. The only solution consistent with this would place LYR near 76.5° in Figure 6.23, for which the initial OCB crossing would have been near 08:03, again somewhat earlier than expected from Figure 6.3. This discussion highlights the difficulty in determining the OCB location without in situ data (and even then interpolation between successive satellite passes 90 minutes apart is a major problem)

6.4 *Event Summary*

Ground based instruments on Svalbard measured strong oscillations in both "proton" and "electron" aurora near noon following the arrival of a pressure pulse in the solar wind. Determining the cause of these emissions is complicated by a simultaneous brief swing of the interplanetary magnetic field southwards. Filtering the ground based data allowed the separation of these two effects and a study of their impact on the magnetospheric/ionospheric system. Using the Lockwood and Morley convection model to emulate the ionospheric flows triggered by the onset of dayside reconnection, or studying the SuperDARN mapped potential plots, both support the filtering method as a way of isolating the effects of the reconnection pulse and of the TCV. Filtering revealed that the subsequent evolution of the ionospheric convection pattern, and the formation of a filamentary field-aligned current system due to impact of the pressure front, both contributed to a bipolar structure observed in the magnetic records of the IMAGE, Greenland and MM210 magnetometer arrays; however, the bipolar signature of the TCV is of much larger amplitude and much shorter duration than that due to the reconnection pulse (the latter showing only brief weak negative deflections before the onset of strong, prolonged positive deflections). The position of the IMAGE array made it possible to study both the reconnection and pressure pulse effect on the ionosphere near noon and investigate the evolution of the temporally and spatially varying convection flows associated with these effects. The ground based data are interpreted in terms of the passage of the open-closed boundary (OCB) over the instruments in response to the onset of a directly-driven pulse of dayside reconnection and the propagation of two trains of vortices tailward across the dawn and dusk sectors in response to the propagation of a fast mode generated by the compression of the bow shock. However, not all features of the optical signatures are well explained, in particular there is a delay between the times when LYR is predicted and inferred to have moved onto open field lines. This discrepancy highlights the limitations of the methods used to try to identify the open-closed boundary (OCB) location from the convection reversal boundary (CRB).

Chapter 7: Event Three

The Magnetospheric and Ionospheric Response to a Solar Wind Pressure Front During a Period of Enhanced Northward IMF

The multi-instrument study presented in this chapter uses data from the morning of 29 December 2001. The event, first introduced in Section 4.2, was linked to a rapid increase in the upstream solar wind pressure, which impacted on the magnetopause at ~ 5:39 UT. Figure 4.13 shows the solar wind parameters that reveal this pressure increase, lagged by the predicted ACE-to-ionosphere time delay calculated in Section 4.3.3. Ground and satellite observations show evidence of magnetospheric compression accompanied by an increase in auroral emissions resulting from both proton and electron precipitation. These emissions initially occurred in the noon sector and were quickly followed by auroral brightening on the nightside. At the same time, a distinct bipolar signature was detected in the magnetic records of the IMAGE, Greenland and MM210 magnetometer arrays similar to those associated with the travelling convection vortices (TCV) of Event two (Chapter 6).

On 29 December 2001, the IMF was northward for almost the entire day. Moreover, it had been so for the entire previous 24 hours as well. As a consequence, the magnetosphere was in a very quiet state throughout both the 28th and 29th. This study exploits the fact that the observed effects of the pressure pulse were not contaminated by the effects of previous substorms, in order to study the energy transfer and deposition caused by the impact of the pressure front on the magnetospheric/ionospheric system. The filtering technique used in the last chapter to

remove ionospheric convection effects reveals some evidence for high-latitude reconnection underlying the pressure front effects.

The position of the satellite-borne and ground-based instruments made it possible to study the overall effect of the pressure front on the high-latitude ionosphere, and investigate the evolution of the temporally and spatially varying field-aligned currents associated with the pressure pulse. The results put forward in this chapter show the existence of an enhanced pair of a train of vortices propagating around the morning and afternoon sectors. The two theories of the generation of these vortices are considered as explanations of their behaviour and of the associated auroral emissions.

In this chapter, the observations from all instruments, space and ground-based, are presented in Section 7.1. The description of these instruments has been discussed previously in Chapter 2. The analysis of the event, presented in Section 7.2, involves the separation of the effects of the pressure pulse from those resulting from convection using a low pass filter, as employed for Event two (Section 6.2). Section 7.3 discusses the interpretation of the data and examines the implications of the methods used to analyse these results.

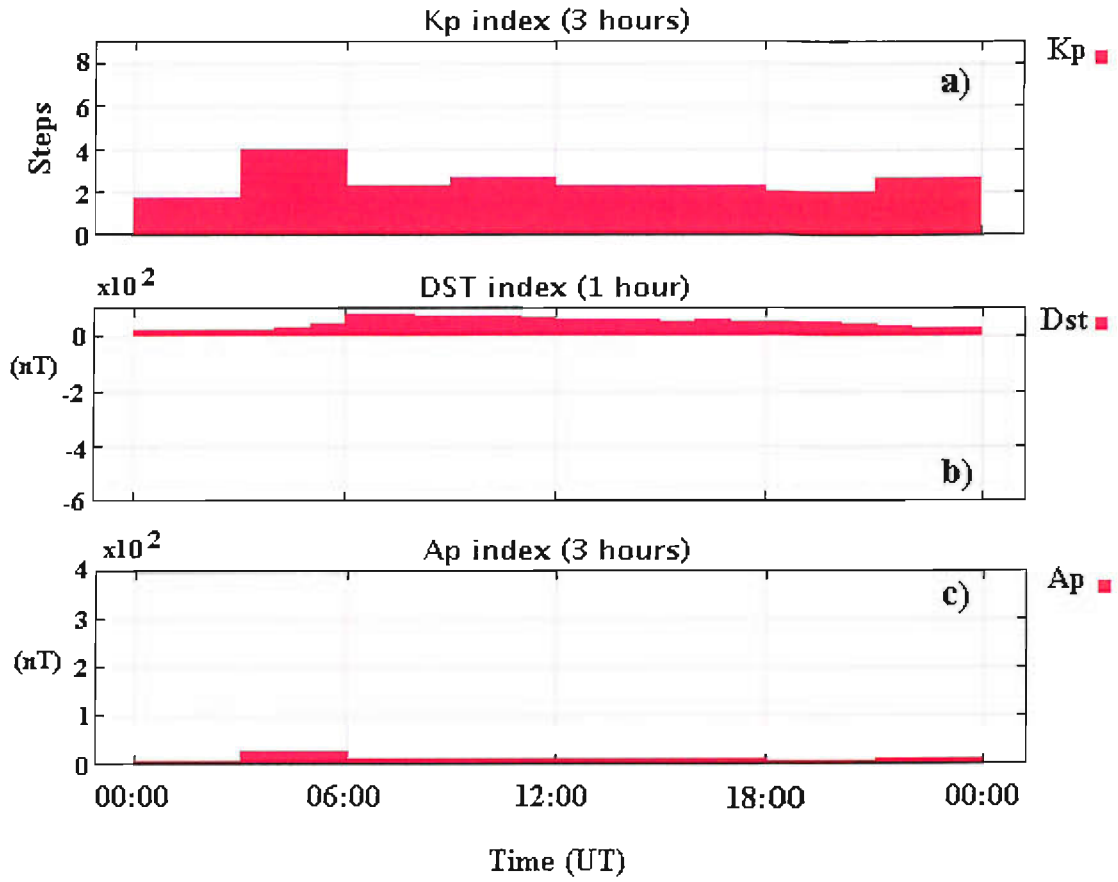

Figure 7.1 The variations in planetary indices on the 29 December 2001. ***a)*** The Kp index gives the expected geomagnetic activity obtained from 12 magnetometer stations at mid-latitudes. ***b)*** The Dst (Disturbance Storm Time) index reflects the state of the ring current, as derived from low-latitude magnetometers. ***c)*** The Ap index, like the Kp index, gives an indication of planetary geomagnetic activity (see Appendix D).

7.2 Observations

On 26 December 2001, there was a significant interplanetary event related to a solar flare. An interplanetary shock and associated fast interplanetary coronal mass ejection (CME) were detected by both the Wind and ACE satellites on the 29 December. At the interplanetary shock the IMF B_z magnitude increased to ~ 20 nT and the pressure increased by a factor of ~ 4.

The upstream solar wind data showed that the hours prior to the shock front were quiet as a result of the IMF remaining persistently northward with a B_z always > 5nT. Consequently, only a low level of geomagnetic activity was detected on the ground. Figure 7.1 shows the variations in planetary geomagnetic activity indices over the 29 December. The Kp and Ap indices both show a quiet period of activity before the shock front impact. This lack of activity is reflected in the Dst index whose small positive values reveal a weak ring current, indicating that the ring current has not been enhanced by particle injections associated with recent substorms. A detailed description of these geomagnetic indices are given in Appendix D.

The effect of the pressure pulse shock front arrival at Earth was recorded by a range of satellite-borne and ground-based instruments. The GOES-8 and LANL satellites provided a means to examine the reaction of the magnetosphere at different points along geosynchronous orbit. Figure 7.2 shows the positions of these satellites over the period of interest. Signatures recorded by the onboard magnetometer of the GOES-8 satellite situated around at the nightside at ~ 01 MLT are presented in figure 7.1. Figure 7.1a, 7.1b and 7.1c show the three components of the magnetic field from GOES-8. The satellite observed oscillations in all three components of the magnetic field commencing at around 5:39 UT and accompanied by an overall change in the magnetic field strength. These changes do not immediately recover to pre-event values but remain at the post-pressure front level after impact, with the exception of the B_x component which steadily increases in strength.

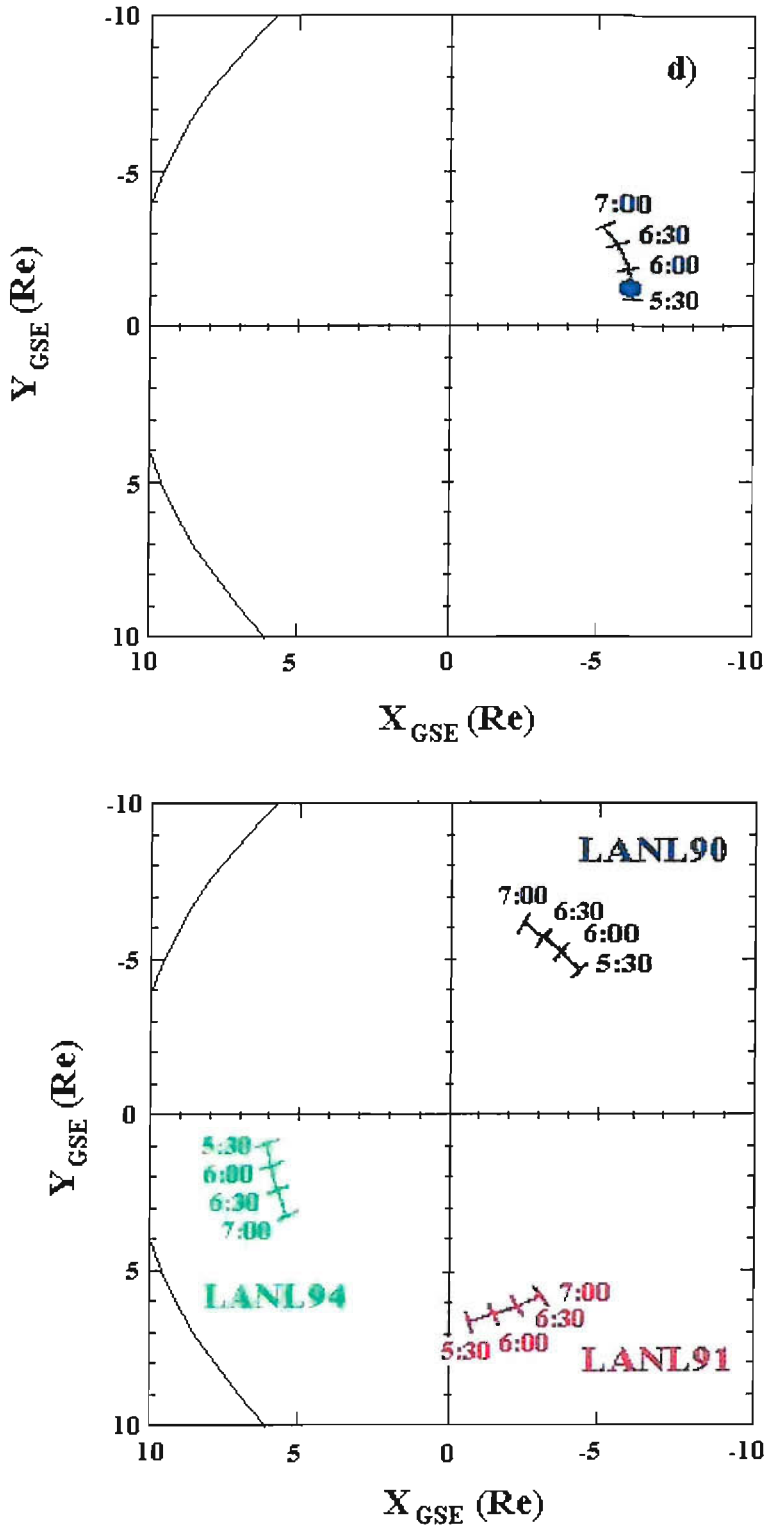

Figure 7.2 The positions of the GOES-8, LANL-90, LANL-91 and LANL-94 satellites over the period of interest from 5:30 – 7:00 UT.

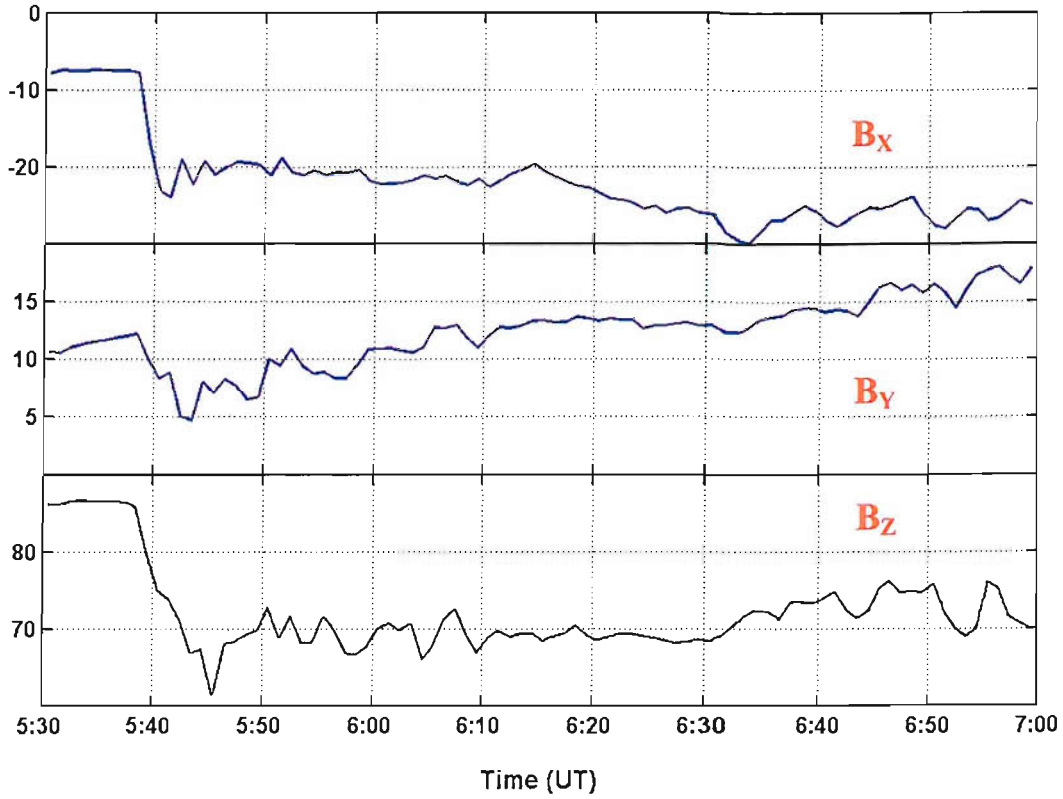

Figure 7.3 a), b) & c) The B_X, B_Y and B_Z magnetic field components in the GSE frame, measured by the GOES-8 onboard magnetometer respectively.

The EPS instrument, on the GOES-8 satellite, measures the flux of protons over a range of energies between 0.7 - 4 MeV and the flux of electrons over an energy range of 0.6 – 2 MeV. Figure 7.4 shows the proton and electron particle flux data over the event. At 5:39 UT, GOES-8 observed a rapid decrease in high-energy electron flux at the same time as the decrease in the magnetic field strength detected by the onboard magnetometers discussed above. As with the magnetometer data, the electron flux remains at the post-pressure front level for ~ 5 hours after the impact. The decrease in electron flux was accompanied by a transient enhancement in high-energy proton flux which lasted for approximately 15 mins. The particle data from the SOPA instruments on three LANL satellites: 1990-05, 1991-080 and 1994-084 are shown in Figures 7.5, 7.6 and 7.7. Similar variations in the electron and proton flux data are observed in a number of MLT sectors defined by the positions of the LANL satellites shown in Figure 7.2. The data also showed evidence of the oscillations seen in the GOES-8 magnetometer data.

Global UV auroral images from the IMAGE satellite were used to investigate the dynamics of the auroral oval in response to the sudden increase in solar wind pressure. The IMAGE satellite was over the Earth's north pole when the pressure front hit the magnetosphere, and obtained a set of Far-Ultraviolet images which showed the overall reaction of the northern auroral oval. The two FUV cameras: SI12 and SI13, obtained simultaneous images of the northern hemisphere once every 2 mins (in proton and electron emissions, respectively). Prior to the arrival of the pressure front, the SI12 channel appeared to detect some nightside proton activity, however the field-of-view of the instrument was limited due to position of the satellite over the polar cap. At this time, a small patch of cusp proton emission is observed, typical of the cusp under these northward IMF conditions. At 5:41 UT, a burst in both proton and electron emission occurred in the noon sector, shortly after the arrival of the pressure front. This was quickly followed by an auroral brightening on the nightside, mainly occurring through the morning sector for electron

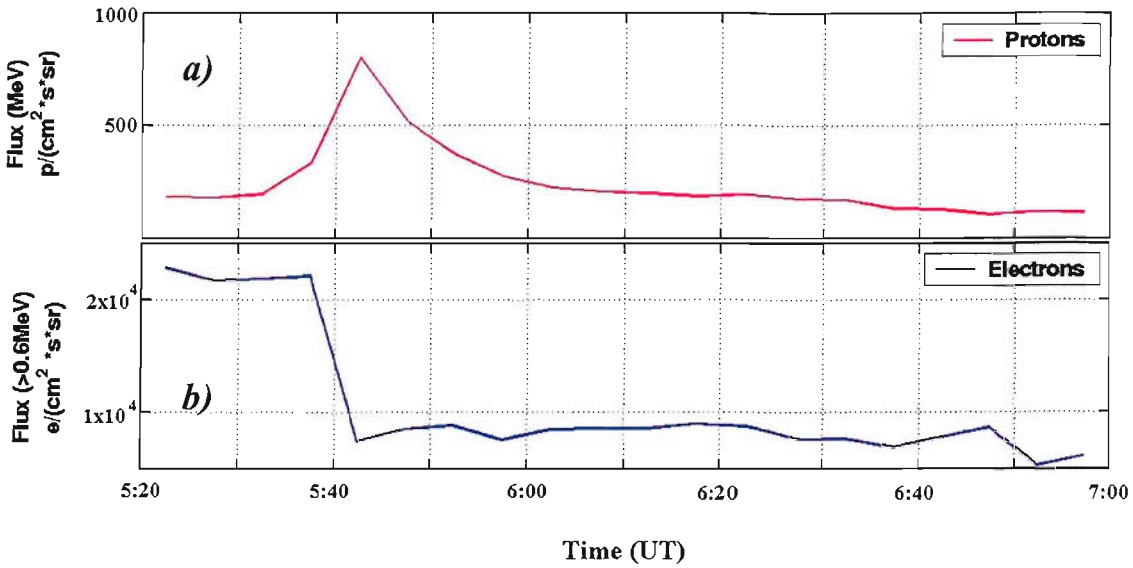

Figure 7.4 Integral particle fluxes from the GOES-8 satellite: ***a)*** protons in the energy range 0.7-4 MeV and ***b)*** electrons in the energy range 0.6-2 MeV

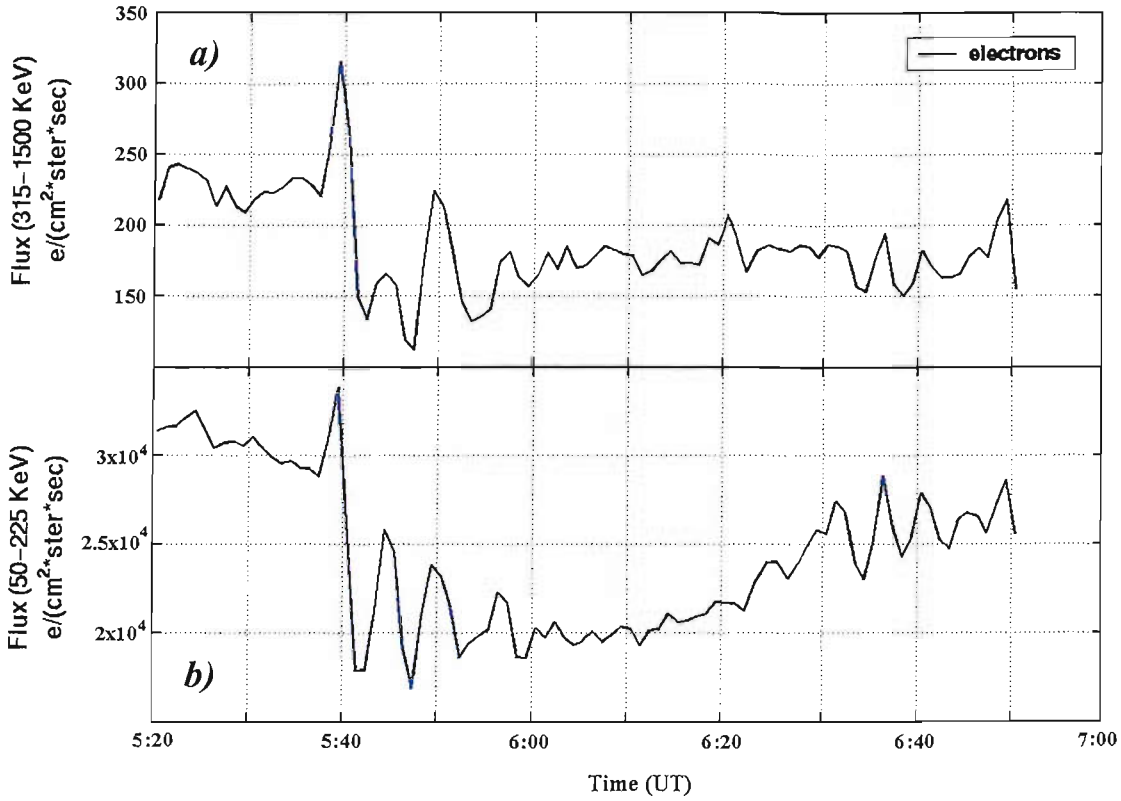

Figure 7.5 Integral electron fluxes observed by the LANL 90 satellite for energy ranges ***a)*** 315-1500 keV and ***b)*** 50-225 keV.

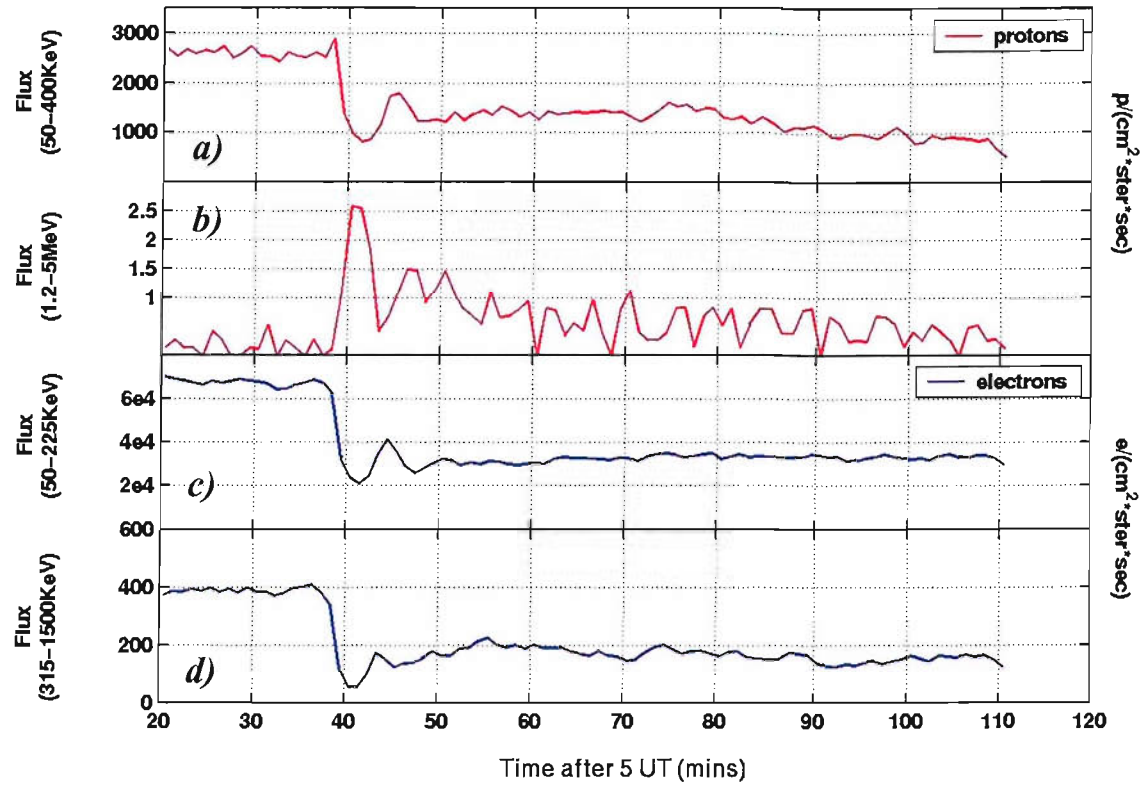

Figure 7.6 Integral particle fluxes from the LANL 91 satellite. The two top panels show protons fluxes in energy ranges *a)* 50-400 keV and *b)* 1.2-5 MeV. The two bottom panels show electron fluxes in energy ranges range *c)* 50-225 keV and *d)* 315-1500 keV

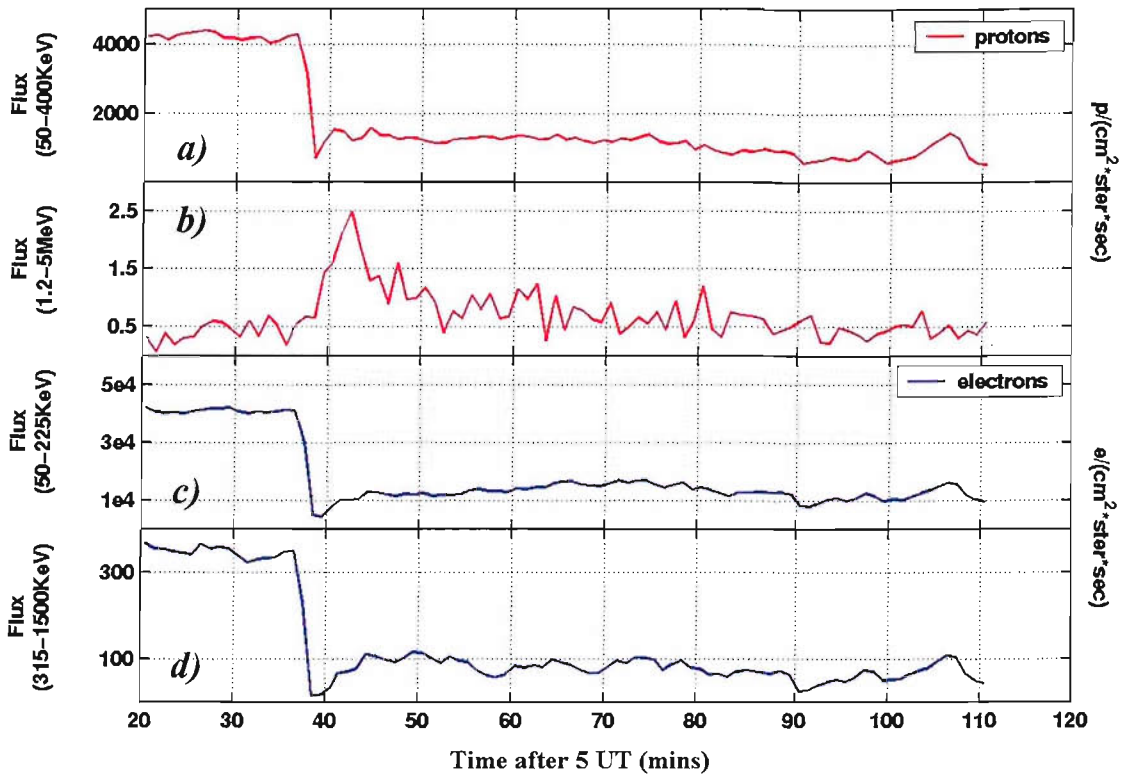

Figure 7.7 Integral particle fluxes from the LANL 94 satellite. The two top panels show protons fluxes in energy ranges ***a)*** 50-400 keV and ***b)*** 1.2-5 MeV. The two bottom panels show electron fluxes in energy ranges ***c)*** 50-225 keV and ***d)*** 315-1500 keV.

precipitation, with the proton precipitation favouring the afternoon sector to a lesser degree.

At LYR, the Meridian Scanning Photometer (MSP) observed bursts in proton and electron precipitation at all the observed wavelengths (both electron and proton emissions) at the time of arrival of the pressure front. Figure 7.10 shows, in time-zenith angle spectrogram format, the intensities observed by these for a) the electron-induced 630.0 nm emission, b) the electron-induced 557.7nm emission and c) the proton H_β (486.1 nm) emission.

Figure 7.10a shows a poleward-moving band of enhanced 630.0nm emissions, commencing at zenith angles near 120° following the impact of the pressure front. Figure 7.10b shows a similar feature in 557.7nm emissions which is initially at similar zenith angles but then moves through a larger range of zenith angles. In the interval 05:41-05:45 both features are close to the LYR field line (zenith angle near 110°), indicating they are close to coincident in space. Allowing for the higher emission altitude of the 630nm emission (~250km), it remains roughly coincident with the 557.7nm (Figure 7.10b) which arises from altitudes near 120km. Figure 7.10c shows that the onset of the poleward-moving feature was accompanied by a shorter-lived burst of 486.1 nm (Hβ) emission that also migrates poleward and is confined to a band extending over the range of zenith angles ~ 50°-120°, placing LYR inside the proton precipitation zone. This emission arises from around 130 km altitude and is close to coincident with the poleward-moving electron precipitation feature seen in the 557.7nm and 630nm emissions. Following the arrival of the pressure pulse, the persistent 557.7nm emission at low elevation angles to the south of LYR is enhanced, such that following the event intensities exceed $I_{557.7}$ = 4kR at all zenith angles above about 120°. The corresponding 630 nm emission intensity I_{630} is typically lower than this so $I_{630}/ I_{557.7}$ is either near or below unity. By contrast, in the poleward-moving structure $I_{630}/ I_{557.7} >> 1$, indicating softer sheath-like precipitation of open field lines. At the time of the event (around 05:40UT) LYR was at about 08:30 MLT and the intensification of the 557.7 nm emission to the south of

LYR can be seen in the SI13 images in Figure 7.9, which also reveal that this enhancement extended throughout the morning sector. The intensification of H_β emission seen at LYR is reflected in the Lyman-α emission seen by IMAGE/FUV (Figure 7.8) at this MLT and UT. The Lyman-α enhancement is first seen near noon at 05:39UT and spreads both eastwards and westwards. Enhanced emission persists at 11-15 MLT but then fades to a small spot near noon by 05:47. A small transient event is seen equatorward of the main enhancement around 13:30 MLT at 05:41.

The SuperDARN radar network provides us with some information on the convection associated with these auroral emissions. Figure 7.11 shows the SuperDARN mapped potential plots over the period of interest. Due to the lack of scattering irregularities on the dayside, information regarding ionospheric flows in this region is scarce. There is however, the evidence for bursts of enhanced nightside flow a few minutes after the pressure pulse arrival 5:43 UT, and at 05:49 which correspond to the initial burst in electron precipitation observed in the nightside by IMAGE.

As for the event studied in the previous chapter, using the IMAGE, Greenland, MM210 and Canadian magnetometer networks in conjunction with one another provide a means of covering a large range of latitudes and longitudes presenting a way of discerning between spatial and temporal responses to an interplanetary structure impacting the magnetosphere. Analysis of magnetic records from all four magnetometer chains reveals an isolated magnetic field variation, bipolar in structure, typical of a TCV. Figure 7.13 shows the magnetometer traces from the five highest latitude IMAGE stations. Figure 7.14 shows the magnetometer traces from four stations on the west coast of Greenland. This chapter presents analysis of data from all four magnetometer networks which reveals two sets of twin vortical structure travelling in the opposite direction away from noon. Further analysis shows evidence of field-line oscillations, apparent in the low-latitude magnetometer stations, which are comparable to the oscillation detected at geosynchronous orbit.

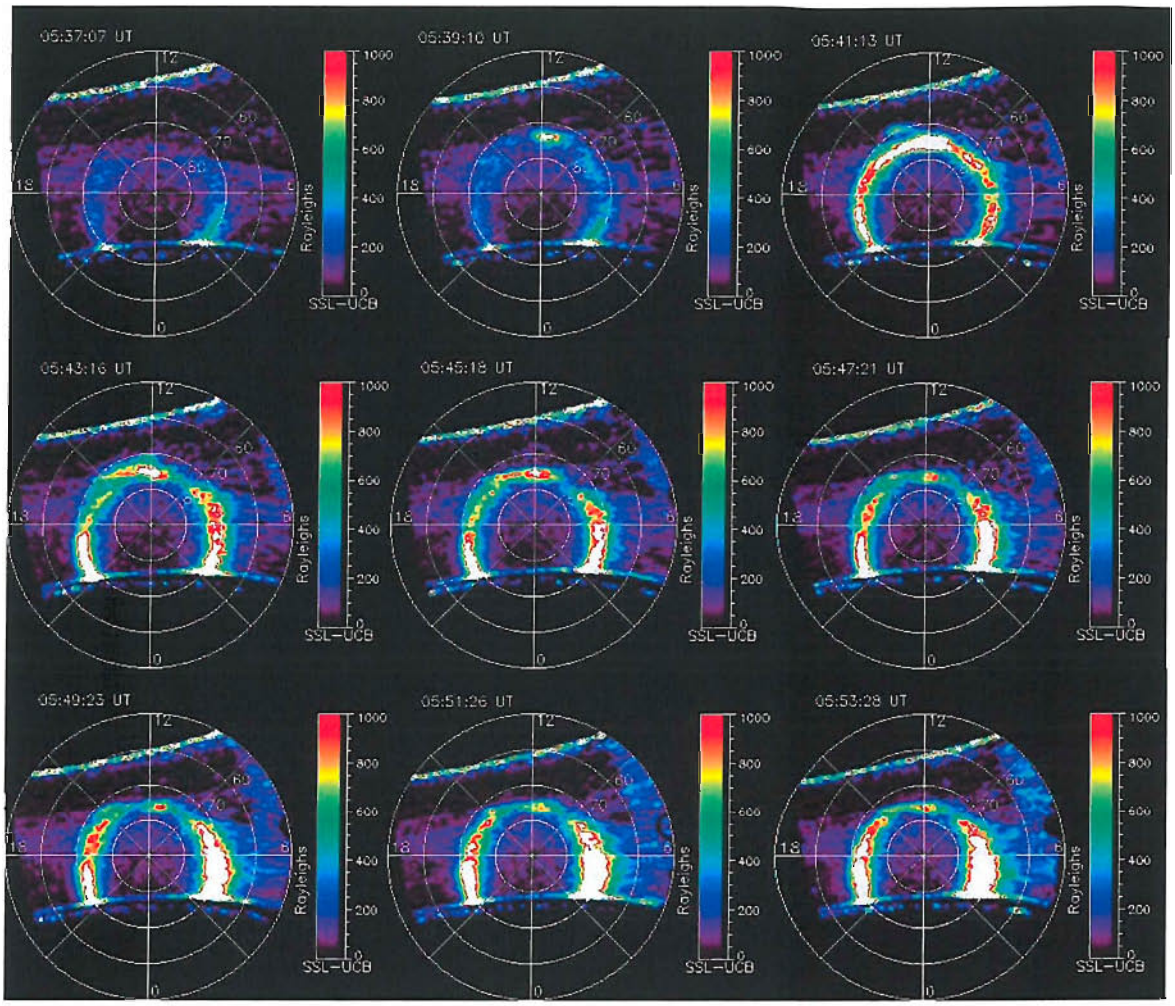

Figure 7.8 Global images of the doppler-shifted Lyman-α emission seen by the SI-12 channel of the FUV instrument on the IMAGE spacecraft. The images are 5 sec integrations, taken once every 122 sec. The intensity scale is the same in each frame. Above each frame is given the time of the FUV image.

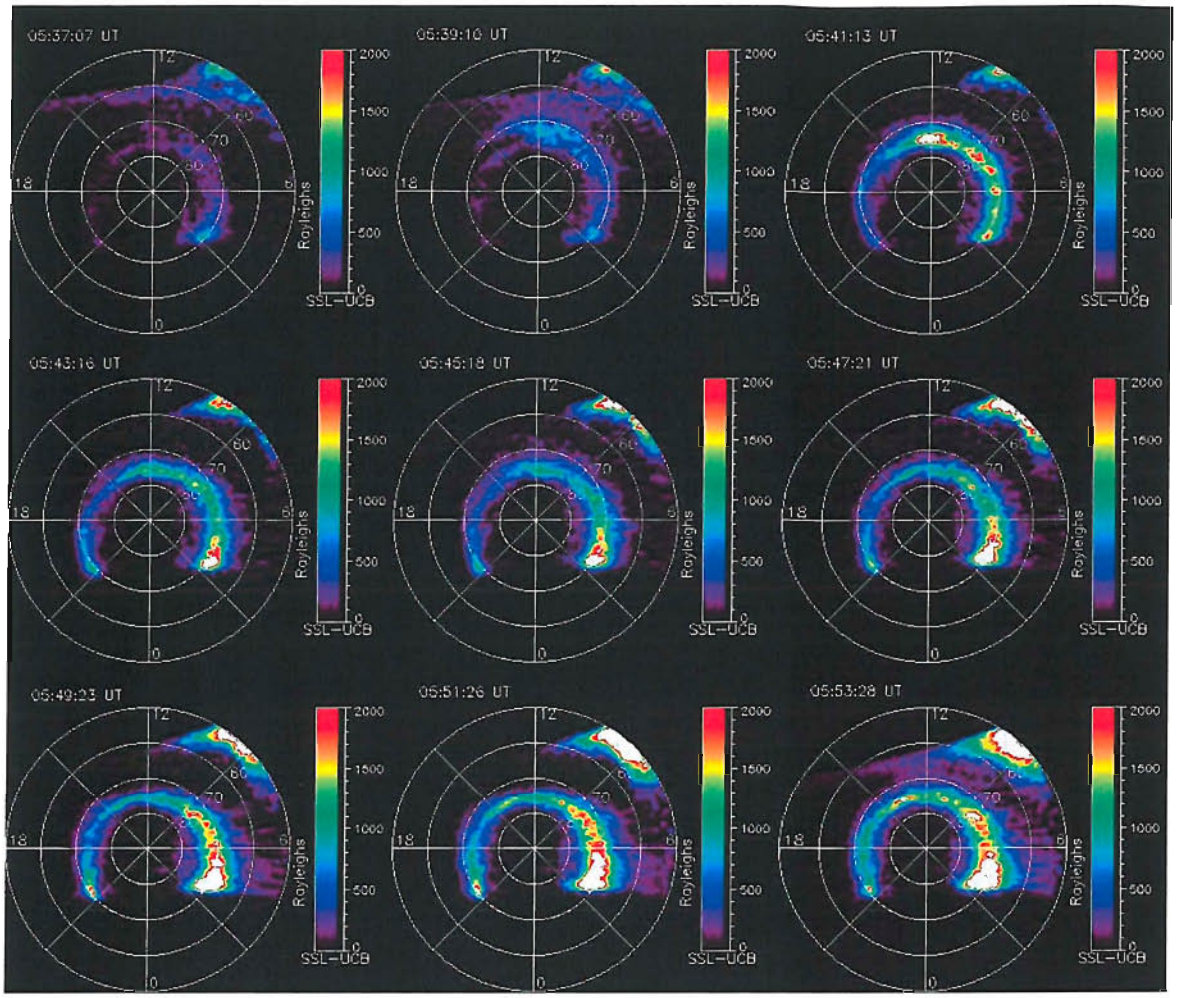

Figure 7.9 Global images of the atomic oxygen emission seen by the SI-13 channel of the FUV instrument on the IMAGE spacecraft. The images are 5 sec integrations, taken once every 122 sec. The intensity scale is the same in each frame. Above each frame is given the time of the FUV image.

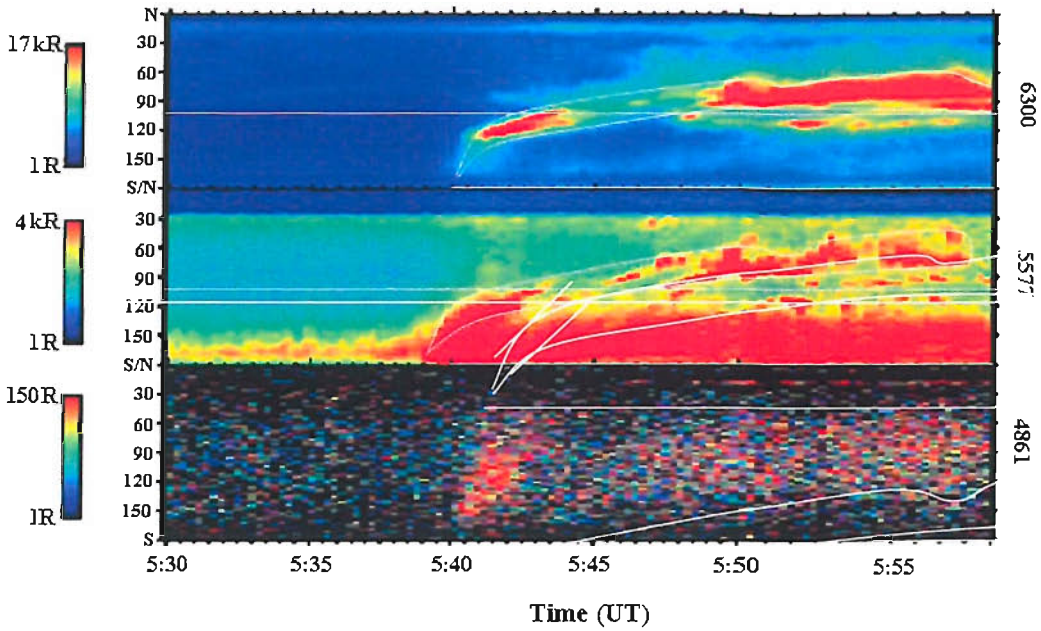

Figure 7.10 Time-zenith angle keograms of the intensity observed by the meridian-scanning photometer at LYR at wavelengths ***a)*** 630nm (oxygen red-line), ***b)*** 557.7nm (oxygen green line) and ***c)*** 486.1 nm (Hydrogen H-β)

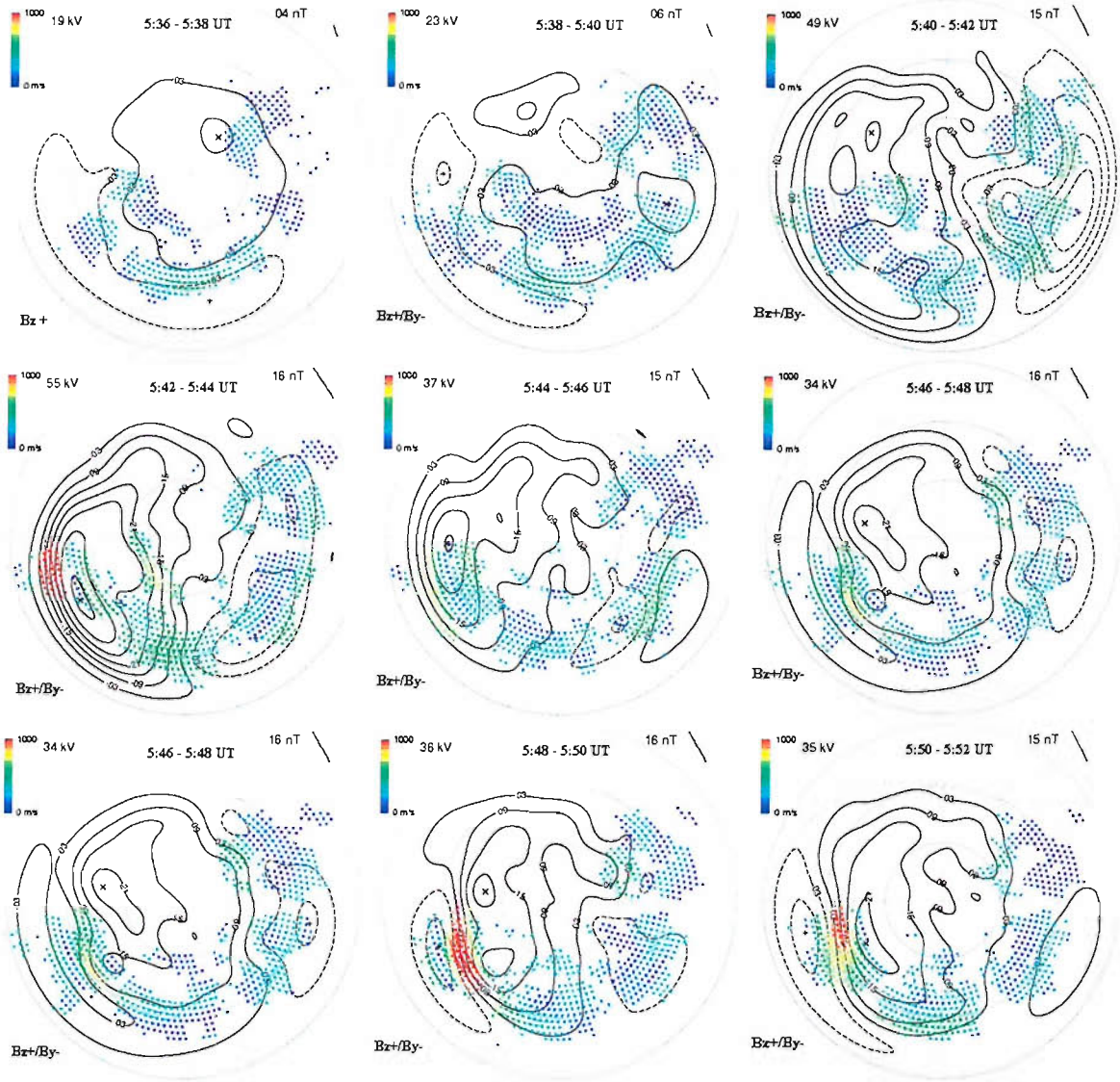

Figure 7.11 Mapped potential plots in the MLT-invariant latitude frame (with noon at the top), derived from the data from SuperDARN radars in the northern hemisphere during this event. The equipotential contours are from a model that is driven by the upstream IMF orientation and then fitted to the line-of-sight velocities observed by the radars. The vectors are also from the model fit and so are based on the observed line-of-sight components and the model fit to the beam-perpendicular components. Vectors are colour coded according to their magnitude. *(Plots courtesy of Dr. G. Provan, Leicester University).*

7.2 *Analysis of the Datasets*

The upstream solar wind and IMF observations during this event reveal a significant increase in the solar wind pressure under conditions of enhanced and persistent northward IMF (see Section 4.1.3). The orientation of the IMF, with a clock angle $\theta < 45°$, predisposes the magnetosphere to high-latitude reconnection, with the X-line lying typically tailward of the magnetopause entrance to the cusp region, as discussed in Section 1.1.2. Figure 4.14 shows that the pressure increase is accompanied by a swing to more northward IMF which may induce changes in the convection pattern. In this chapter, we again use the low pass Butterworth filter to remove any underlying convection effects caused by reconnection in the tail lobes. The convection response times are not necessarily the same for southward and northward IMF, nevertheless, the same cut-off frequency (15 mins), as used in Chapter 6, gives good separation of transient features and longer timescale convection responses.

Figure 7.13 shows both filtered and unfiltered data from the seven highest latitude IMAGE magnetometer stations. The blue line is the unfiltered data, while the red line is the low frequency data separated by the filter outlined in Appendix C. In the five highest latitude stations, which covers a magnetic latitudinal range of 75.3°-71.5°, the low frequency data is seen to vary over periods greater than 900 seconds and is thought to characterise the increase in flow associated with the ionospheric response to any change in high-latitude reconnection, caused by the increased positive IMF B_z. Figure 7.13 shows that the bipolar signature evident in the unfiltered data and commonly associated with pressure pulse effects is removed in the low frequency data, which shows a slower rise commencing at the time of the bipolar signature. This rise in the low-frequency convection flows is weak and lasts for only around 20 mins, suggesting it may have been triggered by a short-lived burst of enhanced lobe reconnection. A similar rise in low-frequency convection flow is also observed by the Greenland and MM210 magnetometers around at and MLT respectively. Figure 7.14

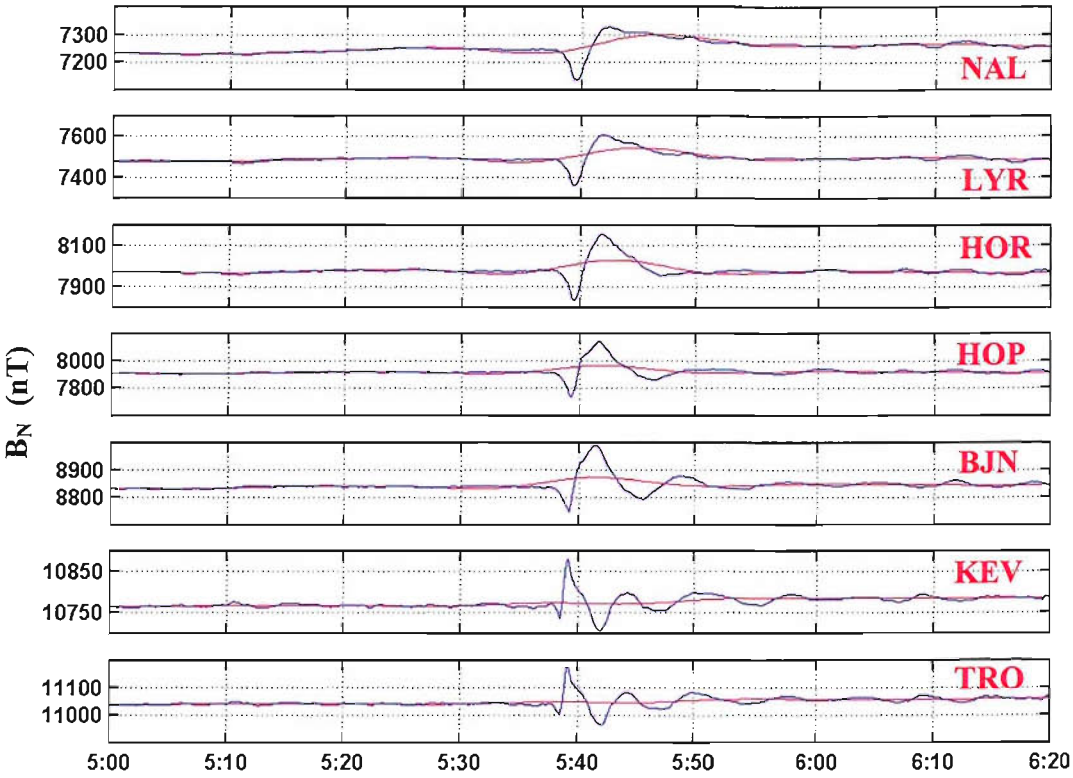

Figure 7.13 Filtered and unfiltered data from the 7 highest latitude IMAGE magnetometer stations. The red line represents the unfiltered data, while the blue line represents the low frequency filtered data.

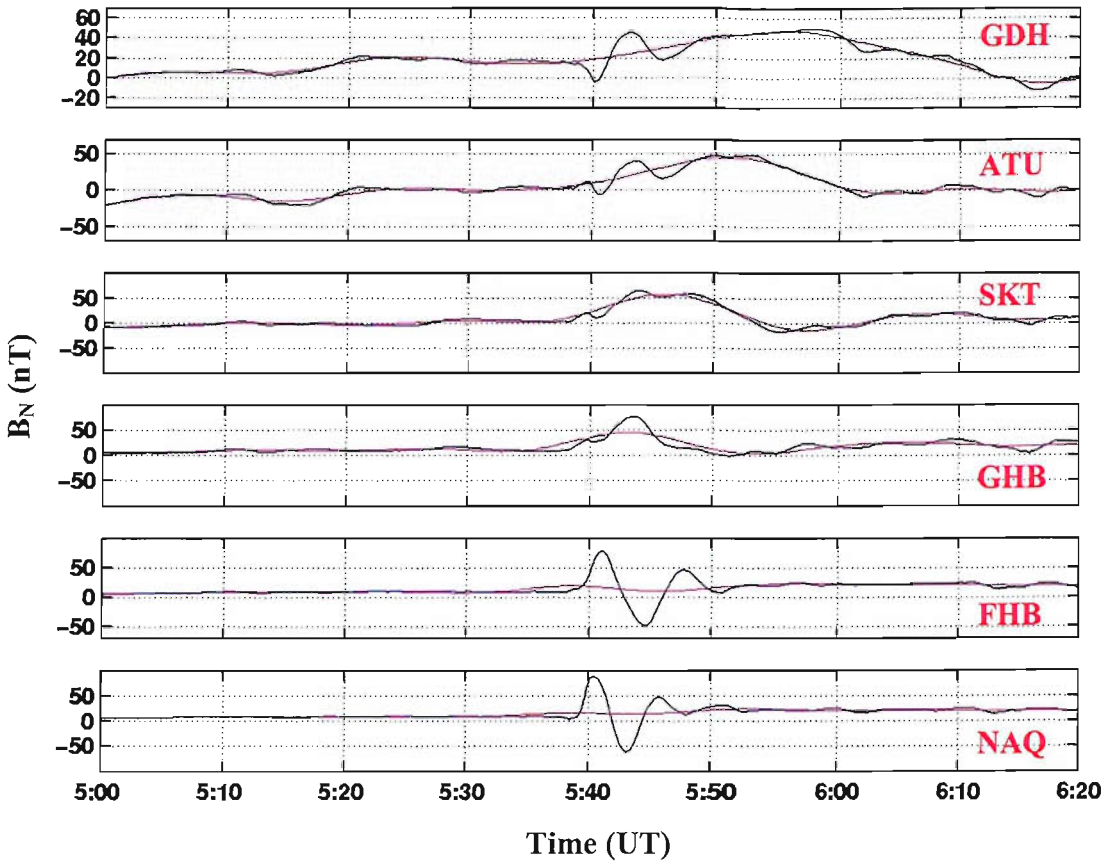

Figure 7.14 Filtered and unfiltered data from the west coast Greenland magnetometer array. The red line represents the unfiltered data, while the blue line represents the low frequency filtered data.

shows the filtered and unfiltered data from the west coast Greenland magnetometer network.

In Chapter 6, the Lockwood and Morley convection model [2003] was used to emulate the ionospheric flow response to dayside reconnection. Because this model deals only with the transfer of flux between the open and closed region it cannot be used to replicate the effect of a reconnection site whose footprint is not constrained to be situated on the open-closed flux boundary (OCB).

Once the longer period effect has been removed, the shorter period effects of the pressure pulse are clearly visible, and can be used to investigate the subsequent evolution of ionospheric flows generated by its arrival. Figure 7.15 shows a stacked plot of the B_N component data for the ten highest-latitude stations of the IMAGE array, with the highest latitude station at the top. This data has been filtered to remove longer periods, as discussed above. The five highest latitude stations observed a negative-to-positive deflection in the magnetic field B_N component, accompanied by a negative deflection in the B_E component (not shown). The five lowest latitude stations see a reversed positive-to-negative deflection in the B_N component, but the same negative excursion in B_E. All ten stations show an approximate 90° phase shift between B_N and B_E. The bipolar variation in B_N accompanied by a single excursion in B_E is consistent with a pair of oppositely directed currents passing over the stations. The 90° phase difference in both components is the signature of the ionospheric vortical flows associated with these field-aligned currents [Zesta et al, 2002].

The orientation of the upstream pressure front, shown in Figure 4.13, means that it hits the duskside magnetopause close to the nose. In response, one set of TCVs is expected to propagate in a westward direction away from the point of impact, towards the IMAGE magnetometer array situated at 8 MLT. A matching set is also expected to propagate eastward into the afternoon sector as occurred in the study presented in the last chapter. The direction of propagation of the of vortices is confirmed by the times of arrival of the signature at each of the IMAGE stations. The data presented in

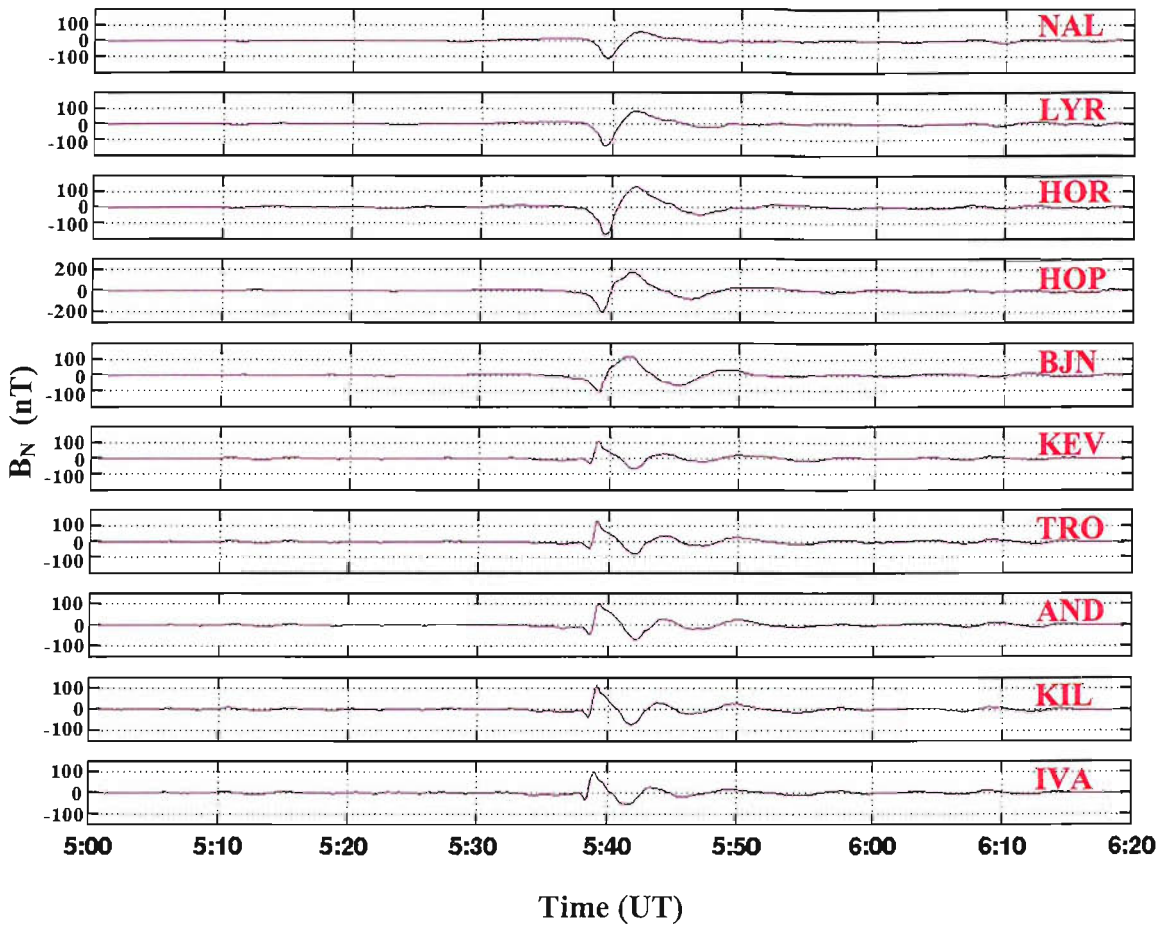

Figure 7.15 A stacked plot of B_N component variations observed at the ten highest-latitude stations of the IMAGE array. These data have been filtered to remove the lower frequency variations.

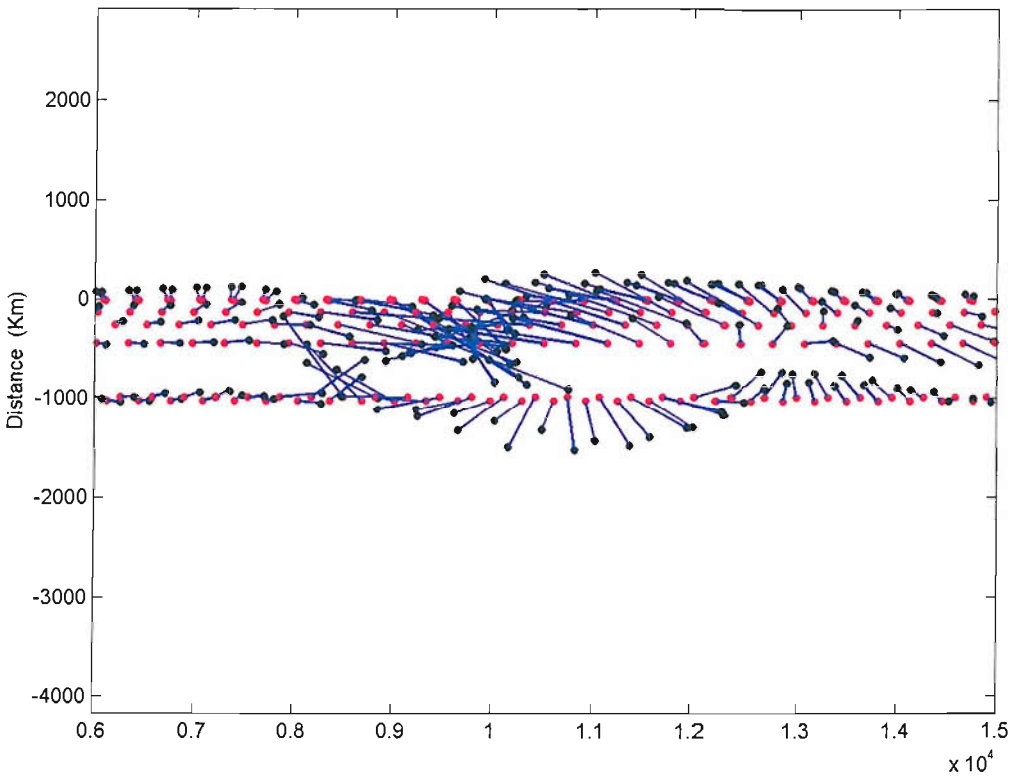

Figure 7.16 The IMAGE magnetometer data presented using the procedure developed by Friis-Christensen et al. (1988); Glaßmeier et al. (1992) and Lühr et al. (1996) in which the magnetic perturbation vectors are lagged and rotated by 90° anticlockwise (see text for details). A train of vortices with east-west scale lengths of ~ 3000 km moving anti-sunward at a westward speed of ~ 18 kms^{-1} and a southwards speed of ~ 2 kms^{-1} is revealed. The figure also provides evidence for the existence of a third vortex not evident in the Figure 7.15 time series plots. The individual blue vectors represent the convection flow direction at that particular point in a reference frame moving with the TCVs.

Figure 7.15 reveal that the TCV signature is first seen at the station of Hopen (HOP), situated to the east of the other stations at a longitude of 115°.

Figure 7.15 also reveals the latitude along which the centre of the vortical flows travel. This is marked by a reversal in polarisation between the stations of BJN and KEV, which shows that the path of the centre of the field-aligned current associated with the TCV lies between magnetic latitudes of 71.5° and 66.3°. Examining the maximum peak-to-peak disturbance in the horizontal field magnitude suggests that the centre of the vortex passes closest to BJN, as indicated by the slightly larger B_N value.

Figure 7.16 offers a way of determining the structure and motion of the vortices. Applying the same method used in Chapter 6, a pair of vortices is seen to be moving anti-sunward with a westward phase motion of ~ 18 kms^{-1} and a southward phase motion of ~ 2 kms^{-1}. Because the IMAGE array is situated at 8 MLT, close to where Greenland chain was situated in the previous event, both the speed and E-W elongation of the vortices is comparable to those observed at Greenland in Figure 6.18.

The Greenland magnetometer array lies to the west of IMAGE, over 6-7 MLT, providing a way of tracking the progression of the TCV. Figure 7.17 shows the high-pass filtered B_N component magnetic traces from eight of the Greenland magnetometer stations. The east chain stations are shown in the top four panels, the west coast stations are shown in the bottom four panels. Analysis of the 20-sec resolution data revealed that the bipolar structure representing the TCV was observed in both chains. This signature is less distinct in the west coast data, as the oscillations observed by the lower latitude IMAGE stations are apparent here.

The progression of the TCV from east to west is revealed by the delay in the bipolar signature between the two chains and its latitude from the reversal in the polarity between two consecutive stations along each chain. In the eastern chain this reversal

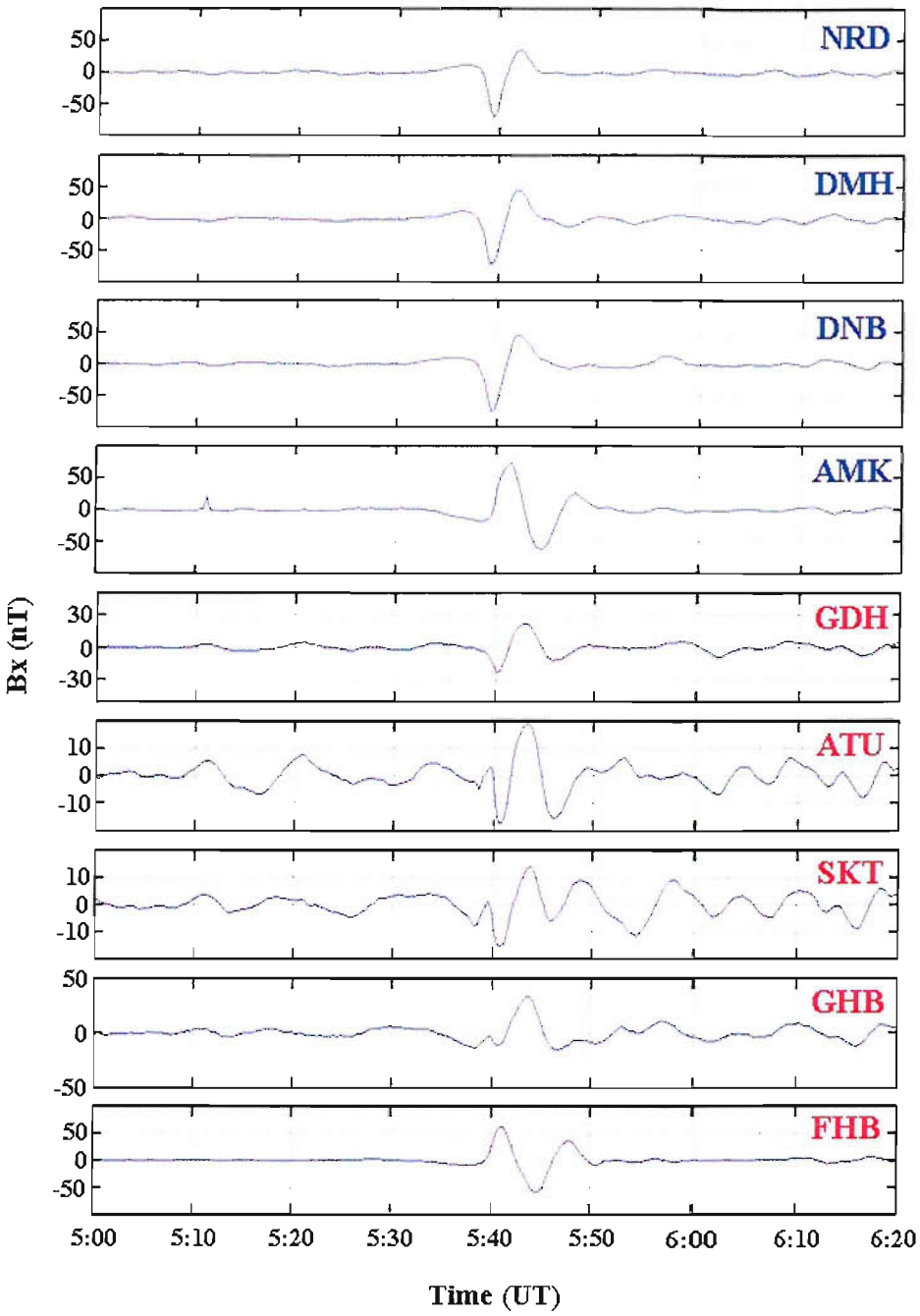

Figure 7.17 The B_N component magnetic traces from seven of the Greenland magnetometer stations. The east chain stations are shown in the top four panels, the west coast stations in the bottom four panels. These data have been filtered to remove the lower frequency variations.

is seen between the DNB and AMK magnetometers situated at magnetic latitudes of 75° and 69° respectively. At the western chain it is seen between the stations of GHB and FHB at latitudes of 70° and 68°. The magnitude of the magnetic deflections at each of these stations provides another way of estimating the path of the TCV. Figure 7.17 shows that on the east coast, the magnitude of the B_N component at DNB is equivalent to that at AMK suggesting that the centre of the vortices pass at a latitude halfway between the two stations. This method also shows that at the west coast stations, the TCV passes closer to the more southerly station of FHB at a latitude of ~ 68°. The path of the TCV is consistent with the previous event which was observed at similar latitudes.

It is also possible to calculate the speed at which the TCV is travelling along the line of propagation. This is done by lagging the B_E component magnetic field data of the three stations identified as lying closest to the path of the centre of the vortices: KEV, AMK and FHB of the IMAGE, Greenland east and Greenland west chains respectively. Lagging the B_E component traces revealed a 80 (± 15) sec time delay between KEV and AMK and a 100 (± 15) sec delay between KEV and FHB. These time delays translate into a constant along-path velocity of 34 (± 1) kms^{-1} between IMAGE, the east and the west coasts of Greenland. Speeds of ~ 30 kms^{-1} west, ~ 2 kms^{-1} south, consistent with the along-path speeds calculated above, are found for the passage of the event over the Greenland magnetometers. Due to the increase in speed, the vortices appear to have become even more elongated in the E-W direction. The convection flow vectors have also become progressively weaker, making it harder to discern the vortices. This weakened signal is also seen in the magnitude of the peak-to-peak disturbance in the horizontal field (B_N) shown in Figure 7.17, which has approximately halved since the event passed over IMAGE.

As in the previous study, an investigation was also made of data from magnetometers lying to the east of the IMAGE chain in the afternoon sector. Figure 7.18 shows the B_N component magnetic traces from four stations from the 210MM magnetometer array whose positions are shown in Figure 2.3. At the time of the event

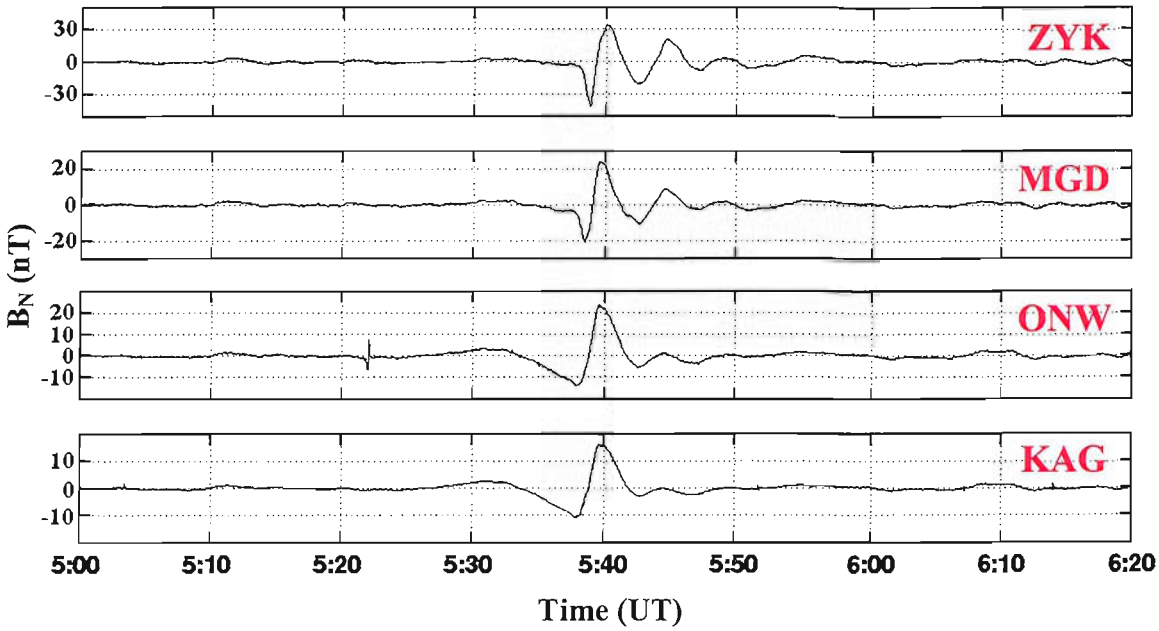

Figure 7.18 The B_N component magnetic traces from stations in the 210MM magnetometer array. These data have been filtered to remove the lower frequency variations.

the chain is located in the afternoon sector at 14-15 MLT. The figure reveals that the bipolar signature is present in the data. Comparing the B_E component magnetic traces from two stations revealed that the KAG magnetometer responded before ZYK which lies 20° further to the east. This suggests that a current structure is travelling eastwards across the stations, the leading vortex rotating with the opposite sense to the corresponding vortex in the westward moving TCV seen at IMAGE. Due to the lack of data from high latitude stations in the afternoon sector, the sense of rotation of the easterly moving TCV is a conjecture and only holds true if both TIX and CHD lie to the south of the vortical system; however, this is likely to be a valid assumption considering that both these stations are located several degrees south of typical TCV latitudes [Zesta et al., 2002].

As in the previous study, there is evidence for the existence of field line resonances (FLRs) in both the ground-based magnetometers and the GOES-8 magnetometer at geosynchronous orbit. Figure 7.19a shows the power spectra of the five lower-latitude magnetometers (see Figure 7.15) for 30 mins over the event (05:35-06:05UT). The most distinct feature in this interval is the continuous 300 sec oscillation seen at all the stations, corresponding to a wave in the Pc5 frequency range. The strength of the oscillation peaks at TRO and decreases on moving to lower latitudes. The same feature is also detected in the west coast Greenland magnetometers shown in Figure 7.19c, the power peaking at FHB and decreasing with latitude. Figure 7.19b shows that the PC5 is also detected at geosynchronous orbit by the GOES-8 magnetometer, along with a second lower period (220 sec) feature.

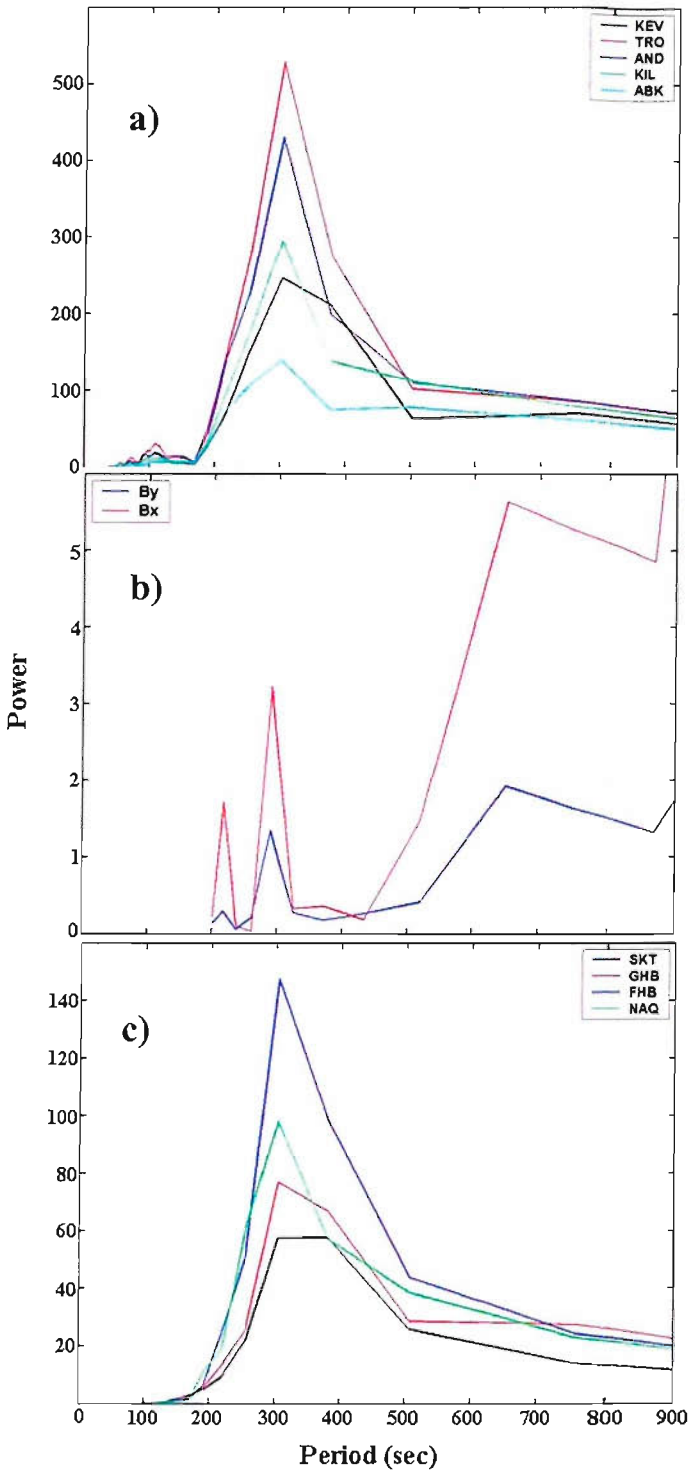

Figure 7.19 ***a)*** The power spectra of the five lower-latitude magnetometers (see Figure 7.15) for 30 mins over the event. The most distinct feature in this interval is the continuous 5 min oscillation seen at all the stations, corresponding to a wave in the Pc5 frequency range. ***b)*** The power spectra for the B_x and B_y magnetic components detected by the GOES-8 onboard magnetometer. The high period 300 sec resonance is evident along with a lower power, shorter period 220 sec oscillation. ***c)*** The power spectra

of the four lower-latitude (see Figure 7.17) west coast Greenland magnetometers , which supports the existence of a global Pc-5 oscillation. The power spectra in all the above cases were taken over a 30 min period from 5:35UT to 6:05 UT.

7.3 Discussion

The 29 December event has been analysed in a similar way to the morning event on 26 November. Both events are characterised by the arrival of enhanced solar wind dynamic pressure, but the IMF orientation variation is different and so the magnetosphere/ionosphere system is expected to show comparable effects in the two cases, with differences arising from the IMF behaviour. Chapter 6 showed that data from the first event was consistent with a solar wind density front being converted into a fast (HM) compressional wave at the bow shock, which propagated across the magnetosheath. Upon reaching the magnetopause, compressional Alfvénic waves are launched into the magnetosphere, generating Pc5 oscillation signatures both on the ground and at geosynchronous orbit over a wide range of local times.

On 29 December, the reaction of the magnetosphere-ionosphere system to the impact of a pressure front paralleled that observed on 26 November. The GOES-8 satellite observed a 5 min oscillation in the magnetic field accompanied by a change in the magnetic field strength. In its position in the southern hemisphere an increase in field strength of both the B_x and B_y components reflects a stretching of magnetic field lines tailward due to the compression of the magnetosphere. This compression squeezes the tail lobes and moves the satellite on to a higher L-shell. This magnetospheric compression is also reflected in the increase in the Dst index at around 6:00 UT, which implies a reconfiguration of the geomagnetic field. After the initial reaction of the magnetosphere to the pressure front, the B_x component does not immediately recover, but instead continues to increase in strength. This could imply that open flux was being added to the system, transported antisunward into the tail lobe; however, the steadily northward IMF indicates that this was not the case and the data demonstrate how the effect of the density pulse is drawn out in time as it propagates down the tail (squeezing the tail at increasingly negative X because the solar wind static pressure $N_{sw}k_BT_{sw}$ is enhanced) and how the step change in solar wind pressure continues to reconfigure the tail field over an extended period.

Geosynchronous orbit is an ideal location from which to study and monitor the access and delivery of plasma sheet material from the magnetotail into the inner magnetosphere. The geosynchronous orbit is complex because it tends to skim the inner boundary of the plasma sheet. In quiet times, geosynchronous satellites are generally Earthward of the plasma sheet. During periods of northward IMF plasma sheet plasma does not typically penetrate into the near-Earth region because of the very weak convection that exists during northward IMF. The conditions under which such plasma can penetrate close to the Earth are (1) a sudden southward IMF that follows an extended interval of northward IMF and (2) a very strong magnetospheric compression caused by a large increase in the solar wind dynamic pressure, under conditions of persistent northward IMF.

A study by Thomsen et al. [2003] of the same event revealed the delivery of cold, dense plasma sheet into the near-Earth region. The pressure shock dramatically compressed the pre-existing hot-ion population (100 eV – 45 keV) observed at geosynchronous orbit. The analysis presented here uses data from the same four geosynchronous satellites to examine the effect of the pressure front on the higher-energy particle population. Figure 7.2 shows the positions of the geosynchronous satellites: GOES-8, 1990-05, 1991-080, 1994-084, whose data was available for the period of interest.

At the nightside, the GOES-8 satellite was in a good position to observe the movement of plasma between the magnetotail and the inner magnetosphere. At 5:39 UT, GOES-8 observed a rapid decrease in high-energy electron flux (>0.6 MeV) corresponding to the decrease in the magnetic field strength. As with the magnetometer data, the electron flux remains at the post-pressure front level for a number hours after the impact. The similarity between the magnetic data and the high-energy electron data implies that the same mechanisms govern the behaviour of both. This means that the decrease in electron flux is due to the repositioning of the satellite onto an L-shell with a higher L-value. The new L-shell is populated with a

lower flux of electrons suggesting that it threads a different plasma regime. The decrease in flux resulting from the impact of the pressure front, therefore, represents the passage of a boundary across the satellite moving it into a new plasma region. The Thomsen et al. [2003] study identifies this region as the plasma sheet.

The particle data from the three LANL satellites show that the motion of the plasma sheet Earthward is observed almost simultaneously at a number of MLT sectors. The simultaneity reveals that the plasma did not appear to drift azimuthally from one satellite to another as would occur during enhanced dayside convection, instead with the IMF B_z continuously northward, it appears that the plasma sheet plasma lay stagnant just outside of geosynchronous orbit and was pushed in to that distance by the dayside shock. This explains the near simultaneous decrease in flux at all four satellites. There is however, a small time discrepancy between the satellite observations which suggests that the dayside magnetospheric field reacted to the shock a few minutes before the nightside explaining why the data from the 1994-084 satellite on the dayside in seen to react before the 1990-05 and 1991-080 satellites on the nightside. The high solar wind density, which characterised the pressure front, remained enhanced for the rest of the day. This meant that the magnetosphere stayed in a compressed state long after the initial shock, providing an explanation of why neither the particle flux nor the GOES-8 magnetometer data returned to pre-pressure front levels.

The compression of the magnetosphere also had a transient effect on the high-energy proton plasma population (< 1.2 MeV) detected by all four geosynchronous satellites. The origin of this burst of energised particles is not clear but it may indicate that the squeezing of the tail has increased the magnetic shear across the cross-tail current sheet and caused a pulse of tail reconnection. This would be consistent with the burst of enhanced nightside flow seen by SuperDARN (Figure 7.11). Because this is only $\Delta t \approx 4$ min after the pressure pulse hit the dayside magnetopause, the effects of the pressure pulse have propagated just $\Delta t V_{sw} \approx 18 R_E$ down the tail and it is debatable that such a near-Earth location can induce a reconnection pulse under

these strongly northward IMF conditions. The SuperDARN data show a second flow burst occurred 6 min later (Figure 7.11) and second weak burst of energetic proton is seen by LANL91 and LANl94 (Figures 7.6 And 7.7). However, at GEOS8 no second burst is seen, but this might be explained by the reconfiguration of the tail field. Other mechanisms proposed to generate enhanced precipitation and aurora during pressure pulses are discussed below. The SuperDARN data presented here show that they are associated with enhanced field-aligned currents which cause enhanced flow over 1-2 hours of MLT.

The main difference between the upstream conditions on the 26 November and the 29 December was the orientation of the IMF. The November event was characterised by a brief southward excursion of the IMF, which occurred in parallel with the increase in solar wind pressure. In the December event, the IMF was northwards for several hours before the arrival of the pressure front, and increased in strength at the same time as the solar wind pressure increased. The filtering technique introduced the possibility that the strengthening of the IMF B_z component could have resulted in a short-lived burst in high-latitude magnetopause reconnection on the sunward edge of the tail lobe. This means that, as in the November event, the simultaneous variations in solar wind pressure and the magnitude of the IMF makes it harder to differentiate between their individual impact on the ionosphere.

The global images from the IMAGE satellite showed that before the two solar wind features were incident on the magnetosphere, the auroral oval was faint, located between latitudes of 75° and 80° on the dayside. After 5:39 UT the Lyman-α oval moved to lower latitude and increased significantly in intensity. This increase in emission was first observed in a small cusp-like region at noon, spreading to the night sector in a few minutes. The upstream trigger for this auroral activity is debatable. Cusp signatures are observable whenever the IMF is northward and the solar wind density is at least slightly increased [Frey et al., 2002]. Milan et al. [2000], described an event study of an interval of northward IMF, where they observed luminosity near local noon poleward of the dayside auroral oval. They interpreted this emission as the

signature of high-latitude reconnection. Frey et al. [2002] used a field line model to map the region of cusp precipitation into the magnetosphere. Under northward IMF conditions, the cusp field lines were mapped to the high-latitude magnetopause and the magnetospheric lobe region. This implies that direct magnetosheath precipitation after magnetic reconnection in the high-latitude lobe region is a possible candidate for the small region of proton and electron emission observed by IMAGE at noon. The ground-based observations show enhanced soft electron precipitation and H_β emission where the satellite observes enhanced Lyman-α. The enhancement in these cusp auroral emission intensities can be associated with the increase in the solar wind density. The increase in the size of the Lyman-α patch seen by IMAGE could signify that more reconfigured lobe open field lines have been generated (i.e. there has been a pulse of lobe reconnection) or that the precipitation flux down already opened field lines is increased because of the increase in solar wind and sheath densities. The filtering technique used here provides evidence from the magnetometer data that there is a background flow response in addition to the TCV transient. This would imply that there was indeed a lobe reconnection pulse. Unfortunately, the lack of SuperDARN echoes on the dayside prevents us from searching for the direct flow signature of such a lobe magnetopause reconnection burst.

Global signatures of the aurora caused by interplanetary shocks have been the subject of several studies in recent years using UV imaging. The global signatures of shock aurora is that the aurora first brightens near local noon in the auroral zone immediately following the arrival of a pressure shock at the dayside magnetopause. High compression of the magnetopause and the outer magnetosphere may lead to particle precipitation due to lowering of the mirror points of trapped particles to altitudes below 100 km [Spann et al., 1998]. The fact that the noon emission region does not appear to be poleward of the main auroral oval favours the pressure shock as the means of generating this auroral signature. It is quite possible however, that both the IMF and solar wind pressure conditions play a contributing role.

The IMAGE data also revealed that the auroral brightening rapidly was almost simultaneously enhanced in the night sector. The effect is predominantly in the morning sector for electron precipitation, with the proton precipitation favouring the afternoon sector to a lesser degree, as expected from azimuthal drift of newly injected plasma. Neither the IMAGE images or the SuperDARN convection patterns show the enhancements spreading from the dayside to the nightside, indicating that the nightside effects are an independent response of the tail and not a dayside phenomenon that has propagated antisunward. Thus the TCV and the nightside auroral enhancements appear to be somewhat independent responses to the one trigger, the pressure pulse. A number of studies have observed this behaviour [Zhou et al., 2001, 2003; Meurant et al., 2004] and a number of mechanisms have been suggested. One of these mechanisms relies on the distortion of the field lines by the compression of the magnetosphere which causes magnetic shearing. This magnetic shearing generates shear Alfvén waves and field-aligned currents in a mechanism comparable to that favoured in the last event to produce TCV signatures (Section 1.3.2). Particles precipitate along these field-aligned currents and cause the aurora observed.

A study by Zhou et al. [2003] calculated that Alfvén waves can propagate at a speed of ~ 1000 kms^{-1} in the magnetosphere and would therefore arrive at the nightside plasma sheet within 2 mins. This implies that the shock aurora could reach the midnight sector in ~ 1-2 mins or faster, which is consistent with the nightside precipitation observed by IMAGE a few minutes after the arrival of the pressure front.

For the 26 November study, set out in the previous chapter, the high-frequency magnetic variations isolated by the filter, were compared to the magnetohydrodynamic modelling of pressure pulse effects introduced in Section 1.3.2. The results of the study concluded that many of the signatures predicted by the model were in fact observed by both the satellite-borne and ground-based instruments. The generation of two sets of TCVs propagating away from noon across

the morning and afternoon sectors; the establishment of short-lived resonances on field-lines at lower than cusp latitudes.

In the 29 December event, the magnetosphere and ionosphere were exposed to similar upstream pressure changes as the November event, but the IMF orientation change was different. The instruments that observed the overall impact of the pressure front revealed a set of signatures that were comparable to the previous event. The IMAGE magnetometer array located in the morning sector and the MM210 array located in the afternoon sector, both tracked a set of twin vortices moving in opposite directions away from noon. The position of the Greenland array to the west of IMAGE, made it possible to study the temporal evolution of the westward travelling TCV. In both the 26 November and 29 December events, the TCV was seen to accelerate toward the nightside, reaching a speed of ~16-18 kms^{-1} at around 8 MLT. In the study of the first event, it was predicted that after reaching this speed the TCV would slow again due to the unit length on the magnetopause maps to increasingly smaller lengths in the ionosphere. The observations on the 29 December are different, showing that the TCV in fact continued to accelerate between IMAGE at 8 MLT and Greenland at 6-7 MLT. This continual increase in speed causes the vortices to become progressively elongated in the E-W direction reflected in the decrease in peak-to-peak amplitude of the B_N component observed during both events.

In the magnetohydrodynamic model, the convection vortices form at locations where field line resonances occur, suggesting that the ground signatures of a pressure pulse at the magnetopause is the excitation of these resonances. This implies that the spatial structure and temporal evolution of the TCV is governed by the characteristics of the oscillating wave modes present on the local field lines, as it propagates away from the resonance region a reduction in wave power and hence amplitude would be expected. Spectral analysis of the lower-latitude IMAGE magnetometer traces show the existence of a 300 sec resonance feature after the arrival of the pressure front at 5:49 UT. The strength of this resonant oscillation peaks at a magnetic latitude between 71.5° (BJN) and 73° (HOP), decreasing away at lower and higher latitudes.

Spectral analysis of the low-latitude IMAGE and Greenland magnetometer data revealed a 5 min resonance feature, which peaked in power at latitudes comparable to the latitudes at which the centre of the TCV was observed.

7.4 Event Summary

The 29 December event has been analysed in a similar way to the morning event on 26 November. Both events are characterised by the arrival of enhanced solar wind dynamic pressure, but the IMF orientation variation is different and so the magnetosphere/ionosphere system is expected to show comparable effects in the two cases, with differences arising from the IMF behaviour. During the 29 December event, a range of ground-based and satellite-borne observations showed evidence of magnetic compression and a short-lived burst in high-latitude magnetopause reconnection on the sunward edge of the tail lobe. The filtering technique, introduced in Chapter 6, revealed an increase in flow associated with the ionospheric response to an increase in B_z accompanied by the formation of a filamentary field-aligned current system due to the impact of the pressure front. The position of the satellite-borne and ground-based instruments made it possible to study the evolution of the ionospheric flows and particle precipitation associated with the two upstream features. The IMAGE satellite observed a burst in both proton and electron emission occurred in the noon sector, quickly followed by an auroral brightening on the nightside. These observations are consistent with direct magnetosheath precipitation after magnetic reconnection at the high-latitude lobe region and that aurora caused by magnetospheric compression, suggesting that both the mechanisms play a contributing role. The same holds true for the generation of the optical signatures at LYR.

Unlike the 26 November event, the reaction of the magnetosphere to both upstream features could be observed at geosynchronous orbit. The compression of the magnetosphere was observed in the magnetic and plasma data of the GOES-8 and

LANL satellites, supported by the increase in the Dst index. This compression squeezes the tail lobe and pushes the plasma sheet into geosynchronous distances. There is evidence that the increase in magnetic compression causes an increase in magnetic shear across the cross-tail current, resulting in a pulse of tail reconnection.

The reaction on the ground to the impact of the pressure front was comparable to the reaction on 26 November. Two trains of vortices were seen to travel tailward across the dawn and dusk sector. The position of the magnetometers meant that the behaviour of the vortices could be studied around at the nightside. Evidence showed that they continued to accelerate and elongate as they propagate. The existence of a global Pc5 oscillation is consistent with the findings of the 26 November study, supporting the magnetohydrodynamic model as a way of generating TCVs.

Chapter 8.

Conclusions and Future Work

The main aim of the research presented in this thesis was to examine the characteristic response of the global magnetospheric-ionospheric system to variations in upstream solar wind parameters. The effect of transient variations in solar wind dynamic pressure and IMF orientation were followed through the solar wind, across the bow shock and magnetosheath, into the magnetosphere and down to the ionosphere. Multi-instrument studies provided plasma, energetic particle and magnetic field data to determine the effects on the open-closed boundary motion and the signatures produced within the magnetosphere and at the high-latitude ground stations. A number of techniques have been developed to provide new ways of examining the impact of individual solar wind features on the magnetosphere-ionosphere system and to provide a means of interpreting the instrument observations presented in this thesis.

Calculating the Propagation Time

The good upstream solar wind coverage provided by the ACE and Wind satellites during the three events, meant that an accurate estimation of the ACE-to-ionosphere propagation time could be made. The orbits of ACE and Wind enabled them to monitor the highly variable speed and composition of solar wind features as they propagate Earthwards. Using the spatial separation of the two satellites it was possible to calculate the orientation of the phase front of a solar wind structure in two dimensions with respect to the propagation flow, and thus provide an accurate estimation of the time it impacts on the dayside magnetopause. From a single spacecraft, we do not know this orientation and an error would be introduced by adopting an assumption (usually it is assumed that the phase front lies in the plane normal to the solar wind low direction). Determining the three-dimensional

orientation requires three craft that are not coplanar. By using data from the ground or satellites within the magnetosphere, or from the Geotail satellite close to the magnetopause, it was shown that the accuracy of the calculations using two craft meant that a third craft was not necessary in establishing a good estimation of the propagation time.

Filtering

This study presented filtering as an effective method of separating the ionospheric response to changes in solar wind pressure and IMF orientation. Sibeck [1990] demonstrated that magnetopause and ground signatures generated by the solar wind pressure variations are almost identical to those previously attributed to impulsive reconnection at the dayside magnetopause, such that distinguishing one from the other is very difficult. Filtering provides a way of differentiating between slow convection variations and the higher frequency pressure front effects. The cut-off frequency of the filter was found to be most effective at 15 min corresponding to the response time of the reconnection-triggered convection patterns predicted by the Cowley-Lockwood [1992] flow excitation theory. The broad similarity of the low-pass filtered observations with predictions from a first-order model of the effects of a reconnection pulse on the convective flows support this technique as a way of separating the magnetosphere-ionosphere responses to these two types of interplanetary events. The high-pass filtered data show the vertical flow forms expected in response to solar wind pressure pulses.

Modelling

The wide range of satellite and ground-based data revealed a number of practical applications for both the Lockwood and Davis [1996] and the Lockwood and Morley [2004] models, in terms of identifying common elements of a global magnetospheric response in different data sets. Data from interplanetary satellites for the first event provided input parameters for the model such that the model output could be compared to the observations. The similarities between the model predictions and the

data for the first event (in terms of the evolution of the open-closed boundary, the cusp aurora, the flow pattern and the transpolar voltage) gave confidence that the predictions made by the model for the second event could be considered a reliable overview of the ionospheric response to the reconnection pulse. The large number of free parameters, due to a lack of suitable input data, limited the extent to which a detailed comparison could be made, placing limits on the application of the model.

Conclusions

The techniques discussed above provide a way of interpreting the data with respect to individual upstream features. The combination of events meant that a study of the individual and combined impact of upstream IMF and solar dynamic pressure on the magnetospheric-ionospheric system could be done.

The major feature of the first event, presented in Chapter 5, was the ionospheric response to two brief swings of the interplanetary magnetic field (IMF) towards a southward orientation. The Lockwood and Davis model was employed to model the cusp ion precipitation and proton aurora emission to fit observed variations of the peak Doppler-shifted Lyman-α intensity. The implications for the detection of pulsed reconnection using proton and electron aurora were discussed, favouring the use of proton emission over commonly-used electron emissions (in particular, the 630 nm oxygen red line). The accuracy of the model fit to the data meant that the observed spatial distributions of this emission on newly-opened field lines could be reproduced by combining the Lockwood and Davis ion precipitation model with the Lockwood and Morley ionospheric convection model. A comparison of the model results to observations by the FUV IMAGE and SuperDARN data confirmed quantitatively the concepts of ionospheric flow excitation by Cowley and Lockwood [1992] on which the model is based.

In the second event, presented in Chapter 6, filtering was introduced as a way of separating the slow convection variations caused by dayside reconnection from the higher frequency pressure-induced variations. The ground-based data were

interpreted in terms of the passage of the open-closed boundary (OCB) over the instruments as a reaction to the onset of reconnection and the passage of the TCV. The study gives an optical interpretation of a pressure pulse event in the region of the cusp. In particular, a ground-based method for detecting the OCB was presented, one not published before in literature. This is important as past studies have relied on passes by polar-orbiting satellites (such as DMSP) to provide information on the OCB location and these are often not at the MLT and/or UT of the ground-based observations. The interpretation supports studies that have linked TCV signatures to compression induced global field-line resonances, which are detected in plasma flows, ionospheric currents, geostationary magnetic fields and particles, and precipitating auroral particles.

The third event, presented in Chapter 7, supported the methods and analysis of the event two study. It highlighted the role of modelling as effective tool in differentiating between the effects of different upstream features on the ionosphere. The lack of model data in this event, due to the inability of the Lockwood and Morley model to replicate the effects of northward IMF, meant that interpreting both the ground-based and satellite data in terms of the upstream variations was difficult.

Future Work

Every event will be different in detail and this thesis has observed just three. More events with similar upstream features need to be investigated in order to test the reliability of the methods described above, and in doing so find data that supports the conclusions drawn.

- More situations of southward IMF, with good instrument coverage of the high-latitude ionosphere, are needed to test the accuracy and limitations of both the Lockwood and Davis [1996] and the Lockwood and Morley [2004] models.

- Examples of pulsed reconnection are required to investigate the effect on proton and electron aurora for a range of interplanetary conditions.
- Multi-instruments studies are necessary to examine the impact of pressure and IMF variations on the magnetosheric-ionopsheric system as a whole.
- More examples of upstream pressure fronts are needed to further investigate the issue of TCV generation, and their relationship to global field-aligned resonances.
- Further work on the optical interpretation of the motion of the OCB under the influence of reconnection and pressure-induced ionospheric flows.
- Pressure front events with good optical coverage would provide a means of testing the interpretation of the optical data in the second event.
- More examples of combined pressure front and southward IMF events would provide a way of testing the filtering technique and the interpretation of the data with respect to the individual upstream variations.

All these lines of investigation are needed to provide further support of the methods and results presented in this thesis.

References

Ahn, B.-H., Kamide, Y., Kroehl, H.W. and Gorney, D.J., Cross-polar potential difference, auroral electrojet indices, and solar wind parameters, *J. Geophys. Res.*, ***97***, 1345-1352, 1992.

Aggson, T.L., Heppner, J.P. and Maynard, N.C., Observations of large magnetospheric electric fields during onset phase of a substorm, *J. Geophys. Res.*, ***88***, 3981-3990, 1983.

Aggson, T.L., Heppner, J.P. and Gambardella, P.J., Electric field measurements at the magnetopause. I Observations of large convective velocities at rotational magnetopause discontinuities, *J/ Geophys. Res.*, ***88***, 10000-10010, 1983.

Araki,T., A physical model of the geomagnetic sudden commencement, in M. J. Engebretson, Takahasi, K. and Scholer, M. (eds.), Solar wind sources of magnetospheric ultra-low frequency waves, *Geophys. Mono* ***81***, *American Geophys. Union,* 1994.

Baker, K.B., Dudeney, J.R., Greenwald, R.A., Pinnock, M., Newell, P.T., Rodger, A.S., Mattin, N. and Meng, C.-I., HF radar signatures of the cusp and low-latitude boundary layer, *J. Geophys. Res.*, ***100,*** A5, 7671-7695, 1995.

Banks, P. M., Araki, T., Clauer, C. R., St-Maurice, J. P., and Foster, J. C., The interplanetary magnetic field, cleft currents, and plasma convection in the polar caps, *Planet. Space Sci.*, ***32,*** 1551-1560, 1984.

Baumjohann, W. and Treumann, R.A., Basic Space plasma physics, *Imperial College Press,* 1997.

Beynon, W.J.G and Williams, P.J.S, Incoherent scatter of radio waves from the ionosphere, *Reports on Progress in Phys.*, ***41***, 909-956, 1978.

Boyle, C.B., Reiff, P.H. and Hairston, M.R., Empirical polar cap potentials, *J. Geophys. Res.*, ***102***, A1, 111-126, 1997.

Boudouridis, A., Zesta, E., Lyons, L., Anderson, P. and Lummerzheim, D., The Effect of Solar Wind Pressure Pulses on the Size and Strength of the Auroral Oval, *American Geophys. Union, Fall Meeting*, #SM42D-04, 12/2001.

Burch, J. L., Rate of erosion of dayside magnetic flux based on a quantitative study of polar cusp latitude on the interplanetary magnetic field, *Radio Sci., 8,* 955-961, 1973.

Burch, J. L., Quasi-neutrality in the polar cusp, *Geophys. Res. Lett., 12,* 469-472, 1985.

Chisham, G., Pinnock, M., Coleman, I. J., Hairston, M. R. and Walker, A.D.M., An unusual geometry of the ionospheric signature of the cusp: implications for magnetopause merging sites, *Annales Geophys., **20***, 29-40, 2002.

Clauer, C. R. and Banks, P. M., Relationship of interplanetary electric field to the high latitude ionospheric electric field and currents: observations and model simulation, *J. Geophys. Res., **91,*** 6959-6971, 1986.

Clauer, C.R., A Statistical Investigation of Travelling Convection Vortices Observed by the West Coast Greenland Magnetometer Chain, *American Geophys. Union, Spring Meeting* #SM61A-03, 5/2001.

Coleman, I. J., Pinnock, M. and Rodger, A.S., The ionospheric footprint of anti-parallel merging regions on the dayside magnetopause, *Annales Geophys., **18,*** 511-516, 2000.

Coleman, I.J., Chisham, G., Pinnock, M. and Freeman, M.P., An ionospheric convection signature of anti-parallel reconnection, *J. Geophys. Res., **106,*** 28995-29008, 2001.

Cowley, S.W.H., Satellites and space science. II, Spaceflight, ***19***, 65-72, 1977.

Cowley, S.W.H., The causes of convection in the Earth's magnetosphere: A review of developments during IMS, *Rev. Geophys., **20,*** 531-565, 1982.

Cowley, S.W.H., Solar wind control of magnetospheric convection, *In ESA Achievements of the Intern. Magnetospheric Study (IMS)*, 483-494, 1984a.

Cowley, S.W.H. and Owen, C.J., A simple illustrative model of open flux tube motion over the dayside magnetopause, *Planet. Space Sci., **37***, 1461-1475, 1989.

Cowley, S.W.H. and Lewis, Z.V., Magnetic trapping of energetic particles on open dayside boundary layer flux tubes, *Planet. Space Sci., **38,*** 1343-1350 1990.

Cowley, S.W.H., Van Eyken, A.P., Thomas, E.C., Williams, P.J.S. and Willis, D.M., Studies of the cusp and auroral zone with incoherent scatter radar – The scientific and technical case for a polar-cap radar, *J. Atmos. & Terrest. Phys., **52,*** 645-663, 1990.

Cowley, S.W.H., Morelli, J.P., and Lockwood, M., Dependence of convective flows and particle precipitation in the high-latitude dayside ionosphere on the X and Y components of the interplanetary magnetic field, *J. Geophys. Res., **96,*** 5557-5564, 1991.

Cowley, S.W.H. and Lockwood, M., Excitation and decay of solar-wind driven flows in the magnetosphere-ionosphere system, *Annales Geophys., **10,*** 103-115, 1992.

Cowley, S.W.H., The behaviour of systems in the space environment, ed. S.-I. Ohtani et al., pp 91-106, *American Geophys. Union,* 2000.

Cowley, S.W.H. and Lockwood, M., Incoherent scatter radar observations related to magnetospheric dynamics, *Adv. Space Res., **20,*** 873-882, 1997.

Crooker, N.U., Dayside merging and cusp geometry, *J. Geophys. Res., **84,*** 951, 1979.

Crooker, N.U., Toffoletto, F. and Gussenhoven, M.S., Opening the cusp, *J. Geophys. Res., **96,*** 3497-3503, 1991.

Crooker, N.U., Reverse convection, *J. Geophys. Res., **97,*** 19363-19372, 1992.

Crooker, N.U. and Rich, F.J., Lobe cell convection as a summer phenomenon, *J. Geophys. Res., **98, 13 403-13 407,*** 1993.

Daly, P.W and Fritz, T.A., Trapped electron distributions on open magnetic field lines, *J. Geophys. Res., **87,*** 6081-6088, 1982.

Davis, C.J. and Lockwood, M., Predicted signatures of pulsed reconnection in ESR data, *Annales Geophys., **14,*** 1246-1256, 1996.

Dungey, J. W., Conditions for the occurrence of electrical discharges in astrophysical systems, *Phil. Mag., **44,*** 725, 1953.

Dungey, J.W., Interplanetary Magnetic Field and the Auroral Zones, *Phys. Rev. Let.,* ***6,*** 47-49, 1961.

Eather, R.H., Radiation from Positive Particles Penetrating the Auroral Atmosphere, *J. Geophys. Res.,* ***72,*** 4602, 1967.

Eather, R.H., Polar cusp dynamics, *J. Geophys. Res.,* ***90,*** 1569-1576, 1985.

Elphinstone, R.D., Hearn, D.J., Murphree, J.S. and Cogger, L.L., Mapping using the Tsyganenko long magnetospheric model and its relationship to Viking auroral images, *J. Geophys. Res.,* ***96,*** 1467-1480, 1991.

Elphinstone, R.D., Murphree, J.S., Hearn, D.J., Cogger, L.L., Newell, P.T. and Vo, H., Viking observations of the UV dayside aurora and their relationship to DMSP particle boundary definitions, *Ann. Geophys.,* ***10,*** 815-826, 1992.

Etemadi, A., Cowley, S.W.H., Lockwood, M., Bromage, B.J.I., Willis, D.M. and Lühr, H., The dependence of high-latitude dayside ionospheric flows on the north-south component of the IMF: a high time resolution correlation analysis using EISCAT "POLAR" and AMPTE UKS and IRM data, *Planet. Space Sci.,* ***36***, 471-498, 1988.

Evans D. and Kroehl, H., Ionospheric convection response to changing IMF direction, *Geophys. Res. Lett.,* ***18***, 721-724, 1991.

Fedder, J.A., Mobarry, C.M. and Lyon, J.G., Reconnection voltage as a function of IMF clock angle, *Geophys. Res. Lett.,* ***18,*** 1047-1050, 1991.

Fejer, B.G. and Kelley, M.C., Ionospheric irregularities, *Rev. Geophys. & Space Phys.,* ***18,*** 401-454, 1980.

Finch, I., Lockwood, M. and Stamper, R., Energy coupling between the solar wind and the upper atmosphere on a range of timescales, *Annales Geophys.*, in press, 2003.

Freeman, M. P. and Southwood, D. J., The effects of magnetospheric erosion on mid- and high- latitude ionospheric flows, *Planet. Space Sci.,* ***36,*** 509, 1988.

Frey, H.U., Mende, S.B., Carlson, C.W., Gérard, G.-C., Hubert, B., Spann, I., Gladstone, R. and Immel, T.J., The electron and proton aurora seen by IMAGE-FUV and FAST, *Geophys. Res. Lett.,* ***28,*** 1135-1139, 2001a.

Frey, H.U., Mende, S.B., Immel, T.J., Fuselier, S.A., Claflin, E.S., Gérard, G.-C. and Hubert, B., Proton aurora in the cusp, *J. Geophys. Res.,* ***10,*** 1029, 2/1 –2/17, July 2002.

Frey, H.U, Phan, T.D., Fuselier, S.A. and Mende, S.B., Continuous magnetic reconnection at Earth's magnetopause, *Nature, **426**,* 6966, 533-537, 2003.

Friis-Christensen, E., Vennerstrom, S., McHenry, M.A., Clauer, C.R., Ionospheric travelling convection vortices observed near the polar cleft: a triggered response to sudden changes in the solar wind, *Geophys. Res. Let., **15, 3,*** 253-256, 1988.

Galand, M., Introduction to special section: Proton precipitation into the atmosphere, *J. Geophys. Res., **106**,* 1-6, 2001.

Gérard, J.-C., Hubert, B., Bisikalo, D.V. and Shematovich, V.I., A model of the Lyman-alpha line profile in the proton aurora, *J. Geophys. Res., **105**, 15795-15806,* 2000.

Gérard, J.-C., Hubert, B., Meurant, M., Shematovich, V.I., Bisoikalo, D.V., Frey, H.U., Mende, S. and Gladstone, G.R., Observations of the proton aurora with IMAGE FUV imager and simultaneous ion flux measurements, *J. Geophys. Res.,* **106**, 28 939-28 948, 2001.

Glaßmeier K.-H. and Heppner,C., Travelling magnetospheric convection twin vortices - Another case study, global characteristics, and a model, *J. Geophys. Res., **97**,* A4, 3977-3992, 1992.

Gonzalez, W.D. and Mozer, F.S., A quantitative model for the potential resulting from reconnection with an arbitrary interplanetary magnetic field, *J. Geophys. Res., **79**,* 4186, 1974.

Greenwald, R.A., Baker, K.B., Dudeney, J.R., Pinnock, M., Jones, T.B., Thomas, E.C., Villain, J.-P., Cerisier, J.-C., Senior, C., Hanuise, C., Hunsucker, R.D., Sofko, G., Koehler, J., Nielsen, E., Pellinen, R., Walker, A.D.M., Sato, N. and Yamagishi, H., Darn/Superdarn: A Global View of the Dynamics of High-Latitude Convection, *Space Sci. Rev., **71**,* 761-796, 1995.

Gussenhoven M.S., Heinemann, N. and Hardy, D.A., Systematics of the equatorward diffuse auroral boundary, *J. Geophys. Res., **88***, 5692-5708, 1983.

Hapgood, M.A., Bowe, G., Lockwood, M., Willis, D.M. and Tulunay, Y., Variability of the interplanetary magnetic field at 1 A.U. over 24 years: 1963-1986, *Planet. Space Sci., **39**,* 411-423, 1991.

Hardy, D.A., Gussenhoven, M.S. and Holeman, E., A statistical model of auroral electron precipitation, *J. Geophys. Res.*, ***90,*** 4229-4248, 1985.

Heppner, J.P. and Maynard, N.C., Empirical high-latitude electric field models, *J. Geophys. Res.*, ***92,*** 4467-4489, 1987.

Hill, T.W. and Reiff, P.H., Evidence of magnetospheric cusp proton acceleration by magnetic merging at the dayside magnetopause, *J. Geophys. Res.*, ***82,*** 3623-3628, 1977.

Horwitz, J.L. and Akasofu, S.-I., The response of the dayside aurora to sharp northward and southward transitions of the interplanetary magnetic field and to magnetospheric substorms, *J. Geophys. Res.* ***82,*** 2723-2734, 1977.

Hudson, P.D., Discontinuities in an anisotropic plasma and their identification in the solar wind, *Planet. And Space Sci.*, ***18***, 1611-1622, 1970.

Kabin, K., Rankin, R., Fenrich, F.R., Rae, I.J. and Marchand, R., Magnetosphere-ionosphere Coupling for the Steady-state Solar Wind Conditions of November 26 2000, *Amer. Geophys. Union,* Fall Meeting 2001, abstract #SM31B-0769.

Kessel, R.L., Chen, S.-H, Green, J.L., Feng, S.F., Boardsen, S.A., Tan, L.C., Eastman, T.E., Craven, J.D. and Frank, L.A., Evidence of high-latitude reconnection during northward IMF: Hawkeye observations, *Geophys. Res. Lett.*, ***23,*** 583-586, 1996.

Khan, H. and Cowley, S.W.H., Observations of the response time of high-latitude ionospheric convection to variations in the interplanetary field using EISCAT and IMP-8 data, *Annales Geophys.*, ***17***, 1306-1355, 1999.

Kivelson, M.G. and Southward, D.J., Ionospheric travelling vortex generation by solar wind buffeting of the magnetosphere, *J. Geophys. Res.*, ***96***, 1661-1667,1991.

Knipp, D.J., Emery, B.A., Richmond, A.D., Crooker, N.U., Hairston, M.R., Cumnock, J.A., Denig, W.F., Rich, F.J., de la Beaujardiere, O., Ruohoniemi, J.M., Rodger, A.S., Crowley, G., Ahn, B.-H., Evans, D.S., Fuller-Rowell, T.J., Friis-Christiansen, E., Lockwood, M., Kroehl, H., McClennan, C., McEwin, A., Pellinen, R.J., Morris, R.J., Burns, G.B., Papitashvili, V., Zaitzev, A., Troshichev, O., Sato, N., Sutcliffe, P. and Tomlinson, L., Ionospheric convection

response to strong, slow variations in a northward interplanetary magnetic field: A case study for January 14, 1988, *J. Geophys. Res.*, ***98***, 19,273-19,292, 1993.

Kobel, E. and Flückiger, E.O., A model of the steady-state magnetic field in the magnetosheath, , *J. Geophys. Res.*, **99**, 23,617, 1994.

Kunkel, T., Untiedt, J., Baumjohann, W. and Greenwald, R.A., Electric fields and currents at the Harang discontinuity - A case study, *J. Geophys.*, ***59***,. 73-86. DFG-NSF-supported research, 1986.

Lanchester B.S., Galand, M., Robertson, S.C., Rees, M.H., Lummerzheim, D., Furniss, I., Peticolas, L.M., Frey, H.U., Baumgardner, J. and Mendillo, M., High resolution measurements and modelling of auroral hydrogen emission line profiles, *Annales Geophs.*, ***21***, 1629-1643, 2003.

Lanzerotti L.J., Maclennan, C.G., Konik, R.M., Wolfe, A. and Venkatesan, D., Cusp latitude magnetic impulse events. I - Occurrence statistics, *J. Geophys. Res.*, ***96***, 14,009, 1991.

Leontyev, S.V., Starkov, G.V., Vorobjev, V.G. and Zverev, V.L., Dayside aurorae and their relations to other geophysical phenomena, *Planet. Space Sci.* ***40***, 621-639, 1992.

Lockwood, M., Ground-Based and Satellite Observations of the Cusp: Evidence for Pulsed Magnetopause Reconnection, in *"Physics of the magnetopause"*, ed. Song, P., Sonnerup, B.U.O. and Thomsen, M.F., American Geophysical Union Monograph **90**, 417-426, 1995.

Lockwood, M., Location and characteristics of the reconnection X-line deduced from low-altitude and ground-based observations. 1. Theory, *J. Geophys. Res.*, ***100***, 21791-21802, 1995a.

Lockwood, M., Energy and pitch angle dispersions of LLBL / cusp ions seen at middle altitudes: predictions by the open magnetosphere model, *Annales Geophys.*, ***15***, 1501-1514, 1997b.

Lockwood, M., An evaluation of the correlation between open solar flux and total solar irradiance, *Astro. and Astrophys.*, ***382***, 678-687, 2002.

Lockwood M., Waite, J.H.,Jr., Moore, T.E., Chappell, C.R. and Chandler, M.O., The cleft ion fountain, *J. Geophys. Res.*, ***90***, 9736-9748, 1985.

Lockwood, M., Cowley, S.W.H and Freeman, M.P., The excitation of plasma convection in the high-latitude ionosphere, *J. Geophys. Res.*, ***95***, 7961-7972, 1990.

Lockwood, M. and Cowley, S.W.H., Ionospheric Convection and the substorm cycle, in "Substorms 1, Proceedings of the First International Conference on Substorms, ICS-1", *ed C. Mattock, ESA-SP-335,* 99-109, European Space Agency Publications, Nordvijk, The Netherlands, 1992.

Lockwood, M., Moen, J., Cowley, S. W. H., Farmer, A. D., Løvhaug, U. P., Lühr, H., and Davda, V. N., Variability of dayside convection and motions of the cusp/cleft aurora, *Geophys. Res. Lett.*, ***20,*** 1011-1014, 1993.

Lockwood, M. and Smith, M.F., Comment on 'Mapping the dayside ionosphere to the magnetosphere according to particle precipitation characteristics' by Newell and Meng, *Geophys. Res. Letts.*, ***20***, 1739-1742, 1993.

Lockwood, M. and Smith, M.F., Low and middle altitude cusp particle signatures for general magnetopause reconnection rate variations. 1:Theory, *J. Geophys. Res.*, ***99***, 8531-8553, 1994.

Lockwood, M., Onsager, T.G., Davis, C.J., Smith, M.F. and Denig, W.F., The characteristic of the magnetopause reconnection X-line deduced from low-altitude satellite observations of cusp ions, *Geophys. Res. Lett., **21**, 2757-2760,* 1994.

Lockwood, M. and Davis, C.J., The occurrence probability, width and number of steps of cusp precipitation for fully-pulsed reconnection at the dayside magnetopause, *J. Geophys. Res.* ***100***, 7627-7640, 1995.

Lockwood, M., Onsager, T.G., Davis, C.J., Smith, M.F. and Denig, W.F., The characteristics of the magnetopause reconnection X-line deduced from low-altitude satellite observations of cusp ions, *Geophys. Res. Lett., **22**,* 867, 1995c.

Lockwood, M. and Davis, C.J., On the longitudinal extent of magnetopause reconnection bursts, *Annales Geophys., **14**,* 865-878, 1996a.

Lockwood, M. and Davis, C.J., An analysis of the accuracy of magnetopause reconnection rate variations deduced from cusp ion dispersion characteristic, *Annales Geophys.*, ***14***, 149-161, 1996.

Lockwood, M. and Hapgood, M.A., On the Cause of a Magnetospheric Flux Transfer Event, *J. Geophys. Res.*, ***103***, 26453-26478, 1998.

Lockwood, M., Davis, C.J., Onsager, T.G and Scudder, J.A., Modelling signatures of pulsed magnetopause reconnection in cusp ion dispersion signatures seen at middle altitudes, *Geophys. Res. Lett.*, ***25***, 591-594, 1998.

Lockwood, M. and Moen, J., Reconfiguration and closure of lobe flux by reconnection during northward IMF: evidence for signatures in cusp/cleft auroral emissions, *Annales Geophys.*, ***17***, 996-1011,1999.

Lockwood, M., Lanchester, B. S., Frey, H. U., Throp, K., Morley, S. K., Milan, S. E. and Lester, M., IMF control of cusp proton emission intensity and dayside convection: Implications for component and anti-parallel reconnection, *Annales Geophys.*, ***21***, 955-982, 2003a.

Lockwood, M., Moen, J., Van Eyken, A.P., Davies, J.A., Oksavik, K., and McCrea, I.W., Motion of the dayside polar cap boundary during substorm cycles: I. Observations of pulses in the magnetopause reconnection rate, *Annales Geophys.*, in press, 2003b.

Lockwood, M. and Morley, S.K., A Numerical Model of the Ionospheric Signatures of Time-Varying Magnetic Reconnection: I. Ionospheric Convection, *Annales Geophys.*, ***22***, 1, 73-91, 2004.

Lockwood, M., Lanchester, B.S., Morley, S.K., Throp, K., Milan, S.E. and Frey, H.U., Modelling the observed proton aurora and ionospheric convection responses to changes in the IMF clock angle: 2. The persistence of ionospheric convection, *J. Geophys. Res.*, 2003.

Lu, G., Reiff, P.H., Hairston, M.R., Heelis, R.A. and Karty, J.L., Distribution of convection potential around the polar cap boundary as a function of Interplanetary magnetic field, *J. Geophys. Res.*, ***94***, 13447-13461, 1989.

Lu, G., Cowley, S.W.H., Milan, S.E., Sibeck, D.G., Greenwald R.A. and Moretto, T., Solar wind effects on ionospheric convection: a review, *J. Atmos. Sol.-Terr. Phys.*, ***64***, 145-157, 2002.

Luhmann, J.G., Walker, R.J., Russell, C.T., Crooker, N.U., Spreiter, J.R. and Stahara, S.S., Patterns of potential magnetic field merging sites on the dayside magnetopause, *J. Geophys. Res.*, ***89***,1741-1744, 1984.

Lühr, H. and Blawert, W., Ground signatures of travelling convection vortices, in Solar Wind Sources of Magnetospheric ULF Waves, *Geophys. Mono. Ser.*, ***81***, edited by Engebretson, M. J., Takahashi, K. and Scholer, M., 273, *AGU*, 1994.

Lühr, H., Lockwood, M., Sandholt, P.E., Hansen, T.L. and Moretto, T., Multi-instrument ground-based observations of a travelling convection vortices event, *Annales Geophys.*, ***14,*** 162-181, 1996.

Lummerzheim, D., Galand, M., Semeter, J., Mendillo, M.J., Rees, M.H. and Rich, F.J., Emission of OI(630 nm) in proton aurora, *J. Geophys. Res.*, ***106,*** 141-148, 2001.

Lysak R.L., Song, Y. and Lee, D.-H., Generation of ULF waves by fluctuations in the magnetopause position, in Solar Wind Sources of Magnetospheric ULF Waves, *Geophys. Mono.* Ser., ***81***, edited by Engebretson, M. J., Takahashi, K. and Scholer, M., 273, AGU, 1994.

McCrea, I. W., Lockwood, M., Moen, J., Pitout, F., Eglitis, P., Aylward, A. D., Cerisier, J.-C., Thorolfsson, A,. and Milan, S. E., ESR and EISCAT observations of the response of the cusp and cleft to IMF orientation changes, *Annales Geophys.*, *18, 1009*-1026, 2000.

Mende, S.B., Heetderks, H., and Frey, H.U., Far ultraviolet imaging from the IMAGE spacecraft, 1. System design, *Space Sci. Rev., 91,* 287, 2000a.

Mende, S.B., Heetderks, H. and Frey, H.U., Far ultraviolet imaging from the IMAGE spacecraft, 3. Spectral imaging of Lyman alpha and OI 135.6 ηm, *Space Sci. Rev.*, ***91***, 287, 2000b.

Meurant, M., Gérard, J.-C, Blockx, C., Hubert, B. and Coumans, V., Propagation of electron and proton shock induced aurora and the role of the interplanetary field and solar wind, *J. Geophys. Res.*, ***109***, 10210, 2004.

Milan, S.E., Lester, M, Greenwald, R.A. and Sofko, G., The ionospheric signature of transient dayside reconnection and the associated pulsed convection return flow, *Annales Geophys.*, ***17,*** 1166-1171, 1999.

Milan, S.E., Lester, M., Cowley, S.W.H. and Brittnacher, M., Dayside convection and auroral morphology during an interval of northward interplanetary magnetic field, *Annales Geophys.*, ***18,*** 436-444, 2000.

Milan, S. E., Lester, M., Cowley, S. W. H., Oksavik, K., Brittnacher, M., Greenwald, R. A., Sofko, G., and Villain, J.-P., Variations in polar cap area during two substorm cycles, *Annales Geophys.*, ***21***, 1121-1140, 2003.

Moen, J., Lockwood, M., Oksavik, K., Carlson, H. C., Denig, W. F., Van Eyken, A.P. and McCrea, I.W., The Dynamics and Relationships of Precipitation, Temperature and Convection Boundaries in the Dayside Auroral Ionosphere, *Annales Geophys.*, in press, 2003.

Murr, D.L. and Hughes, W.J., Reconfiguration timescales of ionospheric convection, *Geophys. Res. Lett.*, ***28***, 2145-2148, 2001.

Murr, D.L., Hughes, W.J., Rodger, A.S., Zesta, E., Frey, H.U. and Weatherwax, A.T. Conjugate observations of travelling convection vortices: The field-aligned current system, *J. Geophys. Res.*, ***107***, A10,1306, 2002.

Murr, D.L. and Hughes, W.J., Solar wind drivers of Travelling Convection Vortices, *Geophys. Res. Let.*, ***30***, 7,1354, 2003.

Newell, P.T. and Meng, C.-I., Dipole tilt angle effects on the latitude of the cusp and cleft/low-latitude boundary layer, *J. Geophys. Res.*, ***94***, 6949-6953, 1989.

Nishida, A., DP-2 and polar substorm, *Planet. And Space Sci.*, ***19***, 205, 1971.

Omholt, A., The optical aurora, *Berlin: Springer,* 1971.

Onsager T.G., Kletzing, C.A., Austin, J.B., and McKiernan, H., Model of magnetosheath plasma in the magnetosphere: Cusp and mantle particles at low-altitudes, *Geophys. Res. Lett., 20,* 479-482, 1993a.

Opgenoorth, H. J., M. Lockwood, D. Alcayde, E. Donovan, M. J. Engebretson, A. P. van Eyken, K. Kauristie, M.Lester, J. Moen, J. Waterman, H. Alleyne, M. Andre, M. W. Dunlop, N. Cornilleau-Wehrlin, P. M. E. Decreau, A. Fazerkerley, H. Reme, R. Andre, O. Amm, A. Balogh, R. Behlke, P.L. Blelly, H. Boholm, E. Borälv, J.M. Bosqued, S. Buchert, M. Candidi, J.C. Cerisier, C. Cully, W.F. Denig, R. Doe, P.Eglitis, R. A. Greenwald, B. Jackal, J. D. Kelly, Ian Krauklis, G. Lu, I. R. Mann, M.F. Marcucci, I. W. McCrea, M. Maksimovic, S. Massetti, A. Masson, D. K. Milling, S. Orsini, F. Pitout, G. Provan, J. M. Ruohoniemi, J. C Samson, J. J. Schott, F. Sedgemore-Schulthess, R. Stamper, P. Stauning, A. Strömme, M. Taylor, A. Vaivads, J. P. Villain, I. Voronkov, J. Wild, and M.

Wild., Coordinated Ground-Based, Low Altitude Satellite and Cluster Observations on Global and Local Scales During a Transient Post-noon Sector Excursion of the Magnetospheric Cusp, *Annales Geophys.* , ***19,*** 1367-1398, 2001.

Østgaard, N., Moen, J., Mende, S.B., Frey, H.U., Immel, T.J., Gallop, P., Oksavik, K. and Fujimoto, M., Estimates of magnetotail reconnection rate based on IMAGE FUV and EISCAT measurements, *Annales Geophys.*, ***23,*** 123-134, 2005.

Parks,G.K., Physics of space plasmas – an introduction, *Redwood City, CA, Addison-Wesley Publishing Co.,* 547, 1991.

Paschmann, G., Baumjohann, W., Sckopke, N., Papamastorakis, I. and Carlson, C.W., *J. Geophys. Res.*, ***91,*** 11099-11115, 1986.

Peredo, M., Slavin, J.A., Mazur, E. and Curtis, S.A., Three-dimensional position and shape of the bow shock and their variations with Alfvénic, sonic and magnetosonic Mack numbers and interplanetary magnetic field orientation, *J. Geophys. Res.*, ***100,*** 7907-7916, 1995.

Pitout, F., Bosqued, J.-M., Alcaydé, D., Denig, W.F. and Rème, H., Observations of the cusp region under northward IMF, *Annales Geophys.*, ***19,*** 1641-1653, 2001.

Pitout, F., Newell, P.T. and Buchert, S.C., Simultaneous high- and low-latitude reconnection: ESR and DMSP observations, *Annales Geophys.*, ***20,*** 1311-1320, 2002.

Potemra, T.A. and Blomberg, L.G., A survey of Pc 5 pulsations in the dayside high-latitude regions observed by Viking, *J. Geophys. Res.*, ***101***, A11, 24801-24814, 1996.

Poulter, E.M., Allan, W., Keys, J.G. and Nielson, E., Plasma trough ion mass densities determined from ULF pulsation eigenperiods, *Planet. Space Sci.*, ***32,*** 1069, 1984.

Rees, M.H. and Luckey, D., Auroral electron energy derived from ratio of spectroscopic emissions. I - Model computations, *J. Geophys. Res.*, ***79***, 5181-5186, 1974.

Rees, M.H, Antarctic upper atmosphere investigations by optical methods, *Planet. Space Sci.*, ***37,*** 955-966, 1989.

Reiff, P.H., Burch, J.L. and Hill, T.W., Solar wind plasma injection at the dayside magnetospheric cusp, *J. Geophys. Res.*, ***82***, 479-491, 1977.

Reiff, P.H., Spiro, R.W. and Burch, J.L., Cusp proton signatures and the interplanetary magnetic field, *J. Geophys, Res.*, ***85,*** 5997-6005, 1980.

Reiff, P.H., Spiro, R.W. and Hill, T.W., Dependence of polar cap potential drop on interplanetary parameters, *J. Geophys. Res.*, ***86,*** 7639-7648, 1981.

Reiff, P.H. and Burch, J.L., IMF B_y – dependent plasma flow and Birkeland currents in the dayside magnetosphere. II – A global model for northward and southward IMF, *J. Geophys. Res.*, ***90,*** 1595-1609, 1985.

Richmond, A.D. and Thayer, J.P., Ionospheric Electrodynamics: A Tutorial, *Magnetic Current Systems. Geophys. Mono., Published by AGU,* 131, 2000.

Ridley, A.J., Clauer, C.R., Lu, G., and Papitashvilli, V.O., Ionospheric convection during non-steady interplanetary magnetic field conditions, *J. Geophys. Res.*, ***102***, 14563-14573, 1997.

Ridley, A.J., Lu, G., Clauer, C.R., and Papitashvilli, V.O., A statistical study of the ionospheric convection response to changing interplanetary magnetic field conditions using the assimilative mapping of ionospheric electrodynamics technique, *J. Geophys. Res.*, ***103***, 4023-4039, 1998.

Rodger, A. S., Ground-Based Imaging of the Magnetospheric Boundaries, *Adv. Space Res.*, ***25,*** 7/8, 1461-1470, 2000.

Roelof, E.C. and Sibeck, D.G., Magnetopause shape as a bivariate function of interplanetary magnetic field Bz and solar wind dynamic pressure, *J. Geophys. Res.*, ***98***, 21421-21450, 1993.

Rosenbauer, H., Gruenwaldt, H., Montgomery, M.D., Paschmann, G. and Sckopke, N., Heos2 plasma observations in the distant polar magnetosphere – The plasma mantle, *J. Geophys. Res.*, ***80,*** 2723-2737, 1975.

Ruohoniemi, J. M. and Baker, K.B., Large-scale imaging of high-latitude convection with Super Dual Auroral Radar Network HF radar observations, *J. Geophys. Res.*, ***103,*** 20 797-20 812, 1998.

Ruohoniemi, J.M. and Greenwald, R.A., The response of high latitude convection to a sudden southward IMF turning, *Geophys. Res. Lett.*, ***25***, 2913-2916, 1998.

Ruohoniemi, J.M., Shepherd S.G. and Greenwald, R.A., The response of the high-latitude ionosphere to IMF variations, *J. Atmos. Sol.-Terr. Phys.*, ***64***, 159-171, 2002.

Samson, J.C., Wallis, D.D., Hughes, T.J., Creutzberg, F., Ruohoniemi, J.M. and Greenwald, R.A., Substorm intensifications and field line resonances in the nightside magnetosphere, *J. Geophys. Res.*, ***97,*** 8495-8518, 1992.

Sanchez, E.R., Siscoe, G.L. and Meng, C.-I., Inductive attenuation of the transpolar voltage, *Geophys. Res. Lett.*, ***18,*** 1173-1176, 1991.

Sandholt, P.E., Henriksen, K., Deehr, C.S., Sivjee, G.G., Romick, G.J. and Egeland, A., Dayside cusp auroral morphology related to nightside magnetic activity, *J. Geophys. Res.*, ***85,*** 4132-4138, 1980.

Sandholt, P.E., IMF control of the polar cusp and cleft auroras, *Adv. in Space Res.*, ***8*** (9)21-(9)34, 1988.

Saunders, M.A., Freeman, M.P., Southwood, D.J., Cowley, S.W., Lockwood, M., Samson, J.C., Farrugia, C.J. and Hughes, T.J., Dayside ionospheric convection changes in response to long-period interplanetary magnetic field oscillations – Determination of the ionospheric phase velocity, *J. Geophys. Res.*, ***97***, 19373-19380, 1992.

Shelley, E.G., Sharp, R.D. and Johnson, R.G., Satellite observations of an ionospheric acceleration mechanism, *Geophys. Res. Letts.*, ***3***, 654-656, 1976.

Sibeck, D.G., Lopez, R.E. and Baumjohann, W., Solar wind dynamic pressure variations and transient magnetospheric signatures, *Geophys. Res. Lett.*, ***16***, 13, 1989a.

S*ibeck, D.G.,** A model for the transient magnetospheric response to sudden solar wind dynamic pressure variations *J. Geophys. Res.*, ***95, 4, 3755-3771, 1990.

Sibeck, D.G. and Crowley, D.J.,Jr., Solar wind dynamic pressure variations and possible ground signatures of flux transfer events, *J. Geophys. Res.*, ***96***, 1, 1669-1683, 1991.

Sibeck, D.G., Transient magnetic field signatures at high latitudes, *J. Geophys. Res.*, ***98,*** 243-256, 1993.

Sibeck, D.G., Trivedi, N.B., Zesta, E., Decker, R.B., Singer, H.J., Szabo, A, Tachihara, H. and Watermann, J., Pressure-pulse interaction with the magnetosphere and ionosphere, *J. Geophys. Res.*, ***108***, A2, 1095, 2003.

Siscoe, G.L. and Huang, T.S., Polar cap inflation and deflation, *J. Geophys. Res.*, ***90***, 543, 1985.

Sivjee, G.G., Romick, G.J. and Deeher, C.S., Optical signatures of some magnetospheric processes on the dayside, *Geophys. Res. Letts.*, ***9***, 676-679, 1982.

Slinker, S.P., Fedder, J.A., Hughes, W.J. and Lyon, J.G., Response of the ionosphere to a density pulse in the solar wind: simulation of travelling convection vortices, *Geophys. Res. Let.*, ***26***, 23, 3549-3552, 1999.

Smith, M.F. and Lockwood, M., Earth's magnetospheric cusps, *Rev. of Geophys.*, ***34***, 233-260, 1996.

Song, P and Russell, C.T., Model of the formation of the low-latitude boundary layer for strongly northward interplanetary magnetic field, *J. Geophys. Res.*, ***97,*** 1411-1420, 1992.

Sonnerup, B.U.Ö., Magnetopause reconnection rate, *J. Geophys. Res.*, ***79***, 1546, 1974.

Sonnerup, B.U.Ö., Paschmann, G., Papamastorakis, I., Sckopke, N., Haerendel, G., Bame, S,J., Asbridge J.R., Gosling, J.T. and Russell, C.T., Evidence for magnetic field reconnection at the Earth's magnetopause, *J. Geophys. Res.*, ***86,*** 10049-10067, 1981.

Sonnerup, B.U.Ö., Papamastorakis, I., Paschmann, G. and Luehr, H., The magnetopause for large magnetic shear – Analysis of convection electric fields from AMPTE/IRM, *J. Geophys. Res.*, ***95***, 10541-10557, 1990.

Southward, D.J., Some features of field line resonances in the magnetosphere, *Planet. Space Sci.*, ***22***, 483, 1974.

Southwood, D.J. and Kivelson, M.G., The magnetohydro-dynamic response of the magnetospheric cavity to changes in the solar wind pressure, *J. Geophys. Res.*, ***95***, 2301, 1990.

Spann, J.F., Brittnacher, M., Elsen, R., Germany, G.A. and Parks, G.K., Initial response and complex polar cap structures of the aurora in response to the January 10, 1997 magnetic cloud, *Geophys. Res. Letts.*, ***25***, 2577-2580, 1998.

Spreiter, J.R., Summers, A.L. and Alksne, A.Y., Hydromagnetic flow around the magnetosphere, *Planet. Space Sci.*, ***14***, 223-253, 1966.

Strickland, D.J., Daniell, R.E.,Jr., Jasperse, J.R. and Basu, B., Transport-theoretic model for the electron-proton-hydrogen atom aurora. 2. Model results, *J. Geophys. Res.*, ***98***, 21533-21548, 1993.

Stubbs, T.J., Lockwood, M., Cargill, P., Fennel, J., Grande, M., Kellett, B., Perry C.H. and Rees, A., Dawn/dusk asymmetry in particles of solar wind origin within the magnetosphere, *Annales Geophys.*, ***19***, 1-9, 2001.

Sivjee, G.C., Romick, G.J. and Deehr, C.S., Optical signatures of some magnetospheric processes on the dayside, *Geophys. Res. Lett.*, ***9***, 676-679, 1982.

Tamao, T., A hydromagnetic interpretation of geomagnetic SSC, *Rep. Ionos. Space Res. Jpn.*, ***18***, 16, 1964.

Thomsen, M.F., Borovsky, J.E. and Skoug, R.M., Delivery of cold, dense plasma sheet material into the near-Earth region, *J. Geophys. Res.*, ***108***, 1151, 2003.

Throp, K., Lockwood, M., Lanchester, B.S., Morley, S.K. and Frey, H.U., Modelling the observed proton aurora and ionospheric convection responses to changes in the IMF clock angle: 1. The persistence of cusp proton aurora, *J. Geophys. Res.*, this issue, 2003.

Todd, H., Cowley, S.W.H., Lockwood, M., Willis, D.M. and Lühr, H., Response time of the high-latitude dayside ionosphere to sudden changes in the north-south component of the IMF, *Planet. Space Sci.*, ***36***, 1415-1428, 1988.

Trivedi, N.B., Sibeck, D.G., Zesta, E., Santos, J.C., Yumoto, K., Kitamura, T., Shinohara, M. and Dutra, S.L.G., Signatures of travelling convection vortices in ground magnetograms under the equatorial electrojet, *J. Geophys. Res.*, ***107***, A6, 2002.

Vegard, L., Hydrogen showers in the auroral region, *Nature*, ***144***, 1089, 1939.

Villain, J.P., Hanuise, C. and Caudal, G., A SAFARI-EISCAT comparison between the velocity of F-region small-scale irregularities and the ion drift, *J. Geophys. Res.*, ***90***, 8433-8443, 1985.

Vorobjev, V.G., Gustafsson, G., Starkov, G.V., Feldstein, Y.-I. and Shevnina, N.F., Dynamics of day and night aurora during substorms, *Planet Space Sci.*, ***23***, 269,1975.

Weimer, D.R., Models of high-latitude electric potentials derived with a least error fit of spherical harmonic coefficients, *J. Geophys. Res.*, ***100***, 19595-19608, 1995.

Wilks, D.S., Statistical methods in the atmospheric sciences, *Academic Press, San Diego,* 1995.

Woch, J. and Lundin, R., Magnetosheath plasma precipitation in the polar cusp and its control by the interplanetary magnetic field, *J. Geophys. Res.*, ***97,*** 1421-1430, 1992.

Wolf, R.A., Magnetospheric configuration, in *Introduction to space physics,* Eds M.G. Kivelson and C.T. Russell, Cambridge, 1995.

Wygant, J.R., Torbert, R.B. and Mozer, F.S., Comparison of S3-3 polar cap potential drops with the interplanetary magnetic field and models of magnetopause reconnection, *J. Geophys. Res.*, ***88,*** 5727-5735, 1983.

Yoshida, N., Fukunishi, H., Frey, H.U., Mende, S.B., Lester, M., Mukai, T and Smith, R.W., Dynamics of duskside proton aurora observed with the Svalbard all-sky imager and the IMAGE satellite under northward IMF condition: November 26, 2000 event, *American Geophys. Union,* Fall meeting, 2001.

Zesta, E., Hughes, W.J. and Engebretson, M.J., A statistical study of travelling convection vortices using the Magnetometer Array for Cusp and Cleft Studies, *J. Geophys. Res.*, ***107***, A10, 1317, 2002.

Zhou, X. and Tsurutani, B.T., Interplanetary shock triggering of nightside geomagnetic activity: Substorms, pseudobreakups, and quiescent events, *J. Geophys. Res.*, ***106***, 18,957-18,967, 2001.

Zhou, X.-Y, Strangeway, R.J., Anderson, P.C., Sibeck, D.G., Tsurutani, B.T., Haerendel, G., Frey, H.U. and Arballo, J.K., Shock aurora: FAST and DMSP observations, *J. Geophys. Res.*, ***108,*** 8019, 2003.

Appendices

A. Coordinate Systems

Earth's Geomagnetic Field

The geomagnetic components (**H**, **D**, **Z**) are measured relative to the geographic (**X**, **Y**, **Z**) system, where **X** and **Y** point to the geographic north and east, respectively. The projection of the magnetic field **B** on the horizontal plane gives the H-component. It is positive in the direction of the magnetic south pole, **D** is the declination angle that **H** makes with **X**.

Geocentric Solar Ecliptic (GSE)

This coordinate system is centred on the Earth, with the x-axis pointing along the Sun-Earth line. The y-axis also lies in the ecliptic plane, in the opposite direction to the Earth's orbit. The z-axis lies perpendicular to both x- and y-axes and points northward out of the ecliptic plane.

Geocentric Solar Magnetospheric (GSM)

This coordinate system is practical when considering interactions between the solar wind and the magnetosphere as it is aligned with the dipole tilt of the Earth's magnetic field. This means that no rotations of coordinates are needed when dealing with interactions between the IMF and the magnetosphere. As with GSE, the x-axis points sunward along the Sun-Earth line. The y-axis is taken as perpendicular to the Earth's magnetic dipole axis, so that the x-z plane contains the dipole axis.

Ground Magnetometer Coordinate System

This coordinate system is used when displaying all the magnetometer data: IMAGE, Greenland East, Greenland West, MM210 and Hermanus. The axes are

orientated along local magnetic north (N), local magnetic east (E) and vertically downward (Z).

B. Statistical Analysis

A generalized look at the statistical methods used in Section 4.1. [c.f. Lockwood et al., 2002]. We evaluate the correlation coefficient between parameters x and y at lag j in the usual way:

$$r_j = \frac{\left| n_j \sum x_i \, y_{i+j} - \sum x_i \sum y_{i+j} \right|}{\left[\left\{ \sum x_i^2 - \left(\sum x_i \right)^2 \right\} \left\{ \sum y_{i+j}^2 - \left(\sum y_{i+j} \right)^2 \right\} \right]^{1/2}}$$

1)

Where all summations are over all i between unity and n_j, the number of pairs of data points at lag j. Substituting y_i for x_i, Equation (1) also gives the autocorrelation function of y, $[\rho_j]_y$. To test for significance level, S, equal to $100\times(1 - c)\%$ where c is the probability that we got the correlation by chance, we use the Students-t statistic:

$$t = |r_j| \left(\frac{N_e - 2}{1 - |r_j|} \right)^{1/2}$$

2)

N_e is the effective number of independent samples, computed from the number of data points n_j, allowing for persistence in the data (Wilks, 1995):

$$N_e = n_j \left(\frac{1-\rho_1}{1+\rho_1} \right)$$

3)

Where ρ_1 is the autocorrelation function at lag 1, which we here take to be the mean of the autocorrelation functions at lag 1 for the two input parameters, $([\rho_1]_x - [\rho_1]_y)/2$.

To test the significance of a difference between two correlation coefficients we use the Fisher-Z test. This involves computation of the Fisher-Z transform:

$$Z(j) = \tfrac{1}{2} \ln \left(\frac{1+|r_j|}{1-|r_j|} \right)$$

4)

and:

$$s = \left[\frac{1}{(n-3)} \right]^{1/2}$$

5)

In particular, we compute Z and s for $r(\delta t)$ (the peak correlation that occurs at a lag $j = \delta t$), and for all other j and $r(j)$. Hence for all j we can compute:

$$z(j) = \left(\frac{Z(\delta t) - Z(j)}{\{s^2(\delta t) + s^2(j)\}^{1/2}} \right)$$

6)

which is normally distributed and thus the value of the significance $S(j)$ of a difference between $r(j)$ and the peak correlation $r(\delta t)$ can be computed from $z(j)$ using a normal distribution.

C. Butterworth Filter

The Butterworth filter provides the best Taylor Series approximation to the ideal low-pass filter response at analogue frequencies $\Omega = 0$ and $\Omega = \infty$; for any order N, the magnitude squared response has $2N$-1 zero derivatives at these locations (maximally flat at $\Omega = 0$ and $\Omega = \infty$). Response is monotonic overall, decreasing smoothly from $\Omega = 0$ to $\Omega = \infty$.

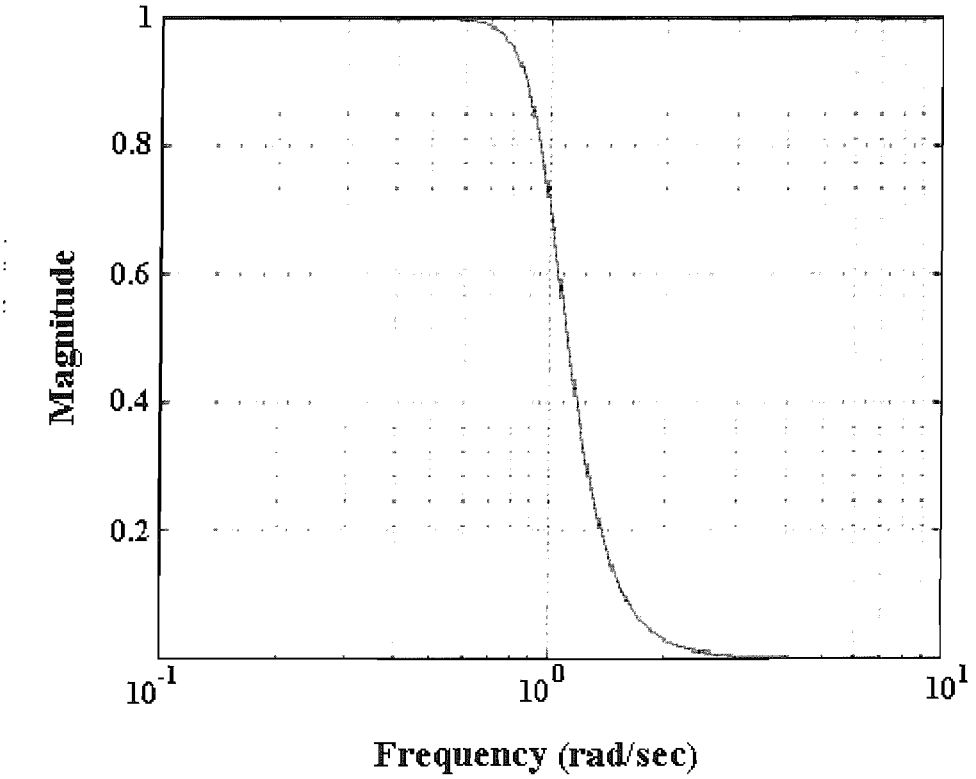

D. Magnetic Activity Indices

- The **Kp index** – was introduced by J. Bartels in 1949. This is short-term forecast describing the expected geomagnetic activity obtained from a number of magnetometer stations at mid-latitudes. When the stations are not greatly influenced by the auroral electrojet currents, conditions are termed magnetically quiet. If the auroral zone expands equatorward, however, these stations can record the effects of the auroral electrojet current system and of the magnetospheric ring current and field-aligned currents that connect it to the ionosphere. This occurs during so-called magnetically disturbed periods. The mid-latitude stations are rarely directly under an intense horizontal current system and thus magnetic perturbations can be dominant in either H or D component. The Kp index utilizes both these perturbations by taking the logarithm of the largest excursion in H or D over a 3-h period and placing it on a scale from 0 to 9.

Kp Index	Activity
0-1	Quiet
2-3	Unsettled
4	Active
5	Minor Storm
6	Major Storm
7-9	Severe Storm

- The **DST (Disturbance Storm Time)** equivalent equatorial magnetic disturbance indices are derived from hourly scalings of low-latitude horizontal magnetic variations. They show the effect of the globally symmetrical westward flowing high altitude equatorial ring current, which

causes the "main phase" depression worldwide in the H-component field during large magnetic storms. Unit = nT.

- The **Ap index** – is a 3-hourly "equivalent amplitude" index of local geomagnetic activity, "a" is related to the 3-hourly Kp index according to the following scale:

Kp	=	0	1	2	3	4	5	6	7	8	9
Ap	=	0	3	7	15	27	48	80	140	240	400